

# **The JADE protein family in renal epithelial cells in the context of cystic kidney disease**

INAUGURAL-DISSERTATION

zur

Erlangung des Doktorgrades  
der Mathematisch-Naturwissenschaftlichen Fakultät  
der Universität zu Köln

vorgelegt von

Lena Kathrin Ebert  
aus Dormagen

Köln 2021

Berichterstatter:  
(Gutachter)

Prof. Dr. Thomas Benzing

Prof. Dr. Thorsten Hoppe

Tag der mündlichen Prüfung: December 8<sup>th</sup>, 2021

# Inhalt

LIST OF FIGURES .....	IV
LIST OF TABLES .....	VI
ABBREVIATIONS .....	VII
1 Abstract .....	1
2 Zusammenfassung.....	2
3 Introduction.....	4
3.1 Polycystic Kidney Diseases .....	4
3.1.1 ADPKD and ARPKD.....	4
3.1.2 Nephronophthisis.....	6
3.1.3 Mouse models of Nephronophthisis.....	7
3.2 Von-Hippel-Lindau disease.....	8
3.3 Primary cilia .....	8
3.4 The ciliary transition zone as gatekeeper.....	9
3.5 The JADE protein family .....	10
3.5.1 JADE1 in the context of Wnt signaling and PKD.....	12
3.5.2 JADE1 as part of the histone acetyltransferase complex.....	15
3.5.3 <i>In vivo</i> functions of Jade1 .....	16
3.5.4 JADE2.....	16
3.5.5 JADE3.....	16
4 Thesis Aims.....	18
5 Materials and Methods .....	19
5.1 Materials.....	19
5.1.1 Chemicals and Reagents.....	19
5.1.2 Assays and Kits .....	22
5.1.3 Buffers and Solutions .....	22
5.1.4 Oligonucleotides.....	26
5.1.5 Plasmids.....	29
5.1.6 Cell lines.....	30
5.1.7 Antibodies.....	30
5.1.8 Enzymes.....	31
5.1.9 Unique target peptides for the PRM assay .....	31
5.1.10 Consumables .....	31
5.1.11 Equipment .....	33
5.1.12 Software and online tools .....	34

5.2	Methods .....	35
5.2.1	Cloning PCR.....	35
5.2.2	Enzymatic digest.....	35
5.2.3	Agarose gel electrophoresis .....	36
5.2.4	Ligation .....	36
5.2.5	Bacterial transformation and plasmid DNA isolation.....	36
5.2.6	Sanger sequencing.....	37
5.2.7	Recombinant protein production.....	37
5.2.8	Cell culture.....	39
5.2.9	Immunoprecipitation .....	42
5.2.10	SDS polyacrylamide gel electrophoresis (SDS-PAGE) and immunoblot .....	43
5.2.11	Colloidal coomassie staining .....	43
5.2.12	Enzyme-linked immunosorbent assay (ELISA).....	44
5.2.13	RNA isolation .....	44
5.2.14	qPCR .....	44
5.2.15	Parallel reaction monitoring (PRM) assay .....	44
5.2.16	Proteome.....	45
5.2.17	Interactome .....	46
5.2.18	mRNA sequencing .....	47
5.2.19	Raw data deposition.....	48
5.2.20	Statistical analyses.....	48
5.2.21	Mouse Work .....	48
6	Results .....	56
6.1	The JADE protein family .....	56
6.1.1	Comparison of structure and expression of JADE family members reveals their high similarity. ....	56
6.1.2	All JADE family members are associated with pVHL and NPH proteins.....	58
6.1.3	Monoclonal JADE3 antibody specifically recognizes human and murine JADE3 .....	61
6.1.4	Subcloning of mIMCD3 cells in preparation of Jade deletion by genome editing .....	65
6.1.5	<i>Jade1/2/3</i> -deficient mIMCD3 cell lines do show neither compensatory upregulation in the other family members nor abnormalities in cell cycle progression under baseline conditions .....	67
6.1.6	Proteomic profiling of <i>Jade</i> -deficient cell lines reveals an upregulation of proteasomal components as a common finding. ....	74
6.1.7	<i>In vitro</i> proteasome assays confirm the role of the Jade protein family in the regulation of the proteasome. ....	80
6.1.8	mRNA expression of proteasomal components is not significantly altered .....	82

6.1.9	Components of the proteasome are part of a Jade protein complex.....	87
6.1.10	Generation of <i>in vivo</i> models for the Jade protein family.....	89
6.2	Generation of knockout models to study NPH.....	96
6.2.1	<i>Glis2</i> mutant mouse models.....	96
6.2.2	<i>Tmem218</i> mutant mouse models .....	99
7	Discussion.....	102
7.1	Jade protein family members share protein interactors related to renal pathology .....	102
7.2	The effect of loss of Jade proteins on cell cycle progression .....	102
7.3	Jade proteins as negative regulator of the proteasome .....	104
7.4	Therapeutic approaches to target the proteasome.....	105
7.5	Loss of a single Jade protein family member does not lead to any obvious phenotype <i>in vivo</i> . . .....	106
7.6	Generation of new models to study renal ciliopathies <i>in vivo</i> .....	108
7.6.1	<i>Glis2<sup>emKO/emKO</sup></i> mice show a late cystic kidney phenotype.....	109
7.6.2	<i>Tmem218<sup>emKO/emKO</sup></i> mice present with cysts arising from distal tubules.....	110
7.6.3	Perspectives of mouse models to study NPH <i>in vivo</i> .....	112
8	Conclusion .....	113
9	References.....	114
10	Publications .....	134
10.1	Publications in Academic Journals .....	134
10.2	Publications in International Academic Conferences.....	134
11	Acknowledgements .....	135
12	Erklärung .....	136

## LIST OF FIGURES

Figure 1. Schematic of different types of cystic kidney diseases compared to a healthy kidney. ....	5
Figure 2. Structural similarity in the JADE protein family. ....	11
Figure 3. Overview of ciliary TZ and BB modulation of WNT signaling. ....	14
Figure 4. Expression profiles of <i>JADE</i> family members across tissues. ....	58
Figure 5. JADE family members interact with pVHL, NPHP4, and NPHP1. ....	59
Figure 6. JADE proteins have the capability to dimerize. ....	60
Figure 7. Antigen selection and production for the generation of JADE2 and JADE3 antibodies. ....	62
Figure 8. Generation of monoclonal antibodies against JADE2 and JADE3. ....	64
Figure 9. Subcloning of mIMCD3 to generate cell lines with a defined genetic background. ....	66
Figure 10. Generation of mIMCD3 mutant cell lines for <i>Jade1/2/3</i> . ....	67
Figure 11. Established mIMCD3 <i>Jade1/2/3</i> -deficient cell lines do not continue to show GFP expression. ....	69
Figure 12. mIMCD3 <i>Jade1/2/3</i> -deficient cell lines reveal no major compensatory upregulation on mRNA and protein level of the other family members under baseline conditions. ....	71
Figure 13. Cell cycle analysis does not show significant changes in the <i>Jade1/2/3</i> -deficient cell lines compared to mIMCD3 wild-type cells. ....	72
Figure 14. Starvation leads to reduced cell cycle arrest in <i>Jade1</i> -deficient cells compared to WT cells. .....	73
Figure 15. Quality control of proteome datasets for <i>Jade1/2/3</i> -deficient and wild-type mIMCD3 cell lines. ....	74
Figure 16. Protein expression profiling of <i>Jade1</i> -deficient cell lines. ....	76
Figure 17. Protein expression profiling of <i>Jade2</i> - and <i>Jade3</i> -deficient cell lines. ....	77
Figure 18. All <i>Jade</i> -deficient cell lines show an upregulation in proteasome associated proteins. ....	79
Figure 19. Components of the protein turnover machinery are upregulated in <i>Jade</i> -deficient cell lines. .....	80
Figure 20. <i>In vitro</i> proteasome activity assay confirms role of Jade proteins in proteasome regulation. .....	81
Figure 21. Transcriptomic expression profiling of <i>Jade</i> -deficient cell lines. ....	83
Figure 22. Transcriptomic expression profiling of <i>Jade2/3</i> -deficient cell lines. ....	85
Figure 23. Mutual regulated genes within the <i>Jade</i> family do not show upregulation of the proteasome or protein turnover machinery. ....	86
Figure 24. Interactome analysis based on co-immunoprecipitations reveals a potential direct link between Jade proteins and proteasomal components. ....	88

Figure 25. Generation of <i>Jade1-deficient</i> mouse models. ....	90
Figure 26. <i>Jade1</i> -deficient mice are not born in Mendelian ratios and have a reduced body weight compared to litter mate controls. ....	91
Figure 27. <i>Jade1<sup>emKO1/emKO1</sup></i> mice show no obvious histological phenotype. ....	93
Figure 28. Generation of <i>Jade2</i> and <i>Jade3</i> mutant mouse models.....	94
Figure 29. <i>Jade2</i> and <i>Jade3</i> mutant mice do not show a histological kidney or liver phenotype at 4 or 6 months of age, respectively. ....	95
Figure 30. Generation of <i>Glis2</i> mutant mouse models. ....	97
Figure 31. <i>Glis2<sub>emKO2</sub></i> mice show a reduced litter size and show a non-Mendelian pattern of inheritance. ....	98
Figure 32. <i>Glis2<sup>emKO2/emKO2</sup></i> mice present with kidney cysts and fibrosis at 1.5 years of age. ....	99
Figure 33. Generation of <i>Tmem218</i> mutant mouse models.....	100
Figure 34. <i>Tmem218<sup>emKO/emKO</sup></i> mice show cysts arising from the distal tubule.....	101

## LIST OF TABLES

Table 1. List of chemicals and reagents used. ....	19
Table 2. List of assays and kits used. ....	22
Table 3. List of buffers and solutions used. ....	22
Table 4. List of oligonucleotides used for genotyping.....	26
Table 5. List of oligonucleotides used for sequencing .....	27
Table 6. List of oligonucleotides used for cloning .....	27
Table 7. List of oligonucleotides used for qPCR .....	28
Table 8. List of guide RNAs .....	28
Table 9. List of plasmids used.....	29
Table 10. List of cell lines.....	30
Table 11. List of primary antibodies used. ....	30
Table 12. List of secondary antibodies used. ....	30
Table 13. List of enzymes used.....	31
Table 14. List of unique target peptides for the PRM assay. ....	31
Table 15. List of consumables used.....	31
Table 16. List of equipment used. ....	33
Table 17. List of software used.....	34
Table 18. List of websites and online tools used.....	35
Table 19. List of reaction compositions for PCRs of Jade mutant cell lines. ....	40
Table 20. List of cycling conditions used for performing PCRs of Jade mutant cell lines.....	41
Table 21. List of reaction compositions of the genotyping PCRs. ....	50
Table 22. List of cycling conditions used for performing genotyping PCRs. ....	51

## ABBREVIATIONS

% (v/v)	Volume concentration
% (w/v)	Mass concentration
(NH <sub>4</sub> ) <sub>2</sub> SO <sub>4</sub>	Ammonium sulfate
°C	Degree celsius
µg	Microgram
µL	Microliter
µM	Micromolar
AATF	Apoptosis Antagonizing Transcription Factor
ADPKD	Autosomal-dominant polycystic kidney disease
ADPLD	Autosomal-dominant polycystic liver disease
Agt	Angiotensinogen
AKI	Acute kidney injury
AKT	Ak thymoma
ANOVA	Analysis of variance
Apc	APC Regulator Of WNT Signaling Pathway
APS	Ammonium persulfate
Arl13b	ADP-ribosylation factor-like 13B
ARPKD	Autosomal-recessive polycystic kidney disease
ATP	Adenosine triphosphate
BB	basal body
BBS	Bardet-Biedl syndrome
BCA	Bicinchoninic acid
Bcl2	B-cell lymphoma 2
bp	base pairs
BSA	Bovine serum albumin
CaCl <sub>2</sub>	Calcium Chloride
Cas9	CRISPR-associated protein 9
ccRCC	clear cell renal cell carcinoma
cDNA	complementary DNA
CECAD	Cologne Cluster of Excellence in Cellular Stress Responses in Aging-associated Diseases
CEP	Centrosomal protein
Chr.	Chromosome
CK1α	Casein kinase 1 alpha
CLS	Ciliary localization sequence
CMV	Cytomegalovirus
CRISPR	Clustered Regularly Interspaced Short Palindromic Repeats
crRNA	crispr RNA
DAPI	4',6-diamidino-2-phenylindole
ddH <sub>2</sub> O	Double distilled water
DDI2	DNA Damage Inducible 1 Homolog 2
DMEM	Dulbecco's Modified Eagle's medium
DMSO	Dimethyl sulfoxide
DNA	Deoxyribonucleic acid
dNTP	Deoxyribonucleotide triphosphate
dotp	Dot product

DTT	Dithiothreitol
Dvl1	Dishevelled segment polarity protein 1
DZIP1L	DAZ Interacting Zinc Finger Protein 1 Like
ECL	Enhanced chemiluminescence
ECM	Extra cellular matrix
EDTA	Ethylenediaminetetraacetic acid
EEZy	Easy Electroporation of Zygotes
EGTA	Triethylene glycol diamine tetraacetic acid
ELISA	Enzyme-linked immunosorbent assay
emKO	endonuclease-mediated knockout
EPC1	Enhancer Of Polycomb Homolog 1
EPS	Epidermal growth factor receptor pathway substrate
ERK	Extracellular signal-regulated kinase
ESRD	End stage renal disease
F / FLAG	FLAG-tag
FACS	Fluorescence Activated Cell Sorting
FBS	Fetal bovine serum
FC	Fold change
FGF	Fibroblast Growth Factor
FL2	Channel 2, S2e, filter set 525/30 (510–540)
fp	Forward primer
FSC	Forward scatter
fsp	Forwards sequencing primer
g	Gram
G0	Gap 0 phase
G1	Gap 1 phase
G2	Gap 2 phase
GFP	Green fluorescent protein
GLIS2	GLIS Family Zinc Finger 2
GO	Gene ontology
GOBP	Gene ontology biological processes
GOCC	Gene ontology cellular compartments
GOMF	Gene ontology molecular functions
gRNA	guide RNA
GSK3 $\beta$	Glycogen-synthase-kinase-3 $\beta$
h	Hours
H2AX	H2A.X Variant Histone
H <sub>2</sub> O	Water
H <sub>2</sub> O <sub>2</sub>	Hydrogen peroxide
H <sub>2</sub> O <sub>2</sub>	Hydrogen Peroxide
H3/4	Histone H3/H4
HAT	Histone acetyltransferase
HBO1	see KAT7
HCl	Hydrogen chloride
HEK	Human embryonic kidney
HIS	Histidine-tag
Hprt1	Hypoxanthine Phosphoribosyltransferase 1
HRP	Horseradish peroxidase
HSP90	Heat shock protein 90

IB	Immunoblot
iBAQ	Intensity-based absolute quantification
ID4	Inhibitor of DNA binding 4
IFT	Intraflagellar transport
IgG	Immunoglobulin G
indel	insertion or deletion of bases
ING	Inhibitor Of Growth Family Member
INVS	Inversin
IP	Immunoprecipitation
IPTG	Isopropyl- $\beta$ -D-thiogalactopyranosid
Iqcb1	IQ Motif Containing B1
JADE	Gene for apoptosis and differentiation in epithelia
JADE1L	long isoform of JADE1
JADE1S	short isoform of JADE1
JBTS	Joubert syndrome
jck	juvenile cystic kidney
Kat7	Histone acetyltransferase KAT7
kb	Kilobase
KCl	Potassium chloride
KCl	Potassium chloride
kDa	Kilodalton
KEGG	Kyoto Encyclopedia of Genes and Genomes
Kif3a	Kinesin family member 3A
KO	Knockout
L	Liter
LB Medium	Lysogeny broth
LFQ	Label-free quantification
LGR5	Leucine-rich repeat-containing G-protein coupled receptor 5
Lrp2	Low Density Lipoprotein receptor-related Protein 2
LSD1	Lysine-specific histone demethylase 1A
M	Mitosis
mA	Milliampere
mg	Milligram
MgCl <sub>2</sub>	Magnesium chloride
MgCl <sub>2</sub>	Magnesium chloride
MgSO <sub>4</sub>	Magnesium sulfate
mIMCD3	Mouse inner medullary collecting duct cell lines
min	Minutes
miR	microRNA
MKS	Meckel-Gruber syndrome
mL	Milliliter
mM	Millimolar
mRNA	Messenger RNA
MS	Mass spectrometry
MSX1	Msh Homeobox 1
mTor	mechanistic target of rapamycin
Na <sub>2</sub> HPO <sub>4</sub>	Sodium hydrogen phosphate
Na <sub>3</sub> VO <sub>4</sub>	Sodium orthovanadate

Na <sub>4</sub> P <sub>2</sub> O <sub>7</sub>	Tetrasodium pyrophosphate
NaAc	Sodium acetate
NaCl	Sodium chloride
NaCl	Sodium chloride
Na-DOC	Sodium deoxycholate
NaF	Sodium fluoride
NaN <sub>3</sub>	Sodium azide
NaOH	Sodium hydroxide
NCBI	National Center for Biotechnology Information
NDS	Normal donkey serum
NEB	New England BioLabs
Nek8	NIMA Related Kinase 8
Ni	Nickel
NLS	Nuclear Localization Sequence
nM	Nanomolar
Nos1	Nitric oxide Synthase 1
NPC	Nuclear Pore Complex
NPH	Nephronophthisis
NPHP	Nephrocystin
Nphs1	NPHS1 Adhesion Molecule, Nephrin
Nphs2	NPHS2 Stomatin Family Member, Podocin
NRF	Nuclear Respiratory Factor
NTA	Nitrilotriacetic acid
OD	Optical density
Oxtr	Oxytocin receptor
p-value	Probability
p53	Tumor suppressor p53
PAA	Polyacrylamide
PAGE	Polyacrylamide gel electrophoresis
PAM	Protospacer adjacent motif
PAS	Periodic acidic schiff
PBS	Phosphate-buffered saline
PC1	Polycystin 1
PC2	Polycystin 2
PCP	Planar cell polarity
PCR	Polymerase chain reaction
PEG	Polyethylenglycol
Pen-Strep	Penicillin-Streptomycin
PEST	candidate destabilizing motif
PFA	Paraformaldehyde
PHD	Plant Homeodomain
PHF	Plant homeo domain finger
PKD	Polycystic kidney disease
PKHD1	Polycystic kidney and hepatic disease 1
Plk1	Polo-like kinase 1
PMSF	Phenylmethylsulfonyl fluoride
PNI	Pronuclear injection
PRM	Parallel reaction monitoring
PtdIns	Propidium iodide

pVHL	Von-Hippel-Lindau protein
qPCR	quantitative PCR
Rap1	Ras-proximate-1
RCC	Renal cell carcinoma
RIPA	Radioimmunoprecipitation assay buffer
RNA	Ribonucleic acid
ROR	Receptor tyrosine kinase-like orphan receptor 2
rp	Reverse primer
Rpgrip1l	Retinitis pigmentosa GTPase regulator-interacting protein 1-like
RPMI	Roswell Park Memorial Institute
rsp	Reverse sequencing primer
RT	Room temperature
s	Second
SD	Standard deviation
Sdccag8	Serologically Defined Colon Cancer Antigen 8
SDS	Sodium dodecyl sulfate
SEM	Standard error of the mean
SEPT2	Septin 2
sgRNA	single-guide RNA
SOC	Super optimal broth medium
SP2/ab	Murine Hematopoiesis myeloma cell line
ssODN	single-stranded oligodeoxynucleotides
TAE	Tris-acetate-EDTA
TEAB	(Triethyl)ammonium bicarbonate
TEMED	N,N,N',N'-tetramethylethylenediamine
TGF	Transforming growth factors
Tip60	60kD Tat-interactive Protein
Tm	Melting temperature
TMB	3,3',5,5'-Tetramethylbenzidine
TMEM/Tmem	Transmembrane
tracrRNA	trans-activating crispr RNA
TRC	Transmembrane domain recognition complex
Tris	Tris(hydroxymethyl)aminomethane
tRNA	transfer RNA
TZ	Transition Zone
U	Units
Umod	Uromodulin
UPS	Ubiquitin-proteasome system
V	Volts
V5	V5-tag
VHL	Von-Hippel-Lindau
Wnt	Wingless/Int1
WT	Wild-type
x g	Standard gravity
YAP1	Yes-associated protein 1

## 1 Abstract

Nephronophthisis (NPH) is the number one genetic cause of end-stage renal disease in children. Since there are no causative treatment options available, the disease usually leads to dialysis or kidney transplantation by the medium age of 13. By now, several genes (*NPHP1-20*) have been identified whose mutations lead to NPH. Characteristics for NPH are interstitial fibrosis, tubular basement membrane thickening, and cyst formation in the kidney. Renal cyst formation is a shared feature of NPH and several other inherited (poly)cystic kidney diseases (PKD), as well as von-Hippel-Lindau (VHL) disease. VHL disease is caused by mutations in the *VHL* gene encoding for the protein pVHL. Moreover, loss of pVHL is also observed in most cases of sporadic renal cell carcinoma (RCC), a very frequent urogenital tumor. Recent groundbreaking studies demonstrated that primary cilia play a pivotal role in the pathogenesis of PKD and cancer biology. As tiny sensory organelles projecting from almost all mammalian cells, primary cilia transmit signals from the environment into the cell and modulate multiple signaling pathways, including Sonic Hedgehog signaling, Hippo signaling, and Wnt signaling, as well as cell cycle progression. The putative E3 ubiquitin ligase JADE1 has been found to interact with various ciliopathy-associated proteins, including pVHL and NPH proteins encoded by the *NPHP* genes. Thus, JADE1 might be involved in the pathogenesis of both VHL disease and NPH. Importantly, JADE1 forms a protein family with JADE2 and JADE3, the functions of which are still largely unknown.

The focus of this work was to unravel the functions of the JADE protein family members, including their shared and distinct role in transcriptional regulation in renal epithelial cells and their impact on the pathogenesis of NPH, VHL disease, and RCC. To this end, two individual loss-of-function cell lines for each of the JADE family members were generated using CRISPR/Cas9-mediated genome engineering. These cell lines were used to study the distinct and mutual functions of *Jade1*, *Jade2*, and *Jade3* in differentiated renal tubular epithelial cells using unbiased transcriptomic and proteomic approaches followed by comprehensive bioinformatic analyses. Moreover, we generated transgenic mouse models to study the loss of each individual Jade protein *in vivo*. In addition, NPH mouse models were generated with the intention to resemble the human phenotype of NPH and to gain novel insights into the disease mechanisms.

The analysis of the Jade-deficient cell lines provided new insight into the role of Jade proteins in several signaling pathways related to cyst formation and cancer development, including Rap1 signaling, focal adhesion and actin cytoskeleton regulation. In addition, we observed increased expression of proteasomal components and augmented proteasomal activity in all cell lines. Moreover, the newly generated *Tmem218<sup>emKO/emKO</sup>* mouse line closely resembles human NPH, which will be a highly valuable preclinical model to study molecular mechanisms of NPH.

## 2 Zusammenfassung

Die zystische Nierenerkrankung Nephronophthise (NPH) ist die häufigste genetische Ursache eines terminalem Nierenversagens bei Kindern und Jugendlichen. Bislang wurden zahlreiche Gene (*Nphp1-20*) identifiziert, deren Mutationen ursächlich für eine NPH sind. Charakteristisch für die NPH ist die Trias aus interstitieller Fibrose, einer Verdickung und Aufsplitterung der tubulären Basalmembran und der Entstehung von kortikomedullären Zysten in der Niere. Da es keine kurativen Behandlungsmöglichkeiten gibt, führt diese Erkrankung in der Regel zur Notwendigkeit einer Nierenersatztherapie, also der Dialyse oder einer Nierentransplantation. Zur Entstehung von renalen Zysten kommt es auch bei weiteren erblichen zystischen Nierenerkrankungen (*polycystic kidney disease*; PKD), etwa der häufigen autosomal-dominanten PKD (ADPKD) oder der autosomal-rezessiven PKD (ARPKD), sowie beim von-Hippel-Lindau (VHL) Syndrom. Nierenzysten beim VHL Syndrom, das durch Mutationen im Gen *VHL* ausgelöst wird, gehen als prä maligne Zysten der Entstehung eines klarzelligen Nierenzellkarzinoms (clear-cell renal cell carcinoma; ccRCC) voraus. Der Verlust von *VHL* wird auch bei den meisten Fällen eines sporadischen ccRCC beobachtet. Fundamentale Studien konnten zeigen, dass primäre Zilien eine entscheidende Rolle der Pathogenese von PKD spielen und auch bei der Entstehung des ccRCC und weiterer Tumore wichtig sind. Als kleine sensorische Organellen befinden sie sich auf der Oberfläche von fast allen Zellen. Dort übertragen sie Signale von der Zellumgebung in die Zelle hinein und modulieren viele Signalwege, wie etwa den Sonic Hedgehog, PDGF oder WNT Signalweg, aber auch die Progression des Zellzyklus. Die mutmaßliche E3 Ubiquitin Ligase JADE1 wurde als Interaktor von mehreren Ziliopathie-assoziierten Proteinen identifiziert, unter anderem von pVHL und von den NPH Proteinen welche von den *NPHP* Genen kodiert werden. Daraus resultierte die Hypothese, dass JADE1 an der Pathogenese der NPH, des VHL Syndroms sowie des ccRCC beteiligt sein könnte. Die Rolle und Funktion der beiden anderen Mitglieder der JADE Proteinfamilie (JADE2 und JADE3) war bislang weitestgehend unbekannt.

Der Fokus dieser Arbeit liegt auf der Entschlüsselung der Funktionen der JADE Proteinfamilienmitglieder, einschließlich ihrer gemeinsamen und individuellen Funktionen in der transkriptionellen und translationalen Regulation in renalen Epithelzellen und ihrer Auswirkung auf die Pathogenese der NPH und des VHL Syndroms. Um dies zu erreichen, wurden zwei unterschiedliche „Loss-of-Function“ Zelllinien für jedes der JADE Familienmitglieder mit Hilfe von CRISPR/Cas9-basiertem Genome Editing generiert. Diese Zelllinien wurden genutzt, um gemeinsame und unterschiedliche Funktionen von *JADE1*, *JADE2* und *JADE3* in renalen Tubulusepithelzellen zu untersuchen. Darüber hinaus haben wir *Jade1/2/3*-defiziente Mausmodelle generiert, um die Funktion der Jade Proteine *in vivo* analysieren zu können. Als Ergänzung dazu haben wir neue NPH Mausmodelle

hergestellt, die viele Aspekte des humanen Phänotyps der NPH widerspiegeln und dazu genutzt werden können, Erkrankungsmechanismus zu studieren.

Die Analyse der Jade-defizienten Zelllinien führte zu neuen Erkenntnissen der Rolle der Jade Proteine in verschiedenen Signalwegen im Zusammenhang mit der Entstehung von Zysten und der Entwicklung von Krebserkrankungen. Als Hinweis auf eine gemeinsame Funktion der Jade Proteine, haben wir eine erhöhte Expression von proteasomalen Komponenten und damit einhergehend eine gesteigerte proteasomale Aktivität in allen Jade-defizienten Zelllinien gefunden. Darüber hinaus zeigt ein im Rahmen dieser Arbeit neugeneriertes Mausmodell mit einer Mutation in *Tmem218* einen der humanen NPH sehr ähnlichen Phänotyp und wird somit ein sehr wertvolles vorklinisches Modell sein, um den molekularen Mechanismus der NPH zu entschlüsseln.

## 3 Introduction

### 3.1 Polycystic Kidney Diseases

Polycystic kidney diseases (PKD) are characterized by kidneys presenting with dilated tubules and liquid-filled cysts (Watnick and Germino, 2003). These arise from the renal tubular epithelial cells of the nephron, cause disruption of the tubular architecture and lead to various degrees of impairment of renal function (Kagan et al., 2017). PKD comprise multiple different disease entities (see following paragraphs), of which the clinical presentation is very heterogeneous: The age of onset varies from prenatal to adulthood (Mitchison and Valente, 2017). Cyst number and size, localization within the kidney, symptom severity, and disease progression are diverse (Wilson, 2009). The renal phenotype can coincide with various extra-renal manifestations (Kagan et al., 2017). In most patients, PKD progresses to end-stage renal disease (ESRD) requiring dialysis and/or kidney transplantation. There are currently no treatment or preventive strategies available (Bergmann et al., 2018). Most PKD are hereditary disorders, even though there are sporadic cases of PKD occurring during development, aging, or as a result of medical treatment (Fick and Gabow, 1994; Wilson and Falkenstein, 1995). Hereditary PKD are mainly monogenetic, i.e., caused by mutations in one individual gene in a dominant or recessive fashion. So far, mutations in more than 95 disease-causing genes have been discovered (Kagan et al., 2017; Vivante and Hildebrandt, 2016).

#### 3.1.1 ADPKD and ARPKD

The most frequent hereditary PKD, with a prevalence of 1:400-1000 worldwide, is autosomal dominant polycystic kidney disease (ADPKD) (Bergmann et al., 2018). It affects more than 10 million people globally and is not only the most prevalent inherited progressive kidney disorder but also the most common potentially lethal monogenetic disorder (Torres et al., 2007). It is characterized by the progressive formation of numerous cysts resulting in massively enlarged kidneys (Figure 1A,B) and loss of kidney function (Grantham et al., 2006). Additional renal symptoms include hypertension, pain, kidney stones, and infections of cysts and the urinary tract. Common extra-renal manifestations include cysts in the liver, the seminal vesicles, and the pancreas, as well as vascular alterations leading to rare but severe intracranial aneurysms (Hildebrandt et al., 2011; Kagan et al., 2017). The disease is typically diagnosed in early adulthood (Cornec-Le Gall et al., 2013; Müller and Benzing, 2018). However, in a limited number of cases, the ADPKD is already observed in children (MacDermot et al., 1998). The average age of ADPKD patients when reaching ESRD is 50-60, necessitating dialysis or kidney transplantation (Müller and Benzing, 2018; Spithoven et al., 2014). ADPKD is caused by mutations in *PKD1* (~80 % of cases) and *PKD2* (15-20 % of cases), which encode for the proteins Polycystin1 (PC1) and Polycystin2 (PC2) respectively (Bergmann, 2017; Torres et al., 2007). The genetic mutations in the

remaining cases are either unknown or are rare mutations in other loci (Cornec-Le Gall et al., 2018). Both, PC1 and PC2 mainly localize to the primary cilium, but also to tight junctions, adherens junctions, desmosomes, and focal adhesions. PC2 also localizes to the endoplasmic reticulum and the Golgi apparatus (Bergmann and Weiskirchen, 2012; Bergmann et al., 2018; Hildebrandt et al., 2011; Scheffers et al., 2002). The mechanisms underlying ADPKD development are not fully understood. It is known that the polycystins play a role in several cellular signaling pathways, including  $Ca^{2+}$ , cAMP, mTOR, WNT, VEGF, and Hippo signaling (Bergmann et al., 2018; Müller and Schermer, 2020).

Autosomal recessive polycystic kidney disease (ARPKD) is a PKD presenting *in utero*, perinatally, or in infancy (Bergmann et al., 2018). Compared to ADPKD, it is much rarer, with an overall prevalence of 1:10.000 in newborns, and it is often more severe with about 50% of ARPKD cases leading to ESRD within the first decade of life (Bergmann et al., 2018; Hoyer, 2015). ARPKD patients present with cysts primarily derived from the renal distal tubules and collecting ducts, enlarged kidneys, and hepatic fibrosis, often leading to the need for a combined kidney and liver transplantation (Hoyer, 2015). The primary genetic cause of ARPKD are mutations in PKD and hepatic disease 1 (*PKHD1*), encoding for fibrocystin (FC) (Onuchic et al., 2002; Ward et al., 2002). FC also localizes to the primary cilium and basal body (Ward et al., 2003). The functions of FC are still mainly unknown. It is known that the cytoplasmic tail is cleaved and can translocate to the nucleus. (Hiesberger et al., 2006; Kaimori et al., 2007). Recently, mutations in a second gene, DAZ-interacting zinc finger protein 1-like (*DZIP1L*), were suggested to cause ARPKD (Lu et al., 2017). However, the patients do not display any liver phenotype. *DZIP1L* localizes to the ciliary transition zone (TZ) and is known to act with Septin 2 (*SEPT2*) which plays a role in maintaining the periciliary diffusion barrier at the TZ (Lu et al., 2017).

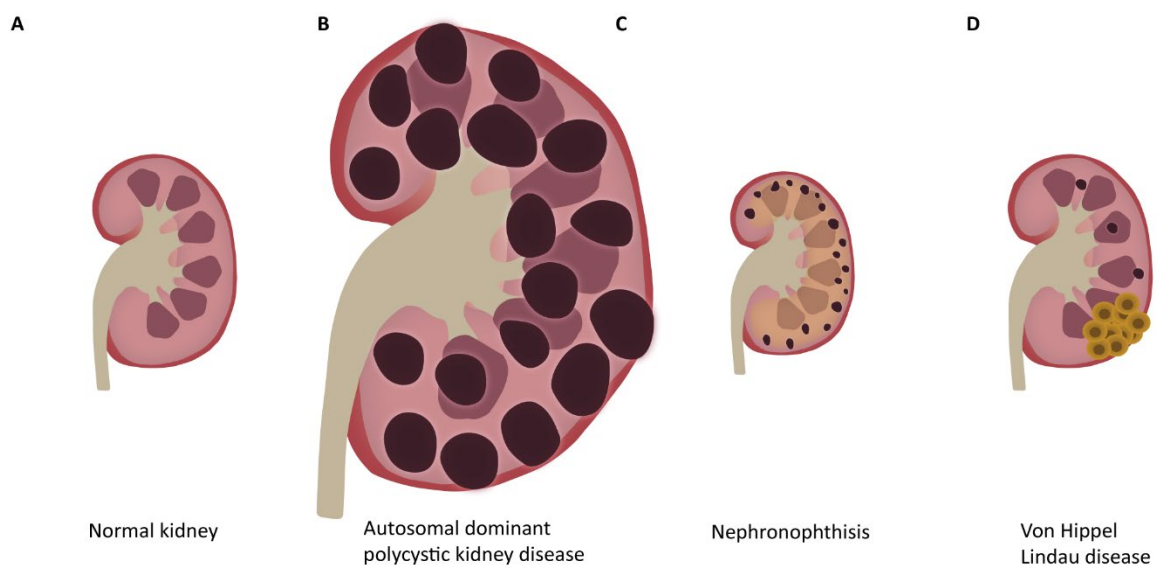


**Figure 1. Schematic of different types of cystic kidney diseases compared to a healthy kidney. (A) Healthy kidney. (B) ADPKD is characterized by massively enlarged kidneys with large cysts. (C) Nephronophthisis is characterized by small to normal-sized kidneys, corticomedullary cysts, and fibrosis. (D) VHL disease causes the formation of small cysts in addition to tumors.**

### 3.1.2 Nephronophthisis

Nephronophthisis (NPH) is an autosomal recessive cystic kidney disease and belongs, with a prevalence between 1:50,000 and 1:1,000,000, to the group of rare diseases (Stokman et al., 1993). Nonetheless, it is the most frequent genetic cause of ESRD within the first three decades of life (Srivastava et al., 2018). NPH is caused by mutations in several genes, with 20 *NPHP* genes being identified so far (Srivastava et al., 2018), and even more are proposed to cause NPH or an NPH-like phenotype (Hurd et al., 2013; O'Toole et al., 2010; Sang et al., 2011; Utsch et al., 2006). Since the known mutations only account for about a third of the cases, it is very likely that NPH causing mutations in other genes will be discovered (Hildebrandt et al., 2009). Moreover, it has also been suggested that mutational load in the form of oligogenicity and triallelism might play a role in the development and progression of NPH (Srivastava et al., 2018). Phenotype, onset, progression, and extra-renal manifestations are diverse and dependent on the mutated gene as well as the type of mutation (Wolf and Hildebrandt, 2011).

The most frequently mutated gene is *NPHP1*, accounting for about 21 % of cases and causing the juvenile form of NPH (Hildebrandt et al., 1997, 2009; Saunier et al., 1997). The median age of developing ESRD is 13 years (König et al., 2017; Stokman et al., 1993). Juvenile NPH is mainly characterized by corticomedullary cysts, tubulointerstitial nephritis, and thickening of the tubular basement membrane (Figure 1C). In contrast to ADPKD and ARPKD, the kidneys are of normal or reduced size (Wolf and Hildebrandt, 2011). With a clinical phenotype that largely resembles the juvenile form, but shifts the mean age of ESRD to 19 years, the adolescent form might be more of an extension of the juvenile form, and is predominantly caused by mutations in *NPHP3* (Olbrich et al., 2003; Omran et al., 2000). A third variant, infantile NPH, is rare with a severe phenotype that can already present in utero and leads to ESRD typically within the first year of life (Gagnadoux et al., 1989). Phenotypically it differs from the other variants of NPH, presenting with enlarged cystic kidneys and no changes in the tubular basement membrane (Wolf and Hildebrandt, 2011). Most commonly mutated genes are *INVS* (*NPHP2*) and *NPHP3* (Haider et al., 1998; Otto et al., 2003; Tory et al., 2009). Approximately 20% of NPH cases present with extra-renal manifestations (Salomon et al., 2009). The most frequently affected organs include retina, brain, and liver (Srivastava et al., 2018). Associated syndromes include Senior-Løken syndrome, Joubert syndrome (JBTS), Bardet-Biedl syndrome (BBS), Meckel-Gruber syndrome (MKS) and others (Hildebrandt et al., 2009, 2011).

Strikingly in the last decade, it became evident that most proteins encoded by genes involved in NPH and associated syndromes (including ARPKD and ADPKD) either localize to primary cilia or the centrosome, or play a role in ciliary function (Hildebrandt et al., 2011; Kagan et al., 2017).

### 3.1.3 Mouse models of Nephronophthisis

There is still an enormous lack of knowledge regarding the underlying mechanisms in NPH and the functions of NPH proteins, and there are currently no specific treatment options available other than renal replacement therapy. Because of the complex nature of the pathologies, most of the questions regarding the disease mechanisms can only be studied *in vivo* with suitable NPH mouse models approximating the human NPH phenotype. Moreover, these will be crucial to investigate the role of disease-related proteins such as the Jade protein family *in vivo*.

Over the last few decades, many approaches were published aiming to generate mouse models for PKD and, in particular, for NPH. The most direct approach includes the generation of mouse lines carrying null alleles for various NPHs. So far, *Nphp1-12* have been targeted to generate mouse models resembling the corresponding human phenotypes. Out of these models, the *Glis2 (Nphp7)* mutant mouse model is the only one clearly displaying all of the hallmarks of human NPH (Attanasio et al., 2007; Kim et al., 2008). In addition, the *Sdccag8 (Nphp10)* (Airik et al., 2014) develops a renal phenotype reminiscent of NPH. The most frequent kidney phenotype in NPH mutant mice, however, is a PKD disease with massively enlarged kidneys mimicking the renal phenotype of ADPKD rather than NPH. This has been observed in mice lacking functional alleles of *Nphp3* (Omran et al., 2001) and *Tmem67 (Nphp11)* (Cook et al., 2009). Mice carrying the *jck* mutation in *Nek8 (Nphp9)* also develop an ADPKD-like renal phenotype (Atala et al., 1993), while a knockout of *Nphp9* results in perinatal lethality with only a few glomerular cysts in the kidneys at P0 (Manning et al., 2013). Retinal degeneration is the most frequent extra-renal phenotype occurring with and without renal defects in NPH mouse models (*Nphp1* (Louie et al., 2010), *Nphp4* (Won et al., 2011), *Cep290 (Nphp6)* (Chang et al., 2006), *Rpgrip1l (Nphp8)* (Won et al., 2009), *Sdccag8 (Nphp10)* (Airik et al., 2014), *Tmem67 (Nphp11)* (Collin et al., 2012)). Other phenotypes in NPH mutant mice include early/embryonic lethality, male infertility, *situs inversus*, and heart abnormalities (Bergmann et al., 2008; Jiang et al., 2008; McQuinn et al., 2001; Morgan et al., 1998; Ronquillo et al., 2016; Stottmann et al., 2009; Vierkotten et al., 2007; Won et al., 2011).

Besides directly targeting NPH proteins, there are several studies on mouse models presenting with a cystic kidney phenotype targeting primarily ciliary proteins (Davenport et al., 2007; Jonassen et al., 2008; Lin et al., 2003). However, these mice present mainly with a polycystic kidney phenotype. One exception is a mouse model with a deletion of the apoptosis antagonizing transcription factor (AATF) in tubular epithelial cells, which develop kidney phenotypes showing the hallmarks of human NPH, including tubular atrophy, interstitial fibrosis, and cysts at the corticomedullary border (Jain et al., 2019). This model strengthens the connection between ciliary signaling defects and DNA damage response pathways in ciliopathies. An additional exception is *Tmem218*, which was first connected to NPH in a large-scale phenotypic screening of knockout mice presenting with PKD and retinal

degradation (Vogel et al., 2015). In addition, the knockout of the polarity protein Mals3 also results in hypomorphic cystic kidneys reminiscent of NPH (Olsen et al., 2007).

### 3.2 Von-Hippel-Lindau disease

Von-Hippel-Lindau (VHL) disease is an hereditary autosomal dominant cancer syndrome with a prevalence of 1:35,000 (Robinson and Ohh, 2014). Tumor formation occurs when, in addition to the heterozygous germline mutation of one *VHL* allele, the remaining wild-type allele is inactivated by a somatic mutation ('second hit') or epigenetically, leading to loss of the VHL protein (pVHL) (Joosten et al., 2018; Knudson, 1971; Robinson and Ohh, 2014; Smits et al., 2008). Patients have a high risk of developing benign tumors in the central nervous system, retina, and adrenal glands, as well as clear cell renal cell carcinoma (ccRCC), a malignant tumor of the kidney (Tarade and Ohh, 2018). ccRCC is the primary cause of morbidity and mortality in VHL disease (Robinson and Ohh, 2014). Moreover, sporadic ccRCC, the most common form of kidney cancer (Figure 1D), also presents with VHL mutations in about 60-80 % of cases (Baldewijns et al., 2008; van Houwelingen et al., 2005; Moore et al., 2011; Shuin et al., 1994). Loss of functional pVHL in the kidney has also been linked to premalignant renal cysts formation (Lubensky et al., 1996; Mandriota et al., 2002). Additionally, like many other proteins linked to PKD, pVHL has been shown to localize to the primary cilium (Schermer et al., 2006).

### 3.3 Primary cilia

Primary cilia are tiny antennae-like organelles projecting from the surface of almost all mammalian cells. In the kidney, they were first observed in 1898 (Zimmermann, 1898), however, it took almost a century before ciliary (dys)function was linked to human diseases (Barr et al., 2001; Pazour et al., 2000) and cilia research became a focus. Today, the importance of the sensory organelle is well established. In 1999, Maureen Barr was the first one to link PKD to primary cilia (Barr and Sternberg, 1999; Barr et al., 2001).

Cilia are microtubule-based structures, which are anchored at the plasma membrane by a basal body (BB). The transition zone (TZ) is formed at the base of the cilium and on top of the BB. The TZ is characterized by Y-shaped structures connecting the membrane with the cytoskeleton. The TZ is a highly specialized ciliary domain that acts as a gatekeeper and tightly regulates the entry and exit of proteins synthesized in the cytoplasm (Reiter et al., 2012). The microtubule-based ciliary cytoskeleton is called the axoneme and is covered by the ciliary membrane. This ciliary membrane is contiguous with the plasma membrane but shows a distinct composition (Garcia et al., 2018). In many cell types, the transition from the plasma membrane to ciliary membrane is characterized by an invagination called the ciliary pocket (Molla-Herman et al., 2010). The ciliary pocket is sought to play an important role in vesicular trafficking as well as in linking the cilium to the actin cytoskeleton (Benmerah, 2013).

Post-Golgi vesicles transport proteins with a ciliary destination to the apical membrane at the ciliary base where they are exocytosed. After passing the transition zone, a mechanism that is not well understood, the proteins are transported through the cilium by a highly specialized transport system, the Intraflagellar Transport (IFT) (Rosenbaum and Witman, 2002). The IFT is divided in an anterograde and a retrograde mechanism, which are catalyzed respectively by kinesins and dyneins (Jordan et al., 2018; Wheway et al., 2018). The classic model of primary cilia axoneme structure of cilia is a '9+0' microtubule structure, referring to a ring of nine peripheral microtubule doublets (Oh and Katsanis, 2012). A second type of cilia, motile cilia, have a '9+2' microtubule structure with an additional doublet in the middle of the ring as well as dynein arms (Mitchison and Valente, 2017). Recently, a groundbreaking study using cryo-electron tomography on primary cilia has challenged this textbook knowledge, showing that the '9+0' microtubule structure only exists for a few micrometer at the ciliary base before revolving towards EB1-decorated microtubules and actin filaments (Kiesel et al., 2020). Interestingly, primary cilia are directly and structurally linked to the cell cycle. During the interphase of the cell cycle, the centrioles travel to the plasma membrane where the mother centriole then forms the basal body. As soon as the centrosome is needed again for the next cell division, the cilium is reabsorbed and the centrosome is released from the plasma membrane (Plotnikova et al., 2009). Cilia are thus organelles, that are constantly assembled and disassembled, and since cell division is only possible after the reabsorption of the cilium, this is commonly described as a ciliary checkpoint within the cell cycle (Bettencourt-Dias et al., 2011). Loss of this ciliary checkpoint has been associated with renal cell carcinoma and other cancers (Higgins et al., 2019; Seeger-Nukpezah et al., 2013), and the checkpoint might play an essential role in injury and repair of tubule cells (Guo and Cantley, 2010).

### 3.4 The ciliary transition zone as gatekeeper

In recent years, major advances in understanding the ciliary protein composition have been made. Advanced proteomic approaches have led to the discovery of new ciliary proteins and super-resolution imaging as well as cryo-electron microscopy have been crucial in further elucidating the ciliary structure and protein localization within the cilium (Kiesel et al., 2020; Kohli et al., 2017; Mick et al., 2015; Tony Yang et al., 2015; Yang et al., 2013). Even though there is no membrane separating the ciliary lumen from the cytoplasm, the cilium is considered an independent organelle, with proteins specifically localizing to the ciliary membrane and the axoneme. The absence of protein synthesis within the cilium requires a barrier regulating the transport of proteins to and from the cilium as well as retention of proteins within the cilium, a role that has been assigned to the TZ (Bhogaraju et al., 2013; Rosenbaum and Witman, 2002).

Although the barrier function of the flagellar TZ had already been proposed in 1972, the mechanisms behind this process are still not well understood (Anderson, 1972; Gilula and Satir, 1972). Early on, the

TZ had been compared to the nuclear pore complex (NPC). NPCs allow proteins under 40 kDa to freely diffuse to and from the nucleus, while proteins between 40 and 60 kDa are slowed down, and proteins above 60 kDa are excluded (Knockenbauer and Schwartz, 2016). For the ciliary TZ it has been shown that even though protein up to 60 kDa would structurally fit through it (Nachury et al., 2010), the passive diffusion rate for even smaller particles is reduced and that proteins larger than 40 kDa need nucleoporins to facilitate the transport (Calvert et al., 2010; Kee et al., 2012). Similar to the nuclear localization sequence for the transport into the nucleus, ciliary localization signals have been proposed and identified in several ciliary proteins including PC1, PC2, and PKDH1 (Dishinger et al., 2010; Follit et al., 2010; Nachury et al., 2010).

Several NPH as well as MKS and JBTS proteins have been shown to specifically localize to the BB and TZ and have been identified to participate in the ciliary gate function. A detailed interaction network for the NPHP-JBTS-MKS proteins was published in 2011 (Sang et al., 2011). Here, the NPHP1-4-8 complex has been found at the TZ and cell-cell contacts. This complex is not essential for ciliation but for epithelial morphogenesis as well as the barrier function (Awata et al., 2014; Sang et al., 2011). The NPHP5-6 complex localizes to the basal body and is connected to the NPHP1-4-8 complex via Inversin (NPHP2). It is essential for ciliation, tissue organization as well as ciliary trafficking (Barbelanne et al., 2015; Sang et al., 2011).

### 3.5 The JADE protein family

Increasing evidence links the putative E3 ubiquitin ligase JADE1 (gene for apoptosis and differentiation in epithelia-1) to PKD (Borgal et al., 2012; Foy et al., 2012), renal cell carcinoma (Chitalia et al., 2008; Shafique and Rashid, 2019; Xiao-Fen et al., 2016), cilia, and cell cycle progression (Borgal et al., 2016; Siriwardana et al., 2015). This puts JADE1, also known as PHF17, in a prime position to study underlying connections, molecular mechanisms and to find potential therapeutic target points for the above-mentioned diseases. Alternative splicing of the *JADE1* mRNA results in two JADE1 isoforms, a full length variant with 842 amino acids (JADE1L), and a truncated variant missing 333 amino acids at the C-terminal end (JADE1S) (Foy et al., 2008). JADE1 shares a protein family with JADE2 (PHF16) and JADE3 (PHF15). The individual JADE proteins are encoded by genes localized on three different chromosomes, Chr 4, Chr 5, Chr X in the human genome and Chr 3, Chr 11, and Chr X in the mouse genome respectively. Their similarity in both sequence and domain structure has been recognized previously (Panchenko, 2016). All three JADE protein family members contain two PHD finger domains, multiple PEST motifs that are rich in amino acid residues proline (P), aspartic acid (E), serine (S), and threonine (T), and nuclear localization signals (NLS) (Figure 2A). Moreover, both JADE1 and JADE2 have acetylation sites in front of the second PHD domain, whereas both JADE2 and JADE3 have acetylation sites between amino acid residue 30 and 40. All of these acetylation sites have been experimentally

identified, however, their functional relevance is unclear. Sequence comparison of human JADE paralogues as well as mouse Jade paralogues revealed a high similarity within the JADE protein family (Figure 2B). The higher protein identity score between JADE2/3 and JADE1S compared to JADE1L indicates that the highest level of similarity lies in the N-terminal part. The JADE family is also highly conserved across species, with 92.45% sequence identity between human and mouse orthologues for JADE1, and 91.44% and 81.92% for JADE2 and JADE3, respectively (Figure 2C)(Panchenko, 2016; Tzouanacou et al., 2003). However, most studies focused exclusively on JADE1S/L so far.

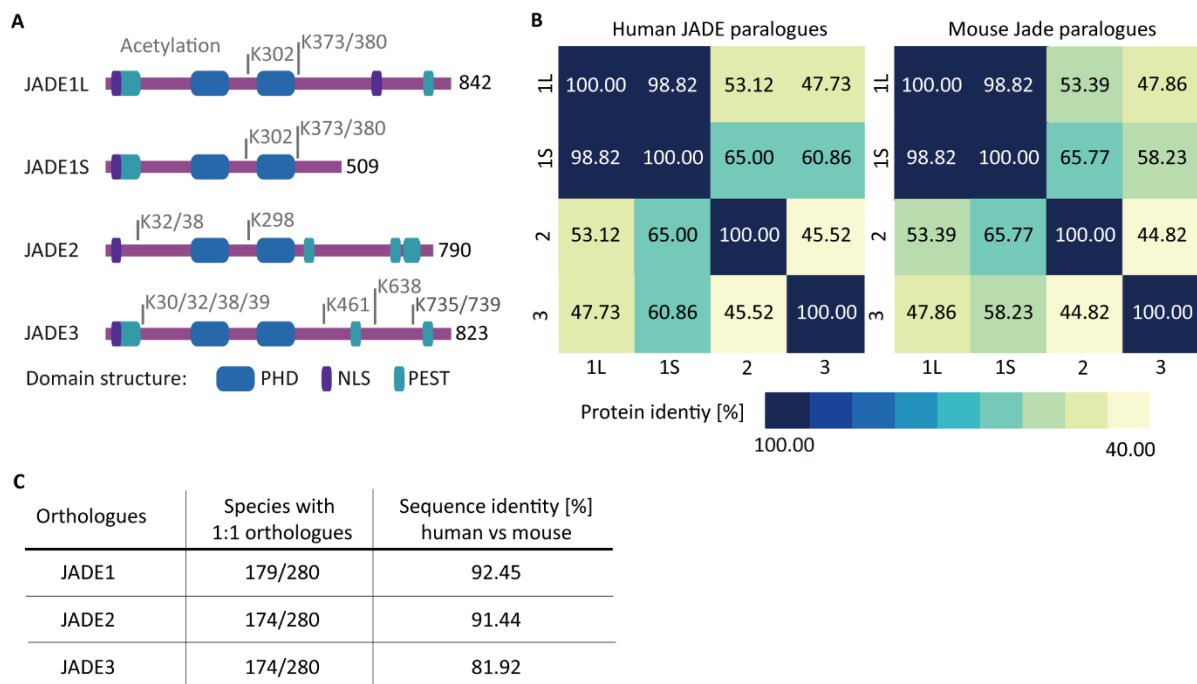


**Figure 2. Structural similarity in the JADE protein family.**

**(A)** Domain structure of human JADE proteins. PHD – plant homeo domain; NLS – nuclear localization signal; PEST – protein degradation amino acid sequence enriched in P, E, S, and T. Domain information obtained from EMBOSS/epstfind (Rice et al., 2000), SMART(Letunic and Bork, 2018), and NLS prediction (consensus sequence K – (K/R) –X – (K/R)). **(B)** Human and mouse JADE family paralogues protein sequence similarities shown in a protein identity matrix. Protein sequences were obtained from Uniport (Consortium, 2019) and the identity score was calculated using Clustal Omega (Madeira F et al., 2019). **(C)** Summary of species (as annotated in Ensembl, including invertebrates) with 1:1 orthologues for the JADE family. Sequence identity is based on the alignment of the protein sequences and was obtained from Ensembl (Howe et al., 2021). See also MS ID#: BIORXIV/2021/462752.

### 3.5.1 JADE1 in the context of Wnt signaling and PKD

JADE1 was first discovered in a yeast-to-hybrid screen as an interactor of pVHL (Zhou et al., 2002). Zhou et al. showed JADE1 expression in the kidney, specifically in proximal tubule cells (Zhou et al., 2002). Moreover, they showed that the reintroduction of pVHL in RCC cells leads to a strong upregulation of JADE1 and that pVHL increased the protein half-life of JADE1, which is generally rather short-lived (Zeng et al., 2013; Zhou et al., 2002). A follow up study showed that the PHD domain of JADE1 is critical for interaction with VHL and the stabilization by pVHL (Zhou et al., 2004). In addition, they observed that mutated pVHL variants linked to renal cancer were not able to stabilize JADE1 and suggested a risk correlation with RCC development (Zhou et al., 2004). Since JADE1 expression in renal cancer cells, in general, is low, it has been suggested that JADE1 is a pro-apoptotic factor, which needs to be overcome for renal cancer to develop (Zhou et al., 2005). This function of JADE1, as a putative tumor suppressor, was linked to apoptosis showing that JADE1 increases apoptosis and decreased levels of the anti-apoptotic factor BCL2 (Zhou et al., 2005). A correlation study in RCC patients showed that not only the downregulation of JADE1 and pVHL correlated in RCC tissue compared to matched normal tissue, but that this downregulation was also correlated to tumor size and tumor grade (Xiao-Fen et al., 2016).

Chitalia et al. demonstrated that pVHL downregulates  $\beta$ -catenin in a JADE1S dependent manner and that JADE1S is able to destabilize wild-type but not a cancer-causing  $\beta$ -catenin variant. Moreover, JADE1S acted as an E3 ubiquitin ligase for phosphorylated as well as non-phosphorylated  $\beta$ -catenin, and was thus able to regulate canonical Wnt signaling in the off and on state (Chitalia et al., 2008). These findings could be linked to a patient cohort, where a low expression of JADE1 and high expression of  $\beta$ -catenin, and especially the combination of both, were linked to poor outcome and decreased survival of RCC patients (Lian et al., 2012). A study by Foy et al. demonstrated that PC1 regulates JADE1 expression levels and its function as a transcription factor, using JADE1 as a mediator to control canonical Wnt/ $\beta$ -catenin signaling (Foy et al., 2012). Moreover, our lab could show that the ciliary protein NPHP4 can stabilize and promote localization of JADE1S to the nucleus leading to an additive inhibition of canonical Wnt signaling (Borgal et al., 2012). JADE1 has been shown to target  $\beta$ -catenin for proteasomal degradation and thus was suggested to play a role in fine-tuning Wnt-signaling (Borgal et al., 2012; Chitalia et al., 2008).

Wnt signaling is important for cell fate decisions and tissue patterning in development, cell cycle progression, and stem cell maintenance (Clevers, 2006; MacDonald et al., 2009). Besides being essential for embryonic development, dysregulation of Wnt signaling is a significant contributor to cancer (Clevers and Nusse, 2012; Taciak et al., 2018). Wnt signaling is often divided into a canonical route which is  $\beta$ -catenin dependent as well as two non-canonical,  $\beta$ -catenin independent, pathways, the Wnt/Planar Cell Polarity (PCP) and the Wnt/ $\text{Ca}^{2+}$  pathway (Gerdes and Katsanis, 2008; Malik et al.,

2020; Oh and Katsanis, 2013). Defects in Wnt signaling have been shown to lead to cyst formation in the kidney in mouse models. Activation of Wnt signaling, through either overexpression of an activated, oncogenic  $\beta$ -catenin (Saadi-Kheddouci et al., 2001), overexpression of the canonical Wnt ligand *Wnt9* (Kiefer et al., 2012), or deletion of the tumor suppressor *Apc* (Qian et al., 2005), leads to a polycystic kidney phenotype. Inversin (NPHP2) provided one of the first direct link of Wnt signaling and its regulation through primary cilia. Inversin has been shown to interact with Dishevelled (Dvl1), targeting the cytoplasmic fraction of Dvl1 for degradation which leads to inhibition of canonical Wnt signaling (Simons et al., 2005). At the same time, Inversin is able to promote PCP signaling and might play a role in switching from canonical to non-canonical Wnt signaling (Lienkamp et al., 2012; Simons et al., 2005). The balance between the different Wnt pathways is crucial for tissue development and homeostasis and might be partially regulated via primary cilia (Figure 1).

Additionally, the AKT signaling pathway, which is relevant for various cellular processes, including cell survival, proliferation, metabolism, and migration, is activated in RCCs and also in kidney cysts (Frew et al., 2008; Zeng et al., 2013). JADE1 has been shown to target phospho-AKT1, linking loss of JADE1 to an activation of AKT signaling (Zeng et al., 2013). Recently, it was shown that microRNA (miR) 135b targets JADE1, and that silencing of miR-135b leads to upregulation in JADE1 and subsequent inhibition of AKT signaling (Zhou et al., 2020). These findings strengthen the role of JADE1 as a tumor suppressor and in the pathogenesis of RCC and cyst formation. However, a detailed understanding of the underlying mechanism is still missing.

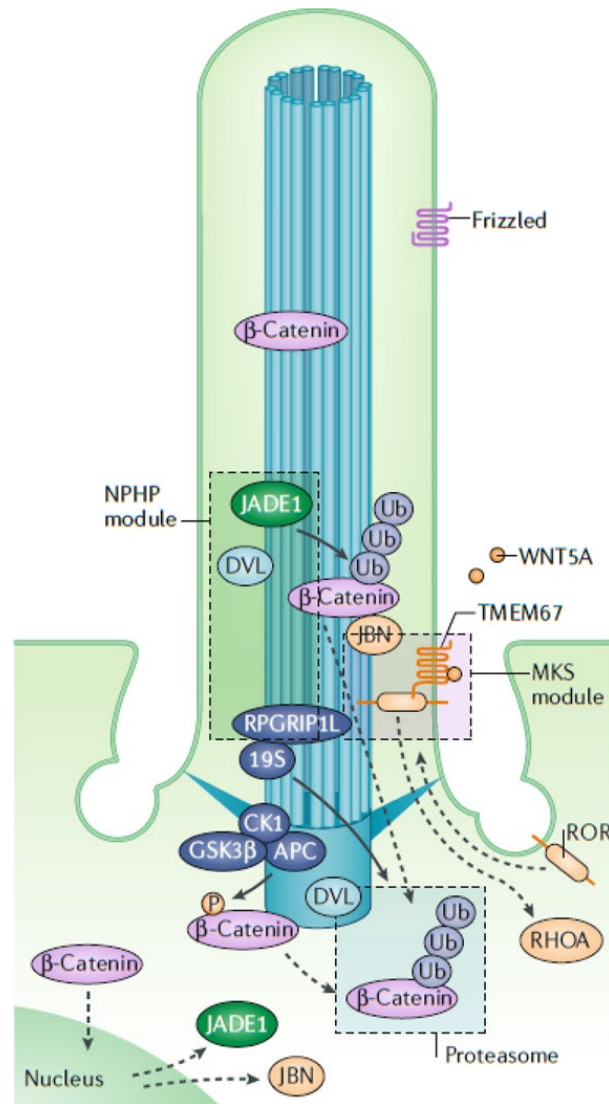


**Figure 3. Overview of ciliary TZ and BB modulation of WNT signaling.**

Both, the NPHP and the MKS module localize to the TZ of primary cilia. Moreover, several Wnt signaling pathway components and components of the  $\beta$ -catenin destruction complex (APC, GSK3 $\beta$ , CK1 $\alpha$ ) localize to primary cilia. RPGRIP1L can inhibit canonical Wnt signaling by interacting with PSMD2, a component of the proteasome. Similarly to JADE1, it promotes degradation of  $\beta$ -catenin and in addition Dvl1. Wnt signaling is further linked to the primary cilia by TMEM67 that has been shown to recruit ROR2 (receptor tyrosine kinase-like orphan receptor 2) which binds the Wnt ligand WNT5A. Joubertin (JBN) regulates translocation of  $\beta$ -catenin to the cilium and nucleus dependent on ciliation. Reprinted by permission from Springer Nature Customer Service Centre GmbH: Springer Nature, Nature Reviews Nephrology, Zeinab Anvarian et al. © 2019 (Anvarian et al., 2019)

### 3.5.2 JADE1 as part of the histone acetyltransferase complex

One of the most studied areas of JADE1 is its role in the HBO1-JADE1 histone acetyl transferase (HAT) complex. As mentioned before, JADE1 does contain two PHD motifs, making it part of a family of over 300 proteins containing PHD fingers (Panchenko et al., 2004). PHD fingers are Cys<sub>4</sub>HisCys<sub>3</sub> motifs around two zinc ions and are primarily found in nuclear proteins. They are suggested to play a role in chromatin remodeling as they are mainly found in transcriptional co-regulators and chromatin modifiers (Aasland et al., 1995; Musselman and Kutateladze, 2009; Sanchez and Zhou, 2011). Along this line, Panchenko et al. showed that JADE1 leads to activated transcription by increasing acetylated H4 expression, suggesting a role as transcriptional activator (Panchenko et al., 2004). Further investigation in the detailed nature of the HBO1-JADE1 complex revealed the importance of the N-terminal region of JADE1 to interact with the H3-H4 substrate and thus facilitate histone acetylation (Han et al., 2018).

Whereas most studies focus on the short isoform of JADE1, Foy et al. could show that co-expression of both JADE1S, JADE1L, and HBO1 is necessary for histone H4 acetylation depending on the presence of the JADE1 PHD domains (Foy et al., 2008). Correlation of JADE1S expression with acetylation of H4 but not H3, provides further evidence for the H4 specificity of JADE1 (Havasi et al., 2013). Siriwardana et al. also linked JADE1S to organ recovery by showing cell-cycle dependent phosphorylation of JADE1S and a shift of JADE1 from the nucleus to the cytoplasm after injury, indicating the proliferative status of the cells (Siriwardana et al., 2015). The kinases CK1 $\alpha$ , Aurora A, and Aurora B have been shown to play a role in JADE1 phosphorylation (Borgal et al., 2014, 2016; Siriwardana et al., 2014, 2015).

Furthermore, JADE1 has been linked to the HAT Tip60 (Panchenko et al., 2004), which also is known to have an H4 specificity (Yamamoto and Horikoshi, 1997). JADE1 mainly forms a complex with HBO1, ING4/5 (Inhibitor of growth 4/5) as well as EAF6, whereas TIP60 usually complexes with EPC1 and ING3 (Doyon et al., 2006). Even though JADE1 seems to work mainly in complex with HBO1, changing to TIP60 might be part of more distinct functions of JADE1. However, neither the underlying mechanisms nor potential triggers for the switch are known. ING proteins are known to influence p53 signaling and proliferation and act as tumor suppressors (Campos et al., 2004), making it tempting to speculate that JADE1 is acting in a similar manner. Functional transcriptional studies revealed that the p53 indeed might be targeted by the JADE1-HBO1 complex (Avvakumov et al., 2012). Yet, even though it is evident that JADE1 plays a role in proliferation, up to date, the transcriptional function of JADE1 as well as specific transcriptional targets are not clear.

### 3.5.3 *In vivo* functions of Jade1

Shortly after the first description of JADE1, a gene-trap mouse model was published (Tzouanacou et al., 2003). Jade1 was identified in a screen for genes expressed in the primitive streak and tail bud during mouse embryogenesis. Additional expression was found in regions with pluripotent or tissue-specific progenitors (Tzouanacou et al., 2003). Animals homozygous for the gene trap allele were viable and fertile, and did not show any morphological phenotype compared to wild-type and heterozygous littermates. It was however noted that the number of weaned homozygous animals was lower than expected from Mendelian ratios (Tzouanacou et al., 2003). Since Jade1 shares a high degree of similarity with two other PHD proteins, Jade2 and Jade3, a compensatory mechanism was proposed, which was supported by partial co-expression of the mRNAs of *Jade1/2/3* (Tzouanacou et al., 2003). Besides the Jade1 gene-trap mouse model, the HBO1-Jade1 complex (3.5.2) has been studied *in vivo* in the context of epithelial regeneration in the kidney (Havasi et al., 2013). Here, it was shown that during acute kidney injury in wild-type mice Jade1 as well as HBO1 expression initially decreases. During recovery, first Jade1S levels are restored to pre-injury levels, and subsequently, Jade1L expression is restored. This time shift correlates with the maximum and the stop of cell proliferation, respectively. This indicated a distinct role of Jade1 proteins in renal tissue regeneration.

### 3.5.4 JADE2

The function of JADE2 is still largely unknown. Similar to JADE1, JADE2 has been associated with the HBO1 complex (Doyon et al., 2006; Foy et al., 2008). In ovarian cancer cells high levels of JADE2 have been observed and lead to the presumption that JADE2 might play a role in histone H4 specific acetylation through HBO1 activating downstream mechano-transduction pathways, including the ovarian cancer oncogene YAP1 (Quintela et al., 2019). Furthermore, JADE2 has been further proposed as an E3-ubiquitin ligase for Histone H3K4 demethylase LSD1 (Anan et al., 2018; Han et al., 2014). LSD1 plays a role in various cellular processes, including stem cell maintenance and carcinogenesis (Amente et al., 2013; Hino et al., 2016). Degradation of LSD1 by JADE2 is linked to cell differentiation and metabolic reprogramming (Anan et al., 2018; Han et al., 2014).

### 3.5.5 JADE3

Similar to JADE1L/2, it has been shown for JADE3 that it also co-purified with the complex formed by H4, HBO1, and ING4/5 (Doyon et al., 2006; Foy et al., 2008). It was shown, however, that even though JADE3 is able to stabilize HBO1 it does not induce acetylation when co-expressed with HBO1 and is less efficient in stimulating the HAT-HBO1 activity as seen for JADE1L (Foy et al., 2008). Additionally, JADE3 has also been shown to function as an oncogene in colon cancer, to correlate with cancer progression and to predict poor survival of patients. In the proposed mechanism, JADE3 is acting in the Wnt/ $\beta$ -

catenin pathway as well as enhancing the transcriptional activity of LGR5 and thus increasing the cancer stem cell properties in colon cancer (Jian et al., 2018). Besides the role of JADE3 in colon cancer, a non-synonymous somatic variant of JADE3 has been identified in hepatocellular carcinoma (Liu et al., 2012), and JADE3 has been associated with the activation of MSX1 in mantle cell lymphoma (Nagel et al., 2014). An additional link has been made between JADE3 and lipid accumulation and differentiation in adipocytes, suggesting JADE3 as a potential negative regulator on Wnt or TGF signaling (Chang et al., 2019).

While there are not many studies focused on JADE2 and JADE3, the current evidence points to similar molecular functions within the JADE protein family. Histone acetylation, Wnt signaling as well as carcinogenesis are reoccurring key aspects linked multiple family members. However, the role of JADE2 and JADE3 in the kidney has not been addressed yet. Moreover, a direct comparison of the functions of the JADE family members in the same cell of tissue type is lacking.

## 4 Thesis Aims

Over the last decades, several proteins and pathways have been identified to play a role in NPH, VHL disease, and RCC. The role of primary cilia in the pathophysiology of renal cyst formation is well established. However, concrete disease mechanism and, more importantly, causative treatment options of PKD are still missing. JADE1 has been identified to interact with NPH- and RCC-related proteins, but its role in disease onset or progression as well as in cilia biology remains to be fully elucidated. The overarching aim of this thesis was to gain deeper insights into the function and molecular mechanism of the JADE protein family and to generate novel mouse models assembling human NPH. The specific aims addressed in this thesis were:

### **(1) Elucidating potentially overlapping functions within the JADE protein family**

A potential compensatory function within the JADE protein family is plausible considering their great structural similarities. To put Jade1 in context with Jade2 and Jade3, we first did an in-depth analysis of published data to illustrate the similarities of JADE1/2/3 and their respective expression levels in different tissues or cell types. Next, we aimed to examine if JADE2 and JADE3 share ciliopathy related protein interactors with JADE1. Moreover, we generated several *Jade1/2/3*-deficient renal tubular epithelial cell lines with CRISPR/Cas9-mediated genome engineering. In these mutant cell lines, we studied how the loss of one Jade family member affected the expression of the others.

### **(2) Unbiased analysis of functions of the Jade protein family in renal epithelial cells**

To gain a better understanding of the functions of the individual protein members of the JADE family, the Jade-deficient cell lines generated in aim (1) were used to produce unbiased transcriptome and proteome datasets. Comprehensive bioinformatics analysis was performed on these datasets to unravel shared and distinct cellular functions of JADE1/2/3.

### **(3) Investigating the role of the Jade family members in *in vivo* models**

*In vivo* models are crucial to study the pathophysiological functions of Jade proteins in tissue and organs. So far, there is only limited *in vivo* information and tools available for *Jade1* and none for *Jade2* and *Jade3*. Therefore, individual mutant mouse lines were generated using CRISPR/Cas9-mediated genome engineering. These models will be important tools to study the role of the individual Jade proteins during kidney development and tissue homeostasis, as well as their role in ccRCC.

### **(4) Generation of NPH mouse models resembling the human phenotype**

There have been many attempts to generate *in vivo* models for NPH, however, the phenotype mostly did not resemble the human NPH phenotype. Within this thesis, four new NPH mouse models were generated and characterized, two with null alleles for *Glis2* (*Nphp7*) and one with a null allele and one with a patient-derived mutation for *Tmem218*.

## 5 Materials and Methods

### 5.1 Materials

#### 5.1.1 Chemicals and Reagents

**Table 1. List of chemicals and reagents used.**

<b>Chemical/Reagent</b>	<b>Product no.</b>	<b>Provider</b>
3,3',5,5'-Tetramethylbenzidine (TMB)	T2885	Sigma-Aldrich
Accutase	#07920	STEMCELL Technologies
Acetic Acid	7332.1	Carl Roth
Acetonitrile	701881	AppliChem
Agarose	A9539	Sigma-Aldrich
Ammonium bicarbonate (TEAB)	A6141	Sigma-Aldrich
Ammonium persulfate (APS)	A0834	AppliChem
Ammonium sulfate ((NH <sub>4</sub> ) <sub>2</sub> SO <sub>4</sub> )	3746	Carl Roth
Ampicillin Sodium Salt	K029.2	Carl Roth
M2 beads (Anti-FLAG) Affinity Gel	A2220	Sigma-Aldrich
Aqua dest. Injectabile (PCR grade water)	PZN-1087335	Berlin-Chemie AG
ATP	R0441	Thermo Fisher Scientific
Bacto™ Yeast Extract	212750	BD Biosciences
Bovine Serum Albumin (BSA)	1066	Gerbu
Bromphenol Blue	A512	Carl Roth
Buffer 3.1	B7203S	New England Biolabs
Calcium chloride (CaCl <sub>2</sub> )	HN04.2	Carl Roth
Cas9 mRNA	040L-6125-1000	Tebu Bio
Cas9 Nuclease 3NLS	1081059	IDT
Casy Ton	5651808001	OMNI Life Science
Casy Clean	5651786001	OMNI Life Science
Chloramphenicol	3886.1	Carl Roth
Chloroacetamide	C0268	Sigma-Aldrich
Coomassie brilliant blue G-250	A3480	AppliChem
Coumaric acid	C9008	Sigma-Aldrich
Deoxyribonucleotide triphosphate (dNTP)-mix	200415	Stratagene
Dimethyl sulfoxide (DMSO) Hybri-Max	D2650	Sigma-Aldrich
Dithiothreitol (DTT)	6908.1	Carl Roth
DMEM/F12	D6421	Sigma-Aldrich
DNase	A3778	AppliChem
Dulbecco's Modified Eagle Medium (DMEM)	D6429	Sigma-Aldrich
Ethanol (99.8%)	9065.3	Carl Roth
Ethanol, denatured (96%)	768723	Th. Geyer
Ethanol, denatured (99%)	769202	Th. Geyer
Ethylenediaminetetraacetic acid (EDTA)	E5134	Sigma-Aldrich
Evan's blue	E2129	Sigma-Aldrich
Fetal Bovine Serum (FBS)	S 0115	Biochrom AG

*Continued on next page*

Formaldehyde (37%)	4979.1	Th. Geyer
Formic Acid	94318	Fluka
Freuds Adjuvant, complete	F5881	Sigma-Aldrich
Freuds Adjuvant, incomplete	F5506	Sigma-Aldrich
GeneRuler 1kb DNA Ladder	SM0311	Thermo Fisher Scientific
GeneRuler 50bp DNA Ladder	SM0372	Thermo Fisher Scientific
Glucose	G7021	Sigma-Aldrich
GlutaMAX	35050061	Thermo Fisher Scientific
Glycerol	3783	Carl Roth
Glycine	3908.2	Carl Roth
Go Taq G2 Flexi Polymerase	M7808	Promega
Halt Protease & Phosphatase Inhibitor Cocktail (100x)	78444	Thermo Fisher Scientific
HAT-Supplement	21060017	Thermo Fisher Scientific
Hematoxylin solution A acc. to Weigert	X906.1	Carl Roth
Hematoxylin solution B acc. to Weigert	X907.1	Carl Roth
Hepes	H0887	Sigma-Aldrich
Histomount	HS-103	National Diagnostics
Hydrogen chloride (HCl)	T134	Carl Roth
Hydrogen Peroxide (H <sub>2</sub> O <sub>2</sub> ) 30%	107209	Merck
Imidazole	792527	Sigma-Aldrich
Incidin PLUS	225194	Igefa
Incuwater-Clean	A5219	AppliChem
Isopropyl-β-D-thiogalactopyranosid (IPTG)	A1008	AppliChem
Isopropanol	5752.3	Carl Roth
Kanamycin	T832.2	Carl Roth
KH <sub>2</sub> PO <sub>4</sub>	P5655	Sigma-Aldrich
LB Medium	X964.2	Carl Roth
LB-Agar	X965.1	Carl Roth
Lipofectamine 2000	11668019	Thermo Fisher Scientific
Loading Dye Solution (6X)	R0611	Thermo Fisher Scientific
Luminol	9253	Fluka
Lysozyme	89833	Lysozyme
Magnesium chloride (MgCl <sub>2</sub> )	1.05833.0250	Merck
Methanol	4627.5	Carl Roth
Meyer's hematoxylin solution	A0884	AppliChem
N,N,N',N'-tetramethylethylenediamine (TEMED)	2367.3	Carl Roth
Ni-NTA Agarose	R90101	Thermo Fisher Scientific
Non-Essential Amino Acids Solution	11140035	Thermo Fisher Scientific
Normal Donkey Serum (NDS)	017-000-121	Dianova
Opti-MEM	31985-047	Thermo Fisher Scientific
PageRuler Plus Protein Ladder	26620	Fermentas
Paraformaldehyde (PFA)	P6148	Sigma-Aldrich
Penicillin-Streptomycin 10,000 U/mL (Pen-Strep)	15140-122	Thermo Fisher Scientific

Continued on next page

Periodic acid (99%)	3257	Carl Roth
Phenylmethylsulfonyl fluoride (PMSF)	A0999	AppliChem
Phosphoric acid (85%)	79617	Sigma-Aldrich
Polyacrylamide (PAA)	T802.1	Carl Roth
Polyethyleneglycol (PEG) 1500	10 783 641 001	Roche
Porpidium Iodide (PtdIns)	P4170	Sigma-Aldrich
Potassium chloride (KCl)	6781	Carl Roth
ProFlow Sort Grade 8x Sheath Fluid	12012932	Bio-Rad
ProLine™ Calibration Beads	1451081	Bio-Rad
Prolong Gold antifade reagent with DAPI	P-36931	Thermo Fisher Scientific
REDTaq Ready Mix	R2523	Sigma-Aldrich
RNase A	A2760.0100	AppliChem
RNase-free water Ultra Pure	10977-035	Thermo Fisher Scientific
RPMI with GlutaMax	61870044	Thermo Fisher Scientific
Schiff's reagent	1.090.330.500	VWR
Sodium acetate (NaAc)	6268	Merck
Sodium azide (NaN <sub>3</sub> )	S2002	Sigma-Aldrich
Sodium chloride (NaCl)	3957.1	Carl Roth
Sodium citrate	HN12.4	Carl Roth
Sodium deoxycholate (Na-DOC)	D6750	Sigma-Aldrich
Sodium dodecyl sulfate (SDS) pellets	CN30.3	Carl Roth
Sodium dodecyl sulfate (SDS) powder	A2263	AppliChem
Sodium fluoride (NaF)	S1504	Sigma-Aldrich
Sodium hydrogen phosphate (Na <sub>2</sub> HPO <sub>4</sub> )	S9390	Sigma-Aldrich
Sodium hydroxide (NaOH, 2N)	T135	Carl Roth
Sodium orthovanadate (Na <sub>3</sub> VO <sub>4</sub> )	S6508	Sigma-Aldrich
Sodium Pyruvate	S8636	Sigma-Aldrich
T4 ligase buffer (10x)	B69	Thermo Fisher Scientific
TE buffer	60191	Thermo Fisher Scientific
Tetrasodium pyrophosphate (Na <sub>4</sub> P <sub>2</sub> O <sub>7</sub> )	106591	Merck
tracrRNA	1072534	IDT
TRI Reagent®	T9424	Sigma-Aldrich
Triethylene glycol diamine tetraacetic acid (EGTA)	E4378	Sigma-Aldrich
Tris Hydrochloride (Tris-HCL)	9090.3	Carl Roth
TritonX-100	3051.2	Carl Roth
Trizma base	T1503	Sigma-Aldrich
Trypsin, MS	T6567	Sigma-Aldrich
Trypsin-EDTA Solution (1X), cell culture	T3924	Sigma-Aldrich
Tryptone	1010817	MP Biomedicals
Tween20	3472	Caesar & Loretz
Urea	U1250	Sigma-Aldrich
Xylene	0371.5000	Th. Geyer
Z-Gly-Gly-Leu-AMC	BML-ZW8505	Enzo Life Sciences
β-Mercaptoethanol	M7522	Sigma-Aldrich

## 5.1.2 Assays and Kits

**Table 2. List of assays and kits used.**

<b>Assay /Kit</b>	<b>Product no.</b>	<b>Provider</b>
Big Dye Terminator version 3.1 Sequencing Kit	4337455	Applied Biosystems
Direct-zol RNA Miniprep Kit	R2052	Zymo Research
GeneJet Gel Extraction Kit	K0692	Thermo Fisher Scientific
GeneJet PCR Purification Kit	K0702	Thermo Fisher Scientific
GeneJet Plasmid Miniprep Kit	K0503	Thermo Fisher Scientific
High-Capacity cDNA Reverse Transcription Kit	4368814	Applied Biosystems
HiScribe T7 High Yield RNA Synthesis Kit	E2040S	New England Biolabs
NucleoBond® Xtra Midi Prep Kit	740410	Macherey-Nagel
PCR Mycoplasma Test Kit I/C	PK-CA91-1096	PromoKine
Pierce™ BCA Protein Assay Kit	23225	Thermo Fisher Scientific
Pierce™ Rapid Isotyping Kit	26178	Thermo Fisher Scientific
NEBNext® Ultra™ II Q5® Master Mix	M0544L	New England Biolabs
RNeasy Mini Kit	74104	Qiagen
Invitrogen™ SuperScript™ III Reverse Transkriptase	10368252	Thermo Fisher Scientific
SuperSignal West Femto Chemiluminescent Substrate	34095	Thermo Fisher Scientific
SYBR Green PCR Master Mix	4309155	Thermo Fisher Scientific

## 5.1.3 Buffers and Solutions

**Table 3. List of buffers and solutions used.**

<b>Buffer / Solution</b>	<b>Composition</b>
Base Solution (1x)	0.5 mL Base solution (50x) 24.5 mL ddH <sub>2</sub> O pH 12
Base Solution (50x)	12.5 mL NaOH (5N) 1 mL EDTA (0.5 M) 36.5 mL ddH <sub>2</sub> O
Blocking Solution	5% (v/v) NDS 0.1% (v/v) TritonX-100 in PBS (1x)
Cell Culture Medium (HEK293T)	10% (v/v) FBS in DMEM with GlutaMAX
Cell Culture Medium (mIMCD3)	10% (v/v) FBS 2 mM GlutaMAX in DMEM/F12
Cell Culture Medium (mIMCD3, serum reduced)	1% (v/v) FBS 0.2 mM GlutaMAX 1x Pen-Strep in DMEM/F12

*Continued on next page*

Cell Culture Medium (mIMCD3, sorted)	10% (v/v) FBS 2 mM GlutaMAX 1 x Pen-Strep in DMEM/F12
Cell Freezing Medium	90% (v/v) FBS 10% (v/v) DMSO
Cell Lysis Buffer	0.45% Tween20 0.45% TritonX-100 2.5 mM MgCl <sub>2</sub> 50 mM KCl 10 mM Tris-HCL pH 8.3 100µg/mL proteinase K
Colloidal Coomassie Solution	80% Colloidal Coomassie Stock solution 20% (v/v) Methanol
Colloidal Coomassie Stock Solution	755 mM (NH <sub>4</sub> ) <sub>2</sub> SO <sub>4</sub> 2.55% (v/v) Phosphoric acid 0.1% (w/v) Coomassie brilliant blue G-250
Electroporation Mix	4 µM crRNA:tracrRNA duplex 4 µM Cas9 nuclease 10 µM ssODN, if required in Opti-MEM
ELISA blocking solution	1% BSA (v/v) 0.02% NaN <sub>3</sub> in 1x PBS
ELISA developer solution	50 mM NaAc pH 5 100 µg/mL TMB 0.05% H <sub>2</sub> O <sub>2</sub>
Enhanced Chemiluminescence Solution (ECL)	100 mM Tris (pH 8.5) 1.25 mM Luminol 0.2 mM Coumaric acid 0.75% (v/v) H <sub>2</sub> O <sub>2</sub> pH 8.5
FACS Buffer	2% (v/v) FBS in 1x PBS
Fixing Solution (Coomassie)	25% (v/v) Isopropanol 10% (v/v) Acetic Acid
HIS Buffer	20 mM Tris pH 8 150 mM NaCl 20 mM Imidazole
HIS Elution Buffer	20 mM Tris pH 8 150 mM NaCl 300 mM Imidazole
HIS Wash Buffer	20 mM Tris pH 8 150 mM NaCl 30 mM Imidazole

*Continued on next page*

IP Buffer	20 mM Tris 1% (v/v) TritonX-100 50mM NaCl 15 mM Na <sub>4</sub> P <sub>2</sub> O <sub>7</sub> 50 mM NaF 44 µg/µl PMSF 2 mM Na <sub>3</sub> VO <sub>4</sub> pH 7.5
Laemmli Sample Buffer (1x)	50 mM Tris 2% (w/v) SDS 10% (v/v) Glycerol Bromphenol Blue 50 mM DTT pH 6.8
Laemmli Sample Buffer (2x)	100 mM Tris (pH 6.8) 4% (w/v) SDS 20% (v/v) Glycerol Bromphenol Blue 100 mM DTT pH 6.8
Modified RIPA buffer	10 mM Tris, pH 8 1 mM EDTA 0.5 mM EGTA 1 % Triton-X100 0.1% Na-DOC 44 µg/µl PMSF 2 mM Na <sub>3</sub> VO <sub>4</sub>
Neutralization Solution (1x)	0.5 mL of stock sol. 50X 24.5 mL H <sub>2</sub> O pH 5
Neutralization Solution (50x)	15.75 g Tris-HCl in 50 mL of H <sub>2</sub> O
PBST	0.05% Tween20 In 1x PBS
Phosphate Buffered Saline (PBS)	137 mM NaCl 2.7 mM KCl 10 mM Na <sub>2</sub> HPO <sub>4</sub> 2 mM KH <sub>2</sub> PO <sub>4</sub>
Plating Medium	1x Pen-Strep 0.5 mM Sodium Pyruvate 1x MEM Non-Essential Amino Acids Solution 1x HAT-Supplement in RPMI with GlutaMax
PNI Mix	400 nM sgRNA /crRNA:tracrRNA duplex 200 nM Cas9 nuclease 30 ng/µL Cas9 mRNA 500 nM ssODN, if required in sterile H <sub>2</sub> O

*Continued on next page*

Proteasomal Activity Assay Buffer	50 mM Tris-HCL pH 7.5 10% (v/v) Glycerol 5 mM MgCl <sub>2</sub> 0.5 mM EDTA 2 mM ATP 1 mM DTT
Protein Wash Buffer	30 mM Tris 300 mM NaCl 0.3% Tween20 pH 7.5
PtdIns Solution	0.38 M sodium citrate 0.75 mM PtdIns 0.73 mM RNase A pH 7.0
Resolving Gel	750 mM Tris 10% (v/v) PAA 0.2% (w/v) SDS pH 8.8
RPMI Pure Medium	1x Pen-Strep 0.5 mM Sodium Pyruvate 1x MEM Non-Essential Amino Acids Solution in RPMI with GlutaMax
Running Buffer	25 mM Trizma base 192 mM Glycine 0.1% (w/v) SDS
SOC Medium	2% (w/v) Tryptone 0.5% (w/v) Yeast Extract 8.6 mM NaCl 2.5 mM KCl 20 mM MgSO <sub>4</sub> 20 mM Glucose
Stacking Gel	250 mM Tris 5% (v/v) PAA 0.2% (w/v) SDS pH 6.8
StageTip Buffer A	0.1% formic acid
StageTip Buffer B	0.1% formic acid 80% acetonitrile
Staining PBS	1 mM CaCl 0.5 mM MgCl <sub>2</sub> in 1 x PBS
Staining Wash Buffer (PBSTx)	0.1% TritinX-100 in PBS (1x)
TAE (1x)	40 mM Tris (pH 8.5) 20 mM Acetic Acid 1mM EDTA
Transfer Buffer	25 mM Tris 188 mM Glycine 0.1% (w/v) SDS

*Continued on next page*

Tris-EDTA Buffer (TE)	10 mM Trizma base 1 mM EDTA pH 9.0
Urea Buffer	8 M Urea 50 mM TEAB 1x Halts phosphatase-protease-Inhibitor
YTA Medium (2x)	16 g/L Tryptone 10 g/L Yeast Extract 5 g/L NaCl

#### 5.1.4 Oligonucleotides

All oligonucleotides were purchased from Integrated DNA Technologies (IDT).

**Table 4. List of oligonucleotides used for genotyping.**

Name	Sequence (5' → 3')
Jade1_emKO1_fp1	TCTGTCTGAGGGAGCTCACT
Jade1_emKO1_fp2	CACCAGTGGCTCTTGGAAC
Jade1_emKO1_rp1	CCCGGGGAGATCATGAAAAC
Jade1_emKO1_rp2	GGGAAGGCGACCTCGTTTC
Jade1_emKO2_fp	ACCCTTTGCTCGGGTTTGTT
Jade1_emKO2_rp	AGGATGCTGCGGAAGTTGTT
Jade2_emKO_fp	GCTGTATCCCAGACACACCC
Jade2_emKO_rp	ACTACCCGAAGGACACTTGC
Jade2_emKO_rp2	CCATCTCGTTGCCATCCTCGCC
Jade3_emKO_fp	AGCAGCTTAGAGATCATAAGAAGT
Jade3_emKO_rp	TCCTGGTATAATTATTGGGTGTCT
Tmem218_fp	TACCCTGCTGGCACCTATCT
Tmem218_rp	CACCCTGAGAACACACTCCC
Glis2_emKO1_fp1	AGTAGGGAGTGGCAGTGGAA
Glis2_emKO1_rp1	TCCACAGCTACAGTCTCGGA
Glis2_emKO1_fp2	AAGCTGAGCATCACCAAGAG
Glis2_emKO1_rp2	TTCTCTTCTCTCTTGCCG
Glis2_emKO2_fp	GCAGGGTCTCTTTACCTAGC
Glis2_emKO2_WT_rp	AACTGGGGACACCATCCAAA
Glis2_emKO2_KI_rp	AACTGGGGACTCCATCCTAT
Jade1_exon6_cellculture_fp	AGGATGCTGCGGAAGTTGTT
Jade1_exon6_cellculture_rp	ACCCTTTGCTCGGGTTTGTT
Jade1_exon7_cellculture_fp	ACAGCAGGCCATTACTCCAGTT
Jade1_exon7_cellculture_rp	CTACTGCTGCCTGTGAGTCACT
Jade2_exon6_cellculture_fp	GCTGAAGCCCAGATCACCAT
Jade2_exon6_cellculture_rp	ACTACCCGAAGGACACTTGC
Jade2_exon7_cellculture_fp	TCTCTGTGCCACCCAGTGTA
Jade2_exon7_cellculture_rp	GGGAACCCAAGAGCTCCTTCTT
Jade3_exon5_cellculture_fp	AGGGTTTTTATCAGGAGATGGACA
Jade3_exon5_cellculture_rp	AGCAGCTTAGAGATCATAAGAAGT
Jade3_exon6_cellculture_fp	CAGATGATGCTACAAGCTTGTTT
Jade3_exon6_cellculture_rp	GAAGACTGGAGGTAGCACAGA

**Table 5. List of oligonucleotides used for sequencing**

<b>Name</b>	<b>Sequence (5' → 3')</b>
Jade1_exon6_cellculture_fp	AGGATGCTGCGGAAGTTGTT
Jade1_exon7_cellculture_fp	ACAGCAGGCCATTACTCCAGTT
Jade2_exon6_cellculture_fp	GCTGAAGCCCAGATCACCAT
Jade2_exon7_cellculture_fp	TCTCTGTGCCACCCAGTGTA
Jade3_exon5_cellculture_fp	AGGGTTTTTATCAGGAGATGGACA
Jade3_exon6_cellculture_fp	CAGATGATGCTACAAGCTTGGTTT
Jade1_emKO1_fp1	TCTGTCTGAGGGAGCTCACT
Jade1_emKO2_fp	ACCTTTTGCTCGGGTTTGTT
Jade2_emKO_fp	GCTGTATCCCAGACACACCC
Jade3_emKO_fp	AGCAGCTTAGAGATCATAAGAAGT
Tmem218_fp	TACCCTGCTGGCACCTATCT
Glis2_emKO1_fp1	AGTAGGGAGTGGCAGTGGAA
Glis2_emKO2_fp	GCAGGGTCTCTTTACCTAGC
pcDNA6_(-mlu)_fsp	CGTGACGGTGGGAGGTCTA
pcDNA6_(-mlu)_rsp	AGGAAAGGACAGTGGGAGTG
pET_fsp1	atg cgt ccg gcg tag a
pET_rsp1	gta gtt att gct cag cgg t
U6_fsp	GAGGGCCTATTTCCCATGATTC

**Table 6. List of oligonucleotides used for cloning**

<b>Name</b>	<b>Sequence (5' → 3')</b>
Jade1_mlu1_fp	CCCGCGACGCGTATGAAACGAGGTGCGCTTCC
Jade1S_not1_rp	CCCGCGGCGGCCGCTTATAAGGTGTCGGTGTCAA
Jade1L_not1_rp	CCCGCGGCGGCCGCTCAAGAGCCAAGATGCTTC
Jade1_sgRNA_exon7_cellculture_top	CACCGCGACATAGCCAACCTGCCCTC
Jade1_sgRNA_exon7_cellculture_bottom	AAACGAGGGCAGTTGGCTATGTCCG
Jade1_sgRNA_exon6_cellculture_top	CACCGATGGTGTACTCGTCCAGCTC
Jade1_sgRNA_exon6_cellculture_bottom	AAACGAGCTGGACGAGTACACCATC
Jade1_sgRNA_emKO1_fp	TTAATACGACTCACTATAGGCCCGGGGAGATCATGAAAC G GTTTTAGAGCTAGAAATAGC
Jade1_sgRNA1_emKO2_fp	TTAATACGACTCACTATAGGCTCACTGCGCACTACTCAG GTTTTAGAGCTAGAAATAGC
Jade1_sgRNA2_emKO2_fp	TTAATACGACTCACTATAGGGAACGGCACCCAGCTCTCTC GTTTTAGAGCTAGAAATAGC
T7_universal_sgRNA_rp	AAAAAGCACCGACTCGGTGCC
Jade2_mlu1_fp	CCCGCGACGCGTATGGAAGAGAAGAGGCGAAA
Jade2_not1_rp	CCCGCGGCGGCCGCTTAGGAGGCCAGCACCCCA
JADE2_not_177rp	CGCGGGGCGGCCGCTTACAGGGTCTCCAGCTCCTCCA
JADE2_mlu1_fp	CCCGCGACGCGTATGGAAGAGAAGAGGCGAAA
JADE2_not1_rp	CCCGCGGCGGCCGCGGAGGCCAGTACGCCCATGC
Jade2_sgRNA_exon7_cellculture_top	CACCGCACTTGGTCCCACTTCTAGT
Jade2_sgRNA_exon7_cellculture_bottom	AAACACTAGAAGTGGGACCAAGTGC
Jade2_sgRNA_exon6_cellculture_top	CACCGGACGTGTGCCGTTCCCCTGA
Jade2_sgRNA_exon6_cellculture_bottom	AAACTCAGGGGAACGGCACACGTCC
Jade3_mlu1_fp	CCCGCGACGCGTATGATGAAACGGCATAGACC
Jade3_not1_rp	CCCGCGGCGGCCGCTCACCTTGCATTGAGCTGT

*Continued on next page*

JADE3_not_178rp	CGCGGGGCGGCCGCTTAATGGCGTTCAGGACTTCTA
JADE3_mlu1_fp	CCCGCGACGCGTATGAAACGCCATAGGCCTGT
JADE3_not1_rp	CCCGCGGCGGCCGCCCTTTGCATTGAACTGTGGG
Jade3_sgRNA_exon8_cellculture_top	CACCGGAACCATGCTATTGAAACAG
Jade3_sgRNA_exon8_cellculture_bottom	AAACCTGTTTCAATAGCATGGTTCC
Jade3_sgRNA_exon9_cellculture_top	CACCGGCATTCTCAAGATTCCAGA
Jade3_sgRNA_exon9_cellculture_bottom	AAACTCTGGAATCTTGAGAATGCC
Glis2_sgRNA_emKO1_fp	TTAATACGACTCACTATAGG CTCTCTTCTCTTGGCGCT G GTTTTAGAGCTAGAAATAGC
Glis2_sgRNA_emKO2_fp	TTAATACGACTCACTATAGG TTTCCAGCCACTTCGCTATT G GTTTTAGAGCTAGAAATAGC

**Table 7. List of oligonucleotides used for qPCR**

Name	Sequence (5' → 3')
Jade1_qPCR_fp	ACCCGCAGCGGAACCAAGTG
Jade1_qPCR_rp	CCGGTGGGCCTCCTCTCGAT
Jade2_qPCR_fp	CCTGTGGTGAGGCTCCTCCC
Jade2_qPCR_rp	CTCTAACGTTAGCTCATCCA
Jade3_qPCR_fp	CAGTGTGCGGCGAGGAA
Jade3_qPCR_rp	ATGCTGGATTCTGCACTCCC
Hprt1_qPCR_fp	GCTGACCTGCTGGATTACAT
Hprt1_qPCR_rp	TTGGGGCTGTACTGCTTAAC

**Table 8. List of guide RNAs**

The guide RNAs were either ordered as Alt-R® CRISPR-Cas9 crRNA from IDT and used in combination with the Alt-R® CRISPR-Cas9 tracrRNA, generated via *in vitro* transcription, or cloned into pSpCas9(BB)-2A-GFP (see section 5.2.21.2.1 and 5.2.8.4).

Name	Sequence (5' → 3') including PAM	Type
Glis2_emKO1	CTCTCTTCTCTTGGCGCT-CGG	<i>In vitro</i> transcription
Glis2_emKO2	TTTCCAGCCACTTCGCTATT-TGG	<i>In vitro</i> transcription
Jade1_emKO1	CCCGGGGAGATCATGAAACG-AGG	<i>In vitro</i> transcription
Jade1_emKO2_exon6_upstream	CTCACTGCGCACTTACTCAG-GGG	<i>In vitro</i> transcription
Jade1_emKO2_exon6_downstream	GAACGGCACCCAGCTCTCTC-TGG	<i>In vitro</i> transcription
Jade2_emKO_exon6_upstream	GCCCAGATCACCATTGTAAA-TGG	IDT
Jade2_emKO_exon6_downstream	CTAGCCCTCCTTAGGGATAC-TGG	IDT
Jade3_emKO_exon8_upstream	CATAAAAGTCTTATAGTAGT-AGG	IDT
Jade3_emKO_exon8_downstream	ACTAGTGTTGACCTTGCATG-AGG	IDT
Tmem218	ACAAAGACGATGGAGAACCT-GGG	IDT
Jade1_sgRNA1_cellculture	ATGGTGTACTCGTCCAGCTC-CGG	pSpCas9(BB)-2A-GFP
Jade1_sgRNA2_cellculture	CGACATAGCCAACCTGCCCTC-TGG	pSpCas9(BB)-2A-GFP
Jade2_sgRNA1_cellculture	GACGTGTGCCGTTCCCTGA-AGG	pSpCas9(BB)-2A-GFP
Jade2_sgRNA2_cellculture	CACTTGGTCCCCTTCTAGT-GGG	pSpCas9(BB)-2A-GFP
Jade3_sgRNA1_cellculture	GAACCATGCTATTGAAACAG-TGG	pSpCas9(BB)-2A-GFP
Jade3_sgRNA2_cellculture	GGCATTCTCAAGATTCCAGA-AGG	pSpCas9(BB)-2A-GFP

*Continued on next page*

ssODN_Glis2_emKO2	GGGGGAAGGAAGGAGGAAGCA GGTAGGTGCAGAGCCCCACCAGA ACCCAGGGGCAAGAAGAAGACTGGA AGGAACTGGGGACACCATCCAATT AGCGAAGTGGCTGGAAATCCTAAG GAGTAAAGACA	IDT
ssODN_Tmem218.R37S	AGGCTTGTCCAGTTAGAAGTCAGC ACAGTTAGAACTAGACTGTCCGCA GTGCAGTGCTTCTGATTTCAACTCA GGTCTCTTTGCTCCCAGTTTCTCCAT CGTCTTTGTCTTCTCGGAGCTCTG ATC	IDT

## 5.1.5 Plasmids

**Table 9. List of plasmids used.**

Name	Vector	Provider
F.JADE1S pcDNA6	pCDNA6	Nephrolab, Cologne
F.JADE1L pcDNA6	pcDNA6	Nephrolab, Cologne
F.Jade1S pcDNA6	pcDNA6	Generated within this work
F.Jade1L pCDNA6	pcDNA6	Generated within this work
F.JADE2 pcDNA6	pcDNA6	Generated within this work
F.JADE3 pcDNA6	pcDNA6	Generated within this work
F.Jade2 pcDNA6	pcDNA6	Generated within this work
F.Jade3 pcDNA6	pcDNA6	Generated within this work
V5.JADE1S pcDNA6	pcDNA6	Nephrolab, Cologne
V5.JADE1L pcDNA6	pcDNA6	Nephrolab, Cologne
V5.Jade1S pcDNA6	pcDNA6	Generated within this work
V5.Jade1L pCDNA6	pcDNA6	Generated within this work
V5.JADE2 pcDNA6	pcDNA6	Generated within this work
V5.JADE3 pcDNA6	pcDNA6	Generated within this work
V5.NPHP1 pcDNA6	pcDNA6	Nephrolab, Cologne
V5.NPHP4 pcDNA6	pcDNA6	Nephrolab, Cologne
F.EPS <sup>1-225</sup> pcDNA6	pcDNA6	Nephrolab, Cologne
V5.VHL pcDNA6	pcDNA6	Nephrolab, Cologne
F.VHL pcDNA	pcDNA6	Nephrolab, Cologne
F.GFP pcDNA6	pcDNA6	Nephrolab, Cologne
F.Podocin pcDNA6	pcDNA6	Nephrolab, Cologne
F.STAT3 pcDNA6	pcDNA6	Nephrolab, Cologne
pSpCas9(BB)-2A-Puro (PX459) V2.0	pSpCas9(BB)-2A-Puro	Addgene #62988
pSpCas9(BB)-2A-GFP	pSpCas9(BB)-2A-GFP	Addgene #48138
Jade1 exon6 pSpCas9(BB)-2A-GFP	pSpCas9(BB)-2A-GFP	Generated within this work
Jade1 exon7 pSpCas9(BB)-2A-GFP	pSpCas9(BB)-2A-GFP	Generated within this work
Jade2 exon6 pSpCas9(BB)-2A-GFP	pSpCas9(BB)-2A-GFP	Generated within this work
Jade2 exon7 pSpCas9(BB)-2A-GFP	pSpCas9(BB)-2A-GFP	Generated within this work
Jade3 exon8 pSpCas9(BB)-2A-GFP	pSpCas9(BB)-2A-GFP	Generated within this work
Jade3 exon9 pSpCas9(BB)-2A-GFP	pSpCas9(BB)-2A-GFP	Generated within this work
His.hJADE2(1-177) pET30b Z Be	pET30b Z Be	Generated within this work
His.hJADE3(1-178) pET30b Z Be	pET30b Z Be	Generated within this work

## 5.1.6 Cell lines

**Table 10. List of cell lines**

Name	Species	Parental cell line	Genotype
HEK293T	human	-	WT
mIMCD3 WT	mouse	-	WT
mIMCD3 WT #2	mouse	mIMCD3 WT	WT
mIMCD3 WT #8	mouse	mIMCD3 WT	WT
mIMCD3 <i>Jade1 KO1</i>	mouse	mIMCD3 WT #8	Compound heterozygote
mIMCD3 <i>Jade1 KO2</i>	mouse	mIMCD3 WT #8	Homozygote
mIMCD3 <i>Jade2 KO1</i>	mouse	mIMCD3 WT #8	Homozygote
mIMCD3 <i>Jade2 KO2</i>	mouse	mIMCD3 WT #8	Homozygote
mIMCD3 <i>Jade3 KO1</i>	mouse	mIMCD3 WT #8	Homozygote
mIMCD3 <i>Jade3 KO2</i>	mouse	mIMCD3 WT #8	Homozygote
SP2/ab	mouse	-	WT

## 5.1.7 Antibodies

**Table 11. List of primary antibodies used.**

Epitope	Product no.	Host	Dilution	Provider
Arl13B	17711-1-AP	Rabbit, polyclonal	1:500	ProteinTech
E-cadherin	610182	Mouse	1:500	BD BioSciences
FLAG (M2)	A2220-5ML	Mouse	1:5000	Sigma-Aldrich
FLAG	F7425	Rabbit	1:2000	Sigma-Aldrich
JADE3 B4	-	Mouse, monoclonal	1:10	Nephrolab, Cologne
JADE3 B7	-	Mouse, monoclonal	1:10	Nephrolab, Cologne
V5	MCA1360	Mouse, monoclonal	1:1000	Serotec
V5	AB3792	Rabbit, polyclonal	1:1000	Millipore

**Table 12. List of secondary antibodies used.**

Epitope	Product no.	Dilution	Provider
Donkey anti mouse A488	715-545-150	1:500	Jackson ImmunoResearch
Donkey anti mouse Cy3	715-165-150	1:500	Jackson ImmunoResearch
Donkey anti mouse Cy5	715-175-150	1:500	Jackson ImmunoResearch
Donkey anti rabbit A488	711-546-152	1:500	Jackson ImmunoResearch
Donkey anti rabbit C3	711-165-152	1:500	Jackson ImmunoResearch
Goat anti mouse IgG-HRP conjugated	115-035-003	1:30.000	Jackson ImmunoResearch
Goat anti rabbit IgG-HRP Conjugated	111-035-003	1:30.000	Jackson ImmunoResearch
Fluorescein Lotus Lectin	VEC-FL-1321	1:250	Biozol

## 5.1.8 Enzymes

**Table 13. List of enzymes used.**

Enzyme	Product no.	Provider
FastDigest BbsI	FD1014	Thermo Scientific
Exonuclease I (ExoI)	EN0581	Thermo Scientific
MluI	R0198L	New England Biolabs
NotI	RO189L	New England Biolabs
Proteinase K	EO0492	Thermo Scientific
Shrimp Alkaline Phosphatase (SAP)	M0371S	New England Biolabs
T4 Ligase	M0202M	New England Biolabs
T4 polynucleotide kinase	M0201S	New England Biolabs
T7 DNA Ligase	M0318S	New England Biolabs

## 5.1.9 Unique target peptides for the PRM assay

**Table 14. List of unique target peptides for the PRM assay.**

Mass [m/z]	Charge state	peptide	Protein
525.2667	2	VLEEFQR	Jade1
566.2982	2	TILAENDEVK	Jade1
857.1147	3	QKLQQLLEDEFYTFVNLLDVAR	Jade1
723.7175	3	ALRLPEEVVDFLYQYWK	Jade1
692.859	2	VQEQIFTQYTK	Jade1
671.7939	2	SLC[CAM]]QEHSDDGGPR	Jade2
559.2766	2	IPEGSWLC[CAM]R	Jade3

## 5.1.10 Consumables

**Table 15. List of consumables used.**

Consumable	Product no.	Provider
10 cm dish for Agar Plates	82.1473	Sarstedt
384 well plates	785290	Greiner BioOne
96-well plate, sterile, f-bottom, with lid	655180	Greiner BioOne
Adhesive qPCR tape	951,999	Sarstedt
Biosphere Filter Tip 10 µl, sterile	70.1116.210	Sarstedt
Biosphere Filter Tip 1000 µl, sterile	70.762.211	Sarstedt
Biosphere Filter Tip 200 µl, sterile	70.760.211	Sarstedt
Blotting paper (Type BF4, 580 x 580)	FT-2-521-580580G	VWR
Bottle Top Filter (150 mL, 0.22 µm)	430626	LMS
BottleTopFilter (500 mL)	430513	Corning
Casy Cups	5651794001	OMNI Life Science
Cell culture dishes (10-cm)	430167	Corning
Cell culture dishes (12-well)	3513	Corning
Cell culture dishes (6-well)	3516	Corning

*Continued on next page*

Cell strainers 40 µm, blau	833945040	Sarstedt
Combs (10 well, 1 mm) for acrylamide gels	NC3010	Invitrogen
Combs (12 well, 1 mm) for acrylamide gels	NC3012	Thermo Fisher Scientific
Coverslips (round 18 mm Nr. 1.5)	631-0153	VWR
Eppendorf tubes (1.5 mL)	72.690.001	Sarstedt
FACS tubes (5 mL)	734-0447	Corning
FACS tubes (5 mL), with cell strainer	734-0001	Corning
Fast Thermal Cycling Plates 96 well	4346907	Applied Biosystems
Gel cassette (1 mm)	NC2010	Invitrogen
Glas Pasteur Pipettes (150 mm, 2 mL)	612-1701	VWR
Histosette® I	M499-11	Simport
Inoculation loop (1 µL)	734-2138	VWR
Luer slip syringe (2 mL)	300185	BD
Luer slip syringe (3 mL)	309658	BD
Microfuge Tube Polypropylene (1.5 mL)	357448	Beckman Coulter
Millipore Immobilon-P Transfer Membranes	T831.1	Carl Roth
Needle 20G x 1½"	301300	BD
Needle 27G x 3/4"	302200	BD
Nitrile gloves S	224685	Abena
Nunc Cryotube™	368632	Thermo Fisher Scientific
Paraplast PLUS	X881.2	Carl Roth
PCR Soft-tubes 0.2 mL 8 Tubes/Flat Caps, clear	710970	Biozym
PCR Soft-tubes 0.2 mL assorted colours	711088	Biozym
PCR Soft-tubes 0.2 mL clear	710920	Biozym
Pipette tips (1000 µl blue)	70.760.002	Sarstedt
Pipette tips (200 µl yellow)	70.762	Sarstedt
Polypropylene conical tube (15 mL)	227261	Greiner BioOne
Polypropylene conical tube (50 mL)	227261	Greiner BioOne
Reservoir V-Form (60 mL)	613-2671	VWR
Safe Lock 1,5 mL Eppendorf tubes	211-2130	VWR
Safe Lock Tubes (1.5 mL)	0030 123.328	Eppendorf
Stripettes (10 mL)	4101	LMS
Stripettes (25 mL)	4251	LMS
Stripettes (5 mL)	4051	LMS
Stripettes (50 mL)	4501	LMS
SuperFrost®/Plus microscope slides	7695002	Th.Geyer Group
Syringe (Plastipak™ 1 mL)	7392/2007	BD
Syringe filters ROTILABO® PVDF, 0,22 µm	P666.1	Carl Roth
TipOne (0.1-10 µl XL), sterile	S1110-3810	Starlab
TipOne (101-1000 µl graduated), sterile	S1111-6811	Starlab
TipOne (1-200 µl beveled), sterile	S1111-1816	Starlab
TipOne Pipette Tip 10 µl, refill	S1111-3700	Starlab
TipOne Pipette Tip 1000 µl, refill	S1111-6700	Starlab
TipOne Pipette Tip 200 µl, refill	S1111-1700	Starlab
Weighing tray 140 x 140 mm	2159.1	Carl Roth
Weighing tray 89 x 89 mm	2150.1	Carl Roth

## 5.1.11 Equipment

**Table 16. List of equipment used.**

<b>Equipment</b>	<b>Model</b>	<b>Provider</b>
Autoclave	V-150	Systec
Avanti centrifuge	J-301	Beckman
AxioCam	MRm	Zeiss
Axiovert microscope	200M	Zeiss
Cell Freezing Containers	CoolCell SV2	Biocision
Centrifuge (refrigerated)	5810 R	Eppendorf
Cryostat	CM1850 UV	Leica
Dumont #5 forceps	14098	WPI
Dumont #55 forceps	14099	WPI
EnSpire Multimode Plate Reader	2300-0000	Perkin Elmer
Eppendorf Research® Multipipette (10-100 µl)	3122000043	Eppendorf
Eppendorf Research® plus, 8-channel, variable, 10 – 100 µL	3122000035	Eppendorf
Fusion Solo chemiluminometer	60-FU-SOLO	PeqLab
Hamilton syringe (50 µl Type 705)	549-1155	VWR
Heatingblock	TH 21	Ditabis
HERAcell Incubator	240	Heraeus
HERAcell Incubator	150	Heraeus
Heraeus B12 Function Line incubator	50042307	Kendro Laboratory Products
Horizontal electrophoresis system size L	40-1214	PeqLab
Horizontal electrophoresis system size S	40-0708	PeqLab
Incubator	BD 115	Binder
Incubator (Agarose)	T 6030	Heraeus
Innova Incubator Shaker	4400	New Brunswick Scientific
Inverted microscope	CK2	Olympus
Laminar Flow Cabinet	HS12	Heraeus
MacsMix Tube Rotator	MX100	Miltenyi Biotech
Microcentrifuge	5424	Eppendorf
Microcentrifuge (refrigerated)	5415 R	Eppendorf
Microcentrifuge (refrigerated)	5417R	Eppendorf
Microtome	RM2235	Leica
Minicentrifuge	521-2844	VWR
Nanodrop Spectrophotometer	1000	PeqLab
Odyssey CLx	-	Li-COR
Operating scissor	501754	WPI
Pipetboy acu	155 015	Integra Biosciences AG
Pipetman Pipette set (P2, P10, P100)	F167500	Gilson
Pipetman Pipette set (P20, P200, P1000)	F167300	Gilson
Power supply	700-0115	VWR
Power supply (for Dan-Kar system)	EPS200	Pharmacia Biotech

*Continued on next page*

Powerpac 200 Power supply	1655052	Bio-Rad
Powerpac 3000 Power supply	1655057	Bio-Rad
S3e Cell Sorter	12007058	Bio-Rad
Shaker	KS 260	IKA
Slidescanner	SCN400	Leica
Sterile hood	Mars Safety Class 2	SCANLAF
Suction pump	181-0067DE	VWR
Suction pump (cell culture)	HLC	DITABIS
TCS SP8	-	Leica
Thermal cycler	S1000	Bio-Rad
Thermal cycler (MJ mini)	PTC-1148	Bio-Rad
Thermomixer Comfort 1.5 mL Thermoblock	5360 000.011	Eppendorf
Thermomixer Comfort shaker & heating plate	5355 000.011	Eppendorf
UV Transilluminator system	MW312	Intas
Vannas Scissors	500086	WPI
Vortex Mixer	444-1372	VWR
Vortex Mixer	MS525-20	Heidolph (Reax)
Water bath	WNB 22	Memmert
Water bath (digital heating bath)	HBR4	IKA
Water bath (for paraffin sections)	HI1210	Leica
XCell SureLock™ Mini-Cell electrophoresis system	100601-1408	Invitrogen

## 5.1.12 Software and online tools

**Table 17. List of software used.**

Software	Version	Provider
Adobe Illustrator 2021	25.4.1	Adobe
FlowJo	10.7.1	FlowJo, LLC
GraphPad Prism9	9.1.0	GraphPad Software Inc.
ImageJ/Fiji	1.53c	Wayne Rasband
ImageScope	12.3.2.8013	Aperio
ImageStudio	5.2	LI-COR
INTAS GelDoc	2019	Intas
LAS	4.13	Leica
Mausoleum	7.3.8 b4	Dr. H.-E. Stöffler
MaxQuant	1.5.2.8.	Computational Systems Biochemistry, Prof. Jürgen Cox (Cox and Mann, 2008)
Microsoft Office Suite	Professional Plus 2016	Microsoft
Nanodrop 1000	3.8.1	Thermo Scientific
Perseus	1.6.1.1/1.6.15.0	Computational Systems Biochemistry, Prof. Jürgen Cox (Tyanova et al., 2016)
ProSort™ Software	1.6.0.12	Bio-Rad
R	4.0	R Core Team
RStudio	1.4	RStudio PBC
QuantStudio	1.4.1	Applied Biosystems
ZEN Blue	3.0	Zeiss
Zotero	5.0.93	Corporation for Digital Scholarship

**Table 18. List of websites and online tools used.**

Online Tool	Website
ArrayExpress	<a href="https://www.ebi.ac.uk/arrayexpress/">https://www.ebi.ac.uk/arrayexpress/</a>
Benchling	<a href="https://www.benchling.com/">https://www.benchling.com/</a>
Ensembl	<a href="https://www.ensembl.org">https://www.ensembl.org</a>
The Human Protein Atlas	<a href="https://www.proteinatlas.org/">https://www.proteinatlas.org/</a>
NCBI	<a href="https://www.ncbi.nlm.nih.gov/">https://www.ncbi.nlm.nih.gov/</a>
NCBI Blast	<a href="https://blast.ncbi.nlm.nih.gov/Blast.cgi">https://blast.ncbi.nlm.nih.gov/Blast.cgi</a>
NCBI PrimerBlast	<a href="https://www.ncbi.nlm.nih.gov/tools/primer-blast/">https://www.ncbi.nlm.nih.gov/tools/primer-blast/</a>
NCBI PubMed	<a href="https://pubmed.ncbi.nlm.nih.gov/">https://pubmed.ncbi.nlm.nih.gov/</a>
PRIDE	<a href="https://www.ebi.ac.uk/pride/">https://www.ebi.ac.uk/pride/</a>
WGE Crispr Finder	<a href="https://wge.stemcell.sanger.ac.uk//find_crisprs">https://wge.stemcell.sanger.ac.uk//find_crisprs</a>

## 5.2 Methods

### 5.2.1 Cloning PCR

Plasmids containing JADE1S, JADE1L, pVHL, EPS<sup>1-225</sup>, STAT3, and Podocin cDNA were previously described (Borgal et al., 2012; Huber et al., 2001, 2003; Schermer et al., 2006). JADE2 and JADE3 cDNA were obtained by PCR from HEK293T cDNA. Jade1S, Jade1L, Jade2, and Jade3 cDNA were obtained by PCR from mIMCD3 cDNA. cDNA was generated from RNA isolated with RNAeasy Mini Kit with the SuperScript<sup>TM</sup> III Reverse Transkriptase kit. PCR was preformed using Q5<sup>®</sup> High-Fidelity DNA Polymerase following the manufacturer's instructions with the cloning primers as indicated in Table 6. On a MJ mini thermal cycler, the polymerase was activated for 30 s at 98°C followed by thirty repetitions of the following tree-step cycle: Denaturing for 20 s at 98°C, annealing for 10 s at [Primer T<sub>m</sub> - (5-10) °C], and extension for 30 s/kb at 72°C. A final extension step of 2 min at 72°C was added. For purification of PCR products the GeneJet PCR Purification Kit was used according to the manufacturer's instructions. The PCR products were analyzed by agarose gel electrophoresis (section 5.2.2).

### 5.2.2 Enzymatic digest

All PCR products intended to be ligated into a pcDNA6 vector backbone or a pET30b Z Be vector backbone were generated with an N-terminal MluI restriction site and a C-terminal NotI restriction site. The PCR products were digested using MluI and NotI and ligated into an existing plasmid with a pcDNA6 vector backbone or pET30b Z Be vector backbone which had been digested with the same enzymes. Both vector backbones had previously been modified to remove an internal MluI site. Enzymes were ordered from New England BioLabs (Table 13) and used according to a modified version of the manufacturer's protocol. Digests of PCR products and vector backbones intended for use in a ligation reaction were performed as a 30 µL reaction using PCR grade water, 1 µg DNA, 3 µL buffer 3.1, 0.5 µL MluI, and 0.5 µL NotI. The reactions were incubated at 37°C for 2h (plasmids) or overnight (PCR

products). Fragments were analyzed using agarose gel electrophoresis (section 5.2.3) after gel extraction and purification. For a diagnostic digest after bacterial transformation and DNA isolation the volume of the reaction was reduced to 15  $\mu\text{L}$  with 500 ng DNA, 1.5  $\mu\text{L}$  buffer 3.1, 0.3  $\mu\text{L}$  MluI, and 0.3  $\mu\text{L}$  NotI. The reactions were incubated at 37°C for 30 min, followed by analysis on a 1% agarose gel (section 5.2.3).

### 5.2.3 Agarose gel electrophoresis

Agarose gel electrophoresis was performed according to standard protocols (Brody and Kern, 2004). Either 1% or 2% agarose gels in 1x TAE buffer were run by applying an appropriate voltage. Intas UV Transilluminator system together with the Intas GDS Windows software were used to visualize the DNA fragments. For 1% agarose gels a 1 kb DNA ladder was used, for 2% agarose gels a 50 bp DNA ladder was used to estimate the DNA fragment size. For gel extraction, the required bands were excised with a scalpel under UV light. Purification of gel fragments was performed with the GeneJET Gel Extraction Kit according to the manufacturer's instructions. The final elution volume was adjusted to 30  $\mu\text{L}$ .

### 5.2.4 Ligation

After agarose gel extraction (section 5.2.3) appropriate pairs of insert DNA and vector DNA were ligated using the T4 ligase kit with a modified version of the manufacturer's protocol. A 21  $\mu\text{L}$  reaction with PCR grade water was set up with the following components: 2.1  $\mu\text{L}$  T4 ligase buffer (10x), 0.4  $\mu\text{L}$  T4 ligase (5 U/ $\mu\text{L}$ ), 1  $\mu\text{L}$  vector DNA, and 5-10  $\mu\text{L}$  insert DNA. A control reaction using water in place of insert DNA was always included. Incubation of the reaction took place for 2 h at room temperature (RT).

### 5.2.5 Bacterial transformation and plasmid DNA isolation

Bacterial transformation was performed using standard techniques (Chen and Dubnau, 2004) and chemocompetent DH10B T1 Phage-Resistant *E. coli* cells unless otherwise stated. 3-5  $\mu\text{L}$  of the ligation or control reaction (section 5.2.4) were added to 25  $\mu\text{L}$  of bacteria and incubated on ice for 30 min. A heat shock was performed for 45 s at 42°C using an IKA digital heating water bath. Afterwards the mixture was placed on ice for 2 min. For each sample 500  $\mu\text{L}$  of pre-warmed SOC medium was added followed by a 1 hour incubation at 37°C at 800 rpm. 100  $\mu\text{L}$  of the bacteria were streaked out on pre-warmed agar plates with 100  $\mu\text{g}/\text{mL}$  of ampicillin antibiotic (pcDNA6 constructs) or 25  $\mu\text{g}/\text{mL}$  of kanamycin (pET30b Z Be constructs). After drying the plate at RT for 15 min, plates were incubated at 37°C overnight. The following day the surviving colonies transformed with the ligation product were compared to the surviving colonies transformed with the control reaction product. An appropriate number of colonies were cultured in a 15 mL falcon tube containing 3 mL of LB medium (20g/L) with

antibiotic (100 µg/mL of ampicillin antibiotic/pcDNA6 constructs, 25 µg/mL of kanamycin/pET30b Z Be constructs). The bacterial mini culture was incubated overnight at 37°C and 120 rpm. For plasmid DNA isolation, the GeneJET Plasmid Miniprep Kit was used according to manufacturer's instructions with 1.5 mL of the bacterial mini culture. The correct insert size was verified with a diagnostic digest (section 5.2.2) and agarose gel electrophoresis (section 5.2.3). The remaining 1.5 mL from a positive clone was used to start a midi culture in 200 mL of LB medium (20g/L) with the appropriate antibiotic (see above). The bacterial midi cultures were incubated overnight at 37°C and 120 rpm. Plasmid DNA was extracted using NucleoBond Xtra Midi Kit according to manufacturer's instructions. The plasmid concentration was determined using the Nanodrop 1000 spectrophotometer according to manufacturer's instructions. The correct insert sequence was verified by Sanger sequencing (section 5.2.6).

### 5.2.6 Sanger sequencing

Automated DNA sequencing service was provided by the Cologne Centre for Genomics (CCG). The samples were prepared using the Big Dye Terminator version 3.1 sequencing kit according to a modified protocol. A 10 µL reaction in PCR grade water was set up with the following components: 2.25 µl Big Dye Terminator sequencing buffer, 0.25 µl Big Dye Terminator version 3.1, 0.25 µl sequencing primer (100µM), 100-200 ng template. Sequencing primers are listed in Table 5. The reactions were run on a MJ mini thermal cycler with the following conditions: An initial 1 min polymerase activation at 96°C followed by 40 repetitions of denaturing for 10 s at 96°C, annealing for 5 s at 55°C, and extension for 4 min at 60°C. Sequence readings were aligned using Benchling (Benchling [Biology Software]. 2021. Retrieved from <https://benchling.com>) and BLAST (Altschul et al., 1990)

### 5.2.7 Recombinant protein production

#### 5.2.7.1 Mini culture

Transformation of the pET30b Z Be plasmids into BL21 (DE3) Codon Plus RIPL cells was performed as described in section 5.2.5. 2-4 colonies were picked in 3 mL of 2 x YTA medium supplemented with 25 µg/mL kanamycin antibiotic and incubated on a shaker at 37°C for about 5 h until the cultures were cloudy. For each culture 2 x 1 mL was transferred into 2 Eppendorf tubes (1.5 mL). 1 mM IPTG was added to one of the tubes. Both tubes were incubated for 2 h at 37°C and 900 rpm ensuring ventilation by poking holes in the lid. The bacteria were pelleted (1 min, 20.000 x g, RT) and resuspended in 1x Laemmli sample buffer. After boiling them for 5 min at 95°C they were directly loaded on an polyacrylamide gel (section 5.2.10) and analyzed by colloidal coomassie staining (section 5.2.11).

### 5.2.7.2 Maxi culture

After successful test of the clones with the mini culture described above, the remaining culture of an inducible clone was added to 100 mL of 2 x YTA medium with 25 µg/mL kanamycin antibiotic and incubated overnight at 30°C and 120 rpm. 50 mL of the overnight culture was added to 1 L of 2 x YTA medium supplemented with 25 µg/mL of kanamycin as well as 34 µg/mL chloramphenicol and incubated at 30°C and 120 rpm. OD600 was measured regularly until an OD600 of 0.6-0.8 is obtained. After adding IPTG to a final concentration of 0.1 mM the solution was incubated for 5 h at 30°C and 120 rpm. The culture was cooled on ice while shaking it carefully to avoid foam. The culture was then transferred to 1 L Beckman centrifuge tubes and centrifuged at 3100 x g for 15 min at 4°C. The supernatant was discarded and the pellet was resuspended in 35 mL of HIS-buffer. To lyse the bacteria 1 µg/mL DNase and 200 µg/mL lysosome were added and incubated on ice for up to 15 min. After adding 10 µL/mL PMSF the culture was sonicated on ice (7 x 10% (= 0,7s sonic, 0,3s pause), time 10 s, power 70%) with 6-12 x 30 pluses. 1.5 mL of the lysate was centrifuged at 20.000 x g for 10 min at 4°C and further processed for the expression control. The remaining lysate was centrifuged in Sorvall tubes at 50.000 x g for 45 min at 4°C and the supernatant was sterile filtered with a 0.45 syringe filter on a precursor syringe.

### 5.2.7.3 Expression test

To the expression control 30 µL of Ni-NTA coupled agarose beads were added to 1 mL of lysate and incubated for 1 h at 4°C. After pelleting the beads (400 x g, 2 min, 4°C) the supernatant is transferred to a new 1.5 Eppendorf tube ("flow through"). The beads were washed three times with HIS-buffer and then boiled with 30 µL of 2x Laemmli sample buffer and loaded on a polyacrylamide gel (section 5.2.10). The amount of protein visualized by colloidal coomassie staining (section 5.2.11).

### 5.2.7.4 Purification

An appropriate amount of Ni-NTA beads (1 mL of beads per 10 mg protein in lysate) was added to the lysate and incubated for 2 h at 4°C. A polypropylene column was set up and moistened with HIS-buffer. Afterwards, the bead-lysate solution was added to the column. The flow-through was collected and stored at 4°C. The falcon tube that contained the bead-lysate solution was rinsed with 50 mL of HIS wash buffer and added to the column. After the column had drained, the proteins were eluted with up to 5 mL of HIS elution buffer. The elution fractions were collected in 5-8 different Eppendorf tubes (1.5 mL). The protein concentration of the elution factions was estimated with a colloidal coomassie staining (section 5.2.11).

### 5.2.8 Cell culture

#### 5.2.8.1 Culturing of immortalized cell lines

Cell culture experiments were performed under sterile working conditions in a laminar-flow hood. All used equipment was disinfected with 70% of ethanol before use. All cell lines were cultured in monolayers and maintained at 37 °C / 5% CO<sub>2</sub>. A list of all cell lines used and generated within this work can be found in Table 10. Human embryonic kidney (HEK) 293T cells were cultivated in DMEM media with GlutaMAX supplemented with 10% fetal bovine serum (FBS). Inner medulla collecting duct cells (mIMCD3) were cultivated in DMEM/F12 supplemented with 10% FBS, 2 mM GlutaMAX. FACS sorted cell lines were supplemented with 1 % Penicillin/Streptomycin. The cells were passaged by washing them once with 1x PBS and adding 1 mL trypsin for 5 min at 37°C until the cells were no longer adherent. After inactivation of the trypsin with pre-warmed medium the desired amount of cells were transferred into a fresh culture dish with pre-warmed medium

#### 5.2.8.2 Freezing and thawing of cells

To maintain a stock of cells at a lower passage number they were frozen. A 80-90% confluent 10 cm dish was washed with 1x PBS, trypsinized, and resuspended in the according cell culture medium. The cells were pelleted at RT at 150 x g. The pellet was resuspended in 1 mL of freezing medium and transferred into a cryogenic vial. After freezing the cells at -80 °C in a cell-freezing container, they were transferred to N<sub>2</sub> tanks.

To thaw the cells, the vials were quickly thawed at 37 °C. The cells were resuspended in 8 mL of pre-warmed medium and transferred to a 15 mL falcon tube. After pelleting them at RT at 150 x g, the supernatant was removed and they were resuspended in 10 mL of pre-warmed medium. After transferring them into a 10 cm culture dish, they were incubated overnight at 37°C. Depending on their growth, either the medium was changed or they were passaged the next day. All cells were tested for mycoplasma using the PCR Mycoplasma Test Kit.

#### 5.2.8.3 Transfection of HEK293T cells

For transfection of HEK293T cells the CaCl<sub>2</sub> method was used (Benzing et al., 2001; Phelan, 2006). For each data point appropriate amounts of plasmids were added into 1.5 mL Eppendorf tubes containing 500 µL of 0.25 M CaCl<sub>2</sub> solution. While vortexing the CaCl<sub>2</sub> solution, 500 µL of 2x HEBS were added dropwise. The mixture was added dropwise to a 50 % confluent 10 cm dish of HEK293T cells. The medium was replaced after 6-8 hours and the cells were harvested the following day.

## 5.2.8.4 Generation of Jade-deficient mIMCD3 cell lines

For each Jade family member two independent single-guide RNAs (sgRNAs) were designed using the WGE CRISPR Finder tool (Hodgkins et al., 2015). Sequence editing was performed with Benchling (Benchling [Biology Software]. 2021. Retrieved from <https://benchling.com>). The targeting strategy is shown in section 6.1.5 The sgRNAs were cloned into the plasmid pSpCas9(BB)-2A-GFP (PX458), a gift from Feng Zhang (Addgene plasmid #48138; <http://n2t.net/addgene:48138>; RRID:Addgene\_48138) (Ran et al., 2013). mIMCD3 WT#8 cells were transfected with the generated plasmids using Lipofectamine 2000 according to the manufacturers' instruction. After 48 h GFP-positive cells were sorted into 5x 96-well plates on a BD FACSAria™III at the Max Planck Institute for Biology of Ageing (Kohli et al., 2017). We extracted DNA using the cell lysis buffer (56 °, 1h; 95°C, 10 min) from the clones and performed a first screen via PCR using the REDTaq® ReadyMix™ PCR reaction mix following the manufacturer's instructions (Table 19 and Table 20) and Sanger sequencing (section 5.2.6). The clones were further validated with qPCR (section 5.2.14) and targeted proteomics (see section 5.2.15).

**Table 19. List of reaction compositions for PCRs of Jade mutant cell lines.**

Gene	Reaction Mix
Jade1 KO1	7.5 µL ddH2O 1.25 pM Jade1_exon6_cellculture_fp 1.25 pM Jade1_exon6_cellculture_rp 12.5 µL REDTaq ReadyMix ~ 50 ng DNA
Jade1 KO2	7.5 µL ddH2O 1.25 pM Jade1_exon7_cellculture_fp 1.25 pM Jade1_exon7_cellculture_rp 12.5 µL REDTaq ReadyMix ~ 50 ng DNA
Jade2 KO1	7.5 µL ddH2O 1.25 pM Jade2_exon6_cellculture_fp 1.25 pM Jade2_exon6_cellculture_rp 12.5 µL REDTaq ReadyMix ~ 50 ng DNA
Jade2 KO2	7.5 µL ddH2O 1.25 pM Jade2_exon7_cellculture_fp 1.25 pM Jade2_exon7_cellculture_rp 12.5 µL REDTaq ReadyMix ~ 50 ng DNA
Jade3 KO1	7.5 µL ddH2O 1.25 pM Jade3_exon8_cellculture_fp 1.25 pM Jade3_exon8_cellculture_rp 12.5 µL REDTaq ReadyMix ~ 50 ng DNA

*Continued on next page*

Jade3 KO2	7.5 $\mu$ L ddH <sub>2</sub> O 1.25 pM Jade3_exon9_cellculture_fp 1.25 pM Jade3_exon9_cellculture_rp 12.5 $\mu$ L REDTaq ReadyMix ~ 50 ng DNA
-----------	---

**Table 20. List of cycling conditions used for performing PCRs of Jade mutant cell lines.**

Gene	Step	Temperature [°C]	Duration [s]	No. of cycles
Jade1 exon6 / Jade1 exon7	Initialization	94	180	
	Denaturation	94	45	
	Annealing	64	60	
	Extension	72	30	go to step 2, 35 repeats
	Final extension	72	180	
	Final hold	15	$\infty$	
Jade2 exon6 / Jade2 exon7	Initialization	94	180	
	Denaturation	94	45	
	Annealing	66	60	
	Extension	72	30	go to step 2, 35 repeats
	Final extension	72	180	
	Final hold	15	$\infty$	
Jade3 exon8 / Jade3 exon9	Initialization	94	180	
	Denaturation	94	45	
	Annealing	62	60	
	Extension	72	30	go to step 2, 35 repeats
	Final extension	72	180	
	Final hold	15	$\infty$	

#### 5.2.8.5 Flow cytometry

The flow cytometry with propidium iodide (PtdIns) staining were performed as previously published (Borgal et al., 2016). mIMCD3 cells (WT#8, Jade-deficient cell lines) were seeded at  $2 \times 10^6$  cells / 10 cm culture dish and harvested 24 h later. For experiments with serum reduced medium, the cells were seeded at  $0.5 \times 10^6$  cells/ 10 cm in full medium. After 24 h the medium was replaced by serum reduced medium for 48 h. The cells were harvested with accutase and washed twice with 5 mL BSA (1% w/v) in 1x PBS the cell pellets were resuspended in 100  $\mu$ L sodium chloride (0.9% w/v). The cell suspension was added dropwise to 5 mL of ice-cold methanol while vortexing. After 45 min incubation on ice the suspension was centrifuged at  $240 \times g$  for 5 min at 4 °C. The cell pellets were resuspended in 1 mL of 2N hydrogen chloride solution with 0.5% (v/v) Triton X-100. After 40 min incubation at RT the cells were centrifuged at  $100 \times g$  for 5 min at 4°C. The pellet was resuspended in 500  $\mu$ L of PtdIns solution and incubate at RT for 30 min. After washing the cells twice with 1x PBS the PtdIns intensity was analyzed using a Bio-Rad S3e Cell Sorter. The acquired data was analyzed with FlowJo software.

### 5.2.8.6 *In vitro* assay of 26S proteasome activity

The proteasomal activity assay was performed as previously described (Kisselev and Goldberg, 2005). For each replicate with the mIMCD3 cells, the cells were grown into 6-well plates and grown until 70% confluency. HEK29T cells were grown into 6-well plates, transfected at 50% confluency with 2  $\mu$ g of DNA using the calcium phosphate method (section 5.2.8.3), and harvested 24 h after transfection. Cells were collected in proteasomal activity assay buffer and immediately frozen in liquid nitrogen. Before performing the assay, samples were lysed and centrifuged at 10000 x g for 10 min at 4°C. 25  $\mu$ g of protein was loaded on a flat-bottom, black fluorescence 96-well microplate and incubated with the fluorogenic substrate (Z-Gly-Gly-Leu-AMC). Fluorescence (360 nm excitation, 430 nm emission) was monitored every 5 min for 2 h at 37°C using an EnSpire Multimode Plate Reader. Samples were assayed in technical triplicates and in biological replicates.

### 5.2.8.7 Immunofluorescence staining of cells

Cells were grown in 12-well culture dishes on glass coverslips. The cells were washed once with 1x staining PBS and fixed with 4% paraformaldehyde (PFA) for 15 min at RT. After three washing steps with 1x staining PBS the cells were blocked for 1 h with 5% normal donkey serum (NDS) in 1x PBSTx. Primary antibodies (Table 11) were diluted in 1x PBSTx and incubated overnight at 4°C, followed by 1 h incubation with the fluorescently labelled secondary antibody (Table 12). Cells were washed thoroughly with 1x staining PBS prior to mounting onto glass slides using Prolong Diamont antifade reagent with DAPI as a mounting medium. Images were acquired with TCS SP8 Confocal Microscope and processed with ImageJ/Fiji.

### 5.2.9 Immunoprecipitation

Immunoprecipitation (IP) experiments were performed as described previously (Borgal et al., 2012). HEK293T cells were harvested on ice in 8 mL of ice-cold 1x PBS and transferred to a 15 mL falcon tube. The cell suspension was pelleted for 5 min at 4°C and 100 x g. The cell pellet was resuspended in 1 mL IP lysis buffer. The cell suspension was incubated for 15 min on a MacsMix tube rotator and centrifuged at 20.000 x g for 15 min at 4°C. The supernatant was transferred into Ultra-Clear ultracentrifugation tubes and centrifuged at 100.000 x g for 30 min at 4°C. 30  $\mu$ L of the post-ultracentrifugation supernatant was kept as IP lysate, mixed with 30  $\mu$ L of 2x Laemmli sample buffer and incubated at 95°C for 5 min. The remaining post-ultracentrifugation supernatant was transferred into new 1.5 mL Eppendorf tubes. 50  $\mu$ L of anti-FLAG beads (M2, 1:2 in Agarose) were added and incubated for 1 h at 4°C using a MacsMix tube rotator. The beads were pelleted at 400 x g for 2 min at 4°C and the supernatant was discarded. The beads were resuspended in 1 mL of IP lysis buffer and again pelleted at 400 x g for 2 min at 4°C. After three washing steps, 50  $\mu$ L of 2x Laemmli sample buffer was added to

the beads and mixed by flicking. Samples were boiled at 95°C for 5 min. Lysates and IP samples were stored at -20°C.

### 5.2.10 SDS polyacrylamide gel electrophoresis (SDS-PAGE) and immunoblot

Proteins were separated by SDS-PAGE electrophoresis and visualized by HRP chemiluminescence. For each gel 6 mL resolving buffer were mixed with 0.15% TEMED and 0.1% APS. After pouring this solute in an empty gel cassette a top layer of Isopropanol was added. After polymerization, isopropanol was removed and 1.7 mL stacking buffer mixed with 0.15% TEMED and 0.1% APS were added and a 10-well or 12 well comb was added. After the stacking gel was solidified, the gels were assembled into a XCell SureLock™ Mini-Cell electrophoresis system filled with 1x running buffer according to manufacturer's instructions. To determine the molecular weight of the proteins 3 µL of Page-ruler Plus protein ladder was used. After loading of the sample the following program was run: 70 V for 30 min, 25 milliamps per gel for approximately 2 h, or until the ladder used had extended the entire length of the gel.

Immuoblotting was preformed using a semi-dry system. Separated proteins were transferred from the gel to a Millipore Immobilon-P polyvinylidene difluoride (PVDF) membrane, which was activated in methanol for 30 s and washed in 1 x transfer buffer. The polyacrylamide gel as well as two filter papers were soaked in 1 x transfer buffer. The blot was assembled as follows: filter paper, PVDF membrane, polyacrylamide gel, second filter paper. Air bubbles were rolled out. Transfer of proteins was performed by a constant current of 12 V for 1 h. After blotting, the membrane was incubated in 5% BSA for 1 h at RT, followed by three washing steps for 5 min with 1 x protein wash buffer. Afterwards the membranes were incubated with the primary antibody (Table 11) diluted in 1 x protein wash buffer for 1 h at RT or at overnight at 4°C. The membranes were washed three time for 5 min in 1x protein wash buffer before incubation with the appropriate HRP-conjugated secondary antibody (Table 12) diluted in 1 x protein wash buffer for 30 min at RT. After the additional wash steps with 1 x protein wash buffer for 10 min each, excess buffer was shaken off the membranes and they were transferred to a plastic tray. The membranes were developed using ECL detection solution or SuperSignal West Femto Chemiluminescent Substrate. The proteins were visualized using a PeqLab Fusion Solo chemiluminometer and Fusion-CAPT software.

### 5.2.11 Colloidal coomassie staining

10 µL of sample containing recombinant protein (section 5.2.7) was mixed with 10 µL of 2x Laemmli sample buffer. As a control a defined amounts (1 µg and 5 µg) of bovine serum albumin (BSA) mixed with 2x Laemmli sample buffer (1:1) were used. Prior to loading the samples and control were boiled at 95°C for 5 min. Gel electrophoresis was performed as described in section 5.2.3. The polyacrylamide gel was incubated for 30 min at RT in fixing solution. This was followed by an overnight incubation in

colloidal coomassie staining solution. For destaining the gel was transferred into water and destaining it until the gel background was clear. Images were acquired with the Odyssey CLx.

### 5.2.12 Enzyme-linked immunosorbent assay (ELISA)

ELISA microplates were coupled with 40 ng of recombinant protein (section 5.2.7) per well in 100  $\mu$ L sterile 1 x PBS and stored at 4°C. After 24 h they were washed with PBST and stored in ELISA blocking solution at 4°C. Before usage, they were washed three times with PBST. 100  $\mu$ L of serum (different dilutions from 1:100 to 1:1.000.000) or hybridoma culture supernatant was added and incubated for 1 h at 37°C. After three washing steps with PBST the HRP-conjugated secondary antibody was added (1:5000 dilution in PBST) and incubated for 1 h. After three additional washing steps with PBST 100  $\mu$ L of ELISA developer solution was added. Depending on signal intensity, the reaction was stopped by adding 50  $\mu$ L of 2N HCL after 30 s to 10 min. The plates were analyzed with the EnSpire Multimode Plate Reader. Absorbance was measured at 480 nm.

### 5.2.13 RNA isolation

RNA extraction for quantitative PCR (qPCR) analysis as well as RNAseq was performed with the Direct-zol RNA Miniprep kit following the manufacturer's instructions including a DNase1 treatment step. The pellet was resuspended in 30  $\mu$ L of RNase-free water. The yield and quality was evaluated using the Nanodrop 1000 spectrophotometer according to manufacturer's instructions.

### 5.2.14 qPCR

After RNA isolation (section 5.2.13) 1 $\mu$ g of total RNA was used as template for a reverse transcription reaction using the High-Capacity cDNA Reverse Transcription kit according to the manufacturer's instructions. mRNA expression was assessed in triplicate by SYBR Green qPCR with Hprt1 as a house keeping gene. All qPCR primers are listed in Table 7 and were validated in a separate experiment by running a standard curve PCR with 4 cDNA dilutions (50 ng; 5 ng; 0.5 ng; 0.05 ng) and a genomic DNA control. The qPCR experiments were performed on a QuantStudio 12K Flex Real-time PCR System. A dissociation curve was run after every experiment. Data were visualized and analyzed with QuantStudio and Prism software. Data were analyzed using a student's t-test and are presented as mean  $\pm$  standard error of the mean (SEM). Significance levels are indicated in the figure legends.

### 5.2.15 Parallel reaction monitoring (PRM) assay

Preparation of the samples for targeted mass spectrometry was performed as previously described (Bartram et al., 2016). Pellets were resuspended in Urea buffer and sonicated (Bioruptor, 10 min, cycle 30/30 sec). After clearing of the sample (20000 x g, 30 min at 4°C) the protein concentration was measured using the Pierce™ BCA Protein Assay Kit following the manufacturer's instructions. The

lysates were reduced (10 mM Dithiothreitol, 1 h, RT) and alkylated (50 mM Chloroacetamide, 30 min, RT, in the dark). An equal amount of protein (50 µg) was diluted with 50 mM TEAB to reach a urea concentration of 2M and subjected to tryptic digestion (enzyme:substrate ratio of 1:50). The overnight digestion was stopped by adding formic acid to a final concentration of 1%. On the next day, double-layered stage-tip clean up (C18) was performed. Double layer SDB-RP StageTips packed in 200 µL pipette tips were provided by the proteomics facility at CECAD. All steps were performed at RT. The StageTips were first equilibrated by adding 20 µL of methanol (650 x g, 1 min), followed by 20 µL of StageTip buffer B (650 x g, 1 min) and twice 20 µL of StageTip buffer A (650 x g, 1.5 and 2 min, respectively). The samples were centrifuged at 20,000 x g for 5 min before loading them onto the StageTips. These were centrifuged for 5 min at 650 x g. This was followed by three washing steps: 30 µL of StageTip buffer A and twice 30 µL of StageTip buffer B (each 650 x g, 3 min). The StageTips were dried with a syringe and stored at 4°C.

All samples were measured by the proteomics facility at CECAD. All samples were analyzed on an Orbitrap Exploris 480 mass spectrometer coupled to an EASY nLC 1200 UPLC (both Thermo Scientific). Peptides were loaded with solvent A (0.1% formic acid in water) onto an in-house packed analytical column (30 cm × 75 µm I.D., filled with 2.7 µm Poroshell EC120 C18 (Agilent)). Peptides were chromatographically separated at a constant flow rate of 300 nl min<sup>-1</sup> using with the following gradient: initial 4 % solvent B (0.1% formic acid in 80% acetonitrile), ramp to 25% B within 72 min, to 55% B within 8 min and to 95% B within 2 min, followed by washing and column equilibration. The Exploris was equipped with a FAIMS Pro Interface (Thermo) set to a CV of -47 and operated in scheduled PRM mode. The MS1 survey scan was acquired from 400 to 1000 m/z at a resolution of 120,000. Target masses were isolated in a 2 h window and fragmented by HCD with collision energy of 30%. The AGC target was set to 100 % and resulting spectra recorded with a resolution of 120,000. Product ions were detected in the Orbitrap at a resolution of 17,500.

Target list generation and follow-up analysis were performed in Skyline 20.2. Unique target peptides and their retention times were chosen based on their detectability in data-independent trials using the identical setup and gradient. Results were compared against their theoretical spectra simulated by the ProSight algorithm (Gessulat et al., 2019) plugin in Skyline (MacLean et al., 2010; Pino et al., 2020). Only areas with a dotp value above 0.7 were included in the analysis to ensure the confidence of the result. The targets are listed in Table 14.

### 5.2.16 Proteome

For each replicate, a 10 cm dish of mIMCD3 cells of the indicated genotype was harvested and snap-frozen. Samples were processed as described under section 5.2.15. All samples were analyzed on a Q Exactive Plus Orbitrap (Thermo Scientific) mass spectrometer that was coupled to an EASY nLC (Thermo

Scientific). Peptides were loaded with solvent A (0.1% formic acid in water) onto an in-house packed analytical column (50 cm — 75  $\mu$ m I.D., filled with 2.7  $\mu$ m Poroshell EC120 C18, Agilent). Peptides were chromatographically separated at a constant flow rate of 250 nL/min using the following gradient: 3-4% solvent B (0.1% formic acid in 80 % acetonitrile) within 1.0 min, 4-27% solvent B within 119.0 min, 27-50% solvent B within 19.0 min, 50-95% solvent B within 1.0 min, followed by washing and column equilibration. The mass spectrometer was operated in data-dependent acquisition mode. The MS1 survey scan was acquired from 300-1750 m/z at a resolution of 70,000. The top 10 most abundant peptides were isolated within a 1.8 Th window and subjected to HCD fragmentation at a normalized collision energy of 27%. The AGC target was set to 5e5 charges, allowing a maximum injection time of 55 ms. Product ions were detected in the Orbitrap at a resolution of 17,500. Precursors were dynamically excluded for 30.0 s.

All mass spectrometric raw data were processed with Maxquant (version 1.5.3.8) using default parameters. Briefly, MS2 spectra were searched against the canonical Uniprot mouse fasta database (UP000000589; May 4, 2020) and the MaxQuant default list of common contaminants. False discovery rates on protein and PSM level were estimated by the target-decoy approach to 1% (Protein FDR) and 1% (PSM FDR) respectively. The minimal peptide length was set to 7 amino acids and carbamidomethylation at cysteine residues was considered as a fixed modification. Oxidation (M) and Acetyl (Protein N-term) were included as variable modifications. The match-between runs option was enabled. Student's t-tests were calculated in Perseus (version 1.6.1.1) after removal of decoys and potential contaminants. Data were filtered for at least 3 out of 3 values in at least one condition. Remaining missing values were imputed with random values from the left end of the intensity distribution using Perseus defaults.

### 5.2.17 Interactome

For each replicate, a 10 cm dish of Jade1 KO1 mIMCD3 cells was transfected with 10  $\mu$ g of either FLAG-tagged Jade1S, Jade1L or an empty vector control using Lipofectamine 2000 following the manufacturer's instructions. 48 h after transfection cells were harvested and lysed in modified RIPA buffer for 15 min @ 4°C. After sonication (Bioruptor, 10 min, cycle 30/30 sec) and centrifugation (16,000 x g, 4°C, 15 min) anti-FLAG agarose beads were added to the supernatant and incubated at 4°C overnight. After three washing steps, 5% SDS in 1xPBS was added to the beads and proteins were released from the beads by incubation at 95°C for 3 min. Subsequently, the supernatant was reduced with DTT and alkylated with CAA followed by two single-pot solid-phase-enhanced sample preparations (SP3) (Hughes et al., 2019).

All samples were analyzed on a Q Exactive Plus Orbitrap (Thermo Scientific) mass spectrometer that was coupled to an EASY nLC (Thermo Scientific). Peptides were loaded with solvent A (0.1% formic acid

in water) onto an in-house packed analytical column (50 cm — 75 µm I.D., filled with 2.7 µm Poroshell EC120 C18, Agilent). Peptides were chromatographically separated at a constant flow rate of 250 nL/min using the following gradient: 3-5% solvent B (0.1% formic acid in 80 % acetonitrile) within 1.0 min, 5-30% solvent B within 65.0 min, 30-50% solvent B within 13.0 min, 50-95% solvent B within 1.0 min, followed by washing and column equilibration. The mass spectrometer was operated in data-dependent acquisition mode. The MS1 survey scan was acquired from 300-1750 m/z at a resolution of 70,000. The top 10 most abundant peptides were isolated within a 1.8 Th window and subjected to HCD fragmentation at a normalized collision energy of 27%. The AGC target was set to 5e5 charges, allowing a maximum injection time of 110 ms. Product ions were detected in the Orbitrap at a resolution of 35,000. Precursors were dynamically excluded for 15.0 s.

All mass spectrometric raw data were processed with Maxquant (version 1.5.3.8) using default parameters. Briefly, MS2 spectra were searched against the canonical Uniprot MOUSE\_UP000000589.fasta (downloaded at: 26.08.2020) database, including a list of common contaminants. False discovery rates on protein and PSM level were estimated by the target-decoy approach to 1% (Protein FDR) and 1% (PSM FDR) respectively. The minimal peptide length was set to 7 amino acids and carbamidomethylation at cysteine residues was considered as a fixed modification. Oxidation (M) and Acetyl (Protein N-term) were included as variable modifications. The match-between runs option was enabled for replicates from the same group. LFQ quantification was enabled using default settings. Student's t-tests were calculated in Perseus (version 1.6.1.1) after removal of decoys and potential contaminants. Data were filtered for at least 4 values in at least one condition.

### 5.2.18 mRNA sequencing

RNA was extracted as described earlier (section 5.2.13). Library preparation and sequencing was performed by the Cologne Center for Genomics as described previously (Lee et al., 2019). Libraries were prepared using the Illumina® TruSeq® mRNA stranded sample preparation Kit. Library preparation started with 300 ng total RNA. After poly-A selection, mRNA was purified and fragmented using divalent cations under elevated temperature. The RNA fragments underwent reverse transcription using random primers, followed by second strand cDNA synthesis with DNA Polymerase I and RNase H. After end repair and A-tailing, indexing adapters were ligated. The products were then purified and amplified to create the final cDNA libraries. After library validation and quantification (TapStation 4200, Agilent), equimolar amounts of library were pooled and quantified by using the Peqlab KAPA Library Quantification Kit and the Applied Biosystems 7900HT Sequence Detection System. The pool was sequenced on an Illumina NovaSeq6000 with PE100 read length and a minimum of 35 million reads per sample.

The reads were trimmed with Trimmomatic version 0.36 (Bolger et al., 2014) using default parameters. The trimmed reads were mapped to the GRCh38 mouse reference genome with STAR version 2.6 (Dobin et al., 2013) using default parameters. mRNA expression was analyzed using DESeq2 (version 1.28.1)(Love et al., 2014) package of R (version 4.0.0) software (<https://www.R-project.org/>). A p-value cut-off of <0.05 was applied to the list of differentially regulated mRNAs after pairwise comparison of the Jade-deficient cell lines with wild-type. P-values were adjusted for multiple testing.

### 5.2.19 Raw data deposition

The proteome and interactome mass spectrometry proteomics data have been deposited to the ProteomeXchange Consortium (<http://proteomecentral.proteomexchange.org>) via the PRIDE partner repository (Perez-Riverol et al., 2019) with the dataset identifier PXD028800. RNA sequencing data have been deposited in the ArrayExpress database at EMBL-EBI ([www.ebi.ac.uk/arrayexpress](http://www.ebi.ac.uk/arrayexpress)) under accession number E-MTAB-11021 (Athar et al., 2019). Login information is available upon request.

### 5.2.20 Statistical analyses

Unless otherwise stated, all data are presented as mean average plus standard error of the mean (SEM), calculated using Prism software. Data was normalized as indicated by figure legends and in the respective methods sections. Statistical analysis was performed using Prism software and differences between means were assessed by one-way ANOVA or Student's t-test as appropriate.

### 5.2.21 Mouse Work

#### 5.2.21.1 Mouse holding

Mice were housed according to standardized specific pathogen-free (SPF) conditions in the CECAD *in vivo* Research Facility. They were kept under a 12 hour light/dark cycle and had free access to food and water. The Animal Care Committee of the University of Cologne and LANUV NRW (Landesamt für Natur, Umwelt und Verbraucherschutz Nordrhein-Westfalen, State Agency for Nature, Environment and Consumer Protection North Rhine-Westphalia) approved the experimental protocols for all mouse experiments performed during this study.

#### 5.2.21.2 Generation of novel mouse lines

All mouse lines in this section were generated within this work by the Nephrolab, Cologne, Germany in cooperation with the transgenic core facility at the CECAD, Cologne, Germany. We generated two Glis2 mutant mouse line and two Tmem218 mutant mouse lines for aim (4), the generation of NPH mouse models resembling the human phenotype. Detailed targeting strategies are shown in section 6.2. As part of aim (3), investigating the role of the Jade family members in *in vivo* models, we generated two Jade1 mutant mouse lines and one for each Jade2 and Jade3, respectively. The targeting

strategies are shown in section 6.1.10. All mice were generated and maintained in C57BL/6N background unless otherwise stated.

### 5.2.21.2.1 Generation of guide RNAs

For the Jade1 and Glis2 mutant mice the sgRNAs (Table 8) were generated via *in vitro* transcription with a T7 RNA polymerase from the pSpCas9(BB)-2A-Puro (PX459) V2.0 plasmid gifted from Feng Zhang (Addgene plasmid # 62988 ; <http://n2t.net/addgene:62988> ; RRID:Addgene\_62988) (Ran et al., 2013). sgRNAs were column purified and stored at -80 °C . Primers for the generation of the sgRNAs are listed in Table 6. For the Jade2\_emKO, Jade3\_emKO, and Glis2 mutant mice custom crRNA (Table 8) and generic tracrRNA were ordered and resuspended in 100 µM in sterile and nuclease-free T<sub>10</sub>E<sub>0.1</sub> buffer (Chu et al., 2016). The ssODN repair templates (Table 8) were ordered as custom Ultramer Oligos and resuspended in T<sub>10</sub>E<sub>0.1</sub> buffer.

### 5.2.21.2.2 Pronuclear injection

The Jade1\_emKO1/2 and Glis2\_emKO1/2 mouse models were generated with a pronuclear injection (PNI)-based approach (Chu et al., 2016; Wefers et al., 2017). In brief, zygotes were collected from superovulated females and inspected for the presence of two pronuclei. Microinjection of the PNI mix was performed with an Axio Observer.D1 microscope (Zeiss) and microinjector devices CellTram and FemtoJet with TransferMan NK2 micromanipulators (Eppendorf). Embryos that developed to the two-cell stage were transferred to pseudo-pregnant females.

### 5.2.21.2.3 Electroporation

Electroporation of zygotes has emerged as an alternative, easier strategy. A novel approach for Easy Electroporation of Zygotes (EEZy) has been developed by the in-house transgenic core facility (Tröder et al., 2018), which not only increased embryo viability but also works with a common electroporator. For the generation of the Jade2\_emKO, Jade3\_emKO, as well as Tmem218 mutant mice we utilized EEZy. A detailed step-by-step protocol is published on protocols.io ([dx.doi.org/10.17504/protocols.io.bwzhp36](https://doi.org/10.17504/protocols.io.bwzhp36)). In brief, zygotes were collected from superovulated females (Behringer, 2014) then were transferred to the electroporation mix and electroporated in a BioRad Gene Pulser XCell electroporator with two square wave pulses (30V, 3 ms pulse duration, 2 pulses, 100 ms interval). After incubation until the two-cell stage, developed embryos were transferred to pseudo-pregnant foster mice.

### 5.2.21.3 DNA extraction from mouse tissue

Ear or tail biopsies were used for DNA isolation as previously described (Truett et al., 2000). The biopsies were incubated in 75-150 µL of 1x base solution at 95°C for 30 min. The reaction was stopped

by adding an equal volume of 1x neutralization solution. The extracted DNA was directly used to perform polymerase chain reactions (PCRs) or stored at -20°C.

5.2.21.4 Genotyping PCR

For genotyping PCRs either REDTaq® ReadyMix™ PCR reaction mix or Go Taq Flexi DNA Polymerase 5U/μl was used according to the manufacturer’s instructions. The specific primer sequences are listed in Table 4. The exact composition and cycling conditions for each reaction are listed below (Table 21 and Table 22, respectively). The PCR products analyzed using a 2% agarose gel (section 5.2.3) For the first two generations of all newly generated mouse strains as well as all mice of the *Glis2\_emKO1/2*, *Tmem218.R37S*, and *Tmem218\_emKO* lines we performed Sanger sequencing of the PCR product to confirm the mutation. The PCR product was cleaned by enzymatic purification. It was incubated with 0.25 U SAP and 0.5 U ExoI for 20 min at 37°C followed by an inactivation step for 15 min at 72°C. The resulting product was used for Sanger sequencing as described under section 5.2.6. Sequencing primers are listed in Table 5.

**Table 21. List of reaction compositions of the genotyping PCRs.**

Gene	Reaction Mix
Glis2_emKO1	5 μL ddH2O 1.25 pM Glis2_emKO1_fp1 1.25 pM Glis2_emKO1_fp2 1.25 pM Glis2_emKO1_rp1 1.25 pM Glis2_emKO1_rp2 12.5 μL REDTaq ReadyMix ~ 50 ng DNA
Glis2_emKO2 WT	13.1 μL ddH2O 1.25 pM Glis2_emKO2_fp 1.25 pM Glis2_emKO2_WT_rp 1.5 mM MgCl2 (25 mM) 0.2 mM dNTP (25 mM) 2 Units Go Taq Flexi DNA Polymerase ~ 50 ng DNA
Glis2_emKO2 point mutation	13.1 μL ddH2O 1.25 pM Glis2_emKO2_fp 1.25 pM Glis2_emKO2_PM_rp 1.5 mM MgCl2 (25 mM) 0.2 mM dNTP (25 mM) 2 Units Go Taq Flexi DNA Polymerase ~ 50 ng DNA

*Continued on next page*

Jade1_emKO1	9.6 µL ddH2O 1.25 pM Jade1_emKO1_fp1 1.25 pM Jade1_emKO1_fp2 1.25 pM Jade1_emKO1_rp1 1.25 pM Jade1_emKO1_rp2 1.5 mM MgCl2 (25 mM) 0.2 mM dNTP (25 mM) 2 Units Go Taq Flexi DNA Polymerase ~ 50 ng DNA
Jade1_emKO2	13.1 µL ddH2O 1.25 pM Jade1_emKO2_fp 1.25 pM Jade1_emKO2_rp 1.5 mM MgCl2 (25 mM) 0.2 mM dNTP (25 mM) 2 Units Go Taq Flexi DNA Polymerase ~ 50 ng DNA
Jade2_emKO	13.1 µL ddH2O 1.25 pM Jade2_emKO_fp 1.25 pM Jade2_emKO_rp 1.5 mM MgCl2 (25 mM) 0.2 mM dNTP (25 mM) 2 Units Go Taq Flexi DNA Polymerase ~ 50 ng DNA
Jade3_emKO	13.1 µL ddH2O 1.25 pM Jade3_emKO_fp 1.25 pM Jade3_emKO_rp 1.5 mM MgCl2 (25 mM) 0.2 mM dNTP (25 mM) 2 Units Go Taq Flexi DNA Polymerase ~ 50 ng DNA
Tmem218.R37S/emKO	13.1 µL ddH2O 1.25 pM Tmem218_fp 1.25 pM Tmem218_rp 1.5 mM MgCl2 (25 mM) 0.2 mM dNTP (25 mM) 2 Units Go Taq Flexi DNA Polymerase ~ 50 ng DNA

**Table 22. List of cycling conditions used for performing genotyping PCRs.**

Gene	Step	Temperature [°C]	Duration [s]	No. of cycles
Glis2_emKO1	Initialization	94	180	go to step 2, 35 repeats
	Denaturation	94	30	
	Annealing	60	30	
	Extension	72	60	
	Final extension	72	600	
	Final hold	15	∞	

*Continued on next page*

Glis2_emKO2 WT	Initialization	94	180	
	Denaturation	94	30	
	Annealing	64	30	
	Extension	72	60	go to step 2, 35 repeats
	Final extension	72	600	
	Final hold	15	$\infty$	
Glis2_emKO2 point mutation	Initialization	94	180	
	Denaturation	94	30	
	Annealing	62	30	
	Extension	72	60	go to step 2, 35 repeats
	Final extension	72	600	
	Final hold	15	$\infty$	
Jade1_emKO1/ Jade1_emKO2	Initialization	94	180	
	Denaturation	94	45	
	Annealing	64	60	
	Extension	72	30	go to step 2, 35 repeats
	Final extension	72	180	
	Final hold	15	$\infty$	
Jade2_emKO	Initialization	94	180	
	Denaturation	94	45	
	Annealing	66	60	
	Extension	72	30	go to step 2, 35 repeats
	Final extension	72	180	
	Final hold	15	$\infty$	
Jade3_emKO	Initialization	94	180	
	Denaturation	94	45	
	Annealing	62	60	
	Extension	72	30	go to step 2, 35 repeats
	Final extension	72	180	
	Final hold	15	$\infty$	
Tmem218.R37S/emKO	Initialization	94	180	
	Denaturation	94	30	
	Annealing	60	30	
	Extension	72	60	go to step 2, 35 repeats
	Final extension	72	180	
	Final hold	15	$\infty$	

#### 5.2.21.5 Body weight measurement

Animal caretakers of the CECAD housing facility weighed the mice biweekly.

#### 5.2.21.6 Survival studies

For the overall survival studies of the Jade1\_emKO1 mutant mice, the mice were monitored on a daily basis. They were euthanized when they reached the human endpoint according to termination criteria of the federal animal care regulations.

### 5.2.21.7 Sample collection

The mice were sacrificed at the indicated time points via cervical dislocation. The organs were harvested and cleaned with ice-cold PBS. After fixation in 4% formaldehyde for 24 h the samples were dehydrated and paraffin-embedded.

### 5.2.21.8 Periodic-Acid Schiff (PAS) staining

PAS staining was used for morphological assessment of the kidney and liver architecture. The paraffin-embedded tissue was cut in to 1-2  $\mu\text{m}$  thick sections, which were incubated at 60°C of 1 h. They were deparaffinized by passing a descending ethanol row (xylene, 2x 5 min; ethanol 100%, 3x 3 min; ethanol 95%, 2x 2 min; ethanol 70%, 1x 1min) and rehydrated in water for 5 min. Samples were oxidized for 10 min in 0.9% periodic acid. After a 1 min washing step in water, they were stained by Schiff's reagent for another 10 min. After counterstaining the nuclei with Meyer's hematoxylin solution for 10 s, the slides were washed in tap water for 10 min. Rehydration was performed by incubating the slides in an ascending ethanol row (ethanol 95%, 2x 1 min; ethanol %, 3x 3 min; xylene, 2x 5min). After mounting with Histomount the slides were dried over night at room temperature and scanned using the slidescanner SCN4000 (Leica Microsystems, Jena, Germany) with 20x magnification.

### 5.2.21.9 Immunofluorescence staining on renal tissue

Cutting and incubation of the slides followed by the descending ethanol row was performed as described above (section 5.2.21.8). The slides were washed twice in 1x staining PBS. 10 mM Tris-EDTA pH9 was used for antigen retrieval followed by 3 washing steps with 1x staining PBS. Afterwards, sections were blocked in 5% NDS in 1x staining PBS for 1 h at RT followed by three washing steps with 1x staining PBS. The primary antibodies (Table 11) were diluted in PBS with 5% BSA and incubated at 4°C overnight. After one additional washing step with 1x staining PBS, the sections were incubated with the fluorescently labelled secondary antibody (Table 12), diluted 1:500 in PBS with 5% BSA, for 1 h at RT in the dark. This was followed by washing the sections 3 times with 1x staining PBS and once with water. ProLong Diamond antifade reagent with DAPI was used for mounting. Images were acquired with TCS SP8 Confocal Microscope and processed with ImageJ/Fiji.

### 5.2.21.10 Immunization

For the immunization 200  $\mu\text{L}$  of complete Freuds Adjuvant were added to 80  $\mu\text{g}$  of purified recombinant protein (section 5.2.7) in 200  $\mu\text{L}$  of sterile water. The samples were incubated for 3 min in an ultrasound bath followed by 15 min on a vortexer. The solution was then collected at the bottom of the Eppendorf tube by shaking and filled into a 1 mL syringe with a 22 g needle. The needle was replaced by a 27 g needle and air was removed from the syringe. 50  $\mu\text{L}$  were injected into to hind leg of eight-week-old Balb/cJRj (provided by CECAD animal facility, fur border, 3 mm deep). The injection

location was then massaged for about 30 s. Subsequent injections were performed using incomplete Freuds Adjuvant and 40 µg of recombinant protein. After multiple immunizations, serum of the mice was tested for immunoreaction by enzyme-linked immunosorbent assay (ELISA) with the recombinant proteins (section 5.2.12). In addition, the serum was used to stain immunoblots with lysates of HEK293T cells overexpressing JADE proteins.

### 5.2.21.11 Fusion and selection of hybridoma clones

After positive testing of the serum, the popliteal lymph node cells were extracted and fused with mouse myeloma SP2/ab cells by a standard fusion protocol. The mice were killed by cervical dislocation. Afterwards blood was taken from the heart. The blood was incubated for 1 h at 37°C, centrifuged at 20.000 x g for 10 min. Serum was mixed with 50% glycerol and used as positive control for ELISA. Immediately after taking the blood, the mouse was disinfected with 70% ethanol and Evan's blue was injected into the feet. The skin of the hind legs was completely dissected. The lymph nodes from the hind legs were taken out with sterile tweezers and scissors under a laminar flow hood and put into RPMI pure medium in a 6 cm culture dish. The lymph nodes were grinded using the pestle of a 10 mL syringe and cells were separated by pipetting them up and down. The cell suspension was evaluated under a microscope to ensure separation of the cells. Afterwards the cells were filtered through a 45 µm cell strainer into a 50 mL falcon tube. The filter was rinsed with 5 mL of RPMI pure medium. In the meantime, the medium of the SP2/ab cells was removed and they were washed with RPMI pure medium, resuspended in 5 mL of RPMI pure medium and transferred to a 50 mL falcon tube. Both falcon tubes were centrifuged at 150 x g for 10 min at RT. After discarding the supernatant the cell pellet of the lymph node cells was resuspended in 5 mL of RPMI pure and transferred to the falcon tube containing the SP2/ab cells. After suspending, the tube was filled up to 50 mL with RPMI pure and the cells were centrifuged at 150 x g for 10 min. During this centrifugation step 10 µL of β-Mercaptoethanol was added to 990 µL of sterile water and 1.5 mL of PEG 1500 were filled into a 3 mL syringe with a 20 g needle. The supernatant for the cells was removed and the pellet resuspended by slightly knocking against the tube. The PEG 1500 was slowly (over 1-2 min) added dropwise to the cells while stirring the cells with a Pasteur pipette. Afterwards the solution was stirred for an additional minute. While gently shaking the tube RPMI pure medium was added: 1 mL in 1 min, 3 mL in 1 min, 16 mL in 2 min. The mixture was centrifuged at 150 x g for 10 min and incubated another 5 min. The supernatant was removed and the cells were resuspended in plating medium to a cell density of around  $3 \times 10^5$  cells/mL and plated into 96-well plate. The monoclonal hybridoma lines were characterized, expanded, and subcloned according to standard procedures (Köhler and Milstein, 1975). Initial screening of clones was performed by ELISA (section 5.2.12) with recombinant JADE protein and

## Materials and Methods

immunoblots (section 5.2.10) using JADE proteins overexpressed in HEK293T cells (section 5.2.8.3). Isotyping of selected clones was performed with Pierce Rapid Isotyping Kit.

## 6 Results

### 6.1 The JADE protein family

#### 6.1.1 Comparison of structure and expression of JADE family members reveals their high similarity.

The members of the JADE protein family share a high structural similarity (section 3.5). Additionally, expression of JADE family members in the same tissue and cell type would be necessary for interchangeable functions, for building up a common protein complex, or for any compensatory mechanism to take place. We compared *JADE* expression in published transcriptomic datasets and could confirm ubiquitous expression of all *JADE* genes across tissue types (Figure 4A) (Uhlén et al., 2015). *JADE1* is highly expressed in pancreas, endocrine, and female tissues. *JADE2* shows a high expression in brain, endocrine tissues, female tissues, and lymphoid tissue, while *JADE3* shows overall the lowest expression levels with the highest *JADE3* expression in brain, endocrine tissues, female and male tissues, and lymphoid tissues. However, in most tissues one *JADE* family member is predominantly expressed. *JADE1* is the predominant family member in pancreas, kidneys, bone marrow, or breasts, *JADE2* in cerebral cortex, lymph node, and midbrain and *JADE3* in epididymis, placenta, and testis. As for protein expression, *JADE1* reveals highest expression levels in squamous epithelial cells of the oral mucosa, esophagus, uterus, hepatocytes, and kidney tubules (Figure 4B) (Uhlén et al., 2015). Protein expression data was only available for *JADE1*. Next, we specifically looked into expression of *Jade1/2/3* in the murine kidney in available single-cell transcriptomic data (Park et al., 2018). These data reveal a high percentage of cells expressing *Jade1*, especially in the renal tubular epithelial cells of the collecting duct. *Jade2* and *Jade3* are expressed to a lesser extent in these cell types (Figure 4C). A recent study on microdissected murine kidney tubule segments also shows that *Jade1* is more highly expressed than *Jade2* and *Jade3* (Chen et al., 2021). This data set shows the highest *Jade1* expression in the long descending limb of the loop of Henle in the inner medulla. *Jade2* and *Jade3* are both expressed mainly in the different segments of the loop of Henle. For all three *Jade* isoforms, expression is the lowest in the proximal tubule segments.

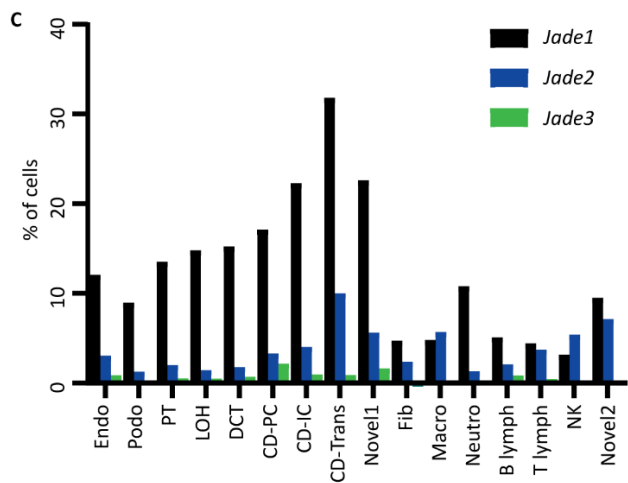
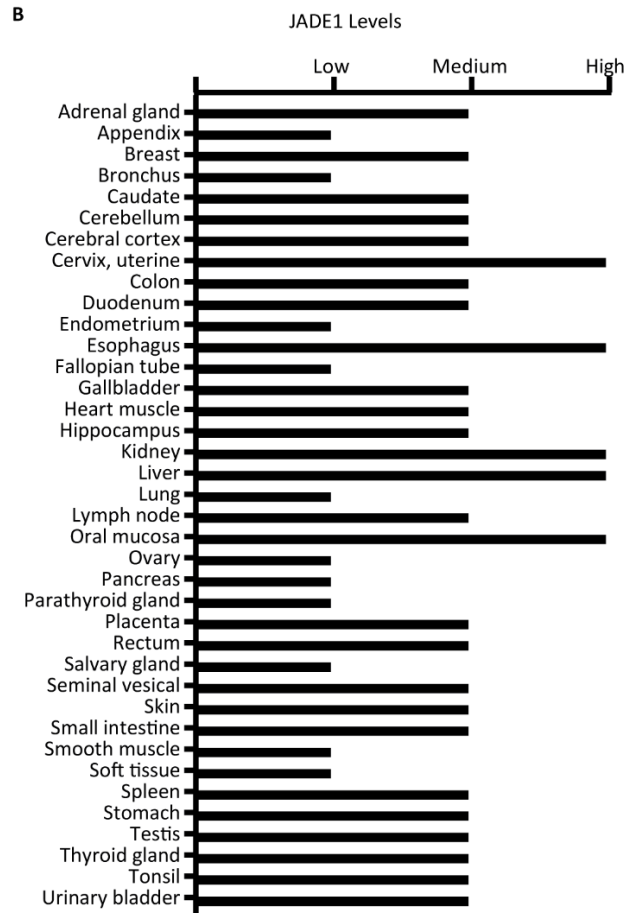
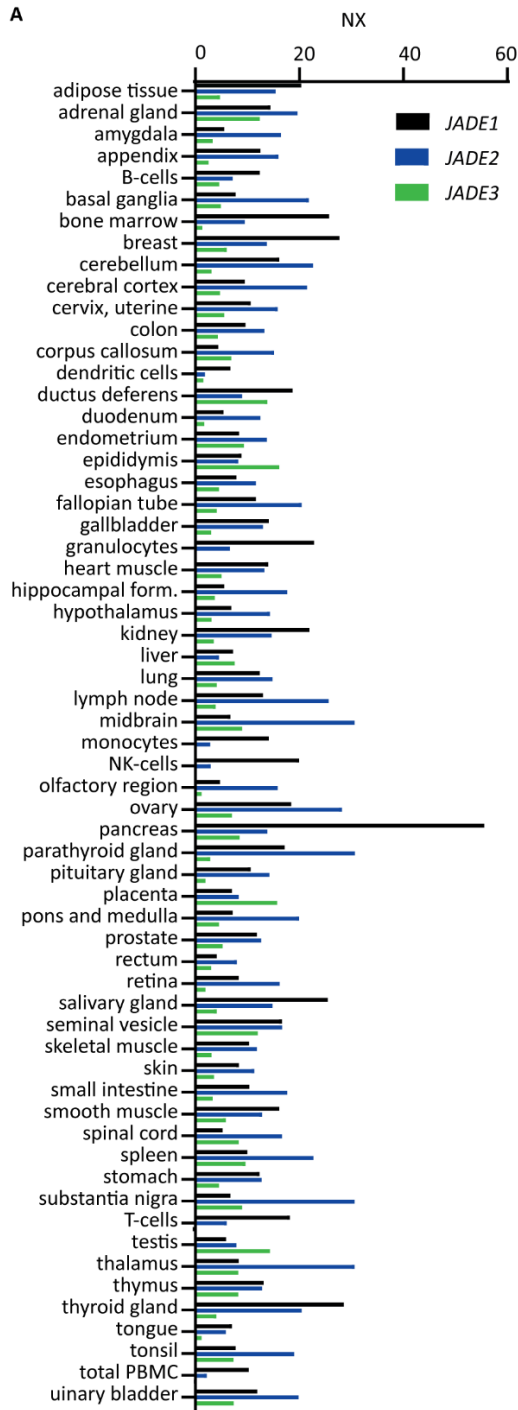


Figure legend on next page

**Figure 4. Expression profiles of JADE family members across tissues.** (*previous page*)

**(A)** RNA expression profiles for *JADE1/2/3* based on transcriptomic data from HPA, GTEx and FANTOM5. Data is depicted as normalized expression (NX) based on the maximum NX for each gene in the different data sets and obtained from The Human Protein Atlas v 19.3 and Ensembl version 92.38. Transcriptomic data available from

[https://v19.proteinatlas.org/download/rna\\_tissue\\_consensus.tsv.zip](https://v19.proteinatlas.org/download/rna_tissue_consensus.tsv.zip). (Uhlén et al., 2015). **(B)** Protein Expression Levels for *JADE1* based on tissue micro arrays obtained from The Human Protein Atlas version 19.3 and Ensembl version 92.38. Proteomic data available from [https://v19.proteinatlas.org/download/normal\\_tissue.tsv.zip](https://v19.proteinatlas.org/download/normal_tissue.tsv.zip) (Uhlén et al., 2015). **(C)** Gene expression data of single cell transcriptomics of mouse kidney. Shown is the percentage of cells expressing each *Jade* gene in the different cell clusters: endothelial, vascular, and descending loop of Henle (Endo), podocyte (Podo), proximal tubule (PT), ascending loop of Henle (LOH), distal convoluted tubule (DCT), collecting duct principal cell (CD-PC), collecting duct intercalated cell (CD-IC), collecting duct transitional cell (CD-Trans), fibroblast (Fib), macrophage (Macro), neutrophil (Neutro), lymphocyte (lymph), natural killer cell (NK) (Park et al., 2018). See also MS ID#: BIORXIV/2021/462752.

#### 6.1.2 All JADE family members are associated with pVHL and NPH proteins

Based on the structural similarities, we decided to investigate whether *JADE2* and *JADE3* can function in a similar way compared to *JADE1* with regard to protein interactions related to hereditary kidney diseases. As described previously, *JADE1* has been identified to be interacting with pVHL as well as to be a part of the NPH-protein-complex. To this end, we first cloned human *JADE2* and *JADE3* cDNA into expression vectors. We co-expressed V5-tagged pVHL (V5.VHL) together with FLAG-tagged *JADE* proteins or a control protein (F.Jade1S, F.JADE2, F.JADE3, F.EPS<sup>1-225</sup>) and performed an anti-FLAG co-immunoprecipitation. Here, we show that pVHL co-precipitates with all three *JADE* proteins (Figure 5A). In similar experiments with V5.NPHP4 (Figure 5B) and V5.NPHP1 (Figure 5C), specific co-precipitation with all three *JADE* proteins could be shown.

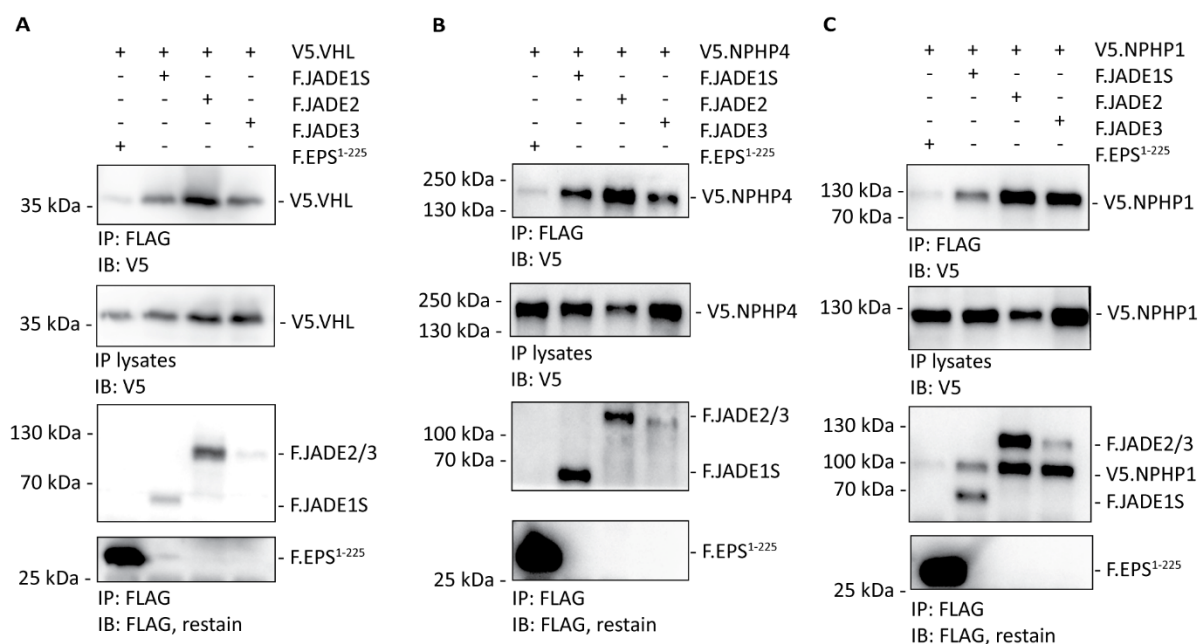


**Figure 5. JADE family members interact with pVHL, NPHP4, and NPHP1.**

HEK293T cells were transiently transfected with (A) V5-tagged pVHL (V5.VHL), (B) V5-tagged NPHP4 (V5.NPHP4), and (C) V5-tagged NPHP1 (V5.NPHP1), and either FLAG-tagged JADE1S (F.JADE1S), JADE2 (F.JADE2), JADE3 (F.JADE3) or a control protein EPS<sup>1-225</sup> (F.EPS<sup>1-225</sup>). Immunoprecipitation was performed with an anti-FLAG antibody. In summary, V5.VHL, V5.NPHP1, and V5.NPHP4 co-immunoprecipitate with F.JADE1S, F.JADE2, and F.JADE3, but not with the control protein F.EPS<sup>1-225</sup>. Blots represent at least three individual experiments. See also MS ID#: BIORXIV/2021/462752.

Next, we used co-immunoprecipitation experiments to show that FLAG-tagged JADE1S and JADE2 are each able to interact with V5 tagged version of the same protein (Figure 6A,B). Thus, in addition to the known common function as co-factors for the HBO1 complex, we show that all JADE proteins share relevant renal protein complexes as well as the capability to homodimerize. Given the high level of similarity between the individual JADE proteins, we checked for heterodimerization among the different JADE proteins. As expected, we could show that V5.JADE1S and V5.JADE3 both co-immunoprecipitate with F.JADE2 (Figure 6C). In conclusion, JADE proteins seem to be able to form hetero-multimeric protein complexes.

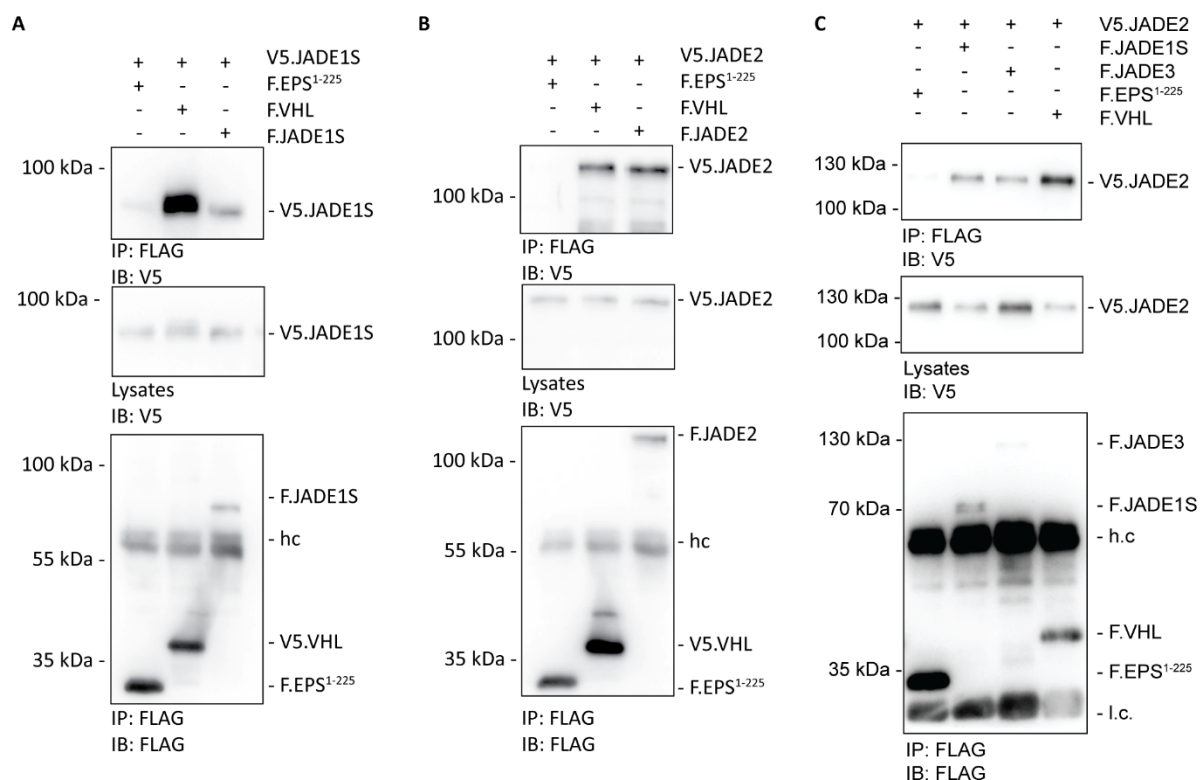


**Figure 6. JADE proteins have the capability to dimerize.**

HEK293T cells were transiently transfected with (A) V5-tagged JADE1S (V5.JADE1S) and (B) V5-tagged JADE2 (V5.JADE2). FLAG-tagged JADE1S (F.JADE1S) and JADE2 (F.JADE2) were co-expressed, respectively. EPS<sup>1-225</sup> (F.EPS<sup>1-225</sup>) and pVHL (F.VHL) function as negative and positive control. Immunoprecipitation was performed with an anti-FLAG antibody. F.JADE1S does co-immunoprecipitate with V5.JADE1S. The same is observed for F.JADE2 with V5.JADE2. (C) HEK293T cells transiently transfected with V5-tagged JADE2 (V5.JADE2) and FLAG-tagged JADE1S (F.JADE1S), JADE3 (F.JADE3), and control proteins. Immunoprecipitation with an anti-FLAG antibody revealed that V5.JADE2 does co-immunoprecipitate with F.JADE1S, F.JADE3, and the positive control F.VHL but not with F.EPS<sup>1-225</sup>. Blots represent at least three individual experiments. See also MS ID#: BIORXIV/2021/462752.

### 6.1.3 Monoclonal JADE3 antibody specifically recognizes human and murine JADE3

Since overexpression of proteins can be a source of potential artefacts, we aimed to generate and validate the necessary tools to study the endogenous proteins. The high similarity within the Jade protein family makes specific detection difficult. For JADE1 there were several commercial antibodies available as well as multiple monoclonal antibodies from our lab previously generated in a collaboration with the lab of Hanswalter Zentgraf († 17.07.2011) at the German Cancer Research Center. However, availability of commercial antibodies for JADE2 and JADE3 was limited. Therefore, we decided to generate our own monoclonal mouse antibodies. To generate antibodies that are specific for either of the JADE proteins, the selected antigen would need to show distinct differences in protein sequence. We decided not to target the more distinct C-terminal area, since we wanted the antibodies also to recognize potential shorter isoforms. For the antigen generation we decided on cloning the N-terminal part of JADE2 (aa 1-177) and JADE3 (aa 1-178) in a bacterial expression vector (Figure 7A). Both HIS-tagged protein fragments were expressed with the expected molecular weight (Figure 7B). After Ni-NTA purification (Figure 7C) the antigen was used for immunization in BALB/c mice.

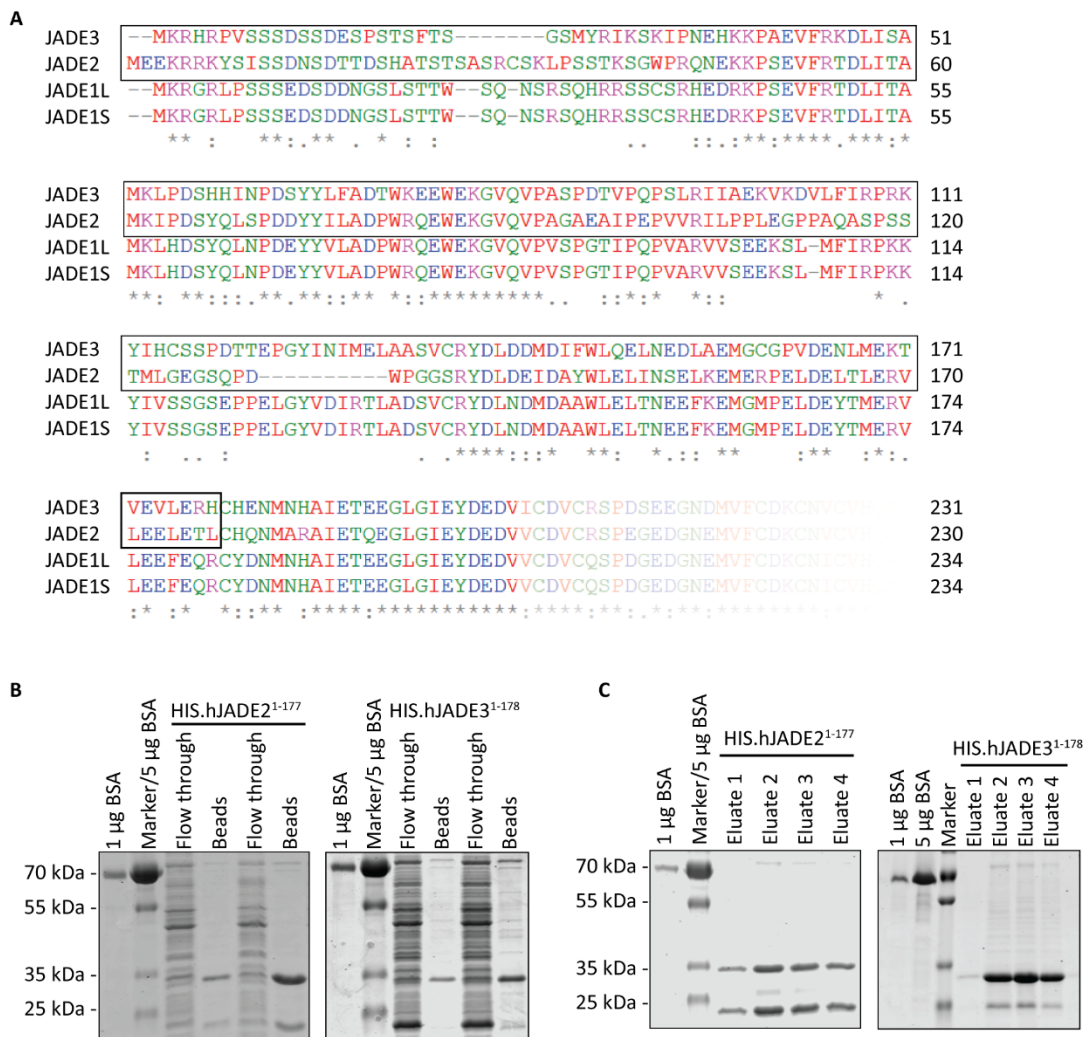


**Figure 7. Antigen selection and production for the generation of JADE2 and JADE3 antibodies.** **(A)** Protein sequence alignment of N-terminal regions of JADE1L, JADE1S, JADE2, and JADE3. Protein fragments selected for antigen generation are marked with a black box. Alignment was performed with CLUSTAL O(1.2.4) multiple sequence alignment tool (Sievers F et al., 2011). **(B)** Expression control and determination of protein concentration of the HIS-tagged recombinant proteins JADE2<sup>1-177</sup> (HIS.hJADE2<sup>1-177</sup>) and JADE3<sup>1-178</sup> (HIS.hJADE3<sup>1-178</sup>) was done by doing a test pulldown with Ni-NTA coupled agarose beads. SDS-PAGE Coomassie blue staining of BSA standard and flow through, and beads. Expression of HIS.hJADE2<sup>1-177</sup> and HIS.hJADE3<sup>1-178</sup> is visible at the expected size of ~ 35 kDa. **(C)** Batch purification of the proteins was done using Ni-NTA followed by imidazole elution. Coomassie blue staining was used to assess the elution fractions.

The workflow of the monoclonal mouse antibody generation is described in Figure 8A. BALB/c mice were injected with the purified proteins in the hind leg every 2-3 days. After 4-5 injections, blood was collected from the submandibular vein. The serum was diluted and used as primary antibody to stain immunoblots. Serum derived from the mouse injected with JADE2<sup>1-177</sup> only recognized overexpressed JADE2. Serum derived from the mouse injected with JADE3<sup>1-178</sup> mainly detected overexpressed JADE3 however showed additional cross-reactivity with JADE2 but not with the control protein (Figure 8B). After this positive serum test, the popliteal lymph nodes were isolated and the obtained B-cells fused to SP2/ab myeloma cells. A first selection of clones was performed by ELISA screening. Positive clones were further validated in immunoblot and immunoprecipitation experiments. Two individual fusions performed with the lymph nodes of two mice immunized with JADE2 antigen did not result in antibody clones, which were able to recognize either human or mouse JADE2. For JADE3, we were able to identify two clones working in immunoblot with overexpressed proteins (Figure 8C). JADE3 clone B4 specifically recognizes human JADE3, whereas clone B7 predominantly recognizes mouse Jade3. With this, we generated a useful tool to study the individual functions of JADE3. Whether the antibody also detects endogenous JADE3 is currently under investigation.

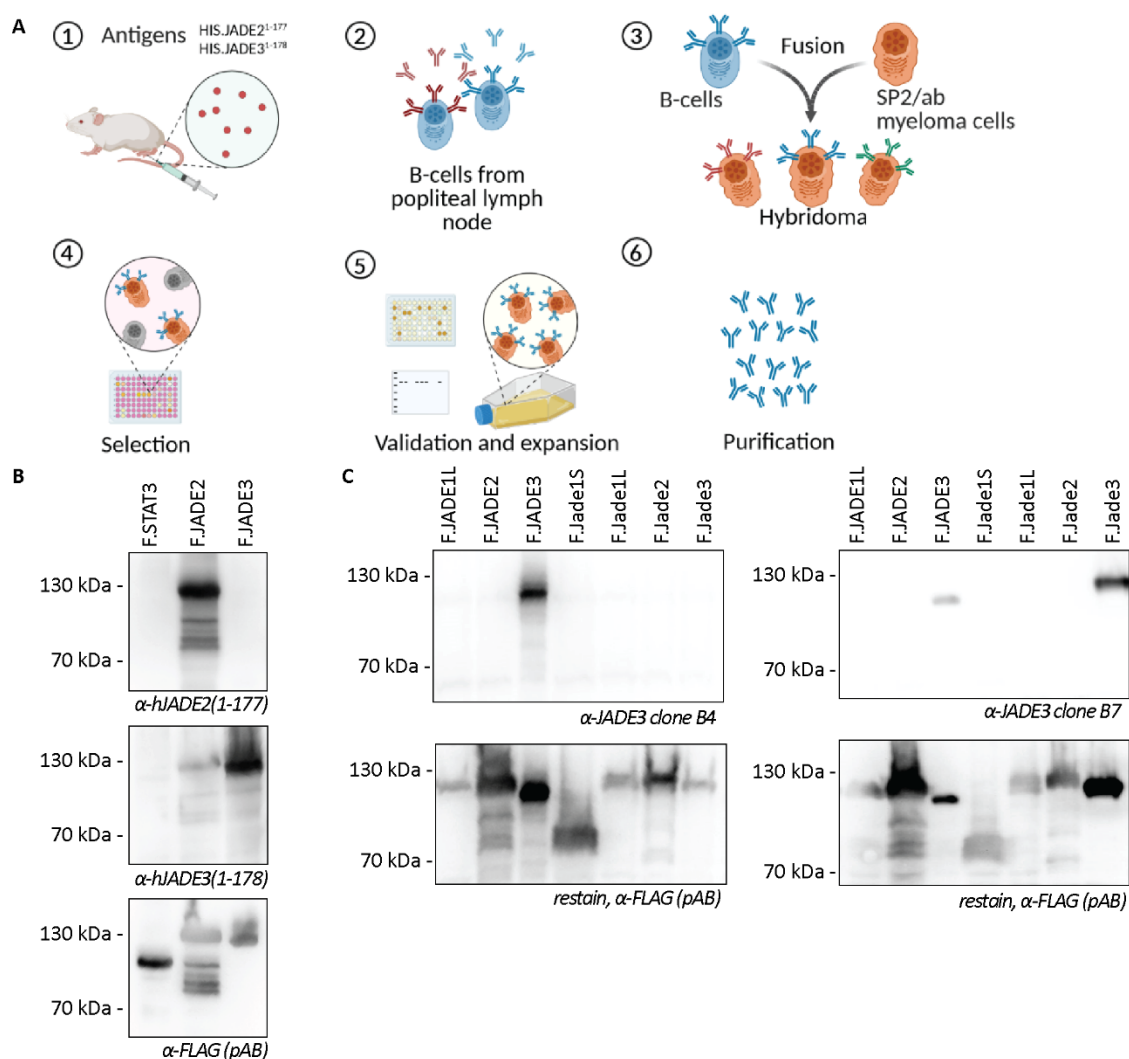


**Figure 8. Generation of monoclonal antibodies against JADE2 and JADE3.**

**(A)** Schematic overview of the generation of monoclonal antibodies using hybridoma cells. BALB/c mice were immunized by injecting the purified proteins in the hind leg. Immunization was repeated every 2-3 days for 4-5 times in total. Before isolating the lymph nodes, the blood titer was evaluated by immunoassay and ELISA. After isolation of the lymph node cells, they were fused to SP2/ab myeloma cells generating hybridoma cells. The cell suspension was plated in multiple 96-well plates. Arising clones were first screen by ELISA and then expanded and validated by immunoblot. Purification was done by ammonium sulfate precipitation followed by affinity chromatography using Protein G. Adapted from “Monoclonal Antibodies Production”, by BioRender.com (2021). Retrieved from <https://app.biorender.com/biorender-templates>. **(B)** Blood was collected from the submandibular vein and the serum was tested by immunoblot. HEK293T cells were transfected with FLAG tagged JADE2, JADE3 or STAT3 as a negative control. Immunoblot of whole cell lysates were stained with either serum of mice injected with HIS.JADE2<sup>1-177</sup> or HIS.JADE3-31-178 or with a polyclonal FLAG antibody. Serum derived from the HIS.JADE2<sup>1-177</sup> injected mouse does only recognize over expression JADE2 whereas serum derived from the Mouse injected with HIS.JADE3<sup>1-178</sup> recognized JADE3 as well as JADE2. FLAG staining shows expression of all three proteins. **(C)** Supernatant of two hybridoma clones derived from HIS-JADE3<sup>1-178</sup> immunization tested for their specificity within the JADE protein family. HEK293T cells were transfected with the indicated plasmids and whole cells lysates were evaluated by immunoblot. JADE3 clone B4 does specifically recognizes human JADE3 whereas clone B7 recognizes both human JADE3 and mouse Jade3. FLAG restraining shows expression of all transfected plasmids.

#### 6.1.4 Subcloning of mIMCD3 cells in preparation of Jade deletion by genome editing

Based on the results of the renal expression profile for *Jade1/2/3* (Figure 4C), we decided to perform the subsequent experiments in murine inner medulla collecting duct (mIMCD3) cells. These are polarized epithelial cells first isolated in 1991 derived from microdissected tubules. As typical for immortalized cell lines, due to passaging, freezing, and thawing, the mIMCD3 cell line developed a heterogenous genetic background over time. To be able to compare our downstream data based on single clones we decided to subclone the cells before generating Jade-deficient cell lines. To this end, we sorted single cells from the earliest available passage of mIMCD3 cells in 96-well plates. Characterization of the subclones identified a high variability on ciliation, ranging from almost 100 % ciliated to barely any ciliation (Figure 9A). For all mIMCD3 experiments within this thesis, mIMCD3 WT subclone #8 was used. This subclone had a high number of almost 100% ciliated cells (Fig. 6A), just like the non-subcloned mIMCD3. Using mRNA sequencing, we checked for expression of classical cell type selective markers for kidney cells. Most makers for mIMCD cells can be found in the mIMCD3 WT#8 cell line (Figure 9B). Looking at a more general marker set for different kidney cells, we do see some expression of markers of proximal tubules (*Agt*, *Lrp2*), loop of Henle (*Umod*), and macula densa cells (*Nos1*, *Oxtr*), but not of podocytes (*Nphs1*, *Nphs2*) (Figure 9C).

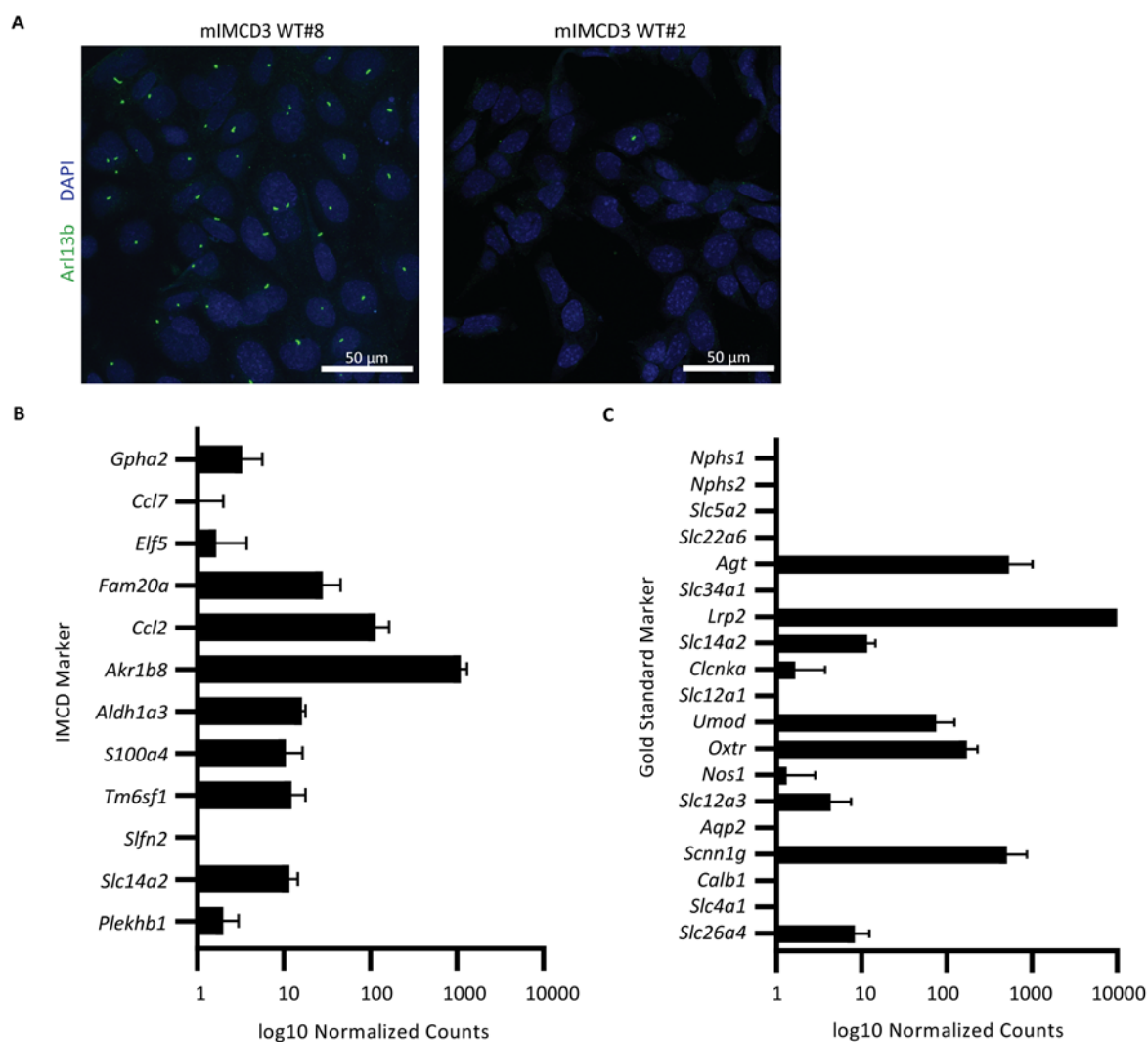


**Figure 9. Subcloning of mIMCD3 to generate cell lines with a defined genetic background.**

**(A)** Two representative mIMCD3 WT subclones (#8 and #2) were immunostained for cilia using Arl13b (green) and nuclei (blue). **(B-C)** Transcriptomic data of mIMCD3 WT#8 cells presented as normalized count values. **(B)** Selected marker genes for mIMCD cells as identified by deep sequencing of micro dissected renal tubules (Clark et al., 2019; Lee et al., 2015). **(C)** Standard marker genes for different kidney cell types (Chen et al., 2019).

### 6.1.5 *Jade1/2/3*-deficient mIMCD3 cell lines do show neither compensatory upregulation in the other family members nor abnormalities in cell cycle progression under baseline conditions

To study the individual and mutual functions of the Jade protein family as well as the consequences of the loss of either one of the Jade proteins, we next generated *Jade*-deficient cell lines by targeting each gene individually with CRISPR/Cas9-mediated genome editing (Figure 10A). We used the mIMCD3 WT#8 cell line described under section 6.5 as a parental clone. To account for potential off-target effects, two independent non-overlapping sgRNAs (single-guide RNAs) were designed for each *Jade* gene. The first sgRNA for each gene was targeted against the region encoding for the first PHD domain, the second sgRNA was targeted against the region upstream of the second PHD domain (Figure 10B). Sanger sequencing of the mRNA was performed to verify mutations in the mutant cell lines. The effect of the gene editing result on the exon structure and expressed protein extrapolated from the sequencing data is depicted in Figure 10C.

#### **Figure 10. Generation of mIMCD3 mutant cell lines for *Jade1/2/3*. (next page)**

**(A)** Schematic overview of the workflow for generation CRISPR/Cas9-mediated mutant cell lines. After selection of suitable sgRNAs, their locus was sequenced for comparison with the reference genome. Plasmids containing the sgRNA under a U6 promotor as well a Cas9-GFP under a CBh promotor were generated following the protocol of Ran et al. (Ran et al., 2013). mIMCD3 WT#8 were transfected with the respective plasmids and after 48 hours single GFP positive cells were sorted in 96 well plates. After expansion clones were screened by PCR and Sanger sequencing of both genomic DNA and mRNA before using them for downstream experiments. Figure created with [BioRender.com](https://www.biorender.com). **(B)** Selection of two independent non-overlapping sgRNAs for each *Jade* gene targeting exons containing the first and second the PHD domain. Wellcome Sanger Institute Genome Editing was used to identify suitable sgRNAs by location and potential off-target effects (<https://wge.stemcell.sanger.ac.uk/>)(Hodgkins et al., 2015). **(C)** Exon structure of the *Jade1/2/3*-deficient cell lines based on Sanger sequencing of mRNA. The first cell line generated for *Jade1* is heterozygous, a frameshift is introduced in one allele, and the second one has a deletion of the region encoding the first PHD domain. The second cell line generated for *Jade1* is homozygous with a deletion of exon 7, including the sequence for part of the second PHD domain. Both cell lines generated for *Jade2* result in deletions leading to frameshifts and early stop codons. The first *Jade2*-deficient cell line is missing exon 6, the second cell line part of exon7. The first *Jade3*-deficient cell line has a deletion in exon 5 leading to an early stop codon shortly after. In the second *Jade3*-deficient cell line exon 6 is skipped. See also MS ID#: BIORXIV/2021/462752.

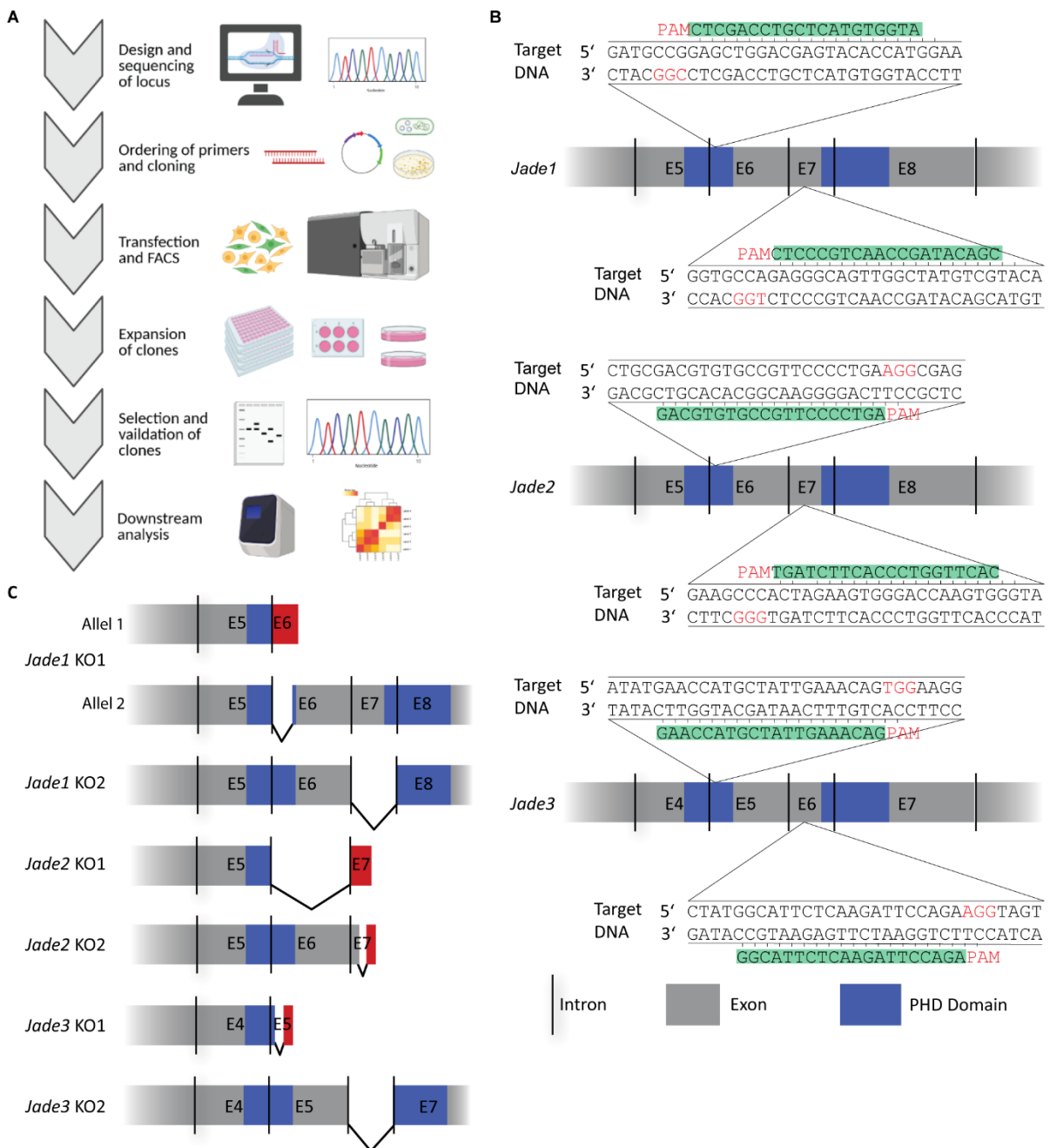
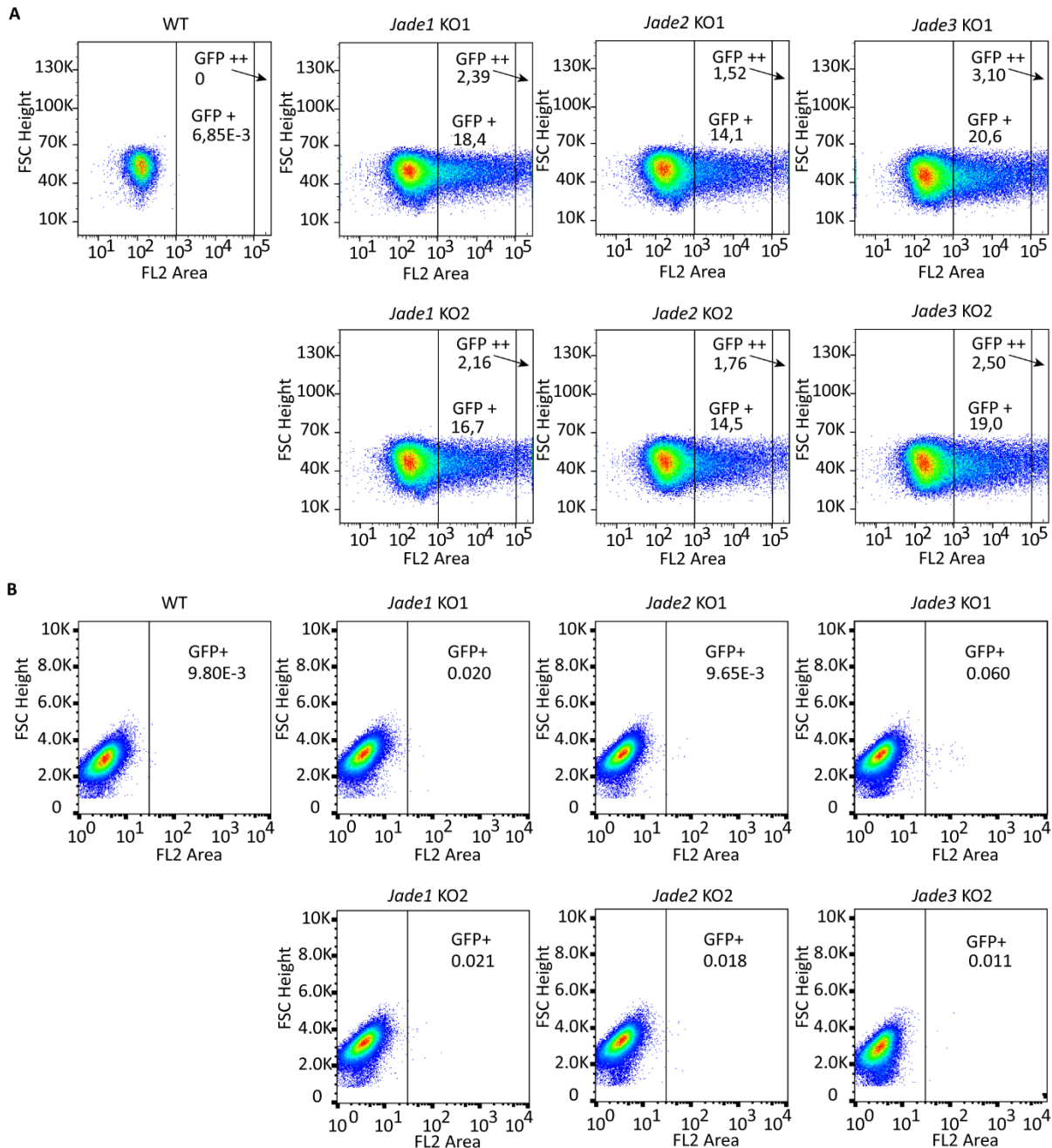


Figure legend on previous page

In the process of cell line generation, the cells were transfected with a SpCas9-2A-GFP plasmid (Ran et al., 2013). This provided the means to sort transfected cells, which generate Cas9 and the sgRNA, into single cells to generate monoclonal cell lines. The GFP signal during the sorting, 48 h after transfection, is depicted in Figure 11A. Since this was intended to be a transient transfection, plasmid concentrations and thus the GFP signal should vanish after a certain amount of culturing time. To confirm that the plasmid encoding Cas9 and GFP was not functionally integrated in the genome of the cells we repeated

the FACS analysis with the established cell lines (minimum of six passages after the initial sorting). As expected, we did not see an increased baseline GFP expression as compared to the wild-type control cell line (Figure 11B).



**Figure 11. Established mIMCD3 *Jade1/2/3*-deficient cell lines do not continue to show GFP expression.**

FACS analysis was carried out as described in methods. The relative fluorescence is indicated on the x-axis (FL2 Area) and the y-axis represents FSC height. **(A)** GFP expression 48 h after transfection with sgRNA and Cas9-GFP containing plasmid. Low to medium GFP positive cells were used for sorting single cells in 96-well plates. **(B)** Established monoclonal mutant cell lines do not show GFP expression, comparable to WT cells.

Next, we validate the *Jade*-deficiency on mRNA and protein level in our selected clones. We performed qPCR analysis from the cell lines. In each of the cell lines we looked at the mRNA expression level of each *Jade* family members. We see a significant reduction of *Jade1* mRNA expression in both *Jade1*-deficient cell line compared to the WT cell line (Figure 12A). The same is observed for *Jade2* and *Jade3* in the *Jade2*- and *Jade3*-deficient cell lines, respectively (Figure 12B-C). Notably, we do not see any compensatory upregulation of either of the *Jade* mRNA expressions upon loss of one *Jade* family member. This is visualized by *Jade2* and *Jade3* expression levels in the *Jade1*-deficient cell lines, that are comparable to WT levels or reduced. The same is observed in *Jade2*- and *Jade3*-deficient cell lines for the respective other *Jade* family members.

Since finding antibodies that are able to recognize and differentiate between the different *Jade* protein family members on endogenous expression levels was challenging, we decided to use a target proteomics approach to validate the mutant cell lines on protein level. In a parallel reaction monitoring (PRM) assay we were able to confirm the loss of the *Jade* proteins in the respective mutant cell lines (Figure 12D-F). Similarly, to the qPCR analysis, we again do not see any clear significant regulation of the not targeted *Jade* family members.

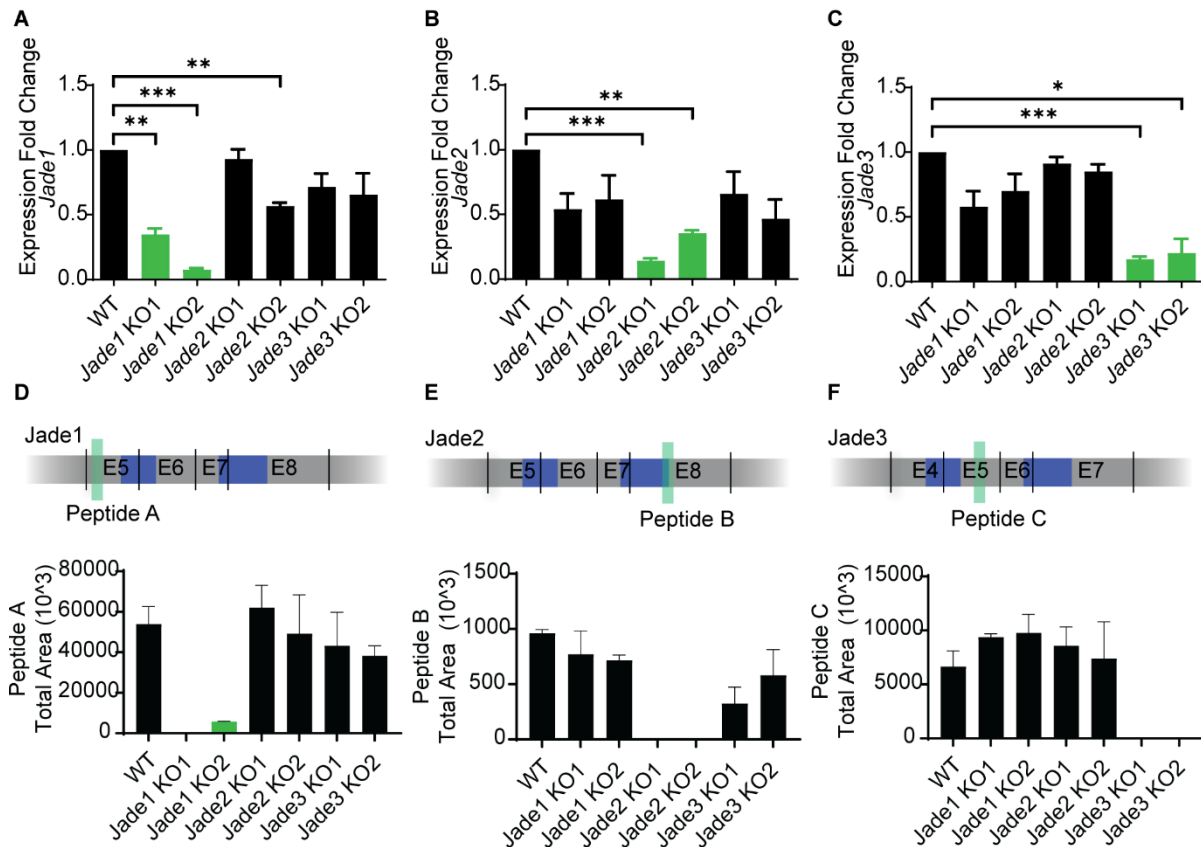


**Figure 12. mIMCD3 *Jade1/2/3*-deficient cell lines reveal no major compensatory upregulation on mRNA and protein level of the other family members under baseline conditions.**

(A-C) qPCR data showing gene expression of each *Jade* family member across the different mutant cell lines. For each mutant cell line a significant reduction of mRNA expression is seen for the target gene. (N=3, students t-test, \*  $p \leq 0.05$ , \*\*  $p \leq 0.01$ , \*\*\*  $p \leq 0.001$ ). (D-F) PRM assay to validate loss of protein in the *Jade1/2/3*-deficient cell lines. Schematic representation of the Peptide locations used for the targeted proteomics approach within the *Jade1/2/3* locus are depicted above graphs. Peak areas for the selected peptides across mIMCD3 WT and *Jade* mutant cell lines are used for protein quantification. Only areas with a dotp value above 0.7 were included in the analysis to ensure the confidence of the result (N=3). See also MS ID#: BIORXIV/2021/462752.

Several studies suggested a role of *Jade1* in proliferation and cell cycle progression (Borgal et al., 2016; Zhou et al., 2005). To investigate whether the loss of one *Jade* protein leads to a change in cell cycle progression we used flow cytometry to determine whether we can observe differences in the cell cycle phases (Figure 13). We do not observe any obvious differences between wild-type and *Jade*-deficient cell lines as seen by a similar amount of cells in each phase of the cell cycle across the different cell lines. If we partially starve the cells, we observe a tendency towards cell cycle arrest in G0/1 as shown in Figure 14. This goes along with a reduced number of cells in S and G2/M phase. However, the reduction of cells in the G2/M phase is significantly stronger in WT cells compared to the *Jade1*-deficient cell lines. First experiments did not indicate any alterations of cilia in the *Jade*-deficient cell lines (data not shown). Further evaluation of ciliation and ciliogenesis in these cell lines is currently ongoing.

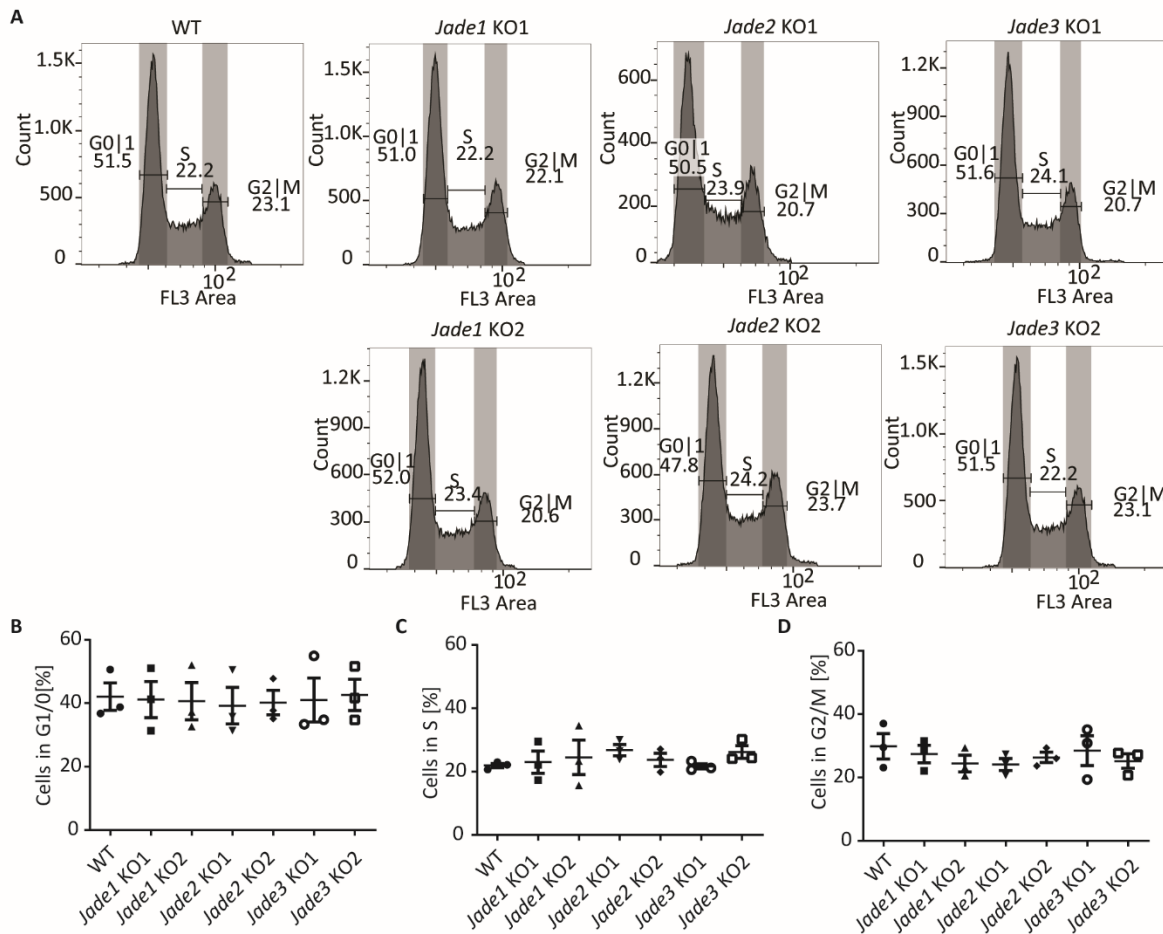


**Figure 13. Cell cycle analysis does not show significant changes in the *Jade1/2/3*-deficient cell lines compared to mIMCD3 wild-type cells.**

(A) mIMCD3 of the indicated genotypes were seeded at  $2 \times 10^6$  cells / 10 cm culture dish and harvested after 24 hours for flow cytometry. Representative histograms of propidium iodide (PtdIns) staining of mIMCD3 WT #8 and each *Jade* mutant cell line. (B-D) Quantification of flow cytometry data represented as percentage of cell in each phase of the cell cycle. The first histogram peak corresponds to 2n DNA / cells in G1/G0 phase (B). Cells in S phase, with an intermediary DNA status, are represented by the area between both peaks (C). The second peak to 4n DNA/ cells in G2/M phase (D). Quantification of the flow cytometry data was performed using FlowJo software. To maintain integrity of individual experimental repetitions the results were analyzed with repeated measures ANOVA. (N=3, Errors bars represent SEM).

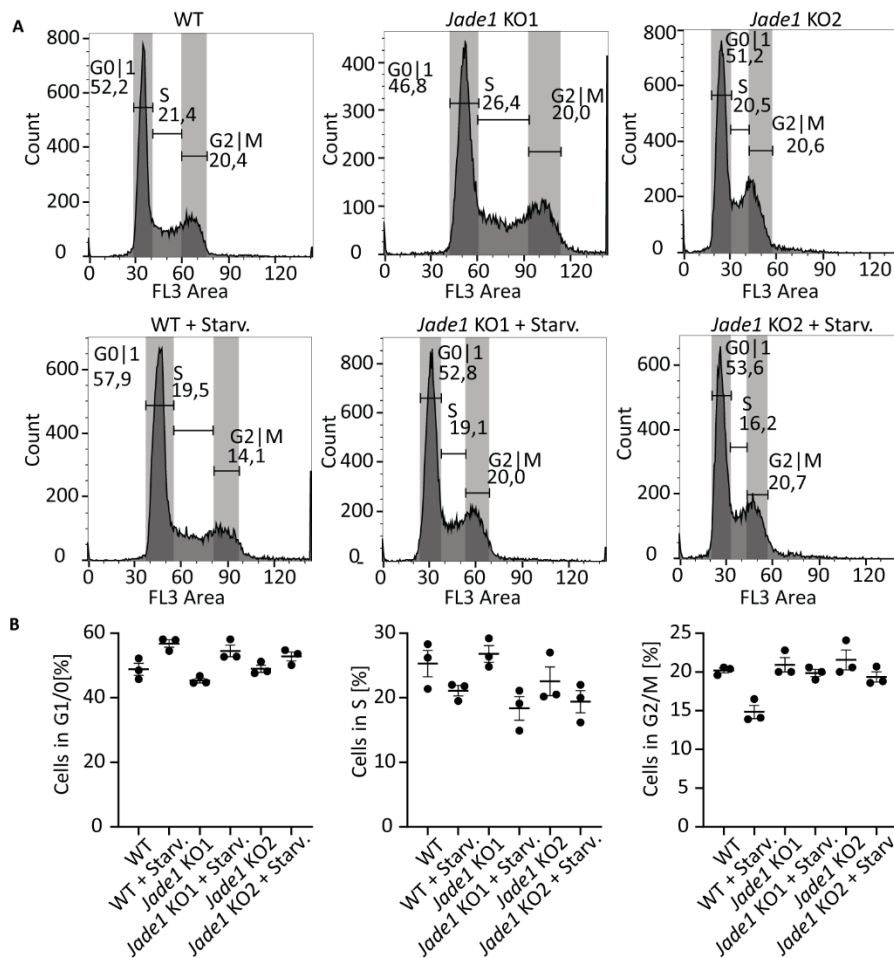


**Figure 14. Starvation leads to reduced cell cycle arrest in *Jade1*-deficient cells compared to WT cells.** (A) mIMCD3 of the indicated genotypes were seeded at  $0.5 \times 10^6$  cells / 10 cm culture dish. After 24 h the medium was replaced by serum reduced medium. 48 h later the cells were harvested for flow cytometry. Representative histograms of propidium iodide (PtdIns) staining of mIMCD3 WT #8 and *Jade1* mutant cell lines. (B-D) Quantification of flow cytometry data represented as percentage of cell in each phase of the cell cycle. The first histogram peak corresponds to 2n DNA / cells in G1/G0 phase (B). Cells in S phase, with an intermediary DNA status, are represented by the area between both peaks (C). The second peak to 4n DNA/ cells in G2/M phase (D). Quantification of the flow cytometry data was performed using FlowJo. (N=3, Errors bars represent SEM).

### 6.1.6 Proteomic profiling of *Jade*-deficient cell lines reveals an upregulation of proteasomal components as a common finding.

After establishing the different *Jade*-deficient cell lines, we utilized a global approach to study the effects of the loss of *Jade* proteins in mIMCD3 cells. Therefore, we generated whole cell proteome profiles for all six *Jade*-deficient cell lines as well the wild-type control cell line. In three independent replicates, we quantified about 3500 proteins on average with little variation across cell lines (Figure 15A). Using principal component analysis on the label-free quantification (LFQ) intensities, we observed clustering of replicates and no outliers (Figure 15B-D). Moreover, the first principle component separated the wild-type sampled from the mutant cell lines explaining 72.8 %, 58.4 %, and 70.6 % variance for the *Jade1*, *Jade2*, and *Jade3* dataset, respectively.

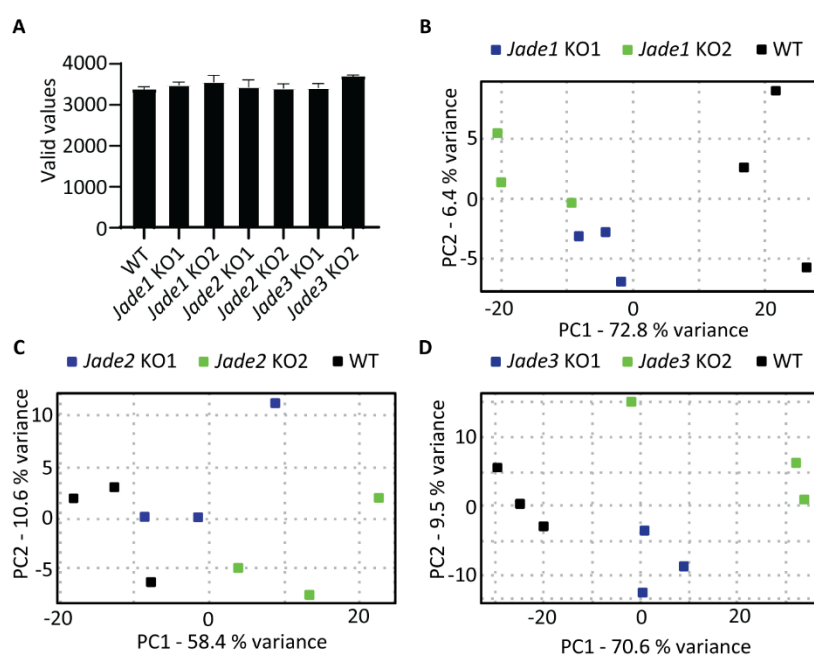


**Figure 15. Quality control of proteome datasets for *Jade1/2/3*-deficient and wild-type mIMCD3 cell lines.**

**(A)** Number of valid values of LFQ intensities measured in each cell line. Principal component analysis scatter plot of the protein expression data of WT versus *Jade1* **(B)**, *Jade2* **(C)**, and *Jade3* **(D)** KO1 and KO2 cell lines. Depicted are the first two principal components (PC1 and PC2). The axes represent the percentages of variation explained by the principal components. The replicates of the different groups cluster together and the difference between mutant and wild-type groups explains the largest variance. See also MS ID#: BIORXIV/2021/462752.

After the quality control, we first took a detailed look on the changes upon loss of *Jade1*. Therefore, we extracted the significantly regulated proteins by statistical analysis on LFQ intensities. Using a two-sample t-test ( $s_0 = 0.2$ ,  $FDR = 0.1$ ), we identified 594 (653) upregulated and 414 (722) downregulated proteins when comparing the *Jade1* KO1 (KO2) cell lines to the wild-type control (Figure 16A,B). Among these was Prom1 as one of the most downregulated proteins, which has been shown to increase cilia length and when mutated causes retinal degeneration through malformation of the outer segment of photoreceptors (Cehajic-Kapetanovic et al., 2019; Jászai et al., 2020; Maw et al., 2000). Here, we already noticed that we had a high overlap between the two individual *Jade1*-deficient cell lines. To further investigate the similarity of both mutant cell lines we plotted the logarithmic fold changes of *Jade1* KO1 versus WT against *Jade1* KO2 versus WT (Figure 16C). As expected, we see a high correlation confirming that the majority of proteins are regulated in the same direction in both *Jade1* KO1 and KO2. To get a better understanding of what the role of these proteins might be, we used the proteins significantly regulated in either *Jade1* KO1, KO2, or both mutant cell lines and performed Gene Ontology (GO) and KEGG pathway enrichment analysis on this subset of 1458 proteins (Figure 16D). This revealed a significant overrepresentation of GO terms such as cytoplasmic translation, translation initiation factor activity, and integral component of membrane and KEGG pathways like proteasome and ribosomal biogenesis.

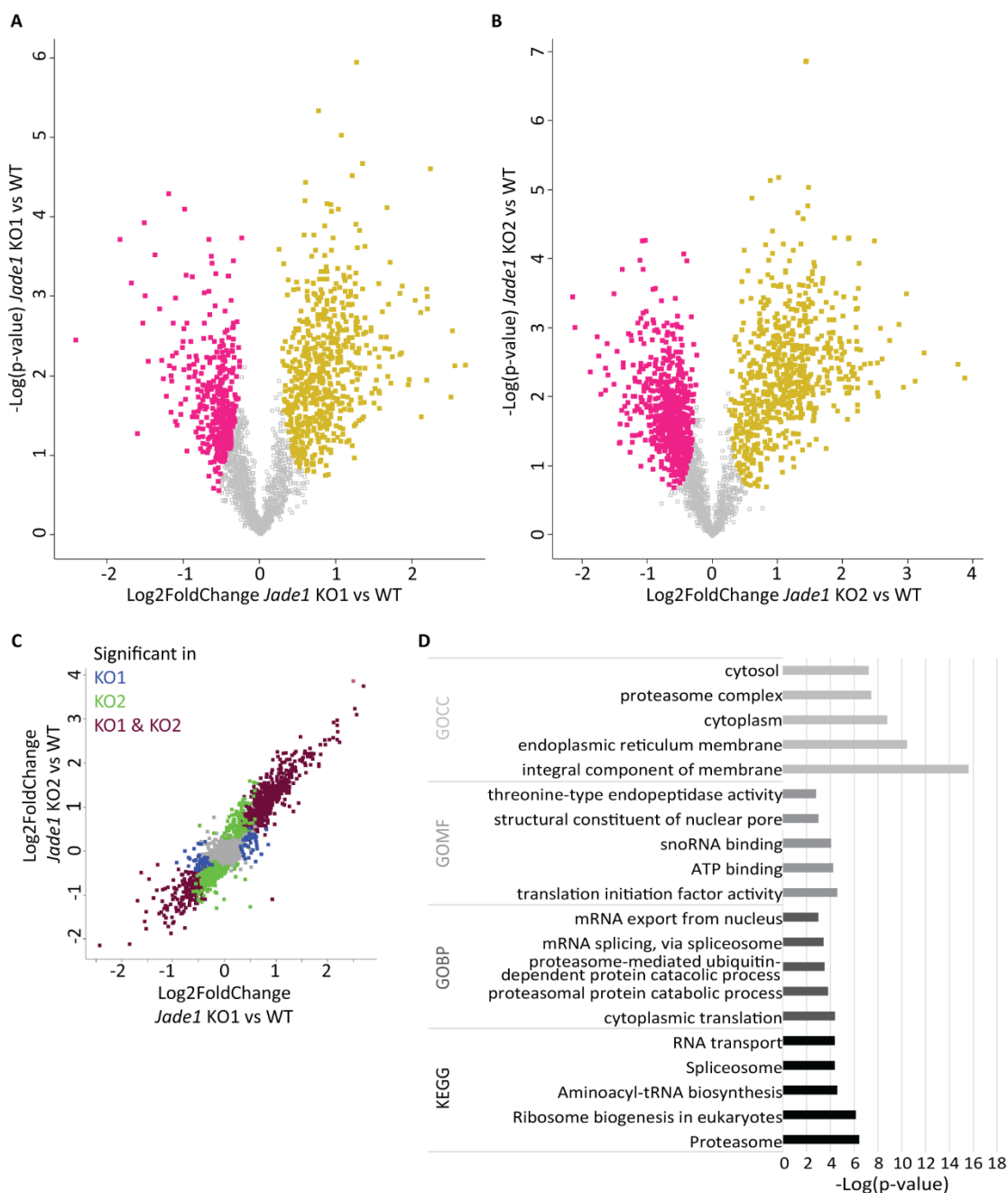


**Figure 16. Protein expression profiling of *Jade1*-deficient cell lines.**

(A) Scatter plot with the t-test differences in protein expression of the *Jade1* KO1 mutant cells vs the wild-type cells on the x-axis and the statistical significance ( $-\log_{10}$  Student's t-test p-value) on the y-axis. Highlighted are proteins that are significantly regulated based the students t-test ( $s_0 = 0.2$ , FDR = 0.1). (B) Same scatter blot as in (A) for *Jade1* KO2. (C) Comparison of the two different mutant cell lines for *Jade1*. The fold change of KO1 is depicted on the x-axis, the fold change of the KO2 on the y-axis. Proteins are highlighted according to their significance based on the students t-test ( $s_0 = 0.2$ , FDR = 0.1) in the *Jade1* KO1 only (blue), the *Jade1* KO2 only (green), and in both *Jade1* KO1 and KO2 (dark red). (D) GO and KEGG pathway annotation based on a Fisher exact test of the 1458 proteins found to be regulated in both *Jade1* mutant cell lines. See also MS ID#: BIORXIV/2021/462752.

When performing the same analysis pipeline for the *Jade2/3*-deficient cell lines identified 17 (420) upregulated and 2 (348) downregulated proteins for *Jade2* KO1 (KO2) and 16 (15) upregulated and 496 (590) downregulated proteins for *Jade3* KO1 (KO2). Also for these two *Jade* family members, we could show the correlation of the two individual mutant cell lines (Figure 17A,C). Combining the proteins with a p-value below 0.05 for either KO1, KO2 or both we ended up a subset of 773 proteins for *Jade2* and 1460 proteins for *Jade3*. Enrichment analysis of proteins regulated upon loss of *Jade2* and *Jade3* revealed terms like ribosome, proteasome, and transcription enriched (Figure 17B,D).

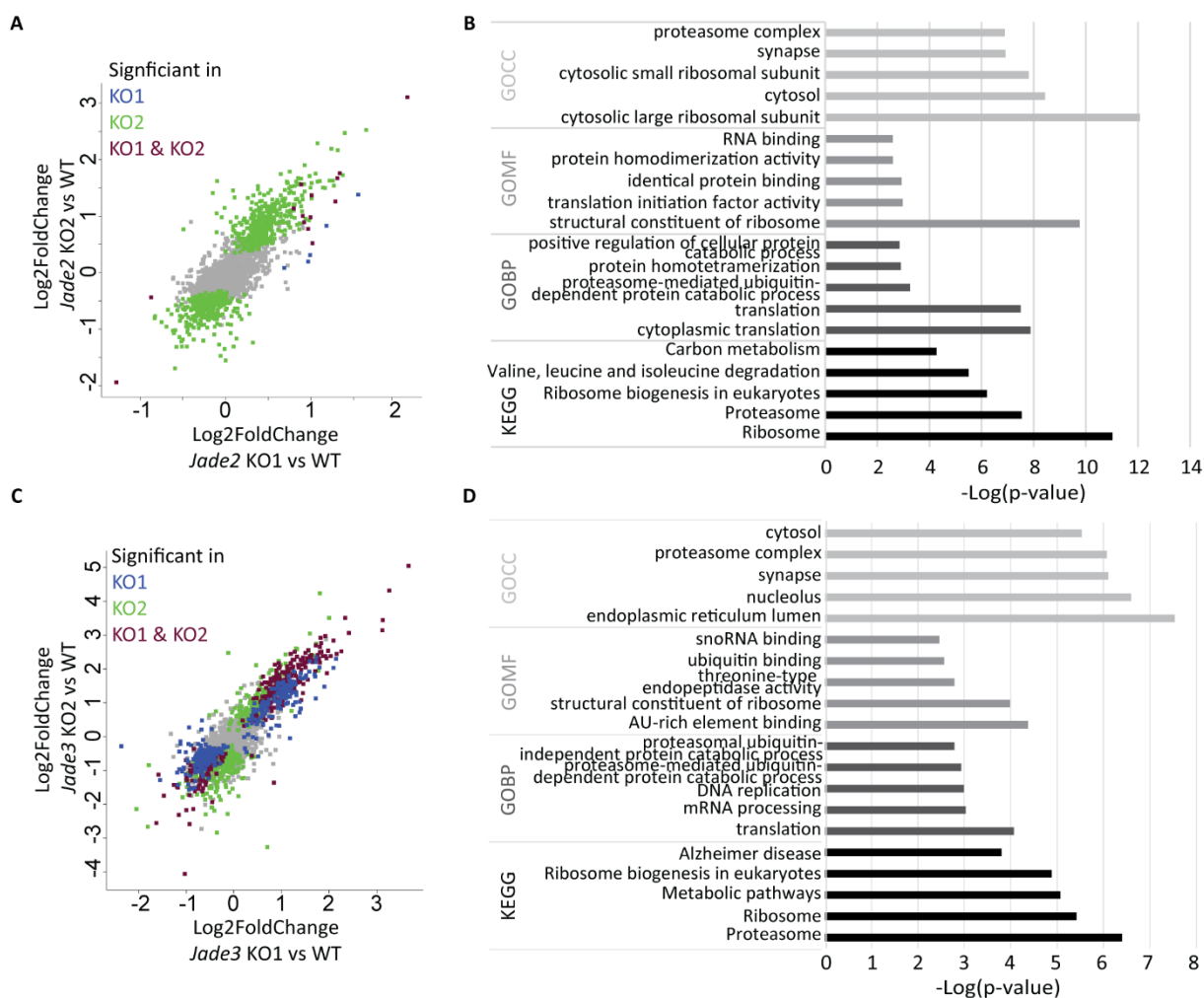


**Figure 17. Protein expression profiling of *Jade2*- and *Jade3*-deficient cell lines.**

**(A)** Comparison of the two different mutant cell lines for *Jade2*. The fold change of KO1 is depicted on the x-axis, the fold change of the KO2 on the y-axis. Proteins are highlighted according to their significance (students t-test,  $s_0 = 0.2$ , FDR = 0.1) as indicated in the figure. **(B)** GO and KEGG pathway annotation based on a Fisher exact test of the 773 proteins found to be regulated in both *Jade2* mutant cell lines. **(C)** Comparison of the two different mutant cell lines for *Jade3*. The fold change of KO1 is depicted on the x-axis, the fold change of the KO2 on the y-axis. Proteins are highlighted according to their significance as indicated in the figure. **(D)** GO and KEGG pathway annotation based on a Fisher exact test of the 1460 proteins found to be regulated in both *Jade3* mutant cell lines. See also MS ID#: BIORXIV/2021/462752.

Already in the individual analysis of the *Jade1/2/3* we saw terms related to proteasome, ribosomes, and translation enriched. To further investigate possible shared functions within the *Jade* family, we used the subsets of regulated proteins for the individual members to calculate the overlap within the *Jade* family (Figure 18A). This revealed 644 proteins that are regulated throughout the *Jade* protein family. GO and KEGG pathway enrichment analysis confirmed overrepresentation of terms associated with the proteasome, ribosome, as well as translation (Figure 18B). Looking specifically at proteins, which are associated with proteasome-related GO terms for biological processes, we indeed see that the majority of these proteins is significantly upregulated in the *Jade1* KO2 cell line (Figure 18C). Visualizing these proteins based on the average LFQ intensities for all seven cell lines in a heatmap, we do see a general upregulation in the *Jade*-deficient lines which is most prominent for proteasome core and regulatory subunit components (Figure 18D). In addition to the upregulation of the proteasome, we also see a similar pattern for ribosomal proteins, tRNA-ligases, and elongation factors, which might indicate an increased protein turnover (Figure 19A-C).

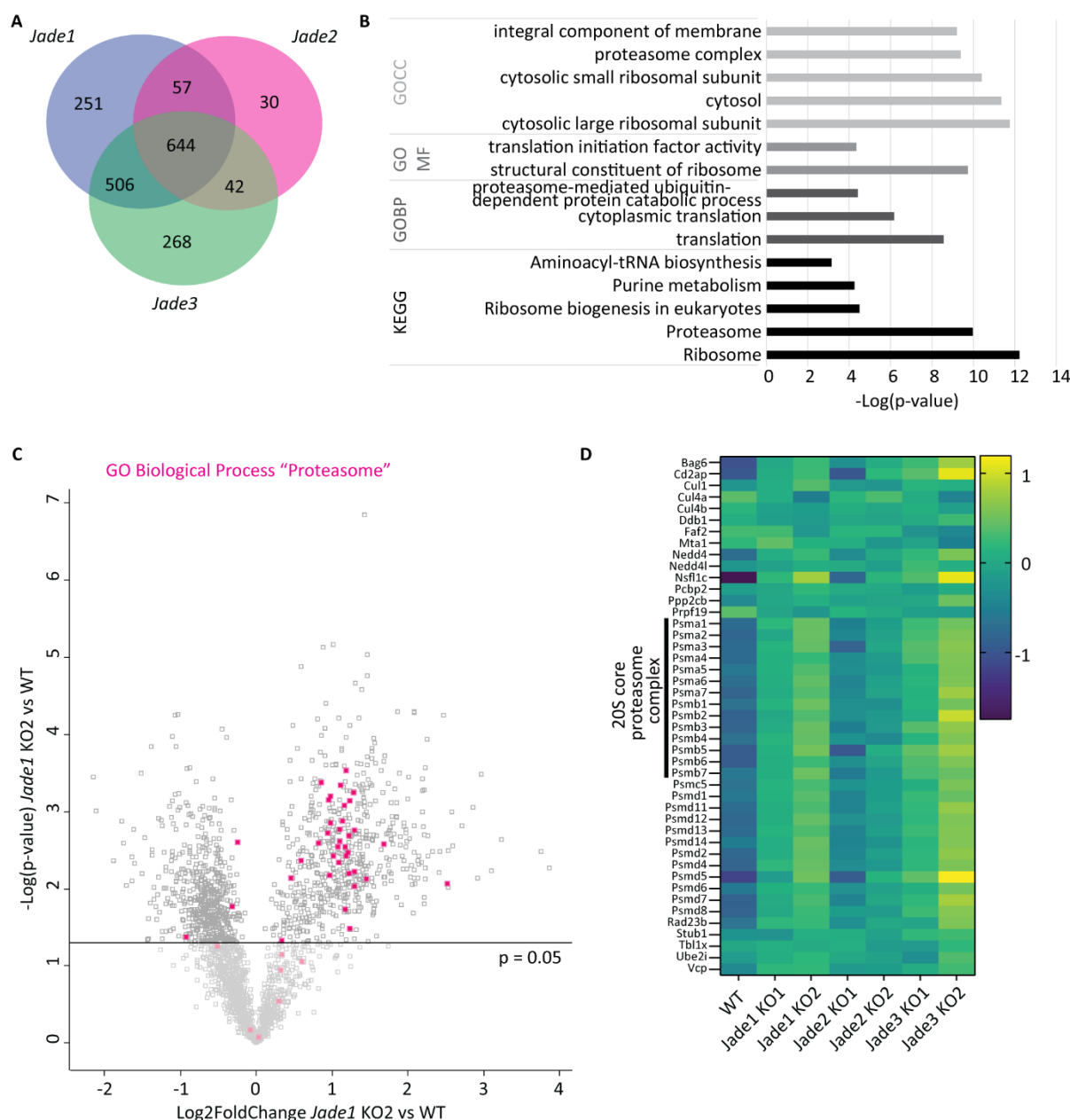


**Figure 18. All *Jade*-deficient cell lines show an upregulation in proteasome associated proteins.**

**(A)** Venn diagram depicting the overlap between significantly regulated proteins across the *Jade*-deficient cell lines. The *Jade1* section includes all proteins that are significantly regulated in either one or both of the *Jade1*-deficient cell lines. The *Jade2* and *Jade3* sections were generated in the same way. **(B)** GO and KEGG pathway annotation based on a Fisher exact test of the 644 proteins found to be regulated in all *Jade* mutant cell lines. Ribosome, proteasome, and translation related areas are regulated the most. **(C)** Scatter plot with the t-test differences in protein expression of the *Jade1* KO2 mutant cells vs the wild-type cells on the x-axis and the statistical significance ( $-\log_{10}$  Student's t-test p-value) on the y-axis. Proteins associated with the GOBP terms associated with the proteasome are highlighted in magenta. **(D)** Heatmap of the proteins highlighted in **(C)** based on logarithmic z-score normalized LFQ values for all seven cell lines to visualize the upregulation of proteasome associated proteins across *Jade*-deficient cell lines. See also MS ID#: BIORXIV/2021/462752.

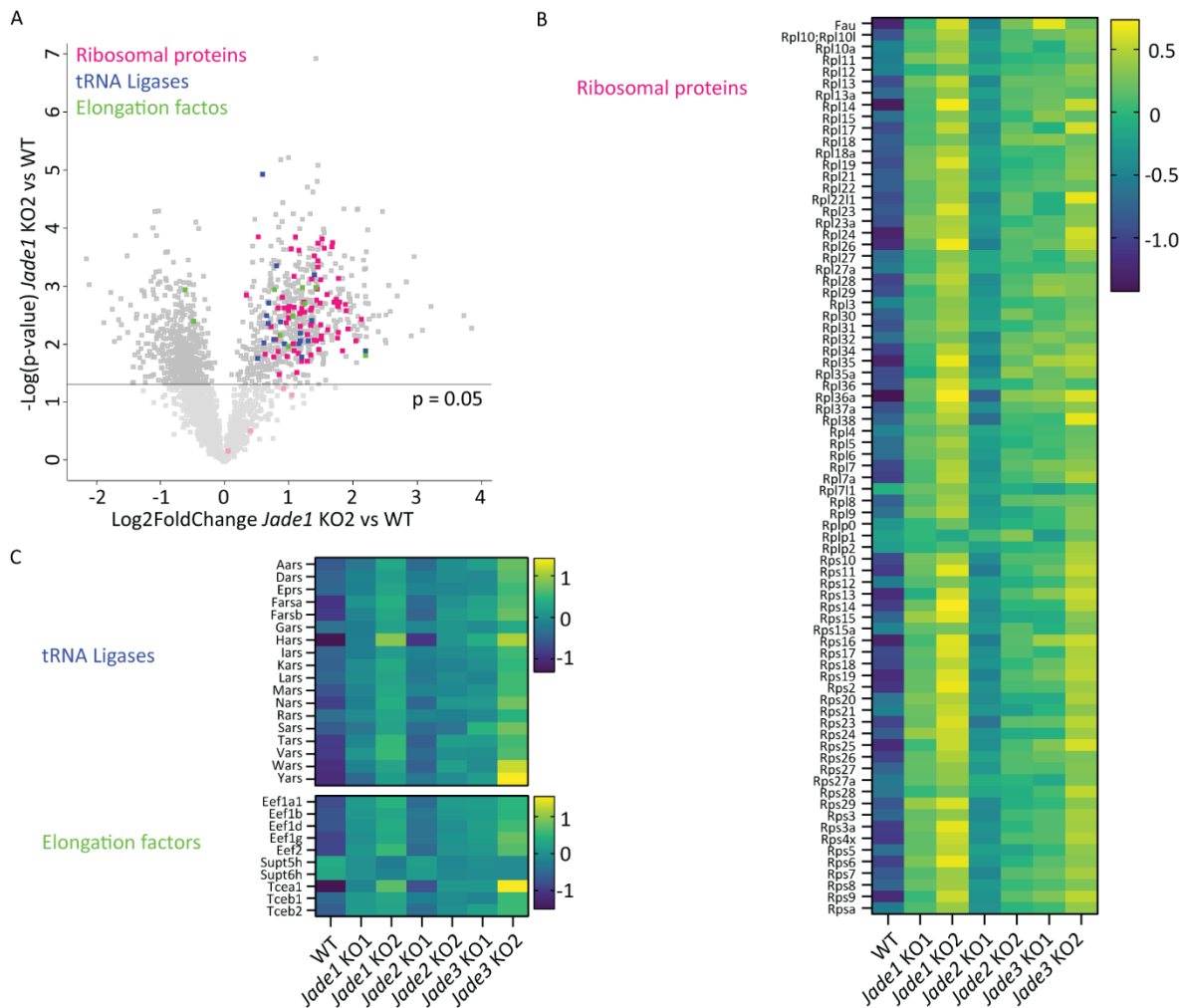


**Figure 19. Components of the protein turnover machinery are upregulated in *Jade*-deficient cell lines.**

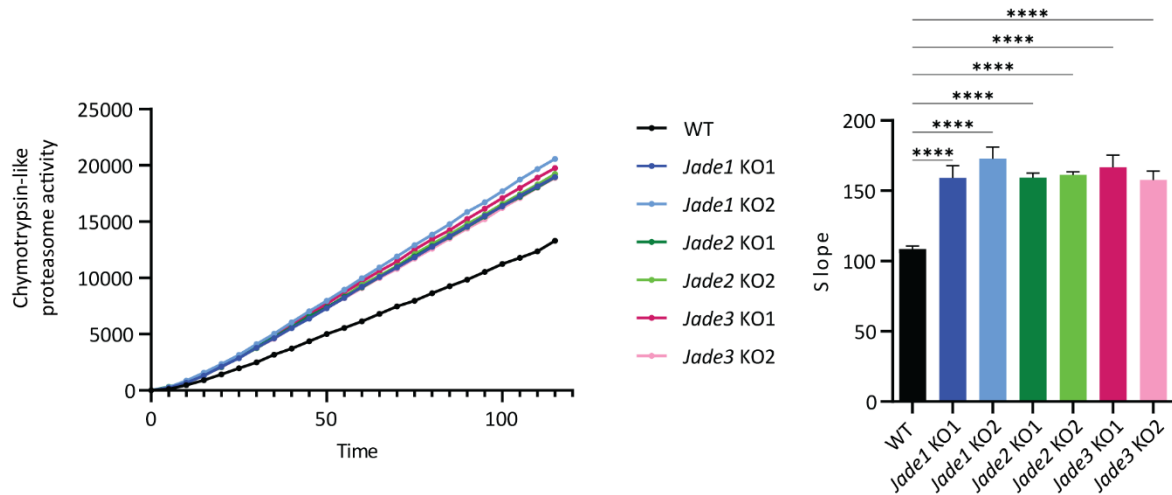
**(A)** Scatter plot with the t-test differences in protein expression of the *Jade1* KO2 mutant cells vs the wild-type cells on the x-axis and the statistical significance (-log<sub>10</sub> Student's t-test p-value) on the y-axis. Ribosomal proteins are highlighted in magenta, tRNA ligases in blue, and elongation factors in green. **(B,C)** Heatmap of the proteins highlighted in (A) based on logarithmic z-score normalized LFQ values for all seven cell lines to visualize the upregulation of ribosomal proteins (B), tRNA ligases, and elongation factors (C) across *Jade*-deficient cell lines. See also MS ID#: BIORXIV/2021/462752.

### 6.1.7 *In vitro* proteasome assays confirm the role of the Jade protein family in the regulation of the proteasome.

Based on the expression profiles for the proteasomal proteins across the *Jade*-deficient cell lines, we aimed to confirm these findings with an *in vitro* based proteasome activity assay. In our protein expression profiles we saw both, components of the proteasomal core subunit 20S as well as the regulator subunit 19S regulated. The 20S subunit contains the proteolytic active site while the 19S subunit forms a cap structure which is necessary for the 20S subunit to be able to degrade proteins as well as for the regulation of the activity (Finley, 2009). Together they form the 26/30S proteasome

(single /double capped). We measured 26S/30S proteasome activity by monitoring the degradation of a fluorogenic substrate (Kisselev and Goldberg, 2005). For all of the *Jade*-deficient cell lines we could observe a significant increase in chymotrypsin-like proteasome activity (Figure 20A). Moreover, when overexpressing the different *Jade* family members we saw a marked decrease in proteasome activity compared to an overexpressed control protein, further confirming the regulatory function Jade protein family members have on the proteasome (Figure 20B).

A



B

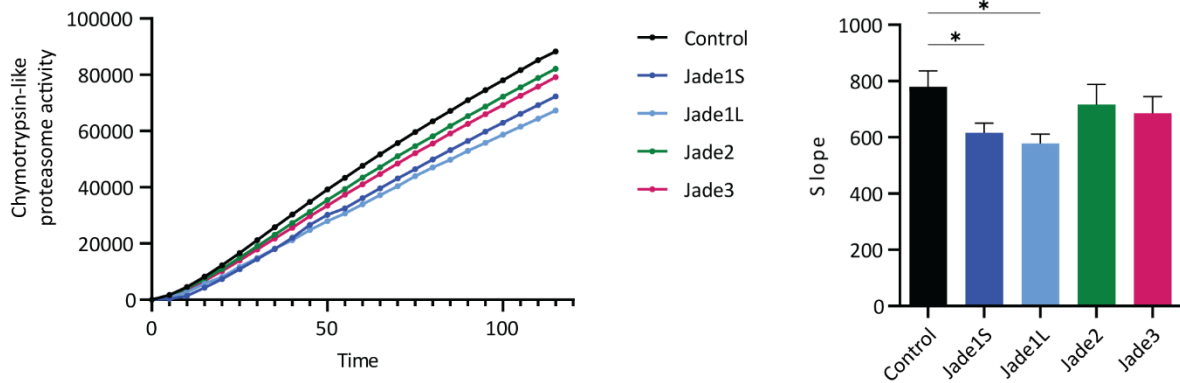


**Figure 20. *In vitro* proteasome activity assay confirms role of Jade proteins in proteasome regulation.**

**(A)** Measurement of the proteasome activity in wild-type and *Jade*-deficient mIMCD3 cell lines. The proteasome activity of *Jade1*, *Jade2*, or *Jade3*-deficient cell lines is increased compared to the wild-type control. Quantification of the slope as readout for proteasome activity (N=3, one-way ANOVA with a Dunnett's multiple comparison test, \*\*\*\* $p \leq 0.0001$ ) **(B)** Measurement of the proteasome activity in HEK293T cell with either *Jade1S*, *Jade1L*, *Jade2*, *Jade3*, or Podocin (control) overexpressed. All cell lines with overexpressed *Jade* proteins show a decreased activity compared to the control. Quantification of the slope as readout for proteasome activity (N=3, one-way ANOVA with a Dunnett's multiple comparison test, \*  $p \leq 0.05$ ). See also MS ID#: BIORXIV/2021/462752.

### 6.1.8 mRNA expression of proteasomal components is not significantly altered

Several studies have implicated the role of *Jade1* as an epigenetic and transcriptional regulator. However, specific targets have been suggested but not been verified (Avvakumov et al., 2012; Panchenko et al., 2004). All *Jade* family members contain two PHD domains, which are zinc-binding motifs and known to be found in proteins involved in transcriptional regulation and chromatin modification (Aasland et al., 1995; Saha et al., 1995). Moreover, it has been shown that transcriptional regulation is one of the main mechanisms to modulate proteasomal activity (Schmidt and Finley, 2014). On one hand, this can occur via regulation of the abundance of proteasome subunits. This is well studied for the transcription factor *Rpn4* in yeast (Mannhaupt et al., 1999; Xie and Varshavsky, 2001) as well as *NRF1/2* in mammals (Kwak et al., 2003; Radhakrishnan et al., 2010). On the other hand, regulation can happen via controlling the assembly of proteasome subunits. For example, inhibition of mTor signaling can induce assembly chaperones of the 19S regulatory subunit, which are essential for proteasome assembly (Rousseau and Bertolotti, 2016).

The potential role of *Jade* family members in transcriptional regulation as well as established mechanism of transcriptional regulation of the proteasome raised the question if the changes we observed on protein expression are caused by transcriptional changes. To answer this question as well as to identify potential transcriptional targets of the *Jade* family we performed unbiased transcriptomic analyses with bulk mRNA-Seq from all six *Jade*-deficient cell lines and the wild-type control cell line. For all samples, we observed narrow clustering of the three replicates (Figure 21A-C). Separation of the mutant samples from the control samples is based on either the first (*Jade1*) or the second (*Jade2* and *Jade3*) principle component. The volcano plot for each *Jade1* mutant depicts the genes with a fold change  $> 1.5$  or  $< -1.5$  as well as a p-value  $< 0.05$  in red (Figure 21D,E). Notably, the vast majority of significantly altered genes are regulated in the same direction in both cell lines (Figure 21F). We used the subset of genes which is significantly regulated in either *Jade1* KO1 or *Jade1* KO2 cell lines to performed GO and KEGG pathway enrichment analysis. We found pathways related to cancer as well as regulation of transcription and binding functions enriched in the *Jade1*-deficient cell lines (Figure 21G).

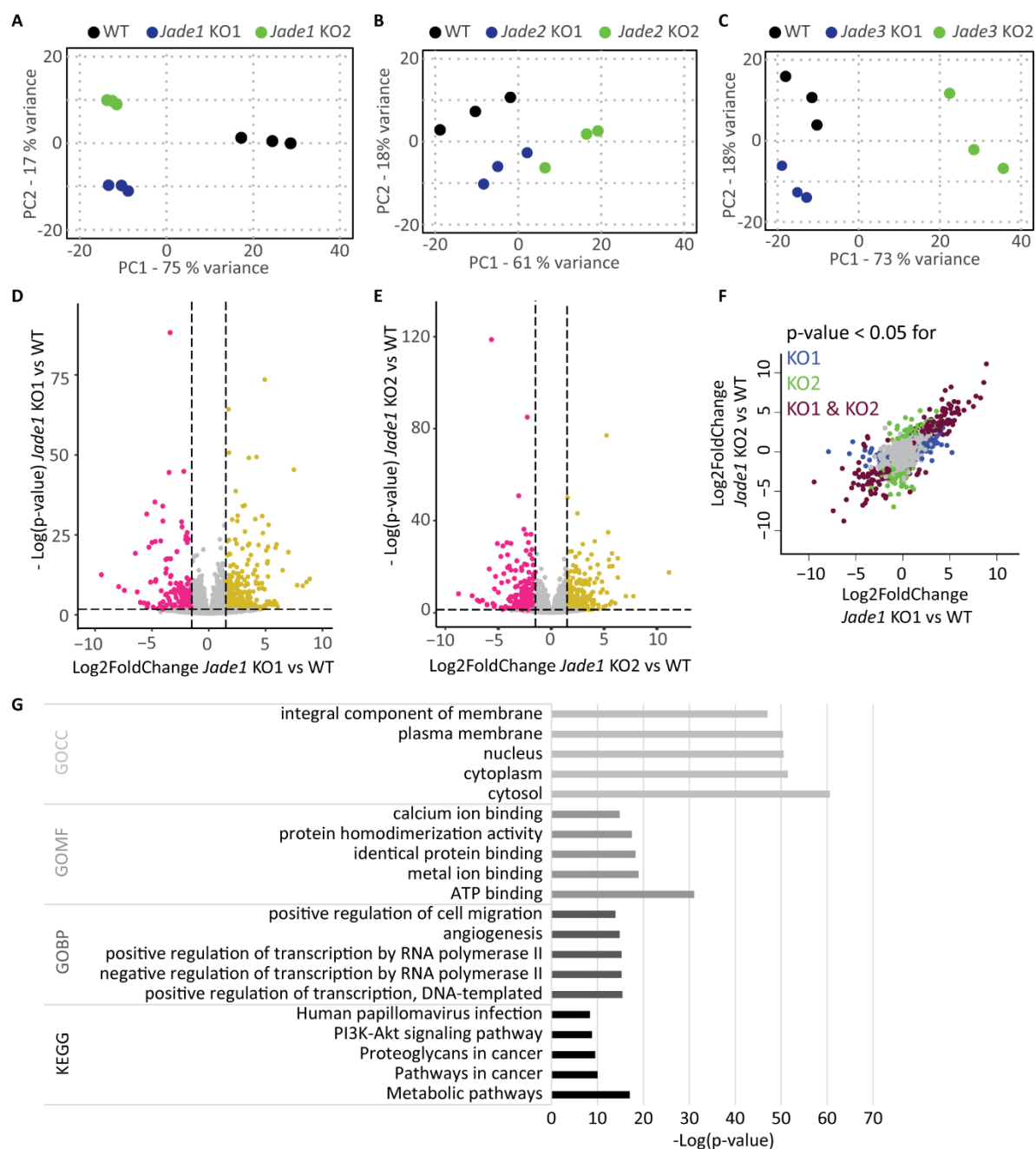


**Figure 21. Transcriptomic expression profiling of *Jade*-deficient cell lines.**

Principal component analysis scatter plot of the gene expression data of WT versus *Jade1* (A), *Jade2* (B), and *Jade3* (B) KO1 and KO2 cell lines. Depicted are the first two principal components (PC1 and PC2). The axes represent the percentages of variation explained by the principal components. (D) Volcano blot for *Jade1* KO1 showing the fold change on the x-axis and the significance on the y-axis. Highlighted are genes with a p-value below 0.05 and a log2 fold change above 1.5 or below -1.5. (E) Volcano blot for *Jade1* KO2 showing the fold change on the x-axis and the significance on the y-axis. Highlighted are genes with a p-value below 0.05 and a log2 fold change above 1.5 or below -1.5. (F) Comparison of the two different mutant cell lines for *Jade1*. The fold change of KO1 is depicted on the x-axis, the fold change of the KO2 on the y-axis. Proteins are highlighted according to their significance as indicated in the figure. (G) GO and KEGG pathway annotation based on a Fisher exact test of the genes regulated in either *Jade1* KO1, *Jade1* KO2, or both mutant cell lines. See also MS ID#: BIORXIV/2021/462752.

We calculated the subset of genes enriched in *Jade2* or *Jade3*-deficient cell lines as well as the GO pathway annotation in a similar manner (Figure 22A-D). Annotation enrichment analysis revealed a high overlap in overrepresented terms between *Jade1/2/3*. To further investigate the shared functions of *Jade1/2/3*, we calculated the overlap of the significantly enriched subsets and found 567 genes as commonly regulated within the family (Figure 23A). GO and KEGG pathways enrichment analysis confirmed that the mutual regulated genes are involved in metabolic and cancer related pathways (Figure 23B). Since the transcriptomic analysis did not reveal any regulation of the proteasome so far, we specifically looked into the expression of the proteasomal complex components (Figure 23C). In contrast to our proteome analysis, we do not see upregulation of the proteasomal proteins on a transcriptomic level. We can further show that ribosomal components, tRNA-ligases and transcription initiation and elongation factors are mainly unaltered as well.

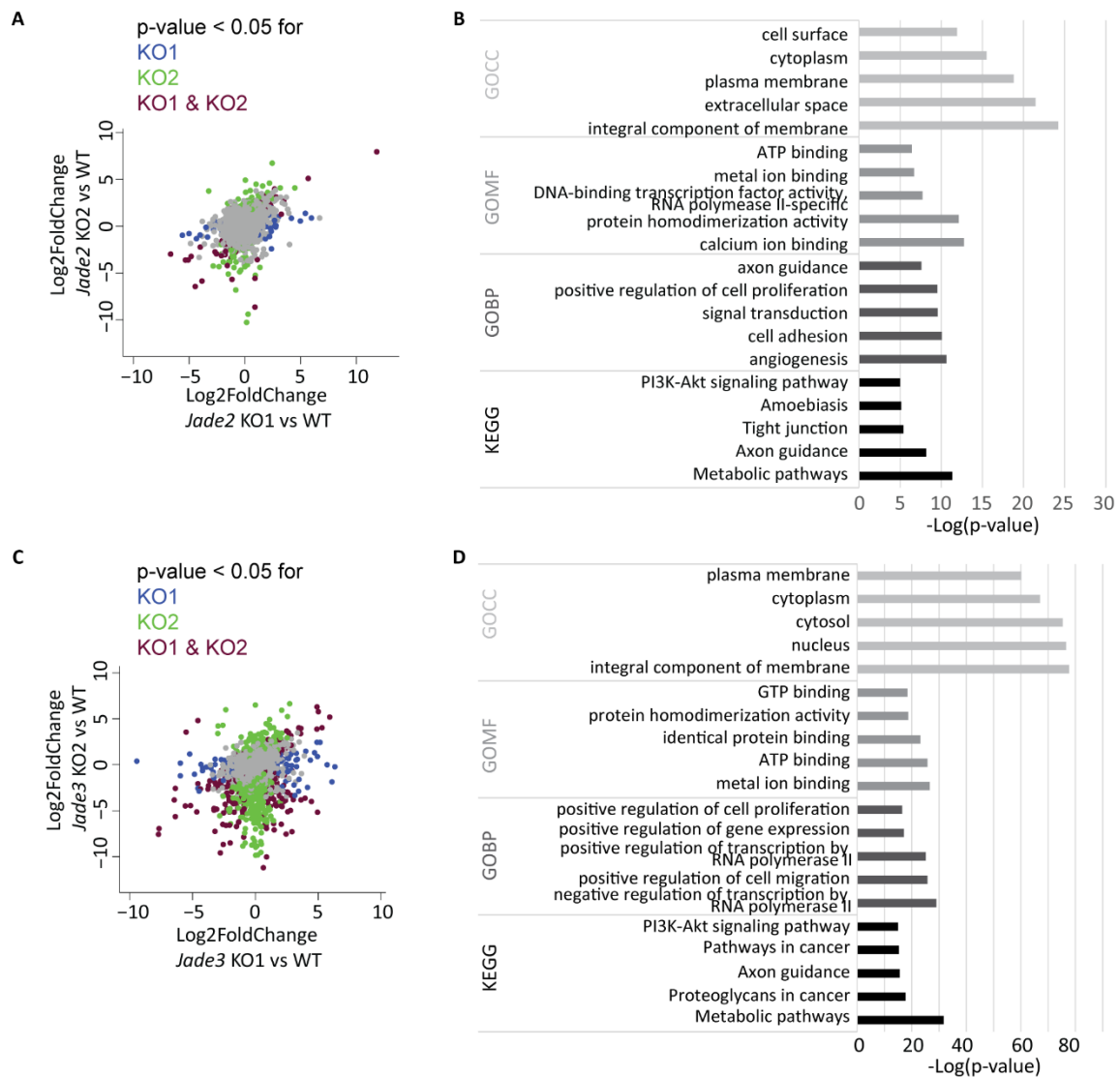


**Figure 22. Transcriptomic expression profiling of *Jade2/3*-deficient cell lines.**

**(A,C)** Comparison of the two different mutant cell lines for *Jade2* **(A)** and *Jade3* **(C)**. The fold change of KO1 is depicted on the x-axis, the fold change of the KO2 on the y-axis. Proteins are highlighted according to their significance as indicated in the figure. **(B,D)** GO and KEGG pathway annotation based on a Fisher exact test of the genes regulated in either *Jade2* **(B)** or *Jade3* **(D)** KO1, KO2 or both mutant cell lines. See also MS ID#: BIORXIV/2021/462752.

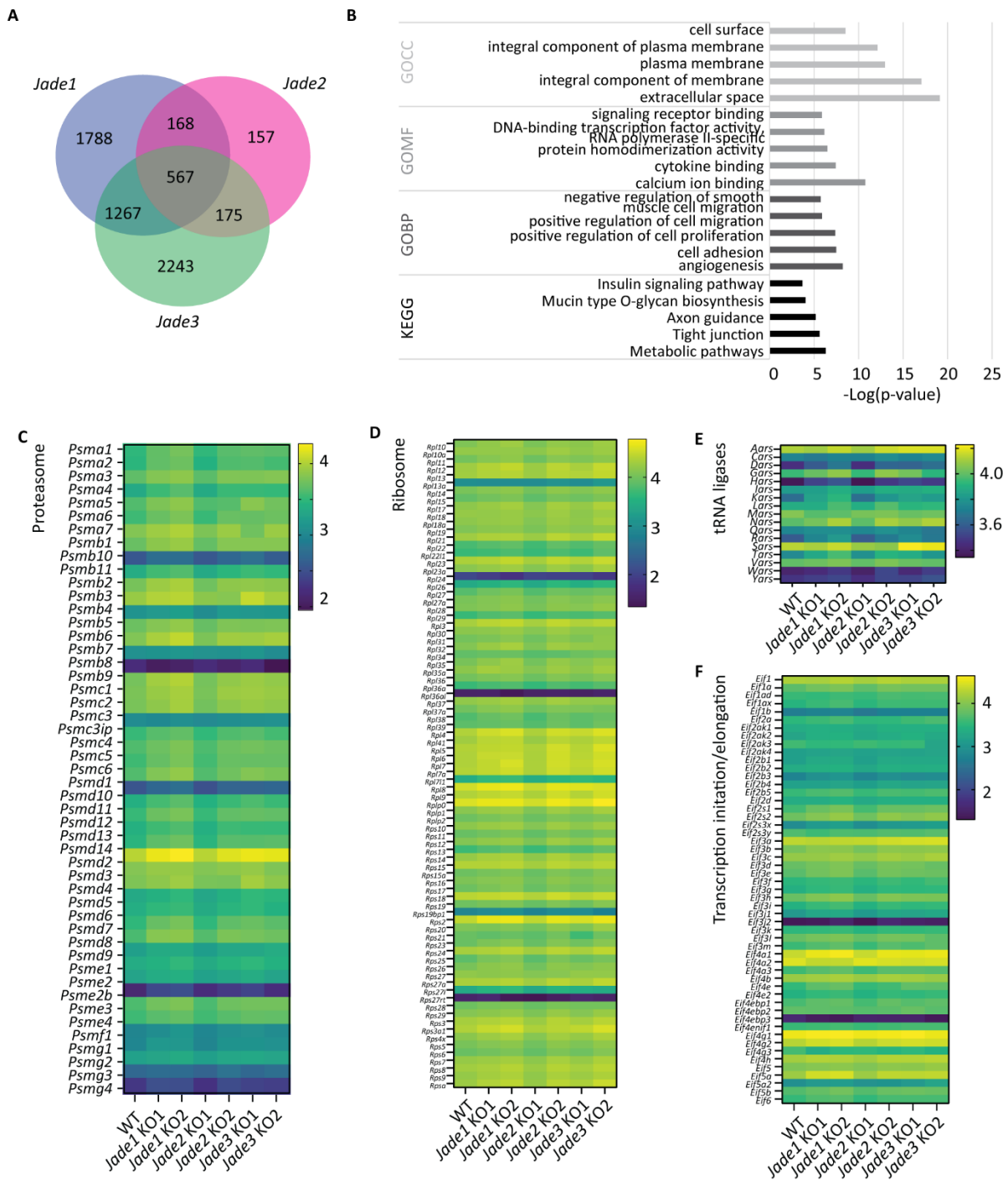


**Figure 23. Mutual regulated genes within the *Jade* family do not show upregulation of the proteasome or protein turnover machinery.**

**(A)** Venn diagram depicting the overlap between significantly regulated genes across the *Jade*-deficient cell lines. The *Jade1* section includes all proteins that are significantly regulated in either one or both of the *Jade1*-deficient cell lines. The *Jade2* and *Jade3* sections are generated in the same way. **(B)** GO and KEGG pathway annotation based on a Fisher exact test of the 567 genes found to be regulated in all *Jade* mutant cell lines. **(C-F)** Heatmap of the genes of the proteasome **(C)**, ribosome **(D)**, tRNA-ligases **(E)** and transcription initiation and elongation **(F)** based on logarithmic z-score normalized counts for all seven cell lines to visualize the transcript levels of proteasome associated proteins across *Jade*-deficient cell lines. See also MS ID#: BIORXIV/2021/462752.

### 6.1.9 Components of the proteasome are part of a Jade protein complex.

After discovering that the regulation of the proteasome is likely not caused by changes on transcriptional level and the function of Jade proteins as transcription factor, we speculated whether regulation might be based on direct interaction or association of Jade proteins with components of the proteasome. To answer this question, we expressed either FLAG-tagged Jade1S or Jade1L in the *Jade1* KO1 cell line. After a FLAG-co-immunoprecipitation, the proteins were eluted from the beads and prepared for proteomic analysis. We identified one of the five replicates of Jade1L as an outlier with only 27 valid values compared to an average of 1178 (SEM  $\pm$  23) valid values in all other samples. This sample was excluded for all further analysis. We continued our analysis with four replicates for Jade1L and five for Jade1S as well as the control. To identify interactors of Jade1L and Jade1S we utilized the intensity Based Absolute Quantification (iBAQ) intensities. First, we looked at proteins which were never measured in the control samples, but either in all replicates for Jade1L, for Jade1S, or both (Figure 24A). Sorting them based on their intensities we could identify Jade1 as the most abundant protein in this subset for Jade1L and Jade1S, confirming a successful pulldown. Moreover, in this subset we also found the known Jade1 interactor Plk1. We performed statistical analysis on the iBAQ intensities to identify significantly enriched proteins (Figure 24B,C). Among these were several known interactors, which are highlighted (green) based on a cross-referencing our list with known interactors for Jade1 annotated in the BioGRID database (Oughtred et al., 2021). Among these were the established interactors such as HBO1/Kat7. Notably, we did identify several components of the proteasome complex. For Jade1S, a main component of the proteasome core complex, Psm1, has been identified as one of the most enriched proteins. However, most of the enriched proteasome components are part of the regulatory S19 subunit, including Psmc3, Psm3, Psm12, and Psm14. Taken together, we could show that loss of either of the Jade protein family members leads to an upregulation of proteasome abundance and activity, which is not caused by transcriptional regulation. Co-immunoprecipitation of proteasomal components with Jade proteins suggest a direct link, for example by targeting the proteasome for degradation.

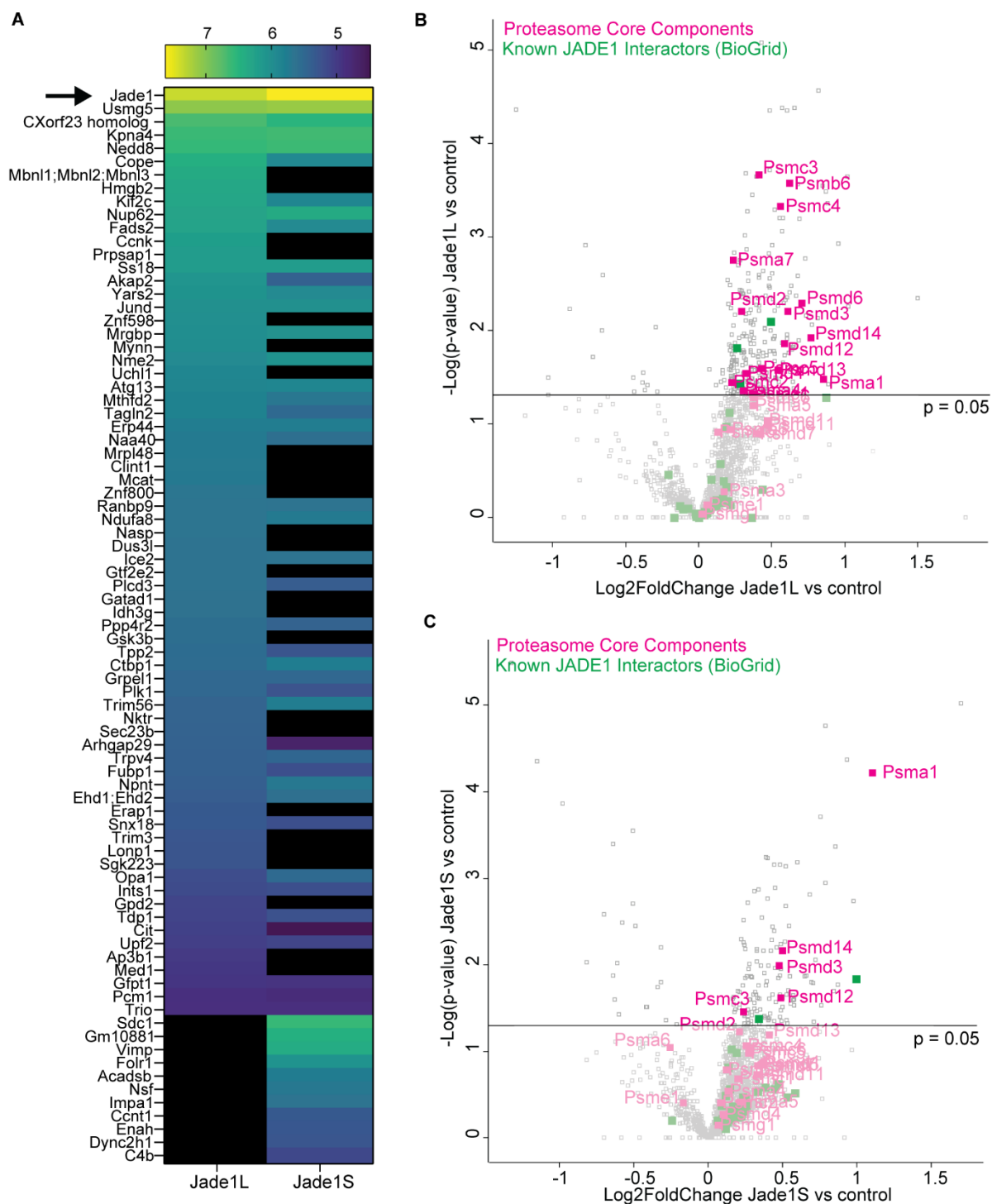


Figure legend on previous page

**Figure 24. Interactome analysis based on co-immunoprecipitations reveals a potential direct link between Jade proteins and proteasomal components.** (*previous page*)

(A) Heatmap of average iBAQ values for proteins which were never measured in the control samples, but in either all replicates for Jade1L, all replicates for Jade1S, or all replicates of both. The protein with the highest iBAQ is Jade1 for both, the Jade1S and the Jade1L pulldown. Quantitative analysis for the Jade1L (B) & Jade1S (C) interactome. *Jade1* KO1 mIMCD3 cells were transiently transfected with either Flag-tagged Jade1L, Jade1S, or a control plasmid. Pulldown was performed with anti-FLAG (M2) agarose beads. Proteins on the right side, above the  $p=0.05$  line, are determined significantly enriched. Proteasomal components are highlighted in magenta, known JADE1/Jade1 interactors based on known interactors annotated in BioGrid (Oughtred et al., 2021) in green. See also MS ID#: BIORXIV/2021/462752.

#### 6.1.10 Generation of *in vivo* models for the Jade protein family

Already in 2003 a gene-trap mouse model for *Jade1* was published, which did not show any obvious phenotype (Tzouanacou et al., 2003). Furthermore, there is a study that show that Jade1 is regulated during repair of damage in the tubule epithelium (Havasi et al., 2013). However, there is only very limited data from genetic mouse models available for *Jade1* and none for *Jade2* and *Jade3*. Since the *in vivo* function of the Jade protein family remains unknown, the development of mutant mouse models is crucial.

##### 6.1.10.1 *Jade1* knockout mouse models

Since there are many open questions about the role of *Jade1* that can only be answered in a more complex *in vivo* model, we decided to generate genetically modified mouse models for all members of the *Jade* family using CRISPR/Cas9-mediated genome engineering. We first generated two independent models for *Jade1*. The *Jade1\_emKO1* (*Jade1* endonuclease mediated knockout 1) model was generated by targeting a sgRNA to the first coding exon, cutting two bp after the start codon (Figure 25A). The offspring (F0) was then screen for so-called 'indel' mutations. This resulted in 23 pups with 5 pups showing the intended mutation at the targeted locus. The *Jade1\_emKO1* allele has a 1 bp insertion right after the start codon leading to a frameshift and a premature stop codon after 10 amino acids (Figure 25B). In a second approach, we targeted exon 6 by designing sgRNAs that cut before and after the exon (Figure 25A). Exon 6 includes the start of the first PHD domain. We screened 24 pups for complete deletion of exon 6, of these 4 had the desired deletion. The *Jade1\_emKO2* allele has a 267 bp deletion including exon 6 and resulting in a frameshift and a stop codon in exon 7 (Figure 25C).

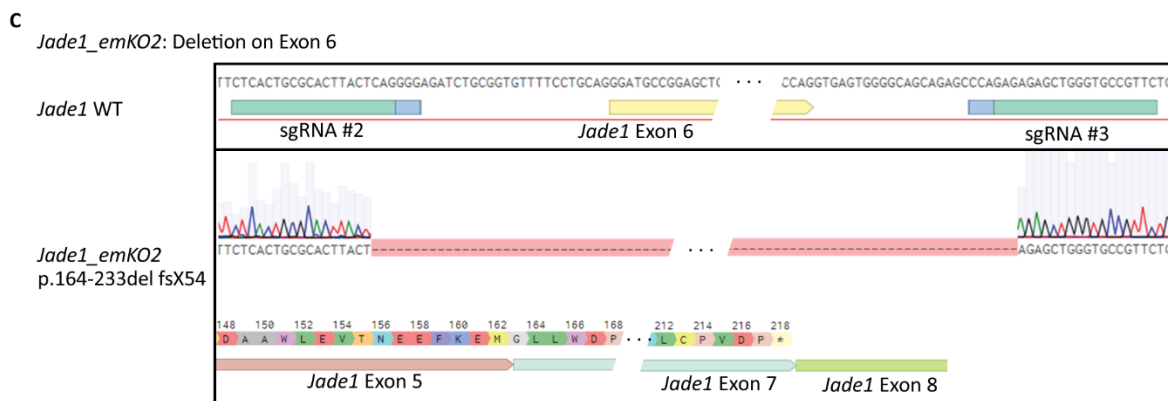
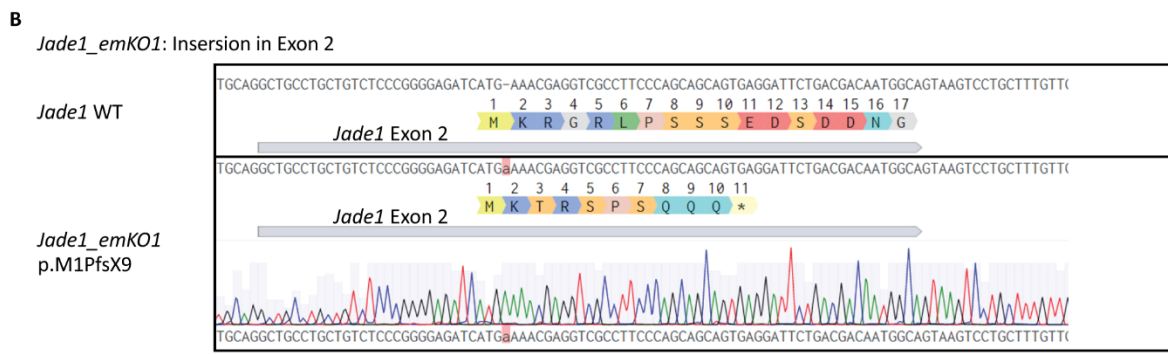
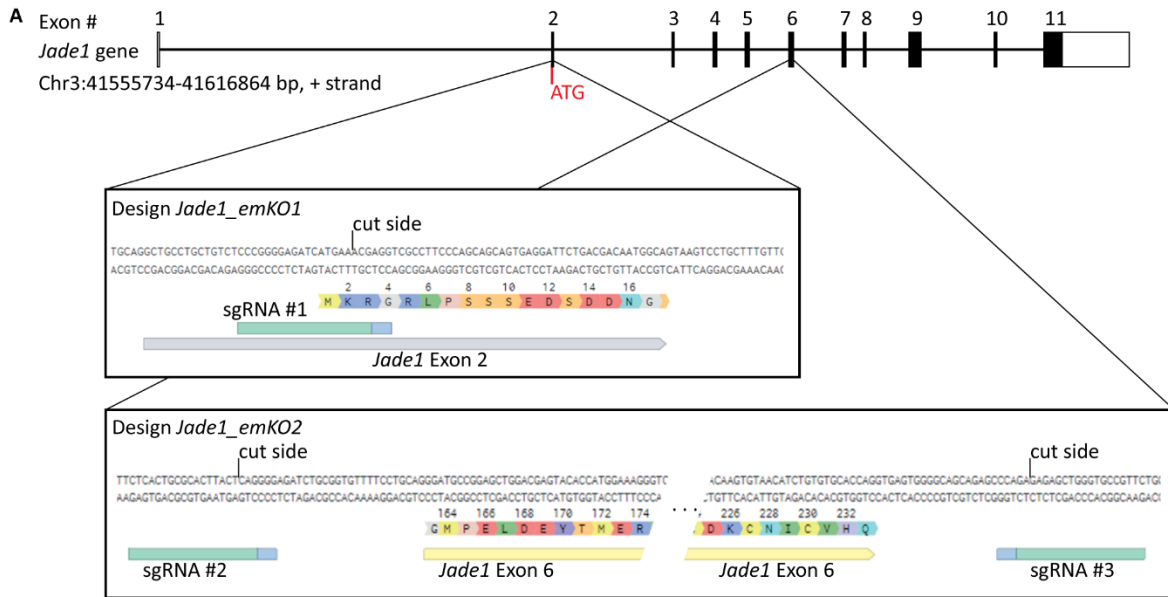


**Figure 25. Generation of *Jade1*-deficient mouse models.**

**(A)** Targeting strategy for *Jade1\_emKO1* and *Jade1\_emKO2* mouse models. On the top the exon (boxes)-intron (lines) structure of *Jade1* is indicated. For *Jade1\_emKO1* one sgRNA targeting the first coding exon was designed. For *Jade1\_emKO2* two sgRNAs targeting up- and downstream of exon 6 were designed. **(B)** Sanger Sequencing of genomic DNA from a *Jade1<sup>emKO1/emKO1</sup>* mouse shows insertion of one adenine right after the start codon leading to a frameshift resulting in a stop codon after 10 amino acids. **(C)** Sanger sequencing of genomic DNA of the *Jade1<sup>emKO2/emKO2</sup>* allele. A 267 bp deletion results in the complete removal of exon 6 followed by a frameshift and a premature stop codon in exon 7.

After backcrossing and sequencing of the F1 generation to account for potential mosaicism, we established allele specific genotypings (Figure 26A,B). To remove potential off target mutations we waited until the F2 generation before mating animals for first experimental mice. The litters from experimental matings ( $Jade1^{wt/emKO1(2)} \times Jade1^{wt/emKO1(2)}$ ) had slightly more males than females (Figure 26C). The average litter size was comparable for both alleles lying between four and five animals/litter (Figure 26D). Genotyping revealed that we did not get a Mendelian distribution of genotypes. We would expect to see around 25% of  $Jade1^{emKO1/emKO1}$  animals, however, we only see around half of that number (Figure 26E). For the  $Jade1\_emKO2$  allele, this effect is only seen for females, but here the number of animals analyzed is still rather low (Figure 26F). The  $Jade1^{emKO1/emKO1}$  and  $Jade1^{emKO2/emKO2}$  were both born viable. Survival and weight data is only available for the first allele so far. Here, we see that the median survival for  $Jade1^{emKO1/emKO1}$  mice is lightly increased compared to wild-type littermates (Figure 26G). Analyzing the weight over two years revealed that the  $Jade1^{emKO1/emKO1}$  mice weigh less than their wild-type and heterozygous litter mates (Figure 26H).

**Figure 26. *Jade1*-deficient mice are not born in Mendelian ratios and have a reduced body weight compared to litter mate controls. (Next page)**

**(A)** PCR products using specific primers to detect the insertion in  $Jade1\_emKO1$  mutant mice. Primer locations are indicated at the top. **(B)** PCR products using specific deletion primers for  $Jade1\_emKO2$ . Primer locations are indicated at the top. **(C)** Sex ratio in litters born from experimental matings ( $Jade1^{wt/emKO1(2)} \times Jade1^{wt/emKO1(2)}$ ) shows that slightly more male than female mice are born for both  $Jade1$  mutant mouse strains. **(D)** Average litter size for experimental ( $Jade1^{wt/emKO1(2)} \times Jade1^{wt/emKO1(2)}$ ) matings was determined. Each dot represents a litter. The lines represent means  $\pm$  SEM. **(E, F)** Genotype distribution in litters born from experimental matings ( $Jade1^{wt/emKO1(2)} \times Jade1^{wt/emKO1(2)}$ ). 180 animals in for  $Jade1\_emKO1$  and 34 for  $Jade1\_emKO2$  have been analyzed. Mendelian ratios are indicated with dotted lines (50 % for wt/emKO and 25 % for wt/wt and emKO/emKO). For both mutant strains, less homozygous mutant mice are born than predicted. **(G)** Survival curve of mice with the indicated genotypes. N represents the number of animals for each genotype. **(H)** Weight curve comparing male  $Jade1^{emKO1/emKO1}$  and their littermate controls. Homozygous knockout mice show a reduced weight (52 weeks,  $P < 0.05$ ), whereas there is no difference between wild-type and heterozygous mice. Statistical analysis was done by Student's-t test compared to wild-type animals.

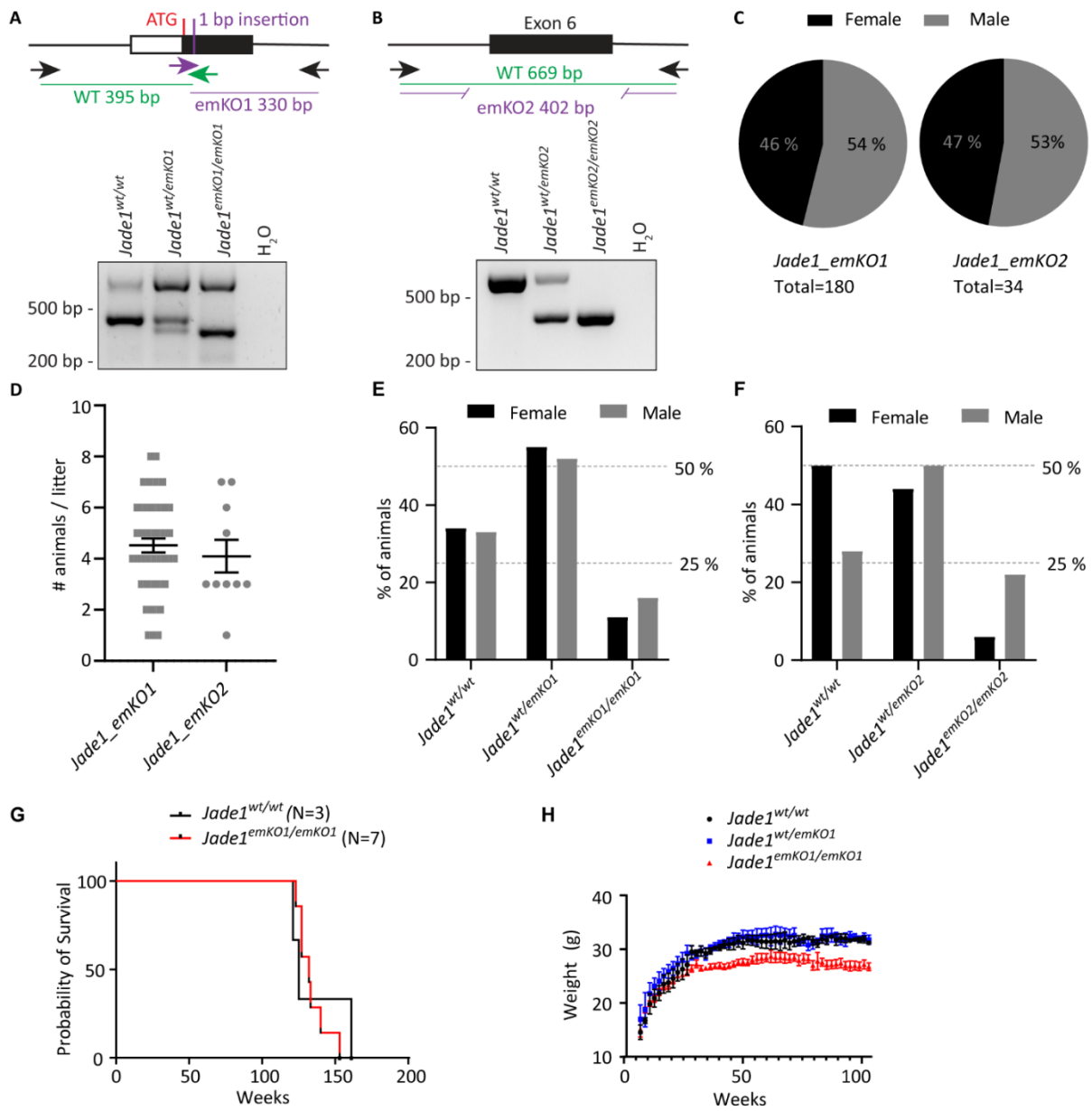
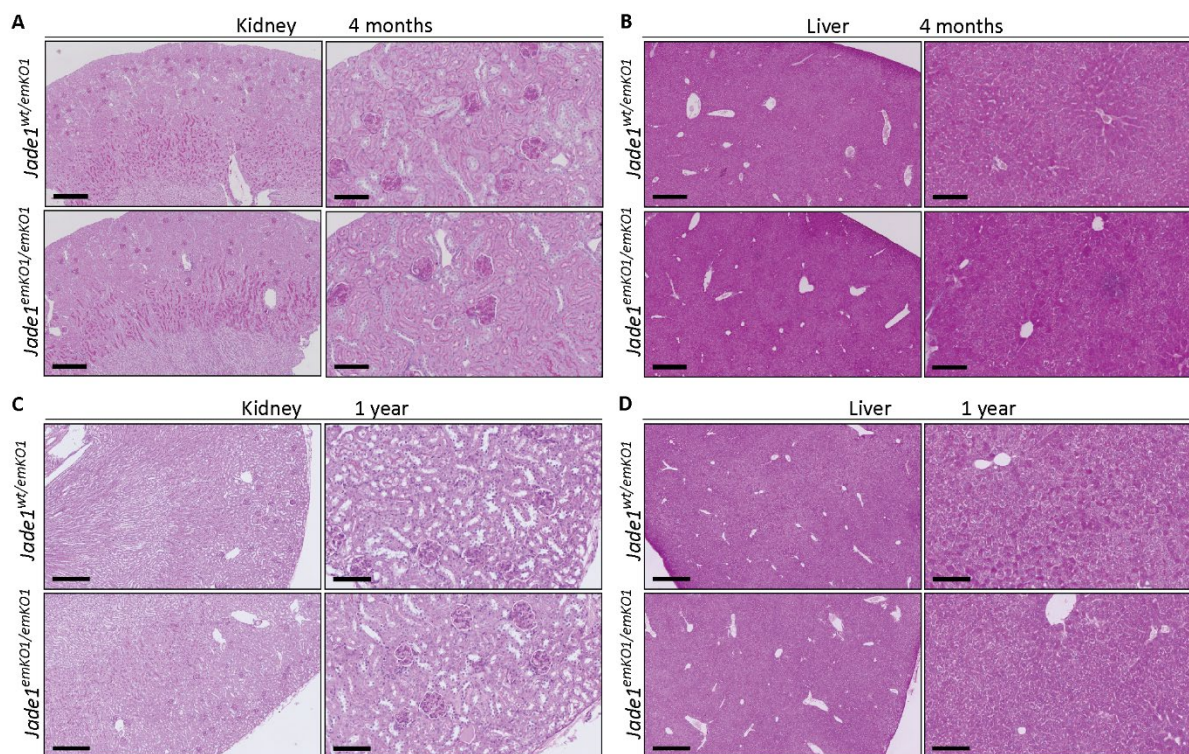


Figure legend on previous page

We performed Periodic acid–Schiff (PAS) stainings to evaluate morphological differences between organs for knockout and wild-type animals. At four months and one year of age, we could not observe any obvious deformities or difference in the kidneys (Figure 27A,C) or livers (Figure 27B,D) of *Jade1<sup>emKO1/emKO1</sup>* animals compared to littermate controls.



**Figure 27. *Jade1<sup>emKO1/emKO1</sup>* mice show no obvious histological phenotype.**

Histopathological analysis from *Jade1<sub>emKO1</sub>* knockout mice at the indicated ages. Images showing PAS staining from mice of indicated genotypes from (A,C) kidney and (B,D) liver. Scale bar = 400  $\mu$ m left side, scale bar = 100  $\mu$ m right side. N=3 for 4 month, N=2 for 1 year.

#### 6.1.10.2 *Jade2* and *Jade3* knockout mouse models

Besides the two mouse models generated for *Jade1*, we also generated mouse models for *Jade2* and *Jade3*. For these mouse models, we followed the same strategy as used for the *Jade1<sub>emKO2</sub>* mouse model. We designed sgRNAs up- and downstream of the exon which contains the start of the first PHD domain, which is exon 6 and exon 8 for *Jade2* and *Jade3*, respectively (Figure 28A,B). The offspring were screened for deletion of the complete exon. For *Jade2* we got 27 pups found of which 16 had a large deletion of the complete exon, four had smaller deletion around one or both of the cutting sites, and seven were wild-type. For *Jade3* we had 24 pups of which three had the desired mutation, the rest was not further analyzed since they showed only one band comparable with the WT band during the initial PCR screen. Using Sanger sequencing we confirmed complete deletion of the targeted exon followed by a frameshift leading to a premature stop codon (Figure 28C,D).



To evaluate morphological changes in kidney and liver tissue between wild-type animals and *Jade2*- or *Jade3*-deficient animals we performed PAS. For *Jade2* analyzed tissue from four months old animals and saw no difference between the genotypes (Figure 29C,D). For *Jade3* six-month-old animals were analyzed. Similarly to the *Jade1*- and *Jade2*-deficient animals, we again do not observe an obvious phenotype (Figure 29E,F). Lifespan and longitudinal weight analyses are currently being performed.

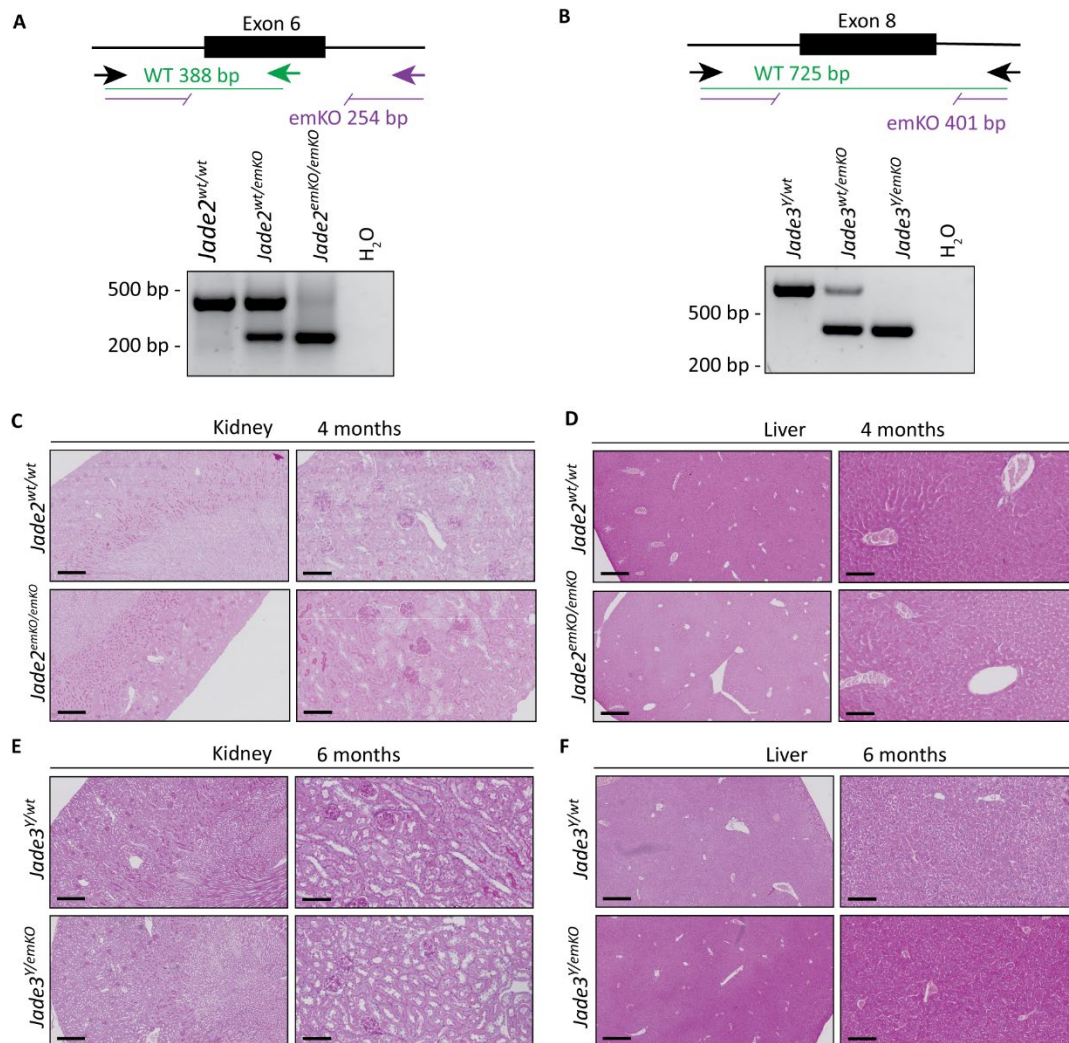


**Figure 29. *Jade2* and *Jade3* mutant mice do not show a histological kidney or liver phenotype at 4 or 6 months of age, respectively.**

(A, B) PCR products using specific deletion primers for *Jade2* and *Jade3* locus. Primer locations are indicated at the top. (C-F) Histopathological analysis from *Jade2* and *Jade3* knockout mice at age 4 months and 6 months respectively. Images showing PAS staining from mice of indicated genotypes from (C, E) kidney and (D, F) liver. Scale bar = 400 μm left side, scale bar = 100 μm right side. N=3.

## 6.2 Generation of knockout models to study NPH

As discussed in section 3.1.3, there is an increasing need for suitable *in vivo* models for NPH. Within this work we target two different genes, *Glis2* and *Tmem218*, which showed promising results in previously published studies (Attanasio et al., 2007; Kim et al., 2008; Vogel et al., 2015). Unfortunately, both mouse models were not available to us.

### 6.2.1 *Glis2* mutant mouse models

For our first novel *Glis2* mutant mouse model (*Glis2\_emKO1*), we selected a sgRNA targeting the area downstream of the start codon within the first coding exon (Figure 30A). The offspring was then screened for *indel* mutations. This resulted in five out of 19 pups with the intended mutation in the targeted locus. We selected one founder animal with a 14 bp deletion leading to a frameshift on the amino acid level resulting in premature stop codon at position 41 (Figure 30B). In a second targeting strategy (*Glis2\_emKO2*), we decided to focus on the area which encodes the zinc-finger domains, which was the locus of a recently published patient mutation. The homozygous point mutation (c.523T>C, p.C175R) was proposed to interfere with the exon splicing (Halbritter et al., 2013). This would result in skipping of exon 5 that encodes for part of the zinc-finger motifs followed by a frameshift in exon 6 resulting in a premature stop codon. Rather than introducing the patient mutation directly, we opted for the introduction of a single point mutation in exon 4, changing amino acid 122 from a tyrosine to a stop codon. This mutation is just upstream of the region encoding for the zinc-finger motifs. For this, we used an asymmetrically designed single-stranded donor oligonucleotide (ssODN) as a repair template (Figure 30A) (Richardson et al., 2016). Out of 15 born pups, three carried the point mutation (Figure 30C).

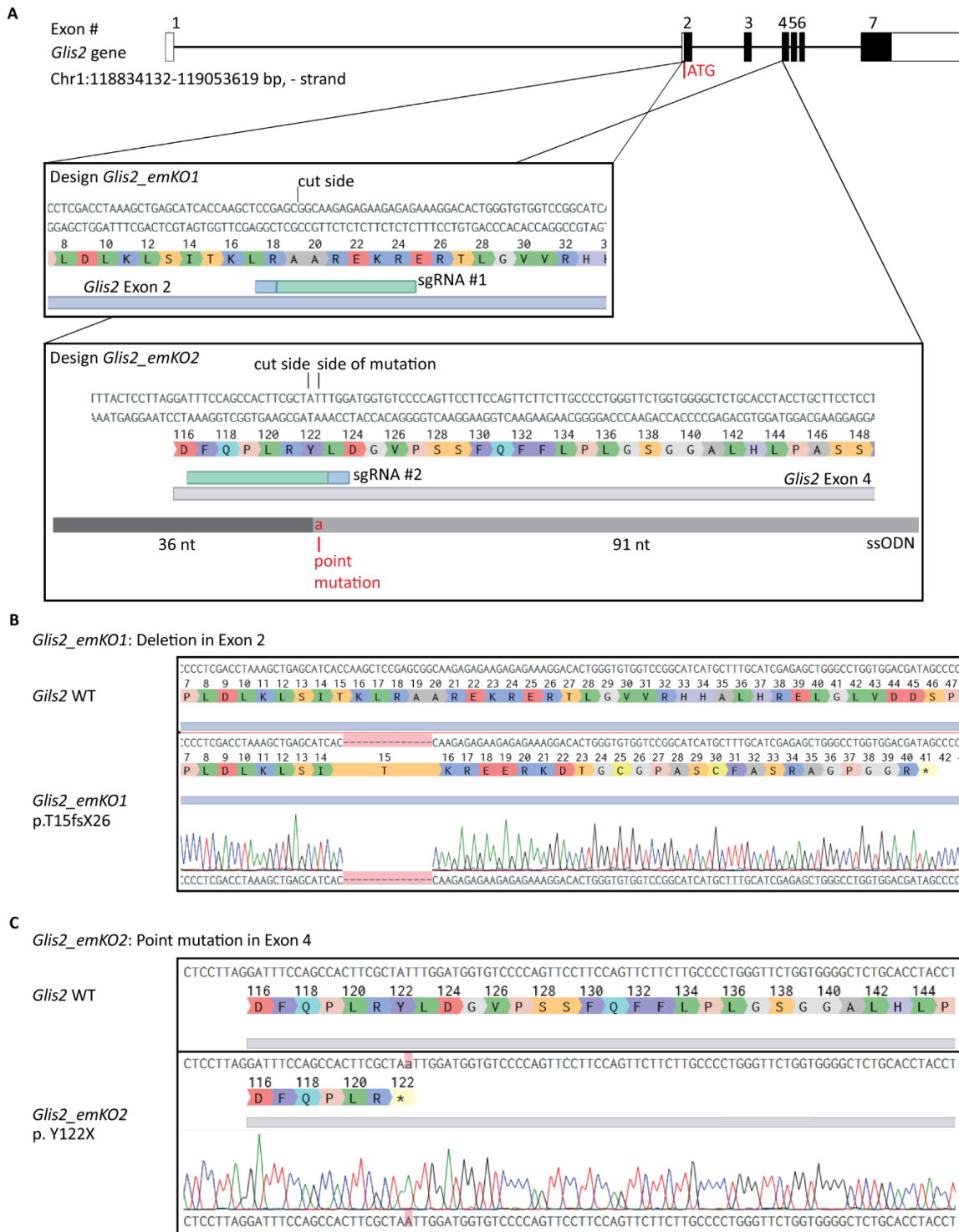


**Figure 30. Generation of *Glis2* mutant mouse models.**

(A) Strategy to generate the *Glis2\_emKO1* and *Glis2\_emKO2* mouse models. On the top the exon (boxes)-intron (lines) structure of *Glis2* is indicated. The *Glis2\_emKO1* strain was generated using a single sgRNA introducing a double-strand break at the region encoding for the amino acid residue 19, followed by screening of the founder generation for *indel* mutations. The *Glis2\_emKO2* strain was generated using one sgRNAs targeting the beginning of exon 4 combined with a ssODN introducing a point mutation which leads to a stop codon. (B) Sanger Sequencing of genomic DNA from a *Glis2<sup>emKO1/emKO1</sup>* mouse shows a deletion of 14 base pairs at the targeted site leading to a frameshift resulting in a stop codon after 26 amino acids. (C) Sanger sequencing of genomic DNA from a *Glis2<sup>emKO2/emKO2</sup>* mouse confirms introduction of the point mutation.

The founder animals were backcrossed to a pure C57BL/N background for at least two generation before we started to generate experimental animal for phenotyping. We do observe a slightly smaller litter size for the *Glis2\_emKO2* model (Figure 31A). The sex ratio of the mice born is almost equal, with slightly more males born in both models (Figure 31B). While the first model shows a normal Mendelian birth ratio of genotypes, we do see a reduced number of homozygous mutant animals in the *Glis2\_emKO2* model (Figure 31C,D). Histological staining at over 2 years of age show a phenotype for the *Glis2<sup>emKO1/emKO1</sup>* mice with some cysts and fibrosis (Figure 32A). The *Glis2<sup>emKO2/emKO2</sup>* mice show a severe phenotype at 1.5 years of age with cysts, fibrosis, and immune infiltration (Figure 32B). The exact time course of the disease onset and progression are currently under investigation.

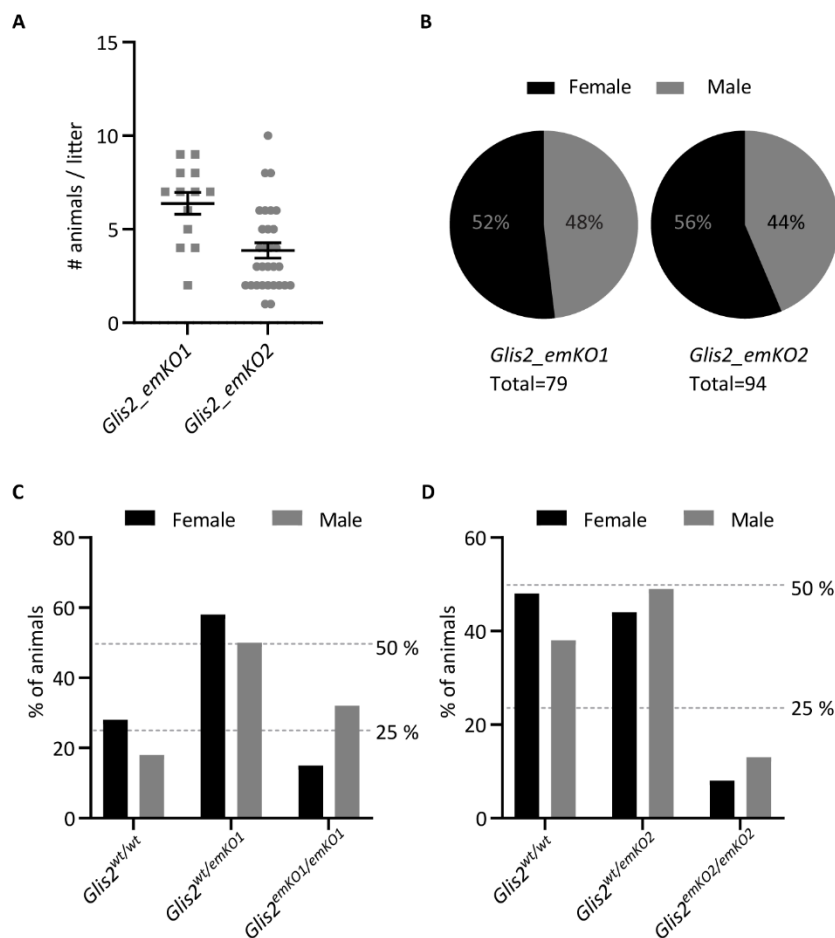


**Figure 31. *Glis2\_emKO2* mice show a reduced litter size and show a non-Mendelian pattern of inheritance.**

**(A)** Average litter size for experimental (*Glis2<sup>wt/emKO1(2)</sup>* × *Glis2<sup>wt/emKO1(2)</sup>*) matings was determined. Each dot presents a litter. The lines represent means ± SEM. **(B)** Sex ratio in litters born from experimental matings (*Glis2<sup>wt/emKO1(2)</sup>* × *Glis2<sup>wt/emKO1(2)</sup>*) shows that slightly more female than male mice are born for both *Glis2* mutant mouse strains. **(C,D)** Genotype distribution in litters born from experimental matings (*Glis2<sup>wt/emKO1(2)</sup>* × *Glis2<sup>wt/emKO1(2)</sup>*). 79 mice were analyzed for *Glis2\_emKO1* and 94 mice for *Glis2\_emKO2*. Expected mendelian ratios are indicated with dotted lines (50 % for wt/emKO and 25 % for wt/wt and emKO/emKO). For both, *Glis2\_emKO1* and *Glis2\_emKO2* line, less homozygous mutant mice are born than expected.

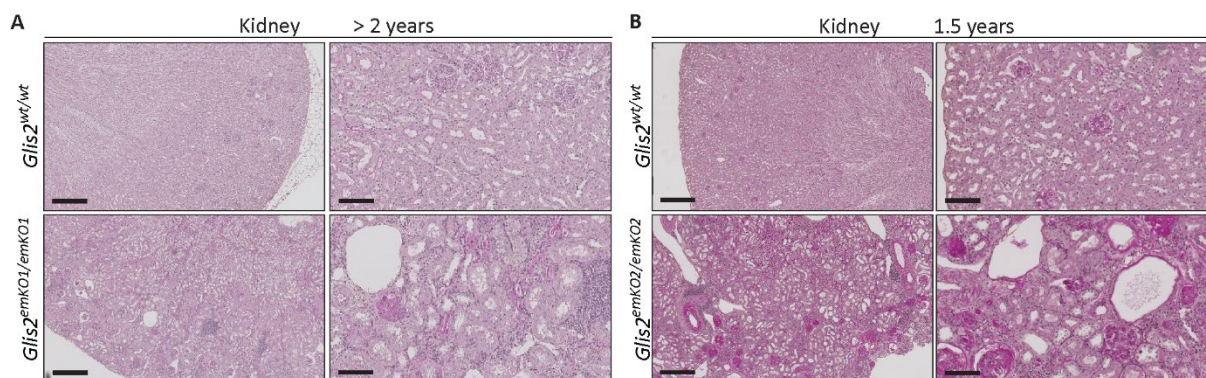


**Figure 32. *Glis2*<sup>emKO2/emKO2</sup> mice present with kidney cysts and fibrosis at 1.5 years of age.**

**(A)** Histopathological analysis from *Glis2\_emKO1* mice over 2 years old. **(B)** Histopathological analysis from *Glis2\_emKO2* mice at 1.5 years of age. Images show PAS stainings from mice of indicated genotypes from kidney. Scale bar = 400  $\mu$ m left side, scale bar = 100  $\mu$ m right side. N=2.

### 6.2.2 *Tmem218* mutant mouse models

In 2015, Vogel et al. published a *Tmem218*<sup>-/-</sup> mouse model that presented with a phenotype closely reminiscent of NPH and retinal degradation in human patients (Vogel et al., 2015). Moreover, a year later the group of Leroux identified *Tmem218* as a novel component of the MKS module in *C.elegans* (Valente et al., 2010). Both, the MKS as well as the NPH complex, are located at the ciliary TZ and are crucial for ciliogenesis and cilia function (Valente et al., 2010). Around the same time, we learned from a patient mutation in *Tmem218* (personal communication) (Figure 33A). *Tmem218* is a small transmembrane protein that has been shown to localize at the TZ of cilia as part of the MKS module in *C.elegans* (Li et al., 2016). Taken together, this put *Tmem218* in a prime position to generate a ciliopathy mouse model carrying a patient mutation. The sequence identity between human and mouse *TMEM218* is 80.87% and the locus of the point mutation is well conserved (Figure 33B,C)(Howe et al., 2021). We chose a single point mutation, where the first nucleotide of exon 4 was mutated from G> T leading to a serine instead of an arginine (Figure 33A). To introduce the point mutation in the mouse genome we selected a sgRNA cutting just downstream of the desired locus and designed an asymmetric ssODN (Figure 33D) (Richardson et al., 2016). Analyzing the founder generation revealed three pups out of 13, which carried the point mutation (*Tmem218.R37S*) (Figure 33E). Besides a founder carrying the patient derived mutation, we also selected a null allele with a deletion of 10 base pairs (*Tmem218\_emKO*) (Figure 33F), which likely disrupts the splicing and thus, in a protein lacking exon 3 and a frameshift in exon 4 leading to a premature stop codon.

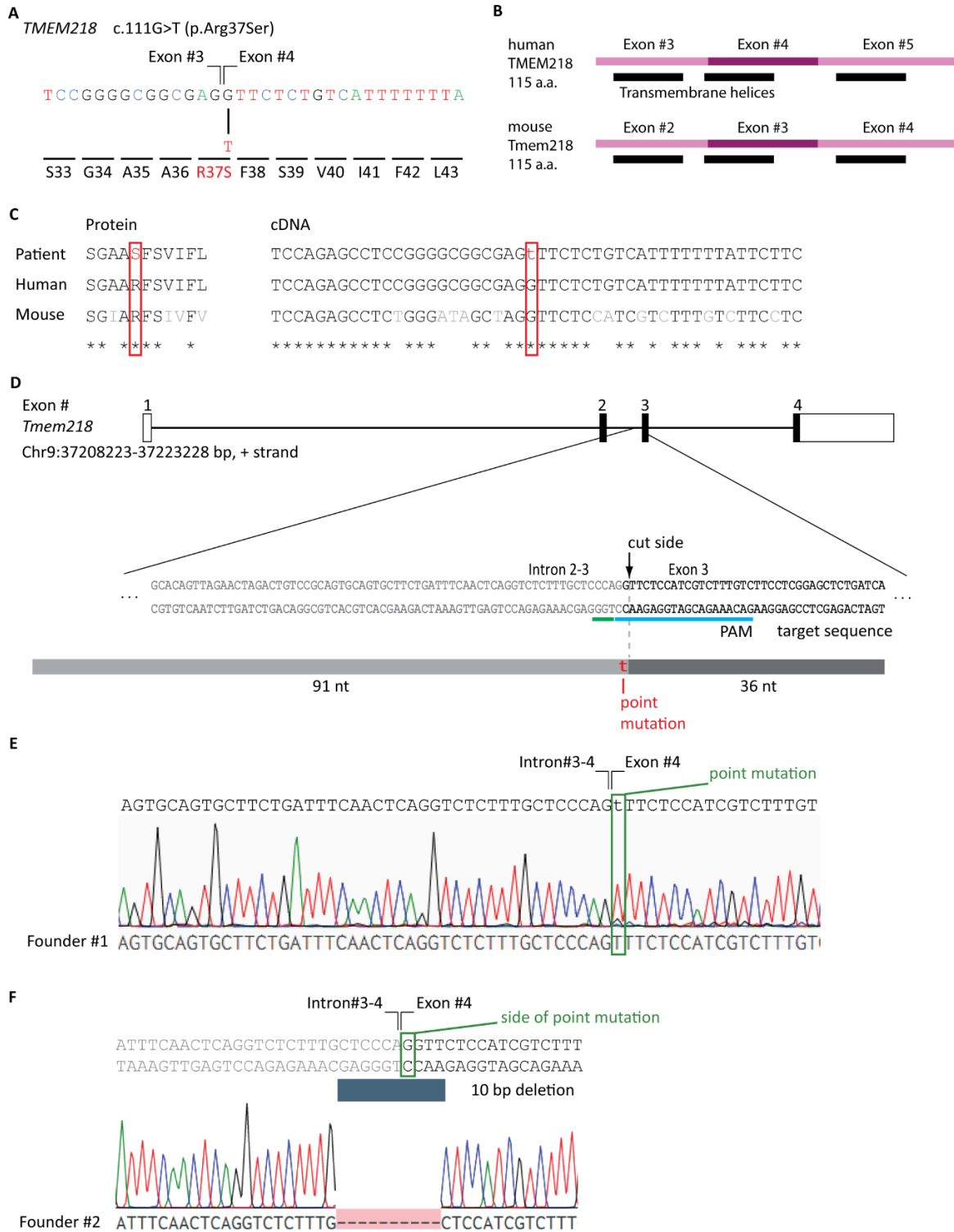


**Figure 33. Generation of *Tmem218* mutant mouse models.**

(A) Location of the patient derived point mutation. (B) Human *TMEM218* and murine *Tmem218* show a very similar protein structure. (C) Locus of the point mutation is conserved on proteins and cDNA level between human and mouse. (D) Strategy to generate *Tmem218.R37S* mutant mice. A sgRNA targeting the side of the mutation was selected. The ssODN carrying the point mutation has an asymmetric design with homology arms of 91 and 36 nt. (E) Sanger sequencing of genomic DNA of a founder animal carrying the point mutation. (F) Sanger sequencing of genomic DNA of a founder animal showing a 10 bp deletion including part of the intron and the start of the exon 4 likely which likely infers with splicing.

The published *Tmem218*<sup>-/-</sup> mouse model showed a clear kidney phenotype with 14 weeks of age (Vogel et al., 2015). We performed PAS on kidney and liver at 6 months of age in the *Tmem218.R37S* mouse model. To our surprise, we could not observe any obvious morphological difference between *Tmem218*<sup>wt/wt</sup> and *Tmem218*<sup>R37S/R37S</sup> mice in the kidney and liver (Figure 34A,B). Interestingly, the *Tmem218*<sup>emKO/emKO</sup> mice did present with kidney cysts in the cortex at 18 weeks of age (Figure 34C). Immunofluorescence staining revealed that the cyst lining tissue stained positive for E-cadherin, a distal tubule marker (Figure 34D). We did not observe loss of ciliation as visualized by staining for Arl13B, a ciliary maker. An in-depth analysis on ciliation and ciliary structure is currently on going. Taken together, our *Tmem218\_emKO* mouse models presents with a key feature of human NPH and will be a valuable model to study the underlying disease mechanisms as well as to test putative therapeutic strategies.

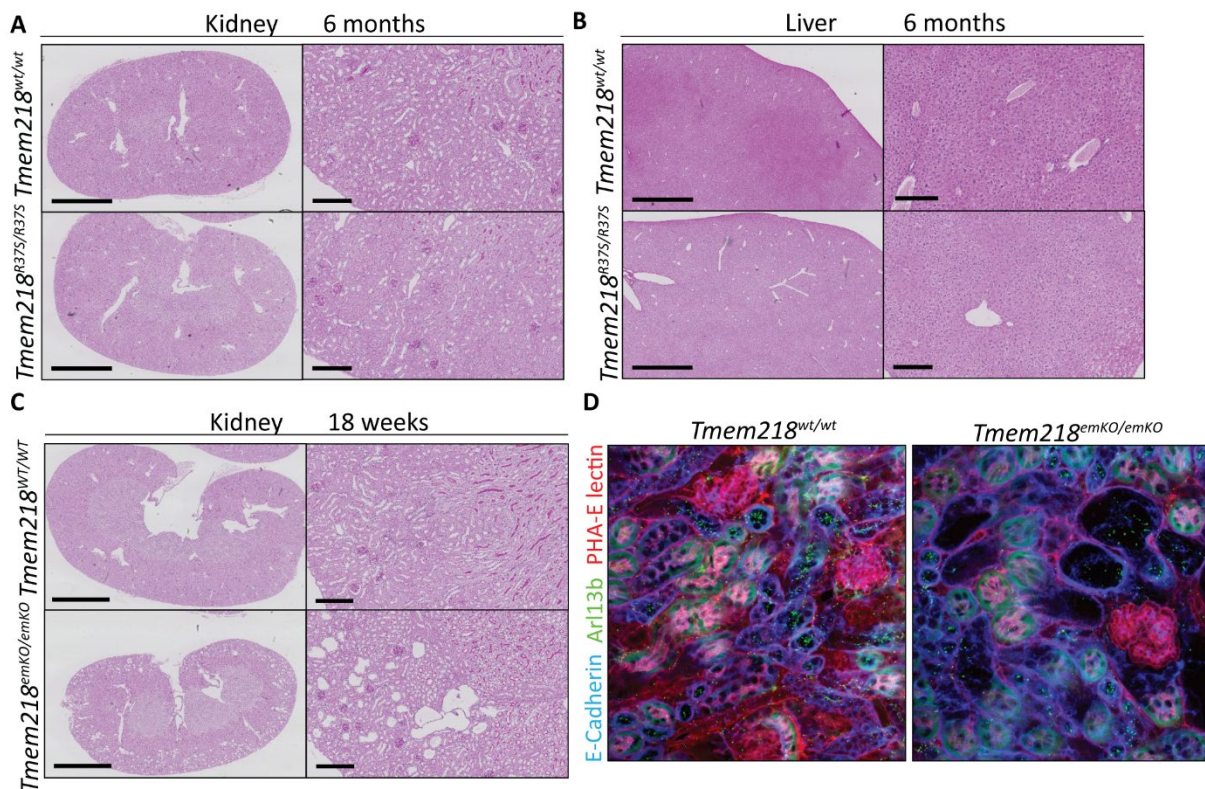


**Figure 34. *Tmem218*<sup>emKO/emKO</sup> mice show cysts arising from the distal tubule.**

(A-C) Histopathological analysis from *Tmem218.R37S* and *Tmem218\_emKO* mice at the indicated time points. Images showing PAS staining from mice of indicated genotypes from (A, C) kidney and (B) liver. Scale bar =2 mm left side, scale bar = 200  $\mu$ m right side. N=3. (D) Immunofluorescence staining of kidney tissue from *Tmem218\_emKO* mice of the indicated genotypes using antibodies against E-cadherin (distal tubule marker), Arl13b (cilia marker), and PHA-E lectin (proximal tubule marker). (N=3).

## 7 Discussion

### 7.1 Jade protein family members share protein interactors related to renal pathology

JADE1 has been first identified as an interactor of pVHL (Zhou et al., 2002). Later, interaction with several NPHPs have been found (Borgal et al., 2012). Up until now, JADE protein research has been primarily focused on JADE1. Here, we could now show that JADE2 and JADE3 also interact with pVHL as well as with NPHP1 and NPHP4 giving us an indication that they might all play a role in renal pathology (Figure 5). Moreover, JADE proteins co-immunoprecipitate with themselves suggesting that they function as homodimers or homomultimers (Figure 6). Based on the structural similarity we hypothesized that they might form heterodimers as well, which we could confirm (Figure 6). This raises the question if a multimeric JADE protein complex exists and whether the function of such a complex depends on the composition.

One of the most studied aspects of JADE1 in the past was the function within the HBO1 HAT complex (Foy et al., 2008; Han et al., 2018; Siriwardana et al., 2014). JADE1 has been shown to form a complex together with HBO1, ING4/5, and EAF6 and proved necessary for histone acetylation (Doyon et al., 2006). ING4/5 are tumor suppressors that have been shown to affect cell proliferation and cell cycle progression (Campos et al., 2004). Interestingly, both ING proteins contain at least one NLS as well as PHD domains (Ormaza et al., 2017, 2019). For ING4 and ING5 it has been published that they form homodimers (Ormaza et al., 2019). Heterodimer formation between them has been observed and suggested as a means to increase their functional diversity (Ormaza et al., 2019). Whether ING4/5 and JADE1/2/3 share hetero-multimeric protein complexes, requires further investigations and was not in the focus of the at hand thesis.

### 7.2 The effect of loss of Jade proteins on cell cycle progression

Most knowledge on the function of the JADE protein family members has been gained by discovering their interactors (Borgal et al., 2012; Foy et al., 2012; Panchenko et al., 2004; Zhou et al., 2002). So far, there has not been a study on the individual and shared functions within the same cellular context. Here, we generated *Jade*-deficient cell lines to perform an unbiased comparison on proteomic and transcriptomic changes upon loss of either *Jade* family member. Since the known links to renal ciliopathy genes for JADE1 could be confirmed for JADE2 and JADE3 by the interaction with NPH proteins NPHP1 and NPHP4, we utilized a well-characterized renal tubular epithelial cell line for further studies. Moreover, previous published datasets showed that all Jade proteins are expressed in renal epithelial cells of the collecting duct (Figure 4). To ensure a more homogenous parental cell line we used a mIMCD3 subclone, which is ciliated and shows expression of inner medulla and collecting duct

makers (Figure 9). With CRISPR/Cas9-mediated genome engineering, we generated two independent *Jade*-deficient cell lines for each family member, ensuring that our findings would not be the effect of off-target mutations (Figure 10). For each cell line generation we used one sgRNA targeting the location of the PHD motifs and screened the monoclonal cell lines for indel mutations. We did an extensive validation of the *Jade*-deficiency with Sanger sequencing, qPCR analyses, and, in addition, a targeted proteomic assay to ensure that the mutations and the loss of expression were verified on mRNA level and on the protein level (Figure 12). Importantly, Smits et al. showed in a screen of 193 cell lines with deletions introduced with CRISPR/Cas9-mediated genome engineering that about a third of them showed residual protein expression (Smits et al., 2019). Therefore, DNA and mRNA analysis are not sufficient to validate knockout models that are based on frameshifting mutations. In our *Jade*-deficient models, however, we did not find any evidence for residual protein expression. Interestingly, mRNA and protein expression of the remaining family members in the *Jade*-deficient cell lines did not point towards a compensatory mechanism in renal epithelial cells. However, compensation in other cell types, during development, or by other means of compensation, like posttranscriptional or posttranslational modifications, cannot be excluded.

Several studies have shown a relation between JADE1 proteins and cell cycle progression (Borgal et al., 2016; Calvi, 2014; Havasi et al., 2013; Siriwardana et al., 2014). We did not observe an obvious effect of the loss of any of the Jade proteins on cell proliferation under baseline conditions in mIMCD3 cells (Figure 13). However, introducing cellular stress through partially starving the cells by reducing the serum concentration revealed that *Jade1*-deficient cells could at least partially escape cell cycle arrest compared to wild-type cells (Figure 14). Low levels of JADE1 have been reported for several cancer cell lines and JADE1 overexpression has been associated with a growth disadvantage. The studies showing a growth disadvantage for cells overexpressing JADE1 were carried out in 786-O, a human VHL-deficient kidney carcinoma cell line, and in HeLa cells, originally derived from cervical cancer. This goes along with our findings that Jade1 loss is not enough under baseline conditions to disrupt cell cycle progression and that an additional stimulus is needed. Our group has previously shown a delay in cell cycle progression for cells expressing a mutant variant of JADE1S lacking the N-terminal CK1 $\alpha$  phosphorylation motif with an accumulation of mutant cells in the S-phase (Borgal et al., 2016). We suggested that the impaired S-phase progression could be caused by dominant-negative effect of the JADE1S mutant with an increased affinity to its interactors important for chromatin remodeling. Interestingly, in our Jade-deficient cell model the checkpoint between S and G2/M phase seems to be affected by loss of Jade1. During the S phase centrosomes undergo duplication. Jade1 might have an effect on the DNA synthesis either by direct interactions, on a transcriptional level or a combination of both. In the *Jade1*-deficient cells underlying our dataset we deleted both the long and short isoform of Jade1 which likely contributes to different functions during cell cycle progression, since only JADE1S

was found to be localized at the centrosomes of dividing cells (Borgal et al., 2014; Siriwardana et al., 2015). Our data supports a diverse role for JADE1 during cell cycle progression likely with different functions at different time points during cell cycle progression. Since cell cycle regulation is an important aspect in PKD, VHL disease, and RCC, unraveling the exact mechanism on how Jade proteins influence the cell cycle regulation is crucial and needs further investigation.

### 7.3 Jade proteins as negative regulator of the proteasome

JADE proteins have been shown to be involved in a broad range of pathways, including Wnt signaling, histone acetylation, and in cell cycle progression (Borgal et al., 2012, 2016; Chitalia et al., 2008; Foy et al., 2008). In addition, they seem to play a role in various diseases like PKD, VHL disease and several cancers (Borgal et al., 2012; Calvi, 2014; Jian et al., 2018, 2018; Xiao-Fen et al., 2016; Zhou et al., 2004). However, the underlying mechanism on how the JADE protein family affects all these different processes and functions is not yet understood in detail. Here, we performed unbiased proteomic expression profiling in cell lines lacking either member of the Jade protein family for the first time. Surprisingly, we found an increased abundance of a multitude of proteasomal components in all six mutant cell lines, including an upregulation of more than 80% of the 26S proteasome subunit components (Figure 18). Besides an increased abundance of the proteasome, we could also show that loss of Jade proteins leads to increased proteasomal activity. Consistently, high JADE levels through overexpression reduced the proteasome activity (Figure 20). The 26S proteasome is part of the ubiquitin-proteasome system (UPS), which is one of the main protein degradation systems in eukaryotes, being responsible for the degradation of over 80% of mainly short-lived, regulatory, or damaged cellular proteins (Meyer-Schwesinger, 2019; Navon and Ciechanover, 2009). The UPS is a key regulator in various cellular processes, from transcription and translation over protein quality control, to cell cycle regulation, cell survival, metabolism, and inflammation (Meyer-Schwesinger, 2019). In a multistep process involving ubiquitin-activating enzymes (E1), ubiquitin-conjugating enzymes (E2), and ubiquitin-ligating enzymes (E3), a chain of ubiquitin molecules is attached to the protein to target it for degradation (Navon and Ciechanover, 2009). E3 ligases are the most diverse with more than 500 different species in humans since they are selective for the proteins targeted for ubiquitylation (Voorhees and Orłowski, 2006). The polyubiquitinated proteins are recognized by the 26S proteasome and then degraded (Bard et al., 2018). The 26S proteasome has a complex architecture. The core complex (20S) is barrel-shaped and with the proteolytic active site inside (Bard et al., 2018). Since it is only accessible through narrow pores, large or folded proteins are excluded from degradation by the 26S proteasome (Bard et al., 2018). Moreover, the 19S regulatory subunit forms a gate and caps either one or both ends of the 20S subunit (Bard et al., 2018).

The proteasome abundance and assembly are tightly regulated in the cell since generation of proteasomes consumes a high amount of energy and dysregulation is linked to several diseases (Schmidt and Finley, 2014). Expression of the different subunits is regulated by the transcription factors *NRF1* and *NRF2* in mammals (Schmidt and Finley, 2014). *NRF2* increases proteasomal gene expression after stabilization upon redox stress (Kwak et al., 2003; Radhakrishnan et al., 2010). *NRF1* is also rapidly degraded by the proteasome under normal conditions (Schmidt and Finley, 2014). However, proteasome dysfunction leads to an active form though cleavage by the aspartyl protease protein *DDI1* *homologue 2* (*DDI2*) and increases proteasome gene expression after translocation to the nucleus (Koizumi et al., 2016; Lehrbach and Ruvkun, 2016; Radhakrishnan et al., 2010). One of the best-known regulators of proteasome assembly is mTor signaling (Schmidt and Finley, 2014; Zhao and Goldberg, 2016). Several additional regulators have been identified, including the transmembrane domain recognition complex (TRC) pathway, the known tumor suppressor *miR-101*, *heat shock protein 90* (*HSP90*), as well as post-translational modifications (Akahane et al., 2013; Imai et al., 2003; Kors et al., 2019; Zhang et al., 2015). However, since our RNA-seq analyses did not indicate upregulation of the proteasomal subunits on the transcription level, it is likely that Jade proteins through posttranslational modifications either play a role in negatively regulating the assembly of the proteasome or are involved in targeting the proteasome for degradation through a specific autophagic process referred to as proteophagy. Seeing that several proteasomal subunits co-precipitate with Jade1S and Jade1L a direct involvement of Jade proteins in the regulation is probable. The exact mechanism how and on which level Jade proteins regulate proteasome abundance and thus activity still needs further investigation. Interestingly, we did observe an upregulation of the protein turnover machinery on proteome level, including ribosomal components, tRNA-ligases, and transcription initiation and elongation factors (Figure 19). The balance between protein synthesis and protein degradation is essential for a healthy metabolism and dysregulation has been implicated in several diseases (Rosenwald et al., 1999; Tokheim et al., 2021; Vellai and Takács-Vellai, 2010). Further analyses of protein production and protein degradation rates in the *Jade*-deficient cell lines are necessary to comprehend the meaning of this result. Dynamic SILAC labeling is a well-established method to analyze protein turnover. Cells are incubated with medium containing isotopically labeled amino acids and then measured by liquid chromatography tandem mass spectrometry (Doherty et al., 2009). The rate of the incorporation of heavy amino acids can be correlated to the rate of protein synthesis, while the rate of decreasing light amino acids can be correlated to the rate of protein degradation (Ross et al., 2021).

#### 7.4 Therapeutic approaches to target the proteasome

Proteasome inhibitors have been successfully used to treat several cancers like myeloma, lymphoma, and amyloidosis. The proteasome inhibitors bortezomib, carfilzomib, and ixazomib have all received

regulatory approval and entered the clinic, adding to the treatment options for patients with haematological malignancies (Manasanch and Orłowski, 2017). However, acquired resistance as well as primary resistance in solid cancers are a challenge and need a more detailed understanding of the underlying mechanism (Manasanch and Orłowski, 2017). Even though bortezomib showed promising results *in vitro* by inducing apoptosis in kidney cancer cell lines (An et al., 2004), clinical trials do not support its use in RCC patients since only very few patients respond to the treatment (Davis et al., 2004; Kondagunta et al., 2004). Carfilzomib, a second-generation proteasome inhibitor, has not lead to promising results in treatment of RCC patients in clinical trials yet (Hasanov et al., 2019). However, even though the current proteasomal inhibitors are not suitable as a single therapeutic drug, it might prove useful in combination with other drugs to make cancers better targetable and/or overcome drug resistance (Voorhees and Orłowski, 2006). Additionally, Carfilzomib has also been used in a mouse model of autosomal-dominant polycystic liver disease (ADPLD) where it decreased proliferation and increased cell death in renal epithelial cells and by this reducing the cystic kidney phenotype (Fedele et al., 2011). Recently, about 8000 components were screened to identify their effect on PKD-deficient cells (Asawa et al., 2020). Interestingly, proteasome inhibitors have been identified among other candidates to reduce viability in these cells (Asawa et al., 2020). The increased proteasome activity caused by *Jade* dysregulation might be a mechanism targeted by proteasome inhibitors. Loss or low levels of *Jade* might make the cells more susceptible to proteasome inhibitors by leading to a more efficient induction of proteolytic stress ultimately resulting in apoptosis.

While the above-mentioned drugs inhibit the 26S core unit directly, there are more and more approaches either to target upstream components of the proteasome or to target degradation of specific proteins by the proteasome (Nalepa et al., 2006, 2006; Navon and Ciechanover, 2009; Solit et al., 2002).

In VHL disease as well as in RCC the ubiquitylation and protein degradation is impaired. Here, activators of the 26S protease would be of interest as a therapeutic strategy (Corn, 2007; Gorospe et al., 1999). However, so far there are no drugs available that activate the proteasome pathway in a non-specific way. Unraveling the mechanism of how the loss of *Jade* proteins leads to the general increase in proteasome abundance and activity might provide valuable insights and help in the identification and development of new drugs.

## 7.5 Loss of a single *Jade* protein family member does not lead to any obvious phenotype *in vivo*.

The 2003 published gene-trap mouse model for *Jade1* did not show any obvious morphological phenotype and only showed that lower than expected ratios of homozygous mutant animals were born (Tzouanacou et al., 2003). Based on the structural similarities between the *JADE* protein family

members this raised the question of a potential compensatory mechanism (Figure 2) (Panchenko, 2016). Here, we did not only generate two new *Jade1* mutant mouse models (Figure 25-31) but also novel mouse models for *Jade2* and *Jade3* (Figure 28 and 33). Similarly, to the published *Jade1* model we observe a lower than expected ratio of homozygous offspring in our *Jade1* mutant models. Moreover, the *Jade1<sup>emKO1/emO1</sup>* mice are significantly lighter than their heterozygous and wild-type littermates. We do not observe any major changes in life span; the homozygous animals might live slightly longer. A larger cohort will be required to study this particular effect. An increased lifespan would be in line with observations in *C.elegans* showing that the proteasome activity is increased in long-lived *glp-1* mutant worms (Vilchez et al., 2012). Moreover, this study could show that *Rpn6*, which is important for the interaction between S20 and S19 subunits, is a regulator of not only proteasomal activity, but also lifespan. Knocking down of *rpn6.1* in *C.elegans* lead to a downregulation of proteasomal activity and a decreased lifespan (Vilchez et al., 2012). *Rpn6* is thus regulating the proteasome in an opposing way compared to Jade protein family. Downregulation of the proteasome could be linked to several aging-related diseases, including neurodegenerative diseases like Alzheimer's and Parkinson's disease (Bosco et al., 2011; Li and Li, 2011; Schmidt and Finley, 2014). Identifying pathways that increase proteasome stability and function during aging will be important for a better understanding of these diseases and to identify druggable targets.

While further phenotyping of the Jade family mutant mouse lines is still ongoing, we did not observe any obvious morphological changes in the kidney for either. Even though we did not see any compensatory regulation of the Jade protein family member in our cell culture model this still needs to be investigated in the *in vivo* models. Here, we have the unique opportunity to study the effect of single, double, and triple *Jade* mutants *in vivo*. Therefore, we started crossing the *Jade1\_emKO2* model with the *Jade2\_emKO* and *Jade3\_emKO* models to investigate any additive effect of the lack of more than one Jade protein on the whole organism. The high conservation rate throughout vertebrate species does point towards an essential function of Jade protein family members and co-expression in various tissues is given as a requisite for functional compensation. This brings back the question raised in section 7.1 whether Jade proteins form heterogenic complexes and if some functions are dependent on the exact composition of such a complex. Moreover, the functional compensation might not happen under baseline conditions but certain stimuli or developmental stages.

Besides the effect of the loss of *Jade* family members *in vivo* under baseline conditions, we now can study how *Jade*-deficiency affects different renal pathologies. Havasi et al. analyzed the Hbo1-Jade1 complex during epithelial regeneration (Havasi et al., 2013) and could show that *Jade1* expression levels dropped after inducing acute kidney injury (AKI) and later recovered to pre-injury levels in relation to cell proliferation. *Jade1* was later again linked to proliferation and organ discovery by showing a shift from the localization in the nucleus to the cytoplasm after injury (Siriwardana et al.,

2015). Additionally, we identified *inhibitor of differentiation 4 (Id4)* as one of the target genes significantly downregulated in all *Jade*-deficient cell lines in our cell culture model. *Id4* has recently been linked to recovery after AKI via canonical BMP signaling by repressing pro-fibrotic signaling proteins and thus, preventing progression of AKI to chronic kidney disease (Vigolo et al., 2019). This brings our *Jade* family mouse models in a prime position to study AKI in a *Jade*-deficient background to gain a detailed understanding of the Jade proteins in organ damage and regeneration.

In our cell culture model, we furthermore found the Rap1 signaling pathway regulated in all mutant cell lines. The Rap1 signaling pathways plays an important role in cell adhesion (Bos, 2005), integrin function (Bos et al., 2003), and is deregulated together with downstream pathways like regulation of the actin cytoskeleton and focal adhesions. Focal adhesions as well as the cytoskeleton are known to be altered in CDK (Castelli et al., 2015; Zhang et al., 2020) as well as RCC (Béraud et al., 2015; Brenner et al., 2008). Along this line, we also observe the upregulation of components of the extra cellular matrix (ECM), like collagens and fibroblast growth factors (FGF). Abnormal ECM composition has previously been linked to cyst growth and fibrosis in PKD (Joly et al., 2006; Mangos et al., 2010; Raman et al., 2018). Taken together, this provides further evidence of the role of Jade proteins in PKD and RCC. Combining the *Jade*-deficient mouse lines with an RCC model (Harlander et al., 2017) or using them in a Renca RCC metastasis model (Danhier et al., 2014; Schokrpur et al., 2016) could help unravel how the Jade family is linked to RCC. The Renca RCC metastasis model utilizes a cell line isolated from a spontaneously arising tumor in BALB/c mice, which if implanted under the kidney capsule metastasizes (Murphy and Hrushesky, 1973). In a similar manner, combing the *Jade*-deficient mouse models with models for PKD would help to understand the relation between Jade family members and PKD. Moreover, the *Jade*-deficient mouse models could help us understand what the effect of a high proteasome activity on various renal pathologies is as well as how it effects potential treatment options.

## 7.6 Generation of new models to study renal ciliopathies *in vivo*

While most individual renal ciliopathies are rare, collectively they affect millions of people worldwide. With very limited specific treatment options, the majority of these patients will ultimately need renal replacement therapy (Stokman et al., 2021) . While *in vitro* experiments are providing important insights in the function of relevant disease causing genes on the cellular level as well as underlying molecular mechanisms, there are many research questions that can only be addressed *in vivo*. Investigating the complex nature of pathology, the role of disease-related proteins in the tissue context or effects of novel therapeutic strategies typically requires suitable animal models. The cystofibrotic degenerative renal phenotype of human NPH with only a rather small number of cysts primarily at the cortico-medullary border has been proven difficult to reproduce in mouse models in the past. The

majority of models either do not show any kidney phenotype or present with massively enlarged kidneys similar to ADPKD (Cook et al., 2009; Omran et al., 2001). Three promising mouse models from previous publications, *Glis2*<sup>-/-</sup> and *Tmem218*<sup>-/-</sup> were unfortunately no longer available (Attanasio et al., 2007; Kim et al., 2008; Vogel et al., 2015). Within this work we generated mouse models with different mutations in *Glis2* and *Tmem218* aiming for a kidney phenotype which resembles the human NPH phenotype.

#### 7.6.1 *Glis2*<sup>emKO/emKO</sup> mice show a late cystic kidney phenotype.

The Gli-similar family zinc finger 2 (GLIS2) was first described as neuronal Kruppel-like protein (NKL) promoting neuronal differentiation (Lamar et al., 2001). It was soon identified as part of the Kruppel-link zinc finger protein family, with five Cys2-His2 zinc finger motifs and a nuclear localization it closely resembles members of the Gli and Zic subfamilies (Zhang et al., 2002). Later, GLIS2 was identified as a cause of NPH when a genome-wide search for linkage in consanguineous kindred's revealed a family with a mutation in *GLIS2*, which was then annotated as *NPHP7* (Attanasio et al., 2007). Moreover, this study showed GLIS2 localization not only in the nucleus but also in primary cilia. Within this study, a *Glis2* mutant mouse lacking the exons coding for the first three zinc fingers (exon 3-5) developed renal cysts as well as fibrosis with increased rates of apoptosis. A second mouse model targeted exon 6, which encodes the last two zinc fingers (Kim et al., 2008). Like the first model, this *Glis2* mutant mouse model developed an NPH-like phenotype with tubular atrophy and fibrosis. Furthermore, an increased level of apoptosis and infiltration of immune cells could be observed.

These studies suggested *GLIS2* as a suitable candidate to study underlying mechanisms of NPH *in vivo*, especially concerning fibrosis and infiltrating immune cells, and to investigate its role in DNA damage. Using CRISPR/Cas9-mediated genome engineering, we generated a mouse model with a 14 bp deletion resulting in a frameshift and a premature stop codon after 41 amino acids (Figure 30). Unfortunately, due to the lack of *Glis2* antibodies we were not able to confirm the knockout on protein level. Surprisingly, the *Glis2*<sup>emKO1/emKO1</sup> mice did not show a phenotype at four months of age, whereas both published *Glis2*<sup>-/-</sup> models report lesions and tubulointerstitial cell infiltration with interstitial fibrosis before the age of three months (Attanasio et al., 2007; Kim et al., 2008). However, Kim et al. also noted that within the same age range, the progression and severity of the observed phenotype was variable (Kim et al., 2008). We discovered that our mice develop a cystic and fibrotic kidney phenotype at two years of age. Trying to explain the delayed disease onset in our model, we realized that *Glis2* does have an additional methionine at position 41, which could result in a truncated protein rather than a null-mutant. For NPH it is also published that mutations within one gene can result in a variable disease onset, progression, as well as extra renal manifestations (Tory et al., 2009). *NPHP3* mutations had first been linked to the adolescent form of NPH leading to ESRD at a median age of 19 years (Omran et al.,

2000). Later *NPHP3* mutations were also found in patients with juvenile NPH and finally found in patients with infantile NPH (Hoefele et al., 2007; Otto et al., 2008). Since both published *Glis2*<sup>-/-</sup> mouse models as well as published patients had mutations in the area downstream, we decided to generate a second mouse model. In the *Glis2*<sup>emKO2/emKO2</sup> model, we now targeted the third coding exon where the zinc finger motifs start (Figure 30). Our second model also presented with a severe phenotype at 1.5 years of age, even though the exact time course of disease onset and progression needs further investigation (Figure 32). Another explanation for the difference in disease onset and severity could be in the background and housing of the mice. It has been shown that for several diseases, including kidney diseases, that the exact genetic background of the used mouse strain has a crucial impact on the phenotype (Arroyo et al., 2021; Ma and Fogo, 2003; Montagutelli, 2000; Rivera and Tessarollo, 2008). It can not only shift the disease onset significantly, but also eliminate the phenotype. Even the more subtle differences as for the C57BL/6J and C57BL/6N can result in different characteristics of the mouse strains (Kang et al., 2018). The *Glis2*<sup>-/-</sup> model published by Attanasio et al. was generated and backcrossed to C57BL/6J (Attanasio et al., 2007). Kim et al. used 129Sv genomic DNA as a template, an embryonic stem cell line derived from 129HsdOla mice, blastocysts from C57BL/6 mice and pseudo pregnant CD1 females for their *Glis2*<sup>-/-</sup> model. Crossing was then done with C57BL/6 mice without specifying the origin. Our mice were generated in and backcrossed to a C57BL/6N background. The differences in genetic background, targeting strategy, and housing facilities could account for the observed variability in disease onset.

The *Glis2*<sup>-/-</sup> mouse model first published by Kim et al. was later on crossed into a mouse model with a conditional deletion of *Kif3a* in kidney tubule cells, a non-orthologous PKD model characterized by loss of primary cilia and severe cyst growth with enlarged kidneys (Lu et al., 2016). In the presence of DNA damage, the *Kif3a* mutant loses the cell cycle arrest due to uncontrolled proliferation and destabilization of p53. This study connects loss-of-function of *Glis2* with activation of DNA damage response by showing increased levels of phosphorylated histone H2AX. They conclude that loss of *Glis2* results in induction of senescence in cells (Jin et al., 2020; Lu et al., 2016) and is therefore partially able to rescue the *Kif3a* mutant phenotype. We now want to utilize our model to study the role of DNA damage and cell death before and during disease onset to get a clearer idea of how these contribute to renal degeneration and fibrosis and how they could be targeted in novel therapeutic strategies.

#### 7.6.2 *Tmem218*<sup>emKO/emKO</sup> mice present with cysts arising from distal tubules.

Mice lacking the transmembrane protein *Tmem218* show impaired development and function of the kidney and eye (Vogel et al., 2015). Diffuse renal cyst development, tubulointerstitial nephropathy, and disruption of the tubular basement membrane have been observed in the kidneys of the mutant mice. Importantly, this model does not show enlargement of the cystic kidneys. The eye phenotype is

characterized by slow-onset loss of photoreceptors similar to the phenotype in *retinitis pigmentosa* in humans. Both phenotypes observed in the *Tmem218*<sup>-/-</sup> mice are hallmarks of the Senior-Løken syndrome, which is characterized by autosomal recessive NPH and *retinitis pigmentosa*. A mouse model of the classical Senior-Løken gene, *Iqcb1* (*Nphp5*), does show the characteristic eye phenotype. However, the *Nphp5* mutant mice do not present with a kidney phenotype, thus, representing only a partial match to the human phenotype (Ronquillo et al., 2016). A later study performed in *C. elegans* linked TMEM218 to the Meckel Gruber Syndrome module and the ciliary transition zone strengthening the connection between TMEM218 and ciliopathies. Similar to NPHP5, TMEM218 only correctly localizes to the TZ in the presence of CEP290 (Li et al., 2016; Sang et al., 2011; Schäfer et al., 2008). Altogether, this made TMEM218 a promising candidate for us to study the molecular mechanism in NPH and generate a much-needed NPH mouse model that closely resembles human phenotype. Strikingly, several patients with mutations in *TMEM218* have been identified with the ciliopathy phenotypes Joubert and Meckel syndrome very recently (Van De Weghe et al., 2021).

Recently, there have been more and more studies successfully implementing patient mutations in mouse models to recreate human phenotypes facilitated by the development of CRISPR/Cas9-mediated genome editing (Butt et al., 2020; Lamprecht Tratar et al., 2018; Shengru et al., 2019). For the *Tmem128* mutant mouse model we decided to implement the *Tmem218* c.111G>T (p.Arg37Ser) patient mutation (Figure 33), of which we learned in the framework of a collaboration with Carsten Bergmann in Freiburg. We used an asymmetric ssODN strategy, which previously had shown high success in cell culture to introduce point mutations (Richardson et al., 2016). Moreover, we also decided to switch from pronuclear injections to electroporation. In a collaboration with the CECAD in vivo research facility (transgenic core unit) we have previously contributed to a study showing this to be efficient and easier to handle (Tröder et al., 2018). The successful integration of the patient mutation could be confirmed on the DNA level. Unfortunately, we cannot make any statements on the protein levels as the available antibodies did not work on mouse tissue so far and due to the nature of the protein, consisting mainly of transmembrane domains, using a targeted MS approach has not shown any success. We also failed to generate specific monoclonal antibodies ourselves (data not shown). However, the *Tmem218.R37S* model did not show any kidney phenotype at 6 months (Figure 34). Whether this model might present with an eye phenotype, similarly to the phenotype of the *Iqcb1* (*Nphp5*) mouse model, is currently under investigation.

Besides the *Tmem218.R37S* model, we generated a mouse model lacking 10 bp at the intron-exon junction at the start of exon3 (Figure 33), which is expected to be a null allele. In contrast to the model with the patient mutation, this model presents with dilated tubule and beginning cysts at three months of age (Figure 34). At four months the models presents with a clear renal phenotype with corticomedullary cysts arising from distal tubules. Whether other organs are affected in this mouse

model is still under investigation. Since the *Tmem218<sup>emKO/emKO</sup>* presents with clear renal cysts and some fibrosis at later stage, this will be a great tool to study cystogenesis *in vivo*. Moreover, the time course of the disease onset and progression will allow us to test different therapeutic strategies *in vivo* to evaluate the effect on cyst growth. This could provide valuable insights into the mechanisms underlying cystogenesis and could ultimately lead to novel therapeutic approaches to stop and/or slow down cyst growth in different PKDs.

### 7.6.3 Perspectives of mouse models to study NPH *in vivo*

Our approaches to find suitable models to study NPH *in vivo* as well as various published studies show how difficult this task is. Very recently, a *NPHP1* mouse model has been published with a NPH phenotype (Li et al., 2021) while other published *NPHP1* models as well one that was generated in our lab (unpublished data) do not show any renal phenotype. The genetic background of the used mouse strains, the targeted region, as well as the exact mutation are important considerations when developing and using *in vivo* disease models.

Moreover, NPH is also a very heterogeneous disease itself. It presents with different onsets, severities, and extra renal functions in patients based on the affected gene and even if the same gene is affected. Moreover, in many cases, the underlying mutations are not yet discovered and there are frequently more disease causing genes proposed and identified (Hildebrandt et al., 2009; Srivastava et al., 2018). Additionally, it has been proposed that in a subset of patients not only one mutation but a combination of mutations in multiple genes might cause the disease (Benzing and Schermer, 2012). For example, *NPHP2* and *NPHP3* mutations are known to occur in the same patients (Tory et al., 2009).

Based on the diversity of the disease, one mouse model will not be enough to study all aspects of this heterogeneous disease. The strength of NPH *in vivo* research will lie in combining different models to study different aspects of NPH and combining the results to get a better understanding of the underlying mechanism of NPH as well as PKD in general. *Glis2<sup>emKO2/emKO2</sup>* mice presenting with a late onset could provide valuable insight in studying the disease onset and the role of DNA damage and cell death. *Tmem218<sup>emKO/emKO</sup>* mice present with a disease onset after 2-3 months and a rather cyst focused phenotype. This presents many opportunities to study cyst development as well as to test preventive and curative therapeutic strategies. Combining these models with, for example, the *Aatf<sup>AKO</sup>* model which lacks *Aatf* in tubular epithelial cells in the distal nephron and presents with a rather fibrotic renal phenotype, or PKD models like the *Pkd1<sup>RC/RC</sup>* model would already cover a large proportion of PKDs (Hopp et al., 2012; Jain et al., 2019).

## 8 Conclusion

*JADE1* and partially also *JADE2* and *JADE3* have been shown to play a role in several different cellular functions, including Wnt signaling, cell cycle progression, and histone acetylation. Moreover, *JADE1* has been implicated in relation to several hereditary renal diseases and kidney cancer. Here, we identified a novel mechanism of how the JADE protein family is able to influence such a broad range of cellular processes in health and diseases. We performed an unbiased analysis of functions of the Jade protein family within renal epithelial cells. This global approach allowed us to identify a novel, common function of the Jade protein family member in regulating proteasomal abundance and activity. Our data suggests that Jade expression levels are tightly linked to proteasomal function. The proteasome is a crucial regulator of multiple essential cellular processes including protein synthesis, cell cycle regulation, cell survival, and inflammation. In recent years, the proteasome has been a popular target in developing novel therapeutic strategies. Global downregulation of the proteasome by inhibiting the core unit with proteasome inhibitors has been successfully implemented in patient care. Upregulation of the proteasome has proven difficult. Here, the JADE protein family now becomes a prime candidate to study the underlying processes. We developed a broad range of tools to discover the exact mechanism of Jade expression dependent proteasomal dysregulation as well as to translate these findings into *in vivo* models. In the future, this could not only lead to a better understanding of PKD but also to identify druggable targets to develop novel therapeutic strategies for PKD and a wide range of diseases in which the same cellular functions are disrupted.

In addition, we generated novel mouse models carrying null alleles within two genes (*Glis2* and *Tmem218*) pathogenic mutations of which can cause NPH-related ciliopathies. NPH-related ciliopathies are hereditary diseases leading to progressive cystic degenerative kidney disease and renal failure in children and adolescents. Research on NPH was limited by the availability of mouse models assembling the disease. Utilizing CRISPR/Cas9-mediated genome editing, we now could generate new mutant mouse models for *Glis2* and *Tmem218*, which cover important aspects of the human NPH phenotype. The new mouse models can now be used to gain novel insights into the underlying disease mechanisms, especially with respect to signaling between cells types and tissues, as well as to test novel therapeutic approaches *in vivo*.

## 9 References

- Aasland, R., Gibson, T.J., and Stewart, A.F. (1995). The PHD finger: Implications for chromatin-mediated transcriptional regulation. *Trends Biochem Sci* 20, 56–59.
- Airik, R., Slaats, G.G., Guo, Z., Weiss, A.-C., Khan, N., Ghosh, A., Hurd, T.W., Bekker-Jensen, S., Schrøder, J.M., Elledge, S.J., et al. (2014). Renal-Retinal Ciliopathy Gene *Sdccag8* Regulates DNA Damage Response Signaling. *J Am Soc Nephrol* 25, 2573–2583.
- Akahane, T., Sahara, K., Yashiroda, H., Tanaka, K., and Murata, S. (2013). Involvement of Bag6 and the TRC pathway in proteasome assembly. *Nat Commun* 4, 2234.
- Altschul, S.F., Gish, W., Miller, W., Myers, E.W., and Lipman, D.J. (1990). Basic local alignment search tool. *J Mol Biol* 215, 403–410.
- Amente, S., Lania, L., and Majello, B. (2013). The histone LSD1 demethylase in stemness and cancer transcription programs. *Biochim Biophys Acta* 1829, 981–986.
- An, J., Sun, Y., Fisher, M., and Rettig, M.B. (2004). Maximal apoptosis of renal cell carcinoma by the proteasome inhibitor bortezomib is nuclear factor-kappaB dependent. *Mol Cancer Ther* 3, 727–736.
- Anan, K., Hino, S., Shimizu, N., Sakamoto, A., Nagaoka, K., Takase, R., Kohrogi, K., Araki, H., Hino, Y., Usuki, S., et al. (2018). LSD1 mediates metabolic reprogramming by glucocorticoids during myogenic differentiation. *Nucleic Acids Res* 46, 5441–5454.
- Anderson, R.G.W. (1972). The three-dimensional structure of the basal body from rhesus monkey oviduct. *J Cell Biol* 54, 246–265.
- Anvarian, Z., Mykytyn, K., Mukhopadhyay, S., Pedersen, L.B., and Christensen, S.T. (2019). Cellular signalling by primary cilia in development, organ function and disease. *Nat Rev Nephrol* 15, 199–219.
- Arroyo, J., Escobar-Zarate, D., Wells, H.H., Constans, M.M., Thao, K., Smith, J.M., Sieben, C.J., Martell, M.R., Kline, T.L., Irazabal, M.V., et al. (2021). The genetic background significantly impacts the severity of kidney cystic disease in the *Pkd1RC/RC* mouse model of autosomal dominant polycystic kidney disease. *Kidney Int* 99, 1392–1407.
- Asawa, R.R., Danchik, C., Zahkarov, A., Chen, Y., Voss, T., Jadhav, A., Wallace, D.P., Trott, J.F., Weiss, R.H., Simeonov, A., et al. (2020). A high-throughput screening platform for Polycystic Kidney Disease (PKD) drug repurposing utilizing murine and human ADPKD cells. *Sci Rep* 10, 4203.
- Atala, A., Freeman, M.R., Mandell, J., and Beier, D.R. (1993). Juvenile cystic kidneys (jck): a new mouse mutation which causes polycystic kidneys. *Kidney Int* 43, 1081–1085.
- Athar, A., Füllgrabe, A., George, N., Iqbal, H., Huerta, L., Ali, A., Snow, C., Fonseca, N.A., Petryszak, R., Papatheodorou, I., et al. (2019). ArrayExpress update – from bulk to single-cell expression data. *Nucleic Acids Res* 47, D711–D715.
- Attanasio, M., Uhlenhaut, N.H., Sousa, V.H., O’Toole, J.F., Otto, E., Anlag, K., Klugmann, C., Treier, A.-C., Helou, J., Sayer, J.A., et al. (2007). Loss of *GLIS2* causes nephronophthisis in humans and mice by increased apoptosis and fibrosis. *Nat Genet* 39, 1018–1024.

- Avvakumov, N., Lalonde, M.-E., Saksouk, N., Paquet, E., Glass, K.C., Landry, A.-J., Doyon, Y., Cayrou, C., Robitaille, G.A., Richard, D.E., et al. (2012). Conserved Molecular Interactions within the HBO1 Acetyltransferase Complexes Regulate Cell Proliferation. *Mol Cell Biol* 32, 689–703.
- Awata, J., Takada, S., Standley, C., Lechtreck, K.F., Bellvé, K.D., Pazour, G.J., Fogarty, K.E., and Witman, G.B. (2014). NPHP4 controls ciliary trafficking of membrane proteins and large soluble proteins at the transition zone. *J Cell Sci* 127, 4714–4727.
- Baldewijns, M.M.L., van Vlodrop, I.J.H., Schouten, L.J., Soetekouw, P.M.M.B., de Bruïne, A.P., and van Engeland, M. (2008). Genetics and epigenetics of renal cell cancer. *Biochim Biophys Acta* 1785, 133–155.
- Barbelanne, M., Hossain, D., Chan, D.P., Peränen, J., and Tsang, W.Y. (2015). Nephrocystin proteins NPHP5 and Cep290 regulate BBSome integrity, ciliary trafficking and cargo delivery. *Hum Mol Genet* 24, 2185–2200.
- Bard, J.A.M., Goodall, E.A., Greene, E.R., Jonsson, E., Dong, K.C., and Martin, A. (2018). Structure and Function of the 26S Proteasome. *Annu Rev Biochem* 87, 697–724.
- Barr, M.M., and Sternberg, P.W. (1999). A polycystic kidney-disease gene homologue required for male mating behaviour in *C. elegans*. *Nature* 401, 386–389.
- Barr, M.M., DeModena, J., Braun, D., Nguyen, C.Q., Hall, D.H., and Sternberg, P.W. (2001). The *Caenorhabditis elegans* autosomal dominant polycystic kidney disease gene homologs *lov-1* and *pkd-2* act in the same pathway. *Curr Biol* 11, 1341–1346.
- Bartram, M.P., Habbig, S., Pahmeyer, C., Höhne, M., Weber, L.T., Thiele, H., Altmüller, J., Kottoor, N., Wenzel, A., Krueger, M., et al. (2016). Three-layered proteomic characterization of a novel ACTN4 mutation unravels its pathogenic potential in FSGS. *Hum Mol Genet* 25, 1152–1164.
- Behringer, R. (2014). *Manipulating the mouse embryo: a laboratory manual* (Cold Spring Harbor, New York: Cold Spring Harbor Laboratory Press).
- Benmerah, A. (2013). The ciliary pocket. *Curr Opin Cell Biol* 25, 78–84.
- Benzing, T., and Schermer, B. (2012). Clinical spectrum and pathogenesis of nephronophthisis. *Curr Opin Nephrol Hypertens* 21, 272–278.
- Benzing, T., Gerke, P., Höpker, K., Hildebrandt, F., Kim, E., and Walz, G. (2001). Nephrocystin interacts with Pyk2, p130(Cas), and tensin and triggers phosphorylation of Pyk2. *Proc Natl Acad Sci U S A* 98, 9784–9789.
- Béraud, C., Dormoy, V., Danilin, S., Lindner, V., Béthry, A., Hochane, M., Coquard, C., Barthelmebs, M., Jacqmin, D., Lang, H., et al. (2015). Targeting FAK scaffold functions inhibits human renal cell carcinoma growth. *Int J Cancer* 137, 1549–1559.
- Bergmann, C. (2017). Recent advances in the molecular diagnosis of polycystic kidney disease. *Expert Rev Mol Diagn* 17, 1037–1054.
- Bergmann, C., and Weiskirchen, R. (2012). It's not all in the cilium, but on the road to it: genetic interaction network in polycystic kidney and liver diseases and how trafficking and quality control matter. *J Hepatol* 56, 1201–1203.

- Bergmann, C., Fliegau, M., Bröchle, N.O., Frank, V., Olbrich, H., Kirschner, J., Schermer, B., Schmedding, I., Kispert, A., Kränzlin, B., et al. (2008). Loss of nephrocystin-3 function can cause embryonic lethality, Meckel-Gruber-like syndrome, situs inversus, and renal-hepatic-pancreatic dysplasia. *Am J Hum Genet* *82*, 959–970.
- Bergmann, C., Guay-Woodford, L.M., Harris, P.C., Horie, S., Peters, D.J.M., and Torres, V.E. (2018). Polycystic kidney disease. *Nat Rev Dis Primers* *4*, 50.
- Bettencourt-Dias, M., Hildebrandt, F., Pellman, D., Woods, G., and Godinho, S.A. (2011). Centrosomes and cilia in human disease. *Trends Genet* *27*, 307–315.
- Bhogaraju, S., Engel, B.D., and Lorentzen, E. (2013). Intraflagellar transport complex structure and cargo interactions. *Cilia* *2*, 10.
- Bolger, A.M., Lohse, M., and Usadel, B. (2014). Trimmomatic: a flexible trimmer for Illumina sequence data. *Bioinformatics* *30*, 2114–2120.
- Borgal, L., Habbig, S., Hatzold, J., Liebau, M.C., Dafinger, C., Sacarea, I., Hammerschmidt, M., Benzing, T., and Schermer, B. (2012). The ciliary protein nephrocystin-4 translocates the canonical Wnt regulator Jade-1 to the nucleus to negatively regulate  $\beta$ -catenin signaling. *J Biol Chem* *287*, 25370–25380.
- Borgal, L., Rinschen, M.M., Dafinger, C., Hoff, S., Reinert, M.J., Lamkemeyer, T., Lienkamp, S.S., Benzing, T., and Schermer, B. (2014). Casein kinase 1  $\alpha$  phosphorylates the Wnt regulator Jade-1 and modulates its activity. *J Biol Chem* *289*, 26344–26356.
- Borgal, L., Rinschen, M.M., Dafinger, C., Liebrecht, V.I., Abken, H., Benzing, T., and Schermer, B. (2016). Jade-1S phosphorylation induced by CK1 $\alpha$  contributes to cell cycle progression. *Cell Cycle* *15*, 1034–1045.
- Bos, J.L. (2005). Linking Rap to cell adhesion. *Curr Opin Cell Biol* *17*, 123–128.
- Bos, J.L., de Bruyn, K., Enserink, J., Kuiperij, B., Rangarajan, S., Rehmann, H., Riedl, J., de Rooij, J., van Mansfeld, F., and Zwartkruis, F. (2003). The role of Rap1 in integrin-mediated cell adhesion. *Biochem Soc Trans* *31*, 83–86.
- Bosco, D.A., LaVoie, M.J., Petsko, G.A., and Ringe, D. (2011). Proteostasis and movement disorders: Parkinson's disease and amyotrophic lateral sclerosis. *Cold Spring Harb Perspect Biol* *3*, a007500.
- Brenner, W., Greber, I., Gudejko-Thiel, J., Beitz, S., Schneider, E., Walenta, S., Peters, K., Unger, R., and Thüroff, J.W. (2008). Migration of renal carcinoma cells is dependent on protein kinase Cdelta via beta1 integrin and focal adhesion kinase. *Int J Oncol* *32*, 1125–1131.
- Brody, J., and Kern, S. (2004). Brody, J.R. & Kern, S.E. History and principles of conductive media for standard DNA electrophoresis. *Anal. Biochem.* *333*, 1-13. *Anal Biochem* *333*, 1–13.
- Butt, L., Unnersjö-Jess, D., Höhne, M., Edwards, A., Binz-Lotter, J., Reilly, D., Hahnfeldt, R., Ziegler, V., Fremter, K., Rinschen, M.M., et al. (2020). A molecular mechanism explaining albuminuria in kidney disease. *Nat Metab* *2*, 461–474.
- Calvert, P.D., Schiesser, W.E., and Pugh, E.N. (2010). Diffusion of a soluble protein, photoactivatable GFP, through a sensory cilium. *J Gen Physiol* *135*, 173–196.
- Calvi, B.R. (2014). HBO1:JADE1 at the cell cycle chromatin crossroads. *Cell Cycle* *13*, 2322.

- Campos, E.I., Chin, M.Y., Kuo, W.H., and Li, G. (2004). Biological functions of the ING family tumor suppressors. *Cell Mol Life Sci* *61*, 2597–2613.
- Castelli, M., De Pascalis, C., Distefano, G., Ducano, N., Oldani, A., Lanzetti, L., and Boletta, A. (2015). Regulation of the microtubular cytoskeleton by Polycystin-1 favors focal adhesions turnover to modulate cell adhesion and migration. *BMC Cell Biol* *16*, 15.
- Cehajic-Kapetanovic, J., Birtel, J., McClements, M.E., Shanks, M.E., Clouston, P., Downes, S.M., Charbel Issa, P., and MacLaren, R.E. (2019). Clinical and Molecular Characterization of PROM1-Related Retinal Degeneration. *JAMA Netw Open* *2*, e195752.
- Chang, B., Khanna, H., Hawes, N., Jimeno, D., He, S., Lillo, C., Parapuram, S.K., Cheng, H., Scott, A., Hurd, R.E., et al. (2006). In-frame deletion in a novel centrosomal/ciliary protein CEP290/NPHP6 perturbs its interaction with RPGR and results in early-onset retinal degeneration in the rd16 mouse. *Hum Mol Genet* *15*, 1847–1857.
- Chang, S.-H., Yun, U.J., Choi, J.H., Kim, S., Lee, A.R., Lee, D.H., Seo, M.-J., Panic, V., Villanueva, C.J., Song, N.-J., et al. (2019). Identification of Phf16 and Pnpla3 as new adipogenic factors regulated by phytochemicals. *J Cell Biochem* *120*, 3599–3610.
- Chen, I., and Dubnau, D. (2004). DNA uptake during bacterial transformation. *Nat Rev Microbiol* *2*, 241–249.
- Chen, L., Clark, J.Z., Nelson, J.W., Kaissling, B., Ellison, D.H., and Knepper, M.A. (2019). Renal-Tubule Epithelial Cell Nomenclature for Single-Cell RNA-Sequencing Studies. *J Am Soc Nephrol* *30*, 1358–1364.
- Chen, L., Chou, C.-L., and Knepper, M.A. (2021). A Comprehensive Map of mRNAs and Their Isoforms across All 14 Renal Tubule Segments of Mouse. *J Am Soc Nephrol* *32*, 897–912.
- Chitalia, V.C., Foy, R.L., Bachschmid, M.M., Zeng, L., Panchenko, M.V., Zhou, M.I., Bharti, A., Seldin, D.C., Lecker, S.H., Dominguez, I., et al. (2008). Jade-1 inhibits Wnt signalling by ubiquitylating beta-catenin and mediates Wnt pathway inhibition by pVHL. *Nat Cell Biol* *10*, 1208–1216.
- Chu, V.T., Weber, T., Graf, R., Sommermann, T., Petsch, K., Sack, U., Volchkov, P., Rajewsky, K., and Kühn, R. (2016). Efficient generation of Rosa26 knock-in mice using CRISPR/Cas9 in C57BL/6 zygotes. *BMC Biotechnol* *16*, 4.
- Clark, J.Z., Chen, L., Chou, C.-L., Jung, H.J., Lee, J.W., and Knepper, M.A. (2019). Representation and relative abundance of cell-type selective markers in whole-kidney RNA-Seq data. *Kidney Int* *95*, 787–796.
- Clevers, H. (2006). Wnt/beta-catenin signaling in development and disease. *Cell* *127*, 469–480.
- Clevers, H., and Nusse, R. (2012). Wnt/ $\beta$ -catenin signaling and disease. *Cell* *149*, 1192–1205.
- Collin, G.B., Won, J., Hicks, W.L., Cook, S.A., Nishina, P.M., and Naggert, J.K. (2012). Meckelin Is Necessary for Photoreceptor Intraciliary Transport and Outer Segment Morphogenesis. *Invest Ophthalmol Vis Sci* *53*, 967–974.
- Consortium, T.U. (2019). UniProt: a worldwide hub of protein knowledge. *Nucleic Acids Res* *47*, D506–D515.

- Cook, S.A., Collin, G.B., Bronson, R.T., Naggert, J.K., Liu, D.P., Akeson, E.C., and Davisson, M.T. (2009). A Mouse Model for Meckel Syndrome Type 3. *J Am Soc Nephrol* 20, 753–764.
- Corn, P.G. (2007). Role of the ubiquitin proteasome system in renal cell carcinoma. *BMC Biochem* 8, S4.
- Cornec-Le Gall, E., Audrézet, M.-P., Chen, J.-M., Hourmant, M., Morin, M.-P., Perrichot, R., Charasse, C., Whebe, B., Renaudineau, E., Jousset, P., et al. (2013). Type of PKD1 mutation influences renal outcome in ADPKD. *J Am Soc Nephrol* 24, 1006–1013.
- Cornec-Le Gall, E., Torres, V.E., and Harris, P.C. (2018). Genetic Complexity of Autosomal Dominant Polycystic Kidney and Liver Diseases. *J Am Soc Nephrol* 29, 13–23.
- Cox, J., and Mann, M. (2008). MaxQuant enables high peptide identification rates, individualized p.p.b.-range mass accuracies and proteome-wide protein quantification. *Nat Biotechnol* 26, 1367–1372.
- Danhier, P., De Preter, G., Magat, J., Godechal, Q., Porporato, P.E., Jordan, B.F., Feron, O., Sonveaux, P., and Gallez, B. (2014). Multimodal cell tracking of a spontaneous metastasis model: comparison between MRI, electron paramagnetic resonance and bioluminescence. *Contrast Media Mol Imaging* 9, 143–153.
- Davenport, J.R., Watts, A.J., Roper, V.C., Croyle, M.J., van Groen, T., Wyss, J.M., Nagy, T.R., Kesterson, R.A., and Yoder, B.K. (2007). Conditional disruption of intraflagellar transport in adult mice leads to hyperphagia-induced obesity and slow onset cystic kidney disease. *Curr Biol* 17, 1586–1594.
- Davis, N.B., Taber, D.A., Ansari, R.H., Ryan, C.W., George, C., Vokes, E.E., Vogelzang, N.J., and Stadler, W.M. (2004). Phase II trial of PS-341 in patients with renal cell cancer: a University of Chicago phase II consortium study. *J Clin Oncol* 22, 115–119.
- Dishinger, J.F., Kee, H.L., Jenkins, P.M., Fan, S., Hurd, T.W., Hammond, J.W., Truong, Y.N.-T., Margolis, B., Martens, J.R., and Verhey, K.J. (2010). Ciliary entry of the kinesin-2 motor KIF17 is regulated by importin- $\beta$ 2 and Ran-GTP. *Nat Cell Biol* 12, 703–710.
- Dobin, A., Davis, C.A., Schlesinger, F., Drenkow, J., Zaleski, C., Jha, S., Batut, P., Chaisson, M., and Gingeras, T.R. (2013). STAR: ultrafast universal RNA-seq aligner. *Bioinformatics* 29, 15–21.
- Doherty, M.K., Hammond, D.E., Clague, M.J., Gaskell, S.J., and Beynon, R.J. (2009). Turnover of the human proteome: determination of protein intracellular stability by dynamic SILAC. *J Proteome Res* 8, 104–112.
- Doyon, Y., Cayrou, C., Ullah, M., Landry, A.-J., Côté, V., Selleck, W., Lane, W.S., Tan, S., Yang, X.-J., and Côté, J. (2006). ING tumor suppressor proteins are critical regulators of chromatin acetylation required for genome expression and perpetuation. *Mol Cell* 21, 51–64.
- Fedeles, S.V., Tian, X., Gallagher, A.-R., Mitobe, M., Nishio, S., Lee, S.H., Cai, Y., Geng, L., Crews, C.M., and Somlo, S. (2011). A genetic interaction network of five genes for human polycystic kidney and liver diseases defines polycystin-1 as the central determinant of cyst formation. *Nat Genet* 43, 639–647.
- Fick, G.M., and Gabow, P.A. (1994). Hereditary and acquired cystic disease of the kidney. *Kidney Int* 46, 951–964.

- Finley, D. (2009). Recognition and Processing of Ubiquitin-Protein Conjugates by the Proteasome. *Annu Rev Biochem* 78, 477–513.
- Follit, J.A., Li, L., Vucica, Y., and Pazour, G.J. (2010). The cytoplasmic tail of fibrocystin contains a ciliary targeting sequence. *J Cell Biol* 188, 21–28.
- Foy, R.L., Song, I.Y., Chitalia, V.C., Cohen, H.T., Saksouk, N., Cayrou, C., Vaziri, C., Côté, J., and Panchenko, M.V. (2008). Role of Jade-1 in the histone acetyltransferase (HAT) HBO1 complex. *J Biol Chem* 283, 28817–28826.
- Foy, R.L., Chitalia, V.C., Panchenko, M.V., Zeng, L., Lopez, D., Lee, J.W., Rana, S.V., Boletta, A., Qian, F., Tsiokas, L., et al. (2012). Polycystin-1 regulates the stability and ubiquitination of transcription factor Jade-1. *Hum Mol Genet* 21, 5456–5471.
- Frew, I.J., Thoma, C.R., Georgiev, S., Minola, A., Hitz, M., Montani, M., Moch, H., and Krek, W. (2008). pVHL and PTEN tumour suppressor proteins cooperatively suppress kidney cyst formation. *EMBO J* 27, 1747–1757.
- Gagnadoux, M.F., Bacri, J.L., Broyer, M., and Habib, R. (1989). Infantile chronic tubulo-interstitial nephritis with cortical microcysts: variant of nephronophthisis or new disease entity? *Pediatr Nephrol* 3, 50–55.
- Garcia, G., Raleigh, D.R., and Reiter, J.F. (2018). How the Ciliary Membrane Is Organized Inside-Out to Communicate Outside-In. *Current Biology* 28, R421–R434.
- Gerdes, J.M., and Katsanis, N. (2008). Ciliary function and Wnt signal modulation. *Curr Top Dev Biol* 85, 175–195.
- Gessulat, S., Schmidt, T., Zolg, D.P., Samaras, P., Schnatbaum, K., Zerweck, J., Knaute, T., Rechenberger, J., Delanghe, B., Huhmer, A., et al. (2019). Prosit: proteome-wide prediction of peptide tandem mass spectra by deep learning. *Nat Methods* 16, 509–518.
- Gilula, N.B., and Satir, P. (1972). The ciliary necklace. A ciliary membrane specialization. *J Cell Biol* 53, 494–509.
- Gorospe, M., Egan, J.M., Zbar, B., Lerman, M., Geil, L., Kuzmin, I., and Holbrook, N.J. (1999). Protective function of von Hippel-Lindau protein against impaired protein processing in renal carcinoma cells. *Mol Cell Biol* 19, 1289–1300.
- Grantham, J.J., Torres, V.E., Chapman, A.B., Guay-Woodford, L.M., Bae, K.T., King, B.F., Wetzel, L.H., Baumgarten, D.A., Kenney, P.J., Harris, P.C., et al. (2006). Volume Progression in Polycystic Kidney Disease. *N Engl J Med* 354, 2122–2130.
- Guo, J.-K., and Cantley, L.G. (2010). Cellular maintenance and repair of the kidney. *Annu Rev Physiol* 72, 357–376.
- Haider, N.B., Carmi, R., Shalev, H., Sheffield, V.C., and Landau, D. (1998). A Bedouin kindred with infantile nephronophthisis demonstrates linkage to chromosome 9 by homozygosity mapping. *Am J Hum Genet* 63, 1404–1410.
- Halbritter, J., Porath, J.D., Diaz, K.A., Braun, D.A., Kohl, S., Chaki, M., Allen, S.J., Soliman, N.A., Hildebrandt, F., Otto, E.A., et al. (2013). Identification of 99 novel mutations in a worldwide cohort of 1,056 patients with a nephronophthisis-related ciliopathy. *Hum Genet* 132, 865–884.

- Han, J., Lachance, C., Ricketts, M.D., McCullough, C.E., Gerace, M., Black, B.E., Côté, J., and Marmorstein, R. (2018). The scaffolding protein JADE1 physically links the acetyltransferase subunit HBO1 with its histone H3–H4 substrate. *J Biol Chem* 293, 4498–4509.
- Han, X., Gui, B., Xiong, C., Zhao, L., Liang, J., Sun, L., Yang, X., Yu, W., Si, W., Yan, R., et al. (2014). Destabilizing LSD1 by Jade-2 promotes neurogenesis: an antibraking system in neural development. *Mol Cell* 55, 482–494.
- Harlander, S., Schönenberger, D., Toussaint, N.C., Prummer, M., Catalano, A., Brandt, L., Moch, H., Wild, P.J., and Frew, I.J. (2017). Combined mutation in Vhl, Trp53 and Rb1 causes clear cell renal cell carcinoma in mice. *Nat Med* 23, 869–877.
- Hasanov, E., Tidwell, R.S.S., Fernandez, P., Park, L., McMichael, C., Tannir, N.M., and Jonasch, E. (2019). Phase II Study of Carfilzomib in Patients With Refractory Renal Cell Carcinoma. *Clin Genitourin Cancer* 17, 451–456.
- Havasi, A., Haegele, J.A., Gall, J.M., Blackmon, S., Ichimura, T., Bonegio, R.G., and Panchenko, M.V. (2013). Histone acetyl transferase (HAT) HBO1 and JADE1 in epithelial cell regeneration. *Am J Pathol* 182, 152–162.
- Hiesberger, T., Gourley, E., Erickson, A., Koulen, P., Ward, C.J., Masyuk, T.V., Larusso, N.F., Harris, P.C., and Igarashi, P. (2006). Proteolytic cleavage and nuclear translocation of fibrocystin is regulated by intracellular Ca<sup>2+</sup> and activation of protein kinase C. *J Biol Chem* 281, 34357–34364.
- Higgins, M., Obaidi, I., and McMorrow, T. (2019). Primary cilia and their role in cancer. *Oncol Lett* 17, 3041–3047.
- Hildebrandt, F., Otto, E., Rensing, C., Nothwang, H.G., Vollmer, M., Adolphs, J., Hanusch, H., and Brandis, M. (1997). A novel gene encoding an SH3 domain protein is mutated in nephronophthisis type 1. *Nat Genet* 17, 149–153.
- Hildebrandt, F., Attanasio, M., and Otto, E. (2009). Nephronophthisis: Disease Mechanisms of a Ciliopathy. *J Am Soc Nephrol* 20, 23–35.
- Hildebrandt, F., Benzing, T., and Katsanis, N. (2011). Ciliopathies. *N Engl J Med* 364, 1533–1543.
- Hino, S., Kohroggi, K., and Nakao, M. (2016). Histone demethylase LSD1 controls the phenotypic plasticity of cancer cells. *Cancer Sci* 107, 1187–1192.
- Hodgkins, A., Farne, A., Perera, S., Grego, T., Parry-Smith, D.J., Skarnes, W.C., and Iyer, V. (2015). WGE: a CRISPR database for genome engineering. *Bioinformatics* 31, 3078–3080.
- Hoefele, J., Wolf, M.T.F., O’Toole, J.F., Otto, E.A., Schultheiss, U., Dêschenes, G., Attanasio, M., Utsch, B., Antignac, C., and Hildebrandt, F. (2007). Evidence of Oligogenic Inheritance in Nephronophthisis. *J Am Soc Nephrol* 18, 2789–2795.
- Hopp, K., Ward, C.J., Hommerding, C.J., Nasr, S.H., Tuan, H.-F., Gainullin, V.G., Rossetti, S., Torres, V.E., and Harris, P.C. (2012). Functional polycystin-1 dosage governs autosomal dominant polycystic kidney disease severity. *J Clin Invest* 122, 4257–4273.
- van Houwelingen, K.P., van Dijk, B.A.C., Hulsbergen-van de Kaa, C.A., Schouten, L.J., Gorissen, H.J.M., Schalken, J.A., van den Brandt, P.A., and Oosterwijk, E. (2005). Prevalence of von Hippel-Lindau gene mutations in sporadic renal cell carcinoma: results from The Netherlands cohort study. *BMC Cancer* 5, 57.

- Howe, K.L., Achuthan, P., Allen, J., Allen, J., Alvarez-Jarreta, J., Amode, M.R., Armean, I.M., Azov, A.G., Bennett, R., Bhai, J., et al. (2021). Ensembl 2021. *Nucleic Acids Res* 49, D884–D891.
- Hoyer, P.F. (2015). Clinical manifestations of autosomal recessive polycystic kidney disease. *Curr Opin Pediatr* 27, 186–192.
- Huber, T.B., Köttgen, M., Schilling, B., Walz, G., and Benzing, T. (2001). Interaction with Podocin Facilitates Nephrin Signaling\*. *J Biol Chem* 276, 41543–41546.
- Huber, T.B., Simons, M., Hartleben, B., Sernetz, L., Schmidts, M., Gundlach, E., Saleem, M.A., Walz, G., and Benzing, T. (2003). Molecular basis of the functional podocin-nephrin complex: mutations in the NPHS2 gene disrupt nephrin targeting to lipid raft microdomains. *Hum Mol Genet* 12, 3397–3405.
- Hughes, C.S., Moggridge, S., Müller, T., Sorensen, P.H., Morin, G.B., and Krijgsveld, J. (2019). Singlepot, solid-phase-enhanced sample preparation for proteomics experiments. *Nat Protoc* 14, 68–85.
- Hurd, T.W., Otto, E.A., Mishima, E., Gee, H.Y., Inoue, H., Inazu, M., Yamada, H., Halbritter, J., Seki, G., Konishi, M., et al. (2013). Mutation of the Mg<sup>2+</sup> transporter SLC41A1 results in a nephronophthisis-like phenotype. *J Am Soc Nephrol* 24, 967–977.
- Imai, J., Maruya, M., Yashiroda, H., Yahara, I., and Tanaka, K. (2003). The molecular chaperone Hsp90 plays a role in the assembly and maintenance of the 26S proteasome. *EMBO J* 22, 3557–3567.
- Jain, M., Kaiser, R.W.J., Bohl, K., Hoehne, M., Göbel, H., Bartram, M.P., Habbig, S., Müller, R.-U., Fogo, A.B., Benzing, T., et al. (2019). Inactivation of Apoptosis Antagonizing Transcription Factor in tubular epithelial cells induces accumulation of DNA damage and nephronophthisis. *Kidney Int* 95, 846–858.
- Jászai, J., Thamm, K., Karbanová, J., Janich, P., Fargeas, C.A., Huttner, W.B., and Corbeil, D. (2020). Prominins control ciliary length throughout the animal kingdom: New lessons from human prominin-1 and zebrafish prominin-3. *J Biol Chem* 295, 6007–6022.
- Jian, Y., Wang, M., Zhang, Y., Ou, R., Zhu, Z., Ou, Y., Chen, X., Liang, X., Ding, Y., Song, L., et al. (2018). Jade family PHD finger 3 (JADE3) increases cancer stem cell-like properties and tumorigenicity in colon cancer. *Cancer Letters* 428, 1–11.
- Jiang, S.-T., Chiou, Y.-Y., Wang, E., Lin, H.-K., Lee, S.-P., Lu, H.-Y., Wang, C.-K.L., Tang, M.-J., and Li, H. (2008). Targeted disruption of Nphp1 causes male infertility due to defects in the later steps of sperm morphogenesis in mice. *Hum Mol Genet* 17, 3368–3379.
- Jin, H., Zhang, Y., Liu, D., Wang, S.S., Ding, Q., Rastogi, P., Purvis, M., Wang, A., Elhadi, S., Ren, C., et al. (2020). Innate Immune Signaling Contributes to Tubular Cell Senescence in the Glis2 Knockout Mouse Model of Nephronophthisis. *Am J Pathol* 190, 176–189.
- Joly, D., Berissi, S., Bertrand, A., Strehl, L., Patey, N., and Knebelmann, B. (2006). Laminin 5 Regulates Polycystic Kidney Cell Proliferation and Cyst Formation\*. *J Biol Chem* 281, 29181–29189.
- Jonassen, J.A., San Agustin, J., Follit, J.A., and Pazour, G.J. (2008). Deletion of IFT20 in the mouse kidney causes misorientation of the mitotic spindle and cystic kidney disease. *J Cell Biol* 183, 377–384.
- Joosten, S.C., Smits, K.M., Aarts, M.J., Melotte, V., Koch, A., Tjan-Heijnen, V.C., and van Engeland, M. (2018). Epigenetics in renal cell cancer: mechanisms and clinical applications. *Nat Rev Urol* 15, 430–451.

- Jordan, M.A., Diener, D.R., Stepanek, L., and Pigino, G. (2018). The cryo-EM structure of intraflagellar transport trains reveals how dynein is inactivated to ensure unidirectional anterograde movement in cilia. *Nat Cell Biol* 20, 1250–1255.
- Kagan, K.O., Dufke, A., and Gembruch, U. (2017). Renal cystic disease and associated ciliopathies. *Curr Opin Obstet Gynecol* 29, 85–94.
- Kaimori, J., Nagasawa, Y., Menezes, L.F., Garcia-Gonzalez, M.A., Deng, J., Imai, E., Onuchic, L.F., Guay-Woodford, L.M., and Germino, G.G. (2007). Polyductin undergoes notch-like processing and regulated release from primary cilia. *Hum Mol Genet* 16, 942–956.
- Kang, S.K., Hawkins, N.A., and Kearney, J.A. (2018). C57BL/6J and C57BL/6N substrains differentially influence phenotype severity in the *Scn1a* +/- mouse model of Dravet syndrome. *Epilepsia Open* 4, 164–169.
- Kee, H.L., Dishinger, J.F., Blasius, T.L., Liu, C.-J., Margolis, B., and Verhey, K.J. (2012). A Size-Exclusion Permeability Barrier and Nucleoporins Characterize a Ciliary Pore Complex that Regulates Transport into Cilia. *Nat Cell Biol* 14, 431–437.
- Kiefer, S.M., Robbins, L., and Rauchman, M. (2012). Conditional expression of *Wnt9b* in *Six2*-positive cells disrupts stomach and kidney function. *PLoS One* 7, e43098.
- Kiesel, P., Alvarez Viar, G., Tsoy, N., Maraspini, R., Gorilak, P., Varga, V., Honigmann, A., and Pigino, G. (2020). The molecular structure of mammalian primary cilia revealed by cryo-electron tomography. *Nat Struct Mol Biol* 27, 1115–1124.
- Kim, Y.-S., Kang, H.S., Herbert, R., Beak, J.Y., Collins, J.B., Grissom, S.F., and Jetten, A.M. (2008). Krüppel-Like Zinc Finger Protein *Glis2* Is Essential for the Maintenance of Normal Renal Functions. *Mol Cell Biol* 28, 2358–2367.
- Kisselev, A.F., and Goldberg, A.L. (2005). Monitoring Activity and Inhibition of 26S Proteasomes with Fluorogenic Peptide Substrates. In *Methods in Enzymology*, (Academic Press), pp. 364–378.
- Knockenbauer, K.E., and Schwartz, T.U. (2016). The Nuclear Pore Complex as a Flexible and Dynamic Gate. *Cell* 164, 1162–1171.
- Knudson, A.G. (1971). Mutation and cancer: statistical study of retinoblastoma. *Proc Natl Acad Sci U S A* 68, 820–823.
- Köhler, G., and Milstein, C. (1975). Continuous cultures of fused cells secreting antibody of predefined specificity. *Nature* 256, 495–497.
- Kohli, P., Höhne, M., Jüngst, C., Bertsch, S., Ebert, L.K., Schauss, A.C., Benzing, T., Rinschen, M.M., and Schermer, B. (2017). The ciliary membrane-associated proteome reveals actin-binding proteins as key components of cilia. *EMBO Rep.* 18, 1521–1535.
- Koizumi, S., Irie, T., Hirayama, S., Sakurai, Y., Yashiroda, H., Naguro, I., Ichijo, H., Hamazaki, J., and Murata, S. (2016). The aspartyl protease *DDI2* activates *Nrf1* to compensate for proteasome dysfunction. *Elife* 5, e18357.
- Kondagunta, G.V., Drucker, B., Schwartz, L., Bacik, J., Marion, S., Russo, P., Mazumdar, M., and Motzer, R.J. (2004). Phase II trial of bortezomib for patients with advanced renal cell carcinoma. *J Clin Oncol* 22, 3720–3725.

- König, J., Kranz, B., König, S., Schlingmann, K.P., Titieni, A., Tönshoff, B., Habbig, S., Pape, L., Häffner, K., Hansen, M., et al. (2017). Phenotypic Spectrum of Children with Nephronophthisis and Related Ciliopathies. *Clin J Am Soc Nephrol* *12*, 1974–1983.
- Kors, S., Geijtenbeek, K., Reits, E., and Schipper-Krom, S. (2019). Regulation of Proteasome Activity by (Post-)transcriptional Mechanisms. *Front Mol Biosci* *6*, 48.
- Kwak, M.-K., Wakabayashi, N., Greenlaw, J.L., Yamamoto, M., and Kensler, T.W. (2003). Antioxidants enhance mammalian proteasome expression through the Keap1-Nrf2 signaling pathway. *Mol Cell Biol* *23*, 8786–8794.
- Lamar, E., Kintner, C., and Goulding, M. (2001). Identification of NKL, a novel Gli-Kruppel zinc-finger protein that promotes neuronal differentiation. *Development* *128*, 1335–1346.
- Lamprecht Tratar, U., Horvat, S., and Cemazar, M. (2018). Transgenic Mouse Models in Cancer Research. *Front Oncol* *8*, 268.
- Lee, H.J., Noormohammadi, A., Koyuncu, S., Calculli, G., Simic, M.S., Herholz, M., Trifunovic, A., and Vilchez, D. (2019). Prostaglandin signals from adult germ stem cells delay somatic aging of *Caenorhabditis elegans*. *Nat Metab* *1*, 790–810.
- Lee, J.W., Chou, C.-L., and Knepper, M.A. (2015). Deep Sequencing in Microdissected Renal Tubules Identifies Nephron Segment-Specific Transcriptomes. *J Am Soc Nephrol* *26*, 2669–2677.
- Lehrbach, N.J., and Ruvkun, G. (2016). Proteasome dysfunction triggers activation of SKN-1A/Nrf1 by the aspartic protease DDI-1. *Elife* *5*, e17721.
- Letunic, I., and Bork, P. (2018). 20 years of the SMART protein domain annotation resource. *Nucleic Acids Res* *46*, D493–D496.
- Li, X.-J., and Li, S. (2011). Proteasomal dysfunction in aging and Huntington disease. *Neurobiol Dis* *43*, 4–8.
- Li, C., Jensen, V.L., Park, K., Kennedy, J., Garcia-Gonzalo, F.R., Romani, M., De Mori, R., Bruel, A.-L., Gaillard, D., Doray, B., et al. (2016). MKS5 and CEP290 Dependent Assembly Pathway of the Ciliary Transition Zone. *PLoS Biol* *14*, e1002416.
- Li, D., Hu, M., Chen, H., Wu, X., Wei, X., Lin, H., Gao, X., Wang, H., Li, M., Ong, A.C.M., et al. (2021). An *Nphp1* knockout mouse model targeting exon 2–20 demonstrates characteristic phenotypes of human Nephronophthisis. *Hum Mol Genet*.
- Lian, X., Duan, X., Wu, X., Li, C., Chen, S., Wang, S., Cai, Y., and Weng, Z. (2012). Expression and clinical significance of von Hippel-Lindau downstream genes: Jade-1 and  $\beta$ -catenin related to renal cell carcinoma. *Urology* *80*, 485.e7-13.
- Lienkamp, S., Ganner, A., and Walz, G. (2012). Inversin, Wnt signaling and primary cilia. *Differentiation* *83*, S49–S55.
- Lin, F., Hiesberger, T., Cordes, K., Sinclair, A.M., Goldstein, L.S.B., Somlo, S., and Igarashi, P. (2003). Kidney-specific inactivation of the KIF3A subunit of kinesin-II inhibits renal ciliogenesis and produces polycystic kidney disease. *Proc Natl Acad Sci U S A* *100*, 5286–5291.

- Liu, Y.-X., Zhang, S.-F., Ji, Y.-H., Guo, S.-J., Wang, G.-F., and Zhang, G.-W. (2012). Whole-exome sequencing identifies mutated PCK2 and HUWE1 associated with carcinoma cell proliferation in a hepatocellular carcinoma patient. *Oncol Lett* 4, 847–851.
- Louie, C.M., Caridi, G., Lopes, V.S., Brancati, F., Kispert, A., Lancaster, M.A., Schlossman, A.M., Otto, E.A., Leitges, M., Gröne, H.-J., et al. (2010). AHI1 is required for photoreceptor outer segment development and is a modifier for retinal degeneration in nephronophthisis. *Nat Genet* 42, 175–180.
- Love, M.I., Huber, W., and Anders, S. (2014). Moderated estimation of fold change and dispersion for RNA-seq data with DESeq2. *Genome Biol* 15, 550.
- Lu, D., Rauhauser, A., Li, B., Ren, C., McEnery, K., Zhu, J., Chaki, M., Vadnagara, K., Elhadi, S., Jetten, A.M., et al. (2016). Loss of Glis2/NPHP7 causes kidney epithelial cell senescence and suppresses cyst growth in the Kif3a mouse model of cystic kidney disease. *Kidney Int* 89, 1307–1323.
- Lu, H., Galeano, M.C.R., Ott, E., Kaeslin, G., Kausalya, P.J., Kramer, C., Ortiz-Brüchle, N., Hilger, N., Metzis, V., Hiersche, M., et al. (2017). Mutations in DZIP1L, which encodes a ciliary-transition-zone protein, cause autosomal recessive polycystic kidney disease. *Nat Genet* 49, 1025–1034.
- Lubensky, I.A., Gnarr, J.R., Bertheau, P., Walther, M.M., Linehan, W.M., and Zhuang, Z. (1996). Allelic deletions of the VHL gene detected in multiple microscopic clear cell renal lesions in von Hippel-Lindau disease patients. *Am J Pathol* 149, 2089–2094.
- Ma, L.-J., and Fogo, A.B. (2003). Model of robust induction of glomerulosclerosis in mice: Importance of genetic background. *Kidney Int* 64, 350–355.
- MacDermot, K.D., Saggat-Malik, A.K., Economides, D.L., and Jeffery, S. (1998). Prenatal diagnosis of autosomal dominant polycystic kidney disease (PKD1) presenting in utero and prognosis for very early onset disease. *J Med Genet* 35, 13–16.
- MacDonald, B.T., Tamai, K., and He, X. (2009). Wnt/beta-catenin signaling: components, mechanisms, and diseases. *Dev Cell* 17, 9–26.
- MacLean, B., Tomazela, D.M., Shulman, N., Chambers, M., Finney, G.L., Frewen, B., Kern, R., Tabb, D.L., Liebler, D.C., and MacCoss, M.J. (2010). Skyline: an open source document editor for creating and analyzing targeted proteomics experiments. *Bioinformatics* 26, 966–968.
- Madeira F, Park Ym, Lee J, Buso N, Gur T, Madhusoodanan N, Basutkar P, Tivey Arn, Potter Sc, Finn Rd, et al. (2019). The EMBL-EBI search and sequence analysis tools APIs in 2019. *Nucleic Acids Res* 47, W636–W641.
- Malik, S.A., Modarage, K., and Goggolidou, P. (2020). The Role of Wnt Signalling in Chronic Kidney Disease (CKD). *Genes (Basel)* 11.
- Manasanch, E.E., and Orlowski, R.Z. (2017). Proteasome Inhibitors in Cancer Therapy. *Nat Rev Clin Oncol* 14, 417–433.
- Mandriota, S.J., Turner, K.J., Davies, D.R., Murray, P.G., Morgan, N.V., Sowter, H.M., Wykoff, C.C., Maher, E.R., Harris, A.L., Ratcliffe, P.J., et al. (2002). HIF activation identifies early lesions in VHL kidneys: evidence for site-specific tumor suppressor function in the nephron. *Cancer Cell* 1, 459–468.
- Mangos, S., Lam, P., Zhao, A., Liu, Y., Mudumana, S., Vasilyev, A., Liu, A., and Drummond, I.A. (2010). The ADPKD genes pkd1a/b and pkd2 regulate extracellular matrix formation. *Dis Model Mech* 3, 354–365.

- Mannhaupt, G., Schnall, R., Karpov, V., Vetter, I., and Feldmann, H. (1999). Rpn4p acts as a transcription factor by binding to PACE, a nonamer box found upstream of 26S proteasomal and other genes in yeast. *FEBS Lett* *450*, 27–34.
- Manning, D.K., Sergeev, M., van Heesbeen, R.G., Wong, M.D., Oh, J.-H., Liu, Y., Henkelman, R.M., Drummond, I., Shah, J.V., and Beier, D.R. (2013). Loss of the ciliary kinase Nek8 causes left-right asymmetry defects. *J Am Soc Nephrol* *24*, 100–112.
- Maw, M.A., Corbeil, D., Koch, J., Hellwig, A., Wilson-Wheeler, J.C., Bridges, R.J., Kumaramanickavel, G., John, S., Nancarrow, D., Röper, K., et al. (2000). A frameshift mutation in prominin (mouse)-like 1 causes human retinal degeneration. *Hum Mol Genet* *9*, 27–34.
- McQuinn, T.C., Miga, D.E., Mjaatvedt, C.H., Phelps, A.L., and Wessels, A. (2001). Cardiopulmonary malformations in the *inv/inv* mouse. *Anat Rec* *263*, 62–71.
- Meyer-Schwesinger, C. (2019). The ubiquitin–proteasome system in kidney physiology and disease. *Nat Rev Nephrol* *15*, 393–411.
- Mick, D.U., Rodrigues, R.B., Leib, R.D., Adams, C.M., Chien, A.S., Gygi, S.P., and Nachury, M.V. (2015). Proteomics of Primary Cilia by Proximity Labeling. *Dev. Cell* *35*, 497–512.
- Mitchison, H.M., and Valente, E.M. (2017). Motile and non-motile cilia in human pathology: from function to phenotypes. *J Pathol* *241*, 294–309.
- Molla-Herman, A., Ghossoub, R., Blisnick, T., Meunier, A., Serres, C., Silbermann, F., Emmerson, C., Romeo, K., Bourdoncle, P., Schmitt, A., et al. (2010). The ciliary pocket: an endocytic membrane domain at the base of primary and motile cilia. *J Cell Sci* *123*, 1785–1795.
- Montagutelli, X. (2000). Effect of the Genetic Background on the Phenotype of Mouse Mutations. *J Am Soc Nephrol* *11*, S101–S105.
- Moore, L.E., Nickerson, M.L., Brennan, P., Toro, J.R., Jaeger, E., Rinsky, J., Han, S.S., Zaridze, D., Matveev, V., Janout, V., et al. (2011). Von Hippel-Lindau (VHL) inactivation in sporadic clear cell renal cancer: associations with germline VHL polymorphisms and etiologic risk factors. *PLoS Genet* *7*, e1002312.
- Morgan, D., Turnpenny, L., Goodship, J., Dai, W., Majumder, K., Matthews, L., Gardner, A., Schuster, G., Vien, L., Harrison, W., et al. (1998). *Inversin*, a novel gene in the vertebrate left-right axis pathway, is partially deleted in the *inv* mouse. *Nat Genet* *20*, 149–156.
- Müller, R.-U., and Benzing, T. (2018). Cystic Kidney Diseases From the Adult Nephrologist’s Point of View. *Front Pediatr* *6*.
- Müller, R.-U., and Schermer, B. (2020). Hippo signaling—a central player in cystic kidney disease? *Pediatr Nephrol* *35*, 1143–1152.
- Murphy, G.P., and Hrushesky, W.J. (1973). A murine renal cell carcinoma. *J Natl Cancer Inst* *50*, 1013–1025.
- Musselman, C.A., and Kutateladze, T.G. (2009). PHD fingers: epigenetic effectors and potential drug targets. *Mol Interv* *9*, 314–323.
- Nachury, M.V., Seeley, E.S., and Jin, H. (2010). Trafficking to the Ciliary Membrane. *Annu Rev Cell Dev Biol* *26*, 59–87.

- Nagel, S., Ehrentraut, S., Meyer, C., Kaufmann, M., Drexler, H.G., and MacLeod, R.A.F. (2014). Oncogenic deregulation of NKL homeobox gene *MSX1* in mantle cell lymphoma. *Leuk Lymphoma* *55*, 1893–1903.
- Nalepa, G., Rolfe, M., and Harper, J.W. (2006). Drug discovery in the ubiquitin-proteasome system. *Nat Rev Drug Discov* *5*, 596–613.
- Navon, A., and Ciechanover, A. (2009). The 26 S Proteasome: From Basic Mechanisms to Drug Targeting. *J Biol Chem* *284*, 33713–33718.
- Oh, E.C., and Katsanis, N. (2012). Cilia in vertebrate development and disease. *Development* *139*, 443–448.
- Oh, E.C., and Katsanis, N. (2013). Context-Dependent Regulation of Wnt Signaling through the Primary Cilium. *J Am Soc Nephrol* *24*, 10–18.
- Olbrich, H., Fliegau, M., Hoefele, J., Kispert, A., Otto, E., Volz, A., Wolf, M.T., Sasmaz, G., Trauer, U., Reinhardt, R., et al. (2003). Mutations in a novel gene, *NPHP3*, cause adolescent nephronophthisis, tapeto-retinal degeneration and hepatic fibrosis. *Nat Genet* *34*, 455–459.
- Olsen, O., Funke, L., Long, J., Fukata, M., Kazuta, T., Trinidad, J.C., Moore, K.A., Misawa, H., Welling, P.A., Burlingame, A.L., et al. (2007). Renal defects associated with improper polarization of the CRB and DLG polarity complexes in *MALS-3* knockout mice. *J Cell Biol* *179*, 151–164.
- Omran, H., Fernandez, C., Jung, M., Häffner, K., Fargier, B., Villaquiran, A., Waldherr, R., Gretz, N., Brandis, M., Rüschenhoff, F., et al. (2000). Identification of a new gene locus for adolescent nephronophthisis, on chromosome 3q22 in a large Venezuelan pedigree. *Am J Hum Genet* *66*, 118–127.
- Omran, H., Häffner, K., Burth, S., Fernandez, C., Fargier, B., Villaquiran, A., Nothwang, H.-G., Schnittger, S., Lehrach, H., Woo, D., et al. (2001). Human Adolescent Nephronophthisis: Gene Locus Synteny with Polycystic Kidney Disease in Pcy Mice. *J Am Soc Nephrol* *12*, 107–113.
- Onuchic, L.F., Furu, L., Nagasawa, Y., Hou, X., Eggermann, T., Ren, Z., Bergmann, C., Senderek, J., Esquivel, E., Zeltner, R., et al. (2002). *PKHD1*, the polycystic kidney and hepatic disease 1 gene, encodes a novel large protein containing multiple immunoglobulin-like plexin-transcription-factor domains and parallel beta-helix 1 repeats. *Am J Hum Genet* *70*, 1305–1317.
- Ormaza, G., Medagli, B., Ibáñez de Opakua, A., Rodríguez, J.A., Merino, N., Villate, M., Onesti, S., and Blanco, F.J. (2017). The tumor suppressor inhibitor of growth 4 binds double-stranded DNA through its disordered central region. *FEBS Lett* *591*, 425–432.
- Ormaza, G., Rodríguez, J.A., Ibáñez de Opakua, A., Merino, N., Villate, M., Gorroño, I., Rábano, M., Palmero, I., Vilaseca, M., Kypta, R., et al. (2019). The Tumor Suppressor *ING5* Is a Dimeric, Bivalent Recognition Molecule of the Histone H3K4me3 Mark. *J Mol Biol* *431*, 2298–2319.
- O’Toole, J.F., Liu, Y., Davis, E.E., Westlake, C.J., Attanasio, M., Otto, E.A., Seelow, D., Nurnberg, G., Becker, C., Nuutinen, M., et al. (2010). Individuals with mutations in *XPNPEP3*, which encodes a mitochondrial protein, develop a nephronophthisis-like nephropathy. *J Clin Invest* *120*, 791–802.
- Otto, E.A., Schermer, B., Obara, T., O’Toole, J.F., Hiller, K.S., Mueller, A.M., Ruf, R.G., Hoefele, J., Beekmann, F., Landau, D., et al. (2003). Mutations in *INVS* encoding inversin cause nephronophthisis type 2, linking renal cystic disease to the function of primary cilia and left-right axis determination. *Nat Genet* *34*, 413–420.

- Otto, E.A., Helou, J., Allen, S.J., O'Toole, J.F., Wise, E.L., Ashraf, S., Attanasio, M., Zhou, W., Wolf, M.T.F., and Hildebrandt, F. (2008). Mutation analysis in nephronophthisis using a combined approach of homozygosity mapping, CEL I endonuclease cleavage, and direct sequencing. *Hum Mutat* *29*, 418–426.
- Oughtred, R., Rust, J., Chang, C., Breitkreutz, B.-J., Stark, C., Willems, A., Boucher, L., Leung, G., Kolas, N., Zhang, F., et al. (2021). The BioGRID database: A comprehensive biomedical resource of curated protein, genetic, and chemical interactions. *Protein Sci* *30*, 187–200.
- Panchenko, M.V. (2016). Structure, function and regulation of jade family PHD finger 1 (JADE1). *Gene* *589*, 1–11.
- Panchenko, M.V., Zhou, M.I., and Cohen, H.T. (2004). von Hippel-Lindau partner Jade-1 is a transcriptional co-activator associated with histone acetyltransferase activity. *J Biol Chem* *279*, 56032–56041.
- Park, J., Shrestha, R., Qiu, C., Kondo, A., Huang, S., Werth, M., Li, M., Barasch, J., and Suszták, K. (2018). Single-cell transcriptomics of the mouse kidney reveals potential cellular targets of kidney disease. *Science* *360*, 758–763.
- Pazour, G.J., Dickert, B.L., Vucica, Y., Seeley, E.S., Rosenbaum, J.L., Witman, G.B., and Cole, D.G. (2000). Chlamydomonas IFT88 and Its Mouse Homologue, Polycystic Kidney Disease Gene Tg737, Are Required for Assembly of Cilia and Flagella. *J Cell Biol* *151*, 709–718.
- Perez-Riverol, Y., Csordas, A., Bai, J., Bernal-Llinares, M., Hewapathirana, S., Kundu, D.J., Inuganti, A., Griss, J., Mayer, G., Eisenacher, M., et al. (2019). The PRIDE database and related tools and resources in 2019: improving support for quantification data. *Nucleic Acids Res* *47*, D442–D450.
- Phelan, M.C. (2006). Techniques for mammalian cell tissue culture. *Curr Protoc Protein Sci Appendix* *3*, Appendix 3C.
- Pino, L.K., Searle, B.C., Bollinger, J.G., Nunn, B., MacLean, B., and MacCoss, M.J. (2020). The Skyline ecosystem: Informatics for quantitative mass spectrometry proteomics. *Mass Spectrom Rev* *39*, 229–244.
- Plotnikova, O.V., Pugacheva, E.N., and Golemis, E.A. (2009). Primary Cilia and the Cell Cycle. *Methods Cell Biol* *94*, 137–160.
- Qian, C.-N., Knol, J., Igarashi, P., Lin, F., Zylstra, U., Teh, B.T., and Williams, B.O. (2005). Cystic renal neoplasia following conditional inactivation of *apc* in mouse renal tubular epithelium. *J Biol Chem* *280*, 3938–3945.
- Quintela, M., Sieglaff, D.H., Gazze, A.S., Zhang, A., Gonzalez, D., Francis, L., Webb, P., and Conlan, R.S. (2019). HBO1 directs histone H4 specific acetylation, potentiating mechano-transduction pathways and membrane elasticity in ovarian cancer cells. *Nanomedicine* *17*, 254–265.
- Radhakrishnan, S.K., Lee, C.S., Young, P., Beskow, A., Chan, J.Y., and Deshaies, R.J. (2010). Transcription factor Nrf1 mediates the proteasome recovery pathway after proteasome inhibition in mammalian cells. *Mol Cell* *38*, 17–28.
- Raman, A., Parnell, S.C., Zhang, Y., Reif, G.A., Dai, Y., Khanna, A., Daniel, E., White, C., Vivian, J.L., and Wallace, D.P. (2018). Periostin overexpression in collecting ducts accelerates renal cyst growth and fibrosis in polycystic kidney disease. *M J Physiol Renal Physiol* *315*, F1695–F1707.

- Ran, F.A., Hsu, P.D., Wright, J., Agarwala, V., Scott, D.A., and Zhang, F. (2013). Genome engineering using the CRISPR-Cas9 system. *Nat Protoc* 8, 2281–2308.
- Reiter, J.F., Blacque, O.E., and Leroux, M.R. (2012). The base of the cilium: roles for transition fibres and the transition zone in ciliary formation, maintenance and compartmentalization. *EMBO Rep* 13, 608–618.
- Rice, P., Longden, I., and Bleasby, A. (2000). EMBOSS: the European Molecular Biology Open Software Suite. *Trends Genet* 16, 276–277.
- Richardson, C.D., Ray, G.J., DeWitt, M.A., Curie, G.L., and Corn, J.E. (2016). Enhancing homology-directed genome editing by catalytically active and inactive CRISPR-Cas9 using asymmetric donor DNA. *Nat Biotechnol* 34, 339–344.
- Rivera, J., and Tessarollo, L. (2008). Genetic Background and the Dilemma of Translating Mouse Studies to Humans. *Immunity* 28, 1–4.
- Robinson, C.M., and Ohh, M. (2014). The multifaceted von Hippel-Lindau tumour suppressor protein. *FEBS Lett* 588, 2704–2711.
- Ronquillo, C.C., Hanke-Gogokhia, C., Revelo, M.P., Frederick, J.M., Jiang, L., and Baehr, W. (2016). Ciliopathy-associated IQCB1/NPHP5 protein is required for mouse photoreceptor outer segment formation. *FASEB J* 30, 3400–3412.
- Rosenbaum, J.L., and Witman, G.B. (2002). Intraflagellar transport. *Nat Rev Mol Cell Biol* 3, 813–825.
- Rosenwald, I.B., Chen, J.-J., Wang, S., Savas, L., London, I.M., and Pullman, J. (1999). Upregulation of protein synthesis initiation factor eIF-4E is an early event during colon carcinogenesis. *Oncogene* 18, 2507–2517.
- Ross, A.B., Langer, J.D., and Jovanovic, M. (2021). Proteome Turnover in the Spotlight: Approaches, Applications, and Perspectives. *Mol Cell Proteomics* 20.
- Rousseau, A., and Bertolotti, A. (2016). An evolutionarily conserved pathway controls proteasome homeostasis. *Nature* 536, 184–189.
- Saadi-Kheddouci, S., Berrebi, D., Romagnolo, B., Cluzeaud, F., Peuchmaur, M., Kahn, A., Vandewalle, A., and Perret, C. (2001). Early development of polycystic kidney disease in transgenic mice expressing an activated mutant of the beta-catenin gene. *Oncogene* 20, 5972–5981.
- Saha, V., Chaplin, T., Gregorini, A., Ayton, P., and Young, B.D. (1995). The leukemia-associated-protein (LAP) domain, a cysteine-rich motif, is present in a wide range of proteins, including MLL, AF10, and MLLT6 proteins. *Proc Natl Acad Sci U S A* 92, 9737–9741.
- Salomon, R., Saunier, S., and Niaudet, P. (2009). Nephronophthisis. *Pediatr Nephrol* 24, 2333–2344.
- Sanchez, R., and Zhou, M.-M. (2011). The PHD finger: a versatile epigenome reader. *Trends Biochem Sci* 36, 364–372.
- Sang, L., Miller, J.J., Corbit, K.C., Giles, R.H., Brauer, M.J., Otto, E.A., Baye, L.M., Wen, X., Scales, S.J., Kwong, M., et al. (2011). Mapping the Nephronophthisis-Joubert-Meckel-Gruber Protein Network Reveals Ciliopathy Disease Genes and Pathways. *Cell* 145, 513–528.

- Saunier, S., Calado, J., Heilig, R., Silbermann, F., Benessy, F., Morin, G., Konrad, M., Broyer, M., Gubler, M.C., Weissenbach, J., et al. (1997). A novel gene that encodes a protein with a putative src homology 3 domain is a candidate gene for familial juvenile nephronophthisis. *Hum Mol Genet* *6*, 2317–2323.
- Schäfer, T., Pütz, M., Lienkamp, S., Ganner, A., Bergbreiter, A., Ramachandran, H., Gieloff, V., Gerner, M., Mattonet, C., Czarnecki, P.G., et al. (2008). Genetic and physical interaction between the NPHP5 and NPHP6 gene products. *Hum Mol Genet* *17*, 3655–3662.
- Scheffers, M.S., Le, H., van der Bent, P., Leonhard, W., Prins, F., Spruit, L., Breuning, M.H., de Heer, E., and Peters, D.J.M. (2002). Distinct subcellular expression of endogenous polycystin-2 in the plasma membrane and Golgi apparatus of MDCK cells. *Hum Mol Genet* *11*, 59–67.
- Schermer, B., Ghenoiu, C., Bartram, M., Müller, R.U., Kotsis, F., Höhne, M., Kühn, W., Rapka, M., Nitschke, R., Zentgraf, H., et al. (2006). The von Hippel-Lindau tumor suppressor protein controls ciliogenesis by orienting microtubule growth. *J Cell Biol* *175*, 547–554.
- Schmidt, M., and Finley, D. (2014). Regulation of proteasome activity in health and disease. *Biochim Biophys Acta* *1843*, 10.1016/j.bbamcr.2013.08.012.
- Schokrpur, S., Hu, J., Moughon, D.L., Liu, P., Lin, L.C., Hermann, K., Mangul, S., Guan, W., Pellegrini, M., Xu, H., et al. (2016). CRISPR-Mediated VHL Knockout Generates an Improved Model for Metastatic Renal Cell Carcinoma. *Sci Rep* *6*, 29032.
- Seeger-Nukpezah, T., Little, J.L., Serzhanova, V., and Golemis, E.A. (2013). Cilia and cilia-associated proteins in cancer. *Drug Discov Today Dis Mech* *10*, e135–e142.
- Shafique, S., and Rashid, S. (2019). Structural basis for renal cancer by the dynamics of pVHL-dependent JADE1 stabilization and  $\beta$ -catenin regulation. *Prog Biophys Mol Biol* *145*, 65–77.
- Shengru, M., Zhou, Y., Yan, X., Li, Y., Sun, Q., Chen, J., and Tang, S. (2019). A Patient-Specific Point Mutation Mouse Model of X-Linked Retinoschisis by CRISPR/Cas9 System. *Invest Ophthalmol Vis Sci* *60*, 4211.
- Shuin, T., Kondo, K., Torigoe, S., Kishida, T., Kubota, Y., Hosaka, M., Nagashima, Y., Kitamura, H., Latif, F., and Zbar, B. (1994). Frequent somatic mutations and loss of heterozygosity of the von Hippel-Lindau tumor suppressor gene in primary human renal cell carcinomas. *Cancer Res* *54*, 2852–2855.
- Sievers F, Wilm A, Dineen D, Gibson Tj, Karplus K, Li W, Lopez R, McWilliam H, Remmert M, Söding J, et al. (2011). Fast, scalable generation of high-quality protein multiple sequence alignments using Clustal Omega. *Mol Syst Biol* *7*, 539–539.
- Simons, M., Gloy, J., Ganner, A., Bullerkotte, A., Bashkurov, M., Krönig, C., Schermer, B., Benzing, T., Cabello, O.A., Jenny, A., et al. (2005). Inversin, the gene product mutated in nephronophthisis type II, functions as a molecular switch between Wnt signaling pathways. *Nat Genet* *37*, 537–543.
- Siriwardana, N.S., Meyer, R., Havasi, A., Dominguez, I., and Panchenko, M.V. (2014). Cell cycle-dependent chromatin shuttling of HBO1-JADE1 histone acetyl transferase (HAT) complex. *Cell Cycle* *13*, 1885–1901.
- Siriwardana, N.S., Meyer, R.D., and Panchenko, M.V. (2015). The novel function of JADE1S in cytokinesis of epithelial cells. *Cell Cycle* *14*, 2821–2834.

- Smits, A.H., Ziebell, F., Joberty, G., Zinn, N., Mueller, W.F., Clauder-Münster, S., Eberhard, D., Fälth Savitski, M., Grandi, P., Jakob, P., et al. (2019). Biological plasticity rescues target activity in CRISPR knock outs. *Nat Methods* 16, 1087–1093.
- Smits, K.M., Schouten, L.J., van Dijk, B.A.C., Hulsbergen-van de Kaa, C.A., Wouters, K.A.D., Oosterwijk, E., van Engeland, M., and van den Brandt, P.A. (2008). Genetic and epigenetic alterations in the von hippel-lindau gene: the influence on renal cancer prognosis. *Clin Cancer Res* 14, 782–787.
- Solit, D.B., Zheng, F.F., Drobnjak, M., Münster, P.N., Higgins, B., Verbel, D., Heller, G., Tong, W., Cordon-Cardo, C., Agus, D.B., et al. (2002). 17-Allylamino-17-demethoxygeldanamycin induces the degradation of androgen receptor and HER-2/neu and inhibits the growth of prostate cancer xenografts. *Clin Cancer Res* 8, 986–993.
- Spithoven, E.M., Kramer, A., Meijer, E., Orskov, B., Wanner, C., Abad, J.M., Aresté, N., de la Torre, R.A., Caskey, F., Couchoud, C., et al. (2014). Renal replacement therapy for autosomal dominant polycystic kidney disease (ADPKD) in Europe: prevalence and survival—an analysis of data from the ERA-EDTA Registry. *Nephrol Dial Transplant* 29 *Suppl* 4, iv15-25.
- Srivastava, S., Molinari, E., Raman, S., and Sayer, J.A. (2018). Many Genes—One Disease? Genetics of Nephronophthisis (NPHP) and NPHP-Associated Disorders. *Front Pediatr* 5.
- Stokman, M., Lilien, M., and Knoers, N. (1993). Nephronophthisis. In *GeneReviews®*, M.P. Adam, H.H. Ardinger, R.A. Pagon, S.E. Wallace, L.J. Bean, G. Mirzaa, and A. Amemiya, eds. (Seattle (WA): University of Washington, Seattle), p.
- Stokman, M.F., Saunier, S., and Benmerah, A. (2021). Renal Ciliopathies: Sorting Out Therapeutic Approaches for Nephronophthisis. *Front Cell Dev Biol* 9, 653138.
- Stottmann, R.W., Tran, P.V., Turbe-Doan, A., and Beier, D.R. (2009). Ttc21b is required to restrict sonic hedgehog activity in the developing mouse forebrain. *Dev Biol* 335, 166–178.
- Taciak, B., Pruszynska, I., Kiraga, L., Bialasek, M., and Krol, M. (2018). Wnt signaling pathway in development and cancer. *J Physiol Pharmacol* 69.
- Tarade, D., and Ohh, M. (2018). The HIF and other quandaries in VHL disease. *Oncogene* 37, 139–147.
- Tokheim, C., Wang, X., Timms, R.T., Zhang, B., Mena, E.L., Wang, B., Chen, C., Ge, J., Chu, J., Zhang, W., et al. (2021). Systematic characterization of mutations altering protein degradation in human cancers. *Mol Cell* 81, 1292-1308.e11.
- Tony Yang, T., Su, J., Wang, W.-J., Craige, B., Witman, G.B., Bryan Tsou, M.-F., and Liao, J.-C. (2015). Superresolution Pattern Recognition Reveals the Architectural Map of the Ciliary Transition Zone. *Sci Rep* 5, 14096.
- Torres, V.E., Harris, P.C., and Pirson, Y. (2007). Autosomal dominant polycystic kidney disease. *Lancet* 369, 1287–1301.
- Tory, K., Rousset-Rouvière, C., Gubler, M.-C., Morinière, V., Pawtowski, A., Becker, C., Guyot, C., Gié, S., Frishberg, Y., Nivet, H., et al. (2009). Mutations of NPHP2 and NPHP3 in infantile nephronophthisis. *Kidney Int* 75, 839–847.

- Tröder, S.E., Ebert, L.K., Butt, L., Assenmacher, S., Schermer, B., and Zevnik, B. (2018). An optimized electroporation approach for efficient CRISPR/Cas9 genome editing in murine zygotes. *PLOS ONE* *13*, e0196891.
- Truett, G.E., Heeger, P., Mynatt, R.L., Truett, A.A., Walker, J.A., and Warman, M.L. (2000). Preparation of PCR-quality mouse genomic DNA with hot sodium hydroxide and tris (HotSHOT). *Biotechniques* *29*, 52, 54.
- Tyanova, S., Temu, T., Sinitcyn, P., Carlson, A., Hein, M.Y., Geiger, T., Mann, M., and Cox, J. (2016). The Perseus computational platform for comprehensive analysis of (prote)omics data. *Nat Methods* *13*, 731–740.
- Tzouanacou, E., Tweedie, S., and Wilson, V. (2003). Identification of Jade1, a gene encoding a PHD zinc finger protein, in a gene trap mutagenesis screen for genes involved in anteroposterior axis development. *Mol Cell Biol* *23*, 8553–8552.
- Uhlén, M., Fagerberg, L., Hallström, B.M., Lindskog, C., Oksvold, P., Mardinoglu, A., Sivertsson, Å., Kampf, C., Sjöstedt, E., Asplund, A., et al. (2015). Tissue-based map of the human proteome. *Science* *347*.
- Utsch, B., Sayer, J.A., Attanasio, M., Pereira, R.R., Eccles, M., Hennies, H.-C., Otto, E.A., and Hildebrandt, F. (2006). Identification of the first *AHI1* gene mutations in nephronophthisis-associated Joubert syndrome. *Pediatr Nephrol* *21*, 32–35.
- Valente, E.M., Logan, C.V., Mougou-Zerelli, S., Lee, J.H., Silhavy, J.L., Brancati, F., Iannicelli, M., Travaglini, L., Romani, S., Illi, B., et al. (2010). Mutations in *TMEM216* perturb ciliogenesis and cause Joubert, Meckel and related syndromes. *Nat Genet* *42*, 619–625.
- Van De Weghe, J.C., Giordano, J.L., Mathijssen, I.B., Mojarrad, M., Lugtenberg, D., Miller, C.V., Dempsey, J.C., Mohajeri, M.S.A., van Leeuwen, E., Pajkrt, E., et al. (2021). *TMEM218* dysfunction causes ciliopathies, including Joubert and Meckel syndromes. *HGG Adv* *2*.
- Vellai, T., and Takács-Vellai, K. (2010). Regulation of protein turnover by longevity pathways. *Adv Exp Med Biol* *694*, 69–80.
- Vierkotten, J., Dildrop, R., Peters, T., Wang, B., and Rütger, U. (2007). *Ftm* is a novel basal body protein of cilia involved in *Shh* signalling. *Development* *134*, 2569–2577.
- Vigolo, E., Markó, L., Hinze, C., Müller, D.N., Schmidt-Ullrich, R., and Schmidt-Ott, K.M. (2019). Canonical BMP signaling in tubular cells mediates recovery after acute kidney injury. *Kidney Int* *95*, 108–122.
- Vilchez, D., Morantte, I., Liu, Z., Douglas, P.M., Merkwirth, C., Rodrigues, A.P.C., Manning, G., and Dillin, A. (2012). *RPN-6* determines *C. elegans* longevity under proteotoxic stress conditions. *Nature* *489*, 263–268.
- Vivante, A., and Hildebrandt, F. (2016). Exome Sequencing Frequently Reveals the Cause of Early-Onset Chronic Kidney Disease. *Nat Rev Nephrol* *12*, 133–146.
- Vogel, P., Gelfman, C.M., Issa, T., Payne, B.J., Hansen, G.M., Read, R.W., Jones, C., Pitcher, M.R., Ding, Z.-M., DaCosta, C.M., et al. (2015). Nephronophthisis and retinal degeneration in *tmem218*<sup>-/-</sup> mice: a novel mouse model for Senior-Løken syndrome? *Vet Pathol* *52*, 580–595.

- Voorhees, P.M., and Orłowski, R.Z. (2006). The proteasome and proteasome inhibitors in cancer therapy. *Annu Rev Pharmacol Toxicol* 46, 189–213.
- Ward, C.J., Hogan, M.C., Rossetti, S., Walker, D., Sneddon, T., Wang, X., Kubly, V., Cunningham, J.M., Bacallao, R., Ishibashi, M., et al. (2002). The gene mutated in autosomal recessive polycystic kidney disease encodes a large, receptor-like protein. *Nat Genet* 30, 259–269.
- Ward, C.J., Yuan, D., Masyuk, T.V., Wang, X., Punyashthiti, R., Whelan, S., Bacallao, R., Torra, R., LaRusso, N.F., Torres, V.E., et al. (2003). Cellular and subcellular localization of the ARPKD protein; fibrocystin is expressed on primary cilia. *Hum Mol Genet* 12, 2703–2710.
- Watnick, T., and Germino, G. (2003). From cilia to cyst. *Nat Genet* 34, 355–356.
- Wefers, B., Bashir, S., Rossius, J., Wurst, W., and Kühn, R. (2017). Gene editing in mouse zygotes using the CRISPR/Cas9 system. *Methods* 121–122, 55–67.
- Wheway, G., Nazlamova, L., and Hancock, J.T. (2018). Signaling through the Primary Cilium. *Front. Cell Dev. Biol.* 6.
- Wilson, P.D. (2009). *Polycystic Kidney Disease* (Massachusetts Medical Society).
- Wilson, P.D., and Falkenstein, D. (1995). The Pathology of Human Renal Cystic Disease. In *Tubulointerstitial and Cystic Disease of the Kidney*, S.M. Dodd, ed. (Berlin, Heidelberg: Springer), pp. 1–50.
- Wolf, M.T.F., and Hildebrandt, F. (2011). Nephronophthisis. *Pediatr Nephrol* 26, 181–194.
- Won, J., Gifford, E., Smith, R.S., Yi, H., Ferreira, P.A., Hicks, W.L., Li, T., Naggert, J.K., and Nishina, P.M. (2009). RPGRIP1 is essential for normal rod photoreceptor outer segment elaboration and morphogenesis. *Hum Mol Genet* 18, 4329–4339.
- Won, J., de Evsikova, C.M., Smith, R.S., Hicks, W.L., Edwards, M.M., Longo-Guess, C., Li, T., Naggert, J.K., and Nishina, P.M. (2011). NPHP4 is necessary for normal photoreceptor ribbon synapse maintenance and outer segment formation, and for sperm development. *Hum Mol Genet* 20, 482–496.
- Xiao-Fen, W., Ting, C., Jie, L., Deng-Yang, M., Qing-Feng, Z., and Xin, L. (2016). Correlation analysis of VHL and Jade-1 gene expression in human renal cell carcinoma. *Open Med (Wars)* 11, 226–230.
- Xie, Y., and Varshavsky, A. (2001). RPN4 is a ligand, substrate, and transcriptional regulator of the 26S proteasome: a negative feedback circuit. *Proc Natl Acad Sci U S A* 98, 3056–3061.
- Yamamoto, T., and Horikoshi, M. (1997). Novel Substrate Specificity of the Histone Acetyltransferase Activity of HIV-1-Tat Interactive Protein Tip60\*. *J Biol Chem* 272, 30595–30598.
- Yang, T.T., Hampilos, P.J., Nathwani, B., Miller, C.H., Sutaria, N.D., and Liao, J.-C. (2013). Superresolution STED microscopy reveals differential localization in primary cilia. *Cytoskeleton (Hoboken)* 70, 54–65.
- Zeng, L., Bai, M., Mittal, A.K., El-Jouni, W., Zhou, J., Cohen, D.M., Zhou, M.I., and Cohen, H.T. (2013). Candidate tumor suppressor and pVHL partner Jade-1 binds and inhibits AKT in renal cell carcinoma. *Cancer Res* 73, 5371–5380.

- Zhang, F., Nakanishi, G., Kurebayashi, S., Yoshino, K., Perantoni, A., Kim, Y.-S., and Jetten, A.M. (2002). Characterization of Glis2, a Novel Gene Encoding a Gli-related, Krüppel-like Transcription Factor with Transactivation and Repressor Functions Roles in Kidney Development and Neurogenesis. *J Biol Chem* 277, 10139–10149.
- Zhang, X., Schulz, R., Edmunds, S., Krüger, E., Markert, E., Gaedcke, J., Cormet-Boyaka, E., Ghadimi, M., Beissbarth, T., Levine, A.J., et al. (2015). MicroRNA-101 Suppresses Tumor Cell Proliferation by Acting as an Endogenous Proteasome Inhibitor via Targeting the Proteasome Assembly Factor POMP. *Molecular Cell* 59, 243–257.
- Zhang, Y., Reif, G., and Wallace, D.P. (2020). Extracellular matrix, integrins, and focal adhesion signaling in polycystic kidney disease. *Cell Signal* 72, 109646.
- Zhao, J., and Goldberg, A.L. (2016). Coordinate regulation of autophagy and the ubiquitin proteasome system by MTOR. *Autophagy* 12, 1967–1970.
- Zhou, J., Wang, H., Che, J., Xu, L., Yang, W., Li, Y., and Zhou, W. (2020). Silencing of microRNA-135b inhibits invasion, migration, and stemness of CD24+CD44+ pancreatic cancer stem cells through JADE-1-dependent AKT/mTOR pathway. *Cancer Cell Int* 20, 134.
- Zhou, M.I., Wang, H., Ross, J.J., Kuzmin, I., Xu, C., and Cohen, H.T. (2002). The von Hippel-Lindau tumor suppressor stabilizes novel plant homeodomain protein Jade-1. *J Biol Chem* 277, 39887–39898.
- Zhou, M.I., Wang, H., Foy, R.L., Ross, J.J., and Cohen, H.T. (2004). Tumor suppressor von Hippel-Lindau (VHL) stabilization of Jade-1 protein occurs through plant homeodomains and is VHL mutation dependent. *Cancer Res* 64, 1278–1286.
- Zhou, M.I., Foy, R.L., Chitalia, V.C., Zhao, J., Panchenko, M.V., Wang, H., and Cohen, H.T. (2005). Jade-1, a candidate renal tumor suppressor that promotes apoptosis. *Proc Natl Acad Sci U S A* 102, 11035–11040.
- Zimmermann, K.W. (1898). Beiträge zur Kenntniss einiger Drüsen und Epithelien. *Archiv f. mikrosk. Anat.* 52, 552–706.

## 10 Publications

### 10.1 Publications in Academic Journals

Butt L, Unnersjö-Jess D, Höhne M, Edwards A, Binz-Lotter J, Reilly D, Hahnfeldt R, Ziegler V, Fremter K, Rinschen MM, Helmstädter M, **Ebert LK**, Castrop H, Hackl MJ, Walz G, Brinkkoetter PT, Liebau MC, Tory K, Hoyer PF, Beck BB, Brismar H, Blom H, Schermer B, Benzing T. A molecular mechanism explaining albuminuria in kidney disease. (2020) *Nat Metab*, 2(5):461-474

de Groot T\*, **Ebert LK\***, Christensen B., Andralojc K, Cheval L, Doucet A, Mao C, Baumgarten R, Low BE, Sandhoff R, Wiles MV, Deen P, & Korstanje R. (2019). Identification of *Acer2* as a First Susceptibility Gene for Lithium-Induced Nephrogenic Diabetes Insipidus in Mice. *JASN*, 30(12):2322–2336. \**Shared first authorship*

Tröder SE, **Ebert LK**, Butt L, Assenmacher S, Schermer B, Zevnik B. (2018) An optimized electroporation approach for efficient CRISPR/Cas9 genome editing in murine zygotes. *PLoS ONE*. 13(5):e0196891.

Kohli P, Höhne M, Jüngst C, Bertsch S, **Ebert LK**, Schauss AC, Benzing T, Rinschen MM, Schermer B. (2017) The ciliary membrane-associated proteome reveals actin-binding proteins as key components of cilia. *EMBO Rep*. 18(9):1521-1535.

### 10.2 Publications in International Academic Conferences

#### *Oral presentation*

**Ebert LK**, Kohli P, Höhne M, Münkner L, Ester L, Benzing T, Rinschen MM, Schermer B. Dynamic alterations of ciliary membrane-associated proteome. EMBO Workshop Cilia 2018, Copenhagen, Denmark, 2018

#### *Poster presentation*

**Ebert LK**, Benzing T, Schermer B. Unraveling the role of the Jade protein family in cilia biology, cell cycle regulation, and renal cell carcinoma. ASCB – EMBO Meeting, Washington, DC, USA, 2019

**Ebert L**, Benzing T, Schermer B. Unraveling the role of the Jade protein family in cilia biology, cell cycle regulation, and renal cell carcinoma. 35<sup>th</sup> Ernst Klenk Symposium in Molecular Medicine, Cologne, Germany, 2019

**Ebert L**, Kohli P, Höhne M, Slaats G, Benzing T, Rinschen M, Schermer B. Dynamic alterations of the ciliary membrane-associated proteome. 35<sup>th</sup> Ernst Klenk Symposium in Molecular Medicine, Cologne, Germany, 2019

**Ebert LK**, Butt L, Slaats GG, Späth MR, Hoyer JR, Burst V, Müller RU, Tröder S, Zevnik B, Benzing T, Schermer B. Crispr/Cas9 mediated genome-engineering to study cystic kidney diseases and related ciliopathies *in vitro* and *in vivo*. Keystone Symposia Conference. Precision Genome Engineering, Breckenridge, Colorado, USA, 2017

**Ebert L**, Butt L, Slaats G, Späth M, Hoyer J, Jain M, Keller S, Münkner L, Frech L, Burst V, Müller RU, Mende Y, Zevnik B, Benzing T, Schermer B. Crispr/Cas9 mediated genome-engineering to study ciliopathies in mice and in human cells. EMBO Workshop Cilia 2016, Amsterdam, The Netherlands, 2016.

### 11 Acknowledgements

First, I would like to thank Prof. Bernhard Schermer for his continuous support, constant motivation, and for sharing his great expertise. Moreover, I am also very thankful for Prof. Dr. Thomas Benzing's support and guidance. Thank you both for giving me the opportunity to do my PhD in the Nephrolab Cologne. I am looking forward to continuing my work here and future projects together.

I also would like to thank the entire Nephrolab. You all had part in making my time in the lab a great experience that I will always value. I would like to thank all members of the cilia team, especially Dr. Claudia Dafinger for being patient with all my mouse questions and Dr. Gisela Slaats for many fruitful discussions and helping with all cilia questions. I would like to thank Dr. Katrin Bohl for her bioinformatics support, Dr. Martin Höhne for always providing a critical view, and Dr. Francesca Fabretti for her guidance. I would like to thank my fellow PhD students for all the discussions, constant reassurance and many coffee breaks during our struggles together. Furthermore, I would like to thank our outstanding technician team. Stefanie Keller who is always willing to share her enormous expertise, Martyna Brütting for all her help with RNA work and histology, Serena Greco-Torres for her help with the mouse work, and Ruth Herzog for introducing me to the world of proteomics.

I would also like to acknowledge the team members of the Proteomics, Imaging and Animal Facility at the CECAD, especially Christian Frese, Jan-William Lackman, and Simon Tröder. Thank you for your support and valuable discussions. Moreover, I would also like to extend my gratitude to Prof. Dr. David Vilchez and Prof. Dr. Thorsten Hoppe for their valuable input and help regarding the proteasome part of the project.

I would like to thank my family, my parents Monika and Helmut Ebert as well as my sister Laura for their love, support, and motivation in all my activities. Last but not least, I would like to thank my husband Kyle Duncan for his patience, for encouraging me, and always believing in me.

## 12 Erklärung

Hiermit versichere ich an Eides statt, dass ich die vorliegende Dissertation selbstständig und ohne die Benutzung anderer als der angegebenen Hilfsmittel und Literatur angefertigt habe. Alle Stellen, die wörtlich oder sinngemäß aus veröffentlichten und nicht veröffentlichten Werken dem Wortlaut oder dem Sinn nach entnommen wurden, sind als solche kenntlich gemacht. Ich versichere an Eides statt, dass diese Dissertation noch keiner anderen Fakultät oder Universität zur Prüfung vorgelegen hat; dass sie - abgesehen von unten angegebenen Teilpublikationen und eingebundenen Artikeln und Manuskripten - noch nicht veröffentlicht worden ist sowie, dass ich eine Veröffentlichung der Dissertation vor Abschluss der Promotion nicht ohne Genehmigung des Promotionsausschusses vornehmen werde. Die Bestimmungen dieser Ordnung sind mir bekannt. Darüber hinaus erkläre ich hiermit, dass ich die Ordnung zur Sicherung guter wissenschaftlicher Praxis und zum Umgang mit wissenschaftlichem Fehlverhalten der Universität zu Köln gelesen und sie bei der Durchführung der Dissertation zugrundeliegenden Arbeiten und der schriftlich verfassten Dissertation beachtet habe und verpflichte mich hiermit, die dort genannten Vorgaben bei allen wissenschaftlichen Tätigkeiten zu beachten und umzusetzen. Ich versichere, dass die eingereichte elektronische Fassung der eingereichten Druckfassung vollständig entspricht.

### **Teilpublikationen:**

Ebert LK, Bargfrede S, Bohl K, Müller R-U, Benzing T, Schermer B. JADE family members regulate proteasome abundance and activity. (*Uploaded to bioRxiv, MS ID#: BIORXIV/2021/462752*)

**Lena Kathrin Ebert**

**Köln, den 3. Oktober 2021**